The Effects of Three-Dimensional Imposed Disturbances on Bluff Body Near Wake Flows

Effects of Taper and Splitter Plates on the Near Wake Characteristics of a Circular Cylinder in Uniform and Shear Flow

Elgin A. Anderson
and
Albin A. Szewczyk

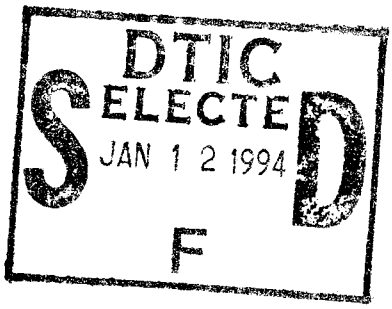

Department of Aerospace and Mechanical Engineering
University of Notre Dame
Notre Dame, Indiana 46556

Final Report on ONR contract no. N00014-90-J-4083

April 1994

EFFECTS OF TAPER AND SPLITTER PLATES ON THE NEAR WAKE CHARACTERISTICS OF A CIRCULAR CYLINDER IN UNIFORM AND SHEAR FLOW

Abstract

The near wake characteristics of a circular cylinder were modified by use of splitter plates, cylinder taper, and shear flow to investigate the relationship between the various near wake parameters. The results are based on hot wire and mean pressure measurements, flow visualization of the near wake, and linear stability analysis of the shear layer.

The straight cylinder variation in Strouhal number with respect to splitter plate length was divided into four regions identified by the flow phenomenon that dominates the shedding frequency selection namely, stabilizing, shear layer elongation, reduced entrainment, and splitter plate-vortex interaction. A sinuous plate increased the 2-dimensionality of the shear layer compared to the straight plate and affected the spanwise coherence of the Kármán vortices. However, within the formation region the sinuous splitter plate produced results similar to those produced by a straight plate of equal average length.

Shear flow past a straight circular cylinder produced spanwise cells of constant shedding frequency. Each cell behaved as a coherent structure whose characteristics were determined by the average flow conditions across the cell. The variation in shedding frequency for each cell with respect to plate length was found to be similar to the uniform flow behavior. However, a reduction in formation length was measured in the low velocity cell which was equivalent to an effective increase in splitter plate length. For intermediate

plate lengths amplitude modulation effects were revealed in the low velocity cell. These effects were attributed to an oscillation between a correlated cell-type behavior and an uncorrelated local-type behavior at the low velocity region of the span.

In uniform flow the tapered cylinder produced spanwise cells of constant shedding frequency similar to those observed for the straight cylinder in shear flow. It was demonstrated that a properly matched shear flow and taper ratio will produce a constant shedding frequency along the span.

Flow visualization images of the evolution of the transition vortices in the separated shear layer were produced. A 'phase-locking' between the transition waves of the two shear layers was observed and attributed to feedback from the Kármán shedding.

TABLE OF CONTENTS

LIST OF TABLES

LIST OF FIGURES

NOMENCLATURE

Alphabetical Symbols

AR	aspect ratio
a	sinuous splitter plate wave amplitude
C1,C2,...,Cn	curve fit constants
C_d	local drag coefficient
C_p	local pressure coefficient
C_{pb}	local base pressure coefficient
c_p	phase velocity
D	local cylinder diameter
d'	local wake width
E	mean voltage
E_{HW}	hot wire mean voltage
E_m	electronic manometer mean voltage
e_{rms}	root mean square of voltage fluctuations
f_s	shedding frequency
f_t	transition wave frequency
H	tunnel height
HP	horse power
ID	inside diameter
i	$\sqrt{-1}$ (Chapter 8)
i	index
k	wave number
K	base pressure parameter, $\sqrt{1-C_{pb}}$

L	cylinder length
ℓ	splitter plate length
ℓ_{avg}	average splitter plate length
ℓ_f	formation region length
ℓ_{fo}	formation region length for cylinder without a splitter plate
N	number of indices
n	index
OD	outside diameter
P_o	total pressure
P_m	freestream static pressure
P_s	shear layer static pressure
P_∞	ambient pressure
q	dynamic pressure
Re	Reynolds number based on cylinder diameter
Re_{ref}	Reynolds number based on cylinder diameter and U_{ref}
St	Strouhal number
St^*	modified Strouhal number
St'	Roshko's version of the Strouhal number
S_{xx}	power spectrum
T	sample period
T_∞	ambient temperature
t	time variable
U	local mean velocity
U_c	vortex convection velocity
U_c	$U_{max} - U_{min}$ (chapter 8)
U_m	mean freestream velocity
U_{max}	maximum measured velocity (chapter 8)

U_{min}	minimum measured velocity (chapter 8)
U_{ref}	mean velocity at mid-point of shear flow
U_s	shear layer velocity
U^*	non-dimensional mean velocity (chapter 8)
u	instantaneous x-direction velocity
u_1	x-direction velocity fluctuation
u_{rms}	root mean square of velocity fluctuations
v	instantaneous y-direction velocity
v_1	y-direction velocity fluctuation
W	wind tunnel width
w_n	Hanning window function
$X(f_k)$	discrete Fourier transform
x	streamwise dimension referenced from base of cylinder
y	transverse dimension referenced from center of cylinder
y^*	non-dimensional transverse dimension (chapter 8)
z	spanwise dimension referenced from center of cylinder

Greek Symbols

α	complex wave number
α^*	non-dimensional complex wave number
β	steepness parameter
β	complex frequency (chapter 8)
β^*	non-dimensional complex frequency (chapter 8)
Δ	difference
δ	boundary layer thickness
δ_o	boundary layer thickness at separation
ε	small perturbation quantity

Λ	shear parameter
λ	sinuous splitter plate wavelength
ρ	density
$\rho(\tau)$	cross-correlation coefficient
θ	angle from stagnation point
θ	shear layer momentum thickness (chapter 8)
θ_o	shear layer momentum thickness at separation (chapter 8)
Ψ	disturbance stream function
ϕ	complex amplitude of disturbance
ν	kinematic viscosity
σ	variance
τ	phase difference in seconds
$\tau_{\rho max}$	time period to maximum cross-correlation coefficient
Ω	non-dimensional vorticity
ω_t	transition wave frequency in rad/sec

CHAPTER 1. INTRODUCTION AND LITERATURE REVIEW

1.1 Introduction to the bluff body problem

Although there is no rigorous definition of a bluff body flow it is generally accepted that it is a flow over a relatively thick body in which flow separation and an unsteady wake are its primary characteristics. It is one of the most common flows encountered in the everyday world and a few examples include, flow over and around automobiles, bridges, skyscrapers, offshore drilling platforms, pilings, struts, and masts. In practical applications, the ability to predict and possibly control the drag and unsteady wake produced by a bluff body would greatly benefit the designers. In a broader sense, fluid mechanicians would benefit from an increased understanding of the complex fluid interactions presented by a flow past a bluff body. The Navier-Stokes equations, which are derived from a set of physical principles subject to a set of constraints (initial, boundary conditions, fluid properties) govern the behavior of bluff body flows for the majority of engineering applications. However, they cannot be solved directly because of the analytical difficulties in the non-linearity of the equations. Numerical solutions are limited by available techniques and computing power and are confined to relatively low speed regimes. As a consequence of these difficulties, most of the recent advances in the bluff body problem have been based on experiments. The current investigation is primarily experimental and focuses on a bluff body with a circular cross section. This geometry has attracted much of the bluff body experimental and theoretical research efforts because it is as simple and basic a streamlined bluff body that one can study and is a common shape found in engineering materials and designs.

There are different flow regimes associated with the bluff body problem and they may be categorized by the ratio of two dominant forces, inertia and viscous. This ratio, known as the Reynolds number, Re, is an important non-dimensional parameter commonly referred to in fluid mechanics. Experimental investigations found that flows of different velocity, viscosity and characteristic length demonstrate similar characteristics if they share a common Reynolds number. Low Reynolds number flows are dominated by viscous forces and behave differently than flows at higher Reynolds number. Flows at high Reynolds number, such as that investigated in this research have high inertia forces. The Reynolds number is defined,

$$Re = \frac{U_m D}{\nu} \tag{1.1}$$

where, U_m is the mean freestream velocity, D is the cylinder diameter, and ν is the kinematic viscosity of the fluid.

To the designer presented with a bluff body flow problem, the most important characteristics are typically the drag on the body and flow induced vibration caused by the unsteady wake. Reduction of drag and aerodynamic load is of importance in the design of most vehicles and structures. Perhaps though, as important to ensure the design of safe and long lasting structures, is an accurate understanding of the magnitude and frequency of the wake flow oscillations and how the wake interacts with the body to produce the unsteady loading. The variation in drag and shedding frequency with Reynolds number are presented in Figures 1.1 and 1.2 in the non-dimensional form of drag coefficient, C_d, and Strouhal number, St, defined,

$$C_d = \frac{\text{Drag Force / unit length}}{\frac{1}{2}\rho U_m^2 D} \tag{1.2}$$

$$St = \frac{f_s D}{U_m} \tag{1.3}$$

where, ρ is the density of the fluid, and f_s is the shedding frequency of the vortices.

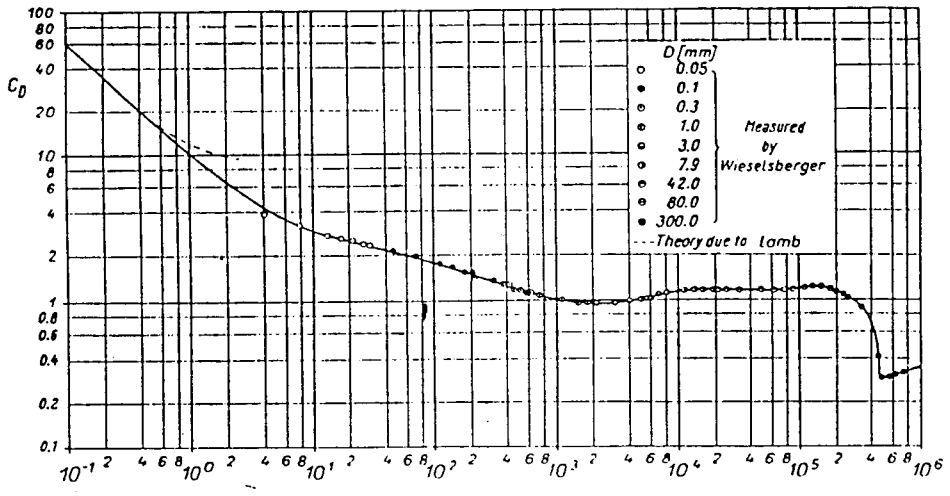

Figure 1.1. Drag coefficient for a circular cylinder as a function of Reynolds number. from Schlichting [1979].

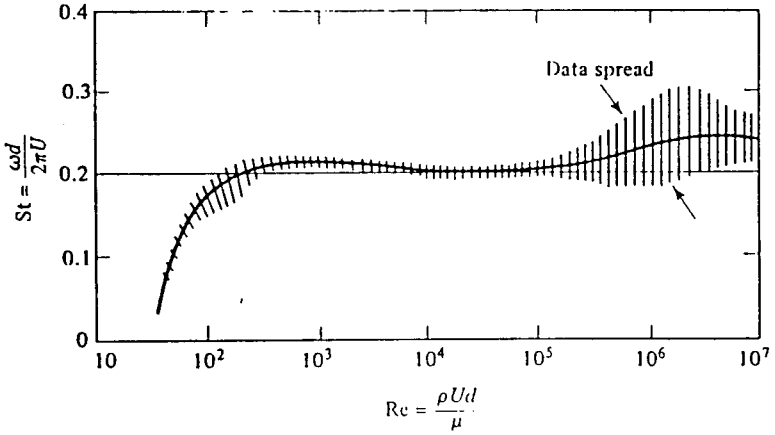

Figure 1.2. Strouhal number for a circular cylinder as a function of Reynolds number. from White [1986].

There are many excellent review papers describing in detail the characteristics of the different Reynolds number regimes. The interested reader is referred to Morkovin [1964],

Sarpkaya [1979], and Coutanceau and Defaye [1991]. The current investigation focuses on the subcritical Reynolds number regime, 150-300 < Re < 100,000-130,000. For the case of a circular cylinder within that regime, laminar boundary layers form on either side of the stagnation point and accelerate with the flow around the curvature of the cylinder. An adverse pressure gradient develops on the downstream portion of the body due to the decelerating flow beyond the maximum thickness point on the cylinder. The adverse pressure gradient is sufficient in the subcritical regime to cause the boundary layer to separate from the body at an angle of approximately 82 degrees from the stagnation point. Shear layers form from the separated boundary layers and their locations define the transverse extent of the wake, separating the potential outer flow from the vortical flow inside the wake. The shear layer of the wake is characterized by a change in the instability from locally absolute to locally convective at a particular downstream location. The shear layer becomes unstable shortly after separation forming small scale transition vortices which increase the shear layer's entrainment capability and define the beginning of the turbulent shear layer. The location of transition in the shear layer moves progressively closer to the cylinder with increasing Reynolds number. The shear layer rolls up and forms a large scale vortex that increases in strength as it is fed by circulation from the shear layer. The forming vortex draws the opposing shear layer closer through the action of Biot-Savart inductance. This action results in the entrainment by the vortex of opposite-sign vorticity. When a sufficient concentration of vorticity is entrained, the vortex growth terminates and it convects away from the body. The process repeats itself with the opposing shear layer and is referred to as vortex shedding, the resulting wake structure is called the Kármán vortex street. For a circular cylinder within the subcritical regime, the Strouhal number is relatively constant, St = 0.20. Other significant characteristics are that, over the majority of the subcritical regime, the drag coefficient remains fairly constant, around $C_d = 1.2$, and the flow is relatively insensitive to surface roughness and freestream turbulence levels.

The characteristic that distinguishes the circular cross section from many other bluff bodies, e.g., rectangular, triangular, D-section, flat plate normal to the flow, etc. is that the separation points are not fixed by the geometry. With other shapes that contain sharp corners, the location of flow separation is constant and stable. The circular cross section however, have separation points that depend on the energy contained in the boundary layer and the unsteady forces in the wake. For instance, in the critical Reynolds number regime, the boundary layer becomes turbulent before separation. The turbulent boundary layer being more energetic than its laminar counterpart is better able to oppose the adverse pressure gradient and remains attached to the cylinder longer. The delayed separation results in a narrower wake and reduced drag. In addition, the unsteady forces in the wake produce an oscillation of the separation points when they are not fixed by the geometry. This results in transverse 'flapping' of the shear layers which is in-phase with the vortex shedding frequency and produces a wider wake width and increased drag.

1.2 Near wake characteristics

The vorticity measured in a vortex near the cylinder is about 50 to 80% less than the vorticity shed from the boundary layer in one shedding cycle. These results are well documented in experimental measurements by Bloor [1964] and Cantwell and Coles [1983]. This reduction in strength is caused by the entrainment of fluid with opposite-sign vorticity from across the shear layer. Gerrard [1966] suggested that the size of the formation region was determined by the balance between these entrainment flows labeled (a), (b), and (c) in Figure 1.3.

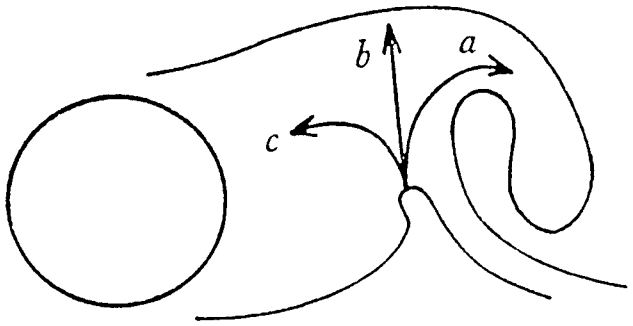

Figure 1.3. Filament-line sketch of the formation region. Arrows showing reverse flow (c) and entrainment (a) and (b). From Gerrard [1966].

Flow (a) is the entrainment of opposite-sign vorticity from the opposing shear layer into the primary vortex. The amount of circulation carried by this flow is not considered to vary significantly with Reynolds number. The entrainment into the shear layer, flow (b), is determined by the length of the shear layer and its level of turbulence and therefore depends on Reynolds number. Flow (c) indicates the remainder of the entrained flow that contributes to the reverse flow region. With increasing Reynolds number the transition point in the shear layer moves upstream. The more turbulent shear layer is able to entrain more fluid, thereby decreasing the shear layer's net circulation and producing a weaker vortex (supported by experiments of Bloor and Gerrard [1966]). The resulting increased flow out of the formation region, due to a more turbulent shear layer, cannot be balanced by an increase in the flow into the formation region because of the weaker vortex's diminished ability to entrain fluid. As a consequence, the region shrinks in size to a state where the entrainment flows are in equilibrium again.

The various parameters used in describing the near wake region are identified in Figure 1.4 along with the notation adopted for the current investigation, cylinder diameter, D, splitter plate length, ℓ, freestream mean velocity, U_m, wake width, d', formation region length, ℓ_f, and shear layer velocity, U_s.

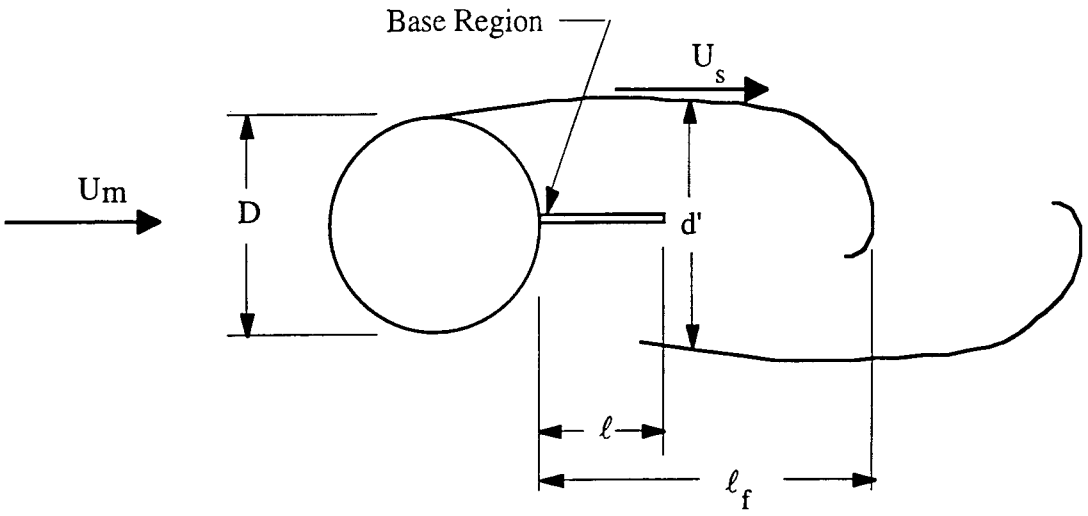

Figure 1.4. Definition of the vortex formation region parameters and notation.

Bloor [1964] defined the vortex formation region as the region of flow inside the wake between the separation point and the first appearance of the periodic vortex street. The transverse extent of the wake is bounded by the shear layers and can be determined through flow visualization or measurement of the wake fluctuations. The resulting wake width depends on whether the region is viewed in a instantaneous or time average sense. Typically, the time average definition is used and the width determined by finding the transverse distance between the highest fluctuation energy locations in the near wake. Since there is curvature associated with the shear layers, the wake widths reported in similar investigations can differ because they depend on the streamwise location of where the wake measurements were conducted. This presents a problem when comparing results from different investigations although, the qualitative trends appear to be consistent regardless of the streamwise measurement location. The length of the region is defined by the location where the forming vortices first cross the centerline of the wake and corresponds to the location of highest measured fluctuation energy along the wake axis.

The base pressure is defined as the pressure measured at the rear stagnation point of the cylinder. On the downstream side of the cylinder beyond the separation points, the pressure varies little from this value. In cases where access to the base may be obstructed, such as with the base mounted splitter plates used in the current study, it is reasonable to define the base pressure at a location slightly offset, say 10° from the base. Roshko [1955] related the base pressure to the shear layer velocity by application of Bernoulli's equation between the base of the cylinder and the flow at the separation point, just outside the boundary layer,

$$P_s - P_m = \frac{\rho}{2}\left(U_m^2 - U_s^2\right) \tag{1.4}$$

where, P_s and P_m are the shear layer and freestream static pressure respectively, and U_s and U_m the corresponding velocities. Due to the constancy of the pressure on the cylinder beyond the separation point, P_s can be replaced by the static pressure at the base, P_b and when the result is expressed as a pressure coefficient gives,

$$C_{pb} = 1 - \left(\frac{U_s}{U_m}\right)^2 = 1 - K^2 \tag{1.5}$$

where C_{pb} is the base pressure coefficient and K is defined as the base pressure parameter,

$$K = \sqrt{1 - C_{pb}} \tag{1.6}$$

The base pressure parameter increases with increasing base suction and therefore, equation 1.6 predicts that the shear layer velocity increases in direct proportion. Results of Roshko [1954], Gerrard [1965], and Bearman [1967] confirm that trend to be accurate. An important distinction must be made between the shear layer velocity discussed by Roshko

[1954] and the shear layer velocity presented in the current investigation. The shear layer velocity considered herein was defined as the mean velocity corresponding to the maximum RMS values of the wake width traverses and reflects the velocity near the center of the shear layer at a streamwise location approximately 0.5D from the cylinder base. This velocity was included primarily because it was available directly from the wake traverse data used to define the wake width. Although it varies significantly in magnitude from Roshko's definition it still provides a characteristic shear layer velocity from which consistent comparisons can be made.

1.3 Stability considerations

A potential flow model of the wake consisting of a double row of staggered point vortices was introduced by von Kármán (see Milne-Thomson [1938]). A linearized stability analysis of that model indicated that the bluff body wake is stable to first order disturbance if the ratio of longitudinal to transverse vortex spacing was equal to 0.281. Although the model ignored 3-dimensional effects and contradicted the known existence of stable vortex streets at Reynolds numbers where higher order disturbances were present, the ratio is accurate for many bluff bodies. Kronauer [1964] suggested that the vortex street arranges itself into a configuration giving minimum vortex street drag and applied his condition to von Kármán's model. Bearman [1967] evaluated the Kronauer criterion through experiment and found that by combining wake parameters predicted by the model with measured parameters a universal Strouhal number was determined that gave accurate results for various bluff bodies.

More recent analysis of the stability characteristics of the bluff body wake involve the introduction of a complex disturbance stream function to the governing equations which are then linearized. The Rayleigh and Orr-Sommerfeld equations represent the result of that procedure for inviscid and viscous formulations respectively. The flow's response to a

finite disturbance can be categorized as either stable, convectively unstable, or absolutely unstable modes. If a disturbance introduced into the flow decreases in amplitude with respect to both time and space the flow is considered stable, if it remains at its point of origin and amplifies in time and space it is considered absolutely unstable and if it grows with time but propagates away from its source it is convectively unstable. Bers [1983] explained that once an absolute instability is excited it creates a permanent motion, limited by the nonlinearities of the flow, whereas a convective instability requires a continuous external excitation to support a permanent motion. Figure 1.5 from Oertel [1990] illustrates the difference between absolute and convective instabilities in the bluff body wake. Ortel demonstrated by numerical simulation the existence of a local absolutely unstable region in bluff body wake close to the body. Further downstream, the instability is of the convectively unstable type. Instability modes are called local when they only influence a small region of the wake and global when their influence encompasses the majority of the wake.

Triantafyllou et al. [1987] investigated the inviscid stability characteristics of the cylinder wake. Their results indicate that an absolute instability exists in the profiles immediately behind a cylinder causes permanent motion once excited and drives the subsequent sections which convect instability waves of diminishing growth rate. The short region over which an absolute instability exists corresponds loosely to the formation region observed experimentally. These bluff body wake stability characteristics are generally accepted although the existence of the absolutely unstable region of the wake is yet to be shown experimentally.

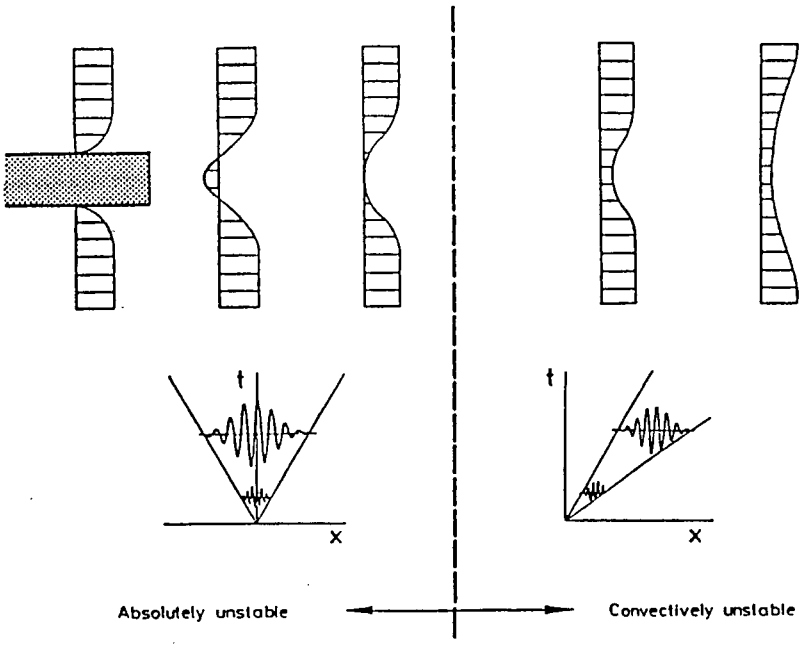

Figure 1.5. Sketch of local wake-instability properties. From Oertel [1990].

Monkewitz and Nguyen [1987] and Triantafyllou et al. [1986] solved the Orr-Sommerfeld equation for various wake profiles predicting with good accuracy the shedding frequency. Evidence from investigations by Provansal et al.[1987] produced by impulsively increasing the Reynolds number from subcritical to supercritical regimes indicates that the initial linear temporal growth rate of the transient is the same everywhere in the wake and not significantly different from the Kármán shedding frequency in the final saturated state. They propose that the Kármán vortex street is a result of a self-excited oscillation of the wake and not a spatial response to continuously supplied upstream disturbances. Chomaz et al. [1988] found that absolute instability is necessary but not sufficient for a global mode to become self-excited. Also, for a given flow, local absolute instability must reach a finite critical size. Therefore, the first appearance of local absolute instability in a transient bluff body wake is not expected to produce any discernible effect.

The stability characteristics of the shear layer have also attracted a significant amount of attention. From a stability point of view, the primary difference between a shear layer and a wake is that the shear layer contains vorticity of predominantly one sign while the wake contains vorticity of both signs. Brown and Roshko [1974] hypothesized that the asymptotic state of a wake is therefore 3-dimensional, while the asymptotic state of the shear layer is 2-dimensional. Experiments by Breidenthal [1980] confirmed that hypothesis. Bloor [1964], Unal and Rockwell [1988] and Kourta et al. [1987] have produced experimental evidence suggesting a possible coupling between the frequency of the Kármán vortices in the wake and that of the shear layer transition vortices. Linearized stability analysis has been successful in predicting the stability characteristics of the mixing layer, see Thomas [1991], which bears a strong resemblance to the bluff body shear layer. Due to those similarities, the methods developed to study mixing layers have proven useful when applied to the bluff body shear layer. For clarity and convenience, additional review and a description of the linearized stability theory for the shear layer is contained in Chapter 8, which is devoted to that subject.

1.4 Splitter plates

Roshko [1953] found that a splitter plate of length 5D placed behind a cylinder of diameter D at Re = 7500, was completely effective in destabilizing the periodic shedding. He deduced that communication between the two shear layers must be an integral part of the periodic shedding process. Further, Roshko [1955] suggests that with a splitter plate the shear layers cannot 'see' each other in the region where they tend to roll-up so there is no stabilizing mechanism to fix a periodically alternating vortex formation. In addition, Roshko used a splitter plate of 1.14 D that was placed so that there was a gap between the cylinder and the plate. He found that although the plate was too short to shield the shear layers from each other, it did interfere with the vortex formation. As the gap was increased the shedding frequency decreased appreciably. When the trailing edge of the plate moved

beyond 4 D, there was an abrupt increase in the shedding frequency which approached the undisturbed value. Roshko concluded that beyond that critical length the plate no longer interfered with the normal vortex development. The use of splitter plates also allowed Roshko to examine the relationships between various wake parameters. Some of his observations are summarized below.

For a given cylinder,

a) A decrease in drag is accompanied by a decrease in shedding frequency.
b) Shedding frequency decreases when wake width increases.
c) Decrease in drag is accompanied by an increase in wake width.
d) An increase in wake width results in a decrease in wake velocities and a net decrease in wake energy.

Roshko also found that the splitter plate had an extremely strong influence on the drag of the cylinder and observed a reduction in some cases of up to 36%.

Gerrard [1966] investigated the effect of base mounted splitter plates on the wake of a circular cylinder at Re = 20,000. He found that increasing the length of a splitter plate resulted in a progressive decrease in the shedding frequency up to the length, $\ell/D = 1.0$. Beyond $\ell/D = 1.0$, the opposite trend occurred. Some of the results of Gerrard's study are presented in Figure 1.6.

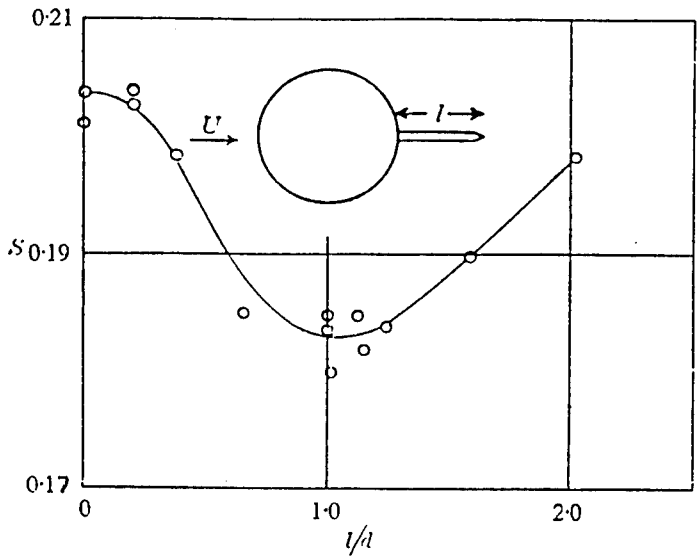

Figure 1.6. Variation in Strouhal number with respect to splitter plate length. From Gerrard [1966].

Gerrard's results demonstrated the fundamental importance of the flow in the interior of the formation region in determining the shedding frequency. He suggested that a decrease in the wake width facilitates the interaction between the two shear layers increasing the shedding frequency. An increase in the formation length however, results in more entrainment by the shear layer and therefore a weaker forming vortex, decreasing the interaction and reducing the shedding frequency. Furthermore, a thicker, more diffused shear layer will require a stronger concentration of circulation to draw it across the wake to initiate shedding. That should result in a decrease in shedding frequency although its reduced entrainment will produce a stronger forming vortex. Unfortunately, it is impossible to isolate any one of those effects from the others. It is likely that in many instances two competing effects will occur and cancel out, leaving the shedding frequency unaltered.

Apelt et al. [1973] investigated the effect of splitter plates on the near wake of a circular cylinder at Re = 10,000 - 50,000. They found a variation in Strouhal number with

Reynolds number similar to that observed by Gerrard [1966] with the exception of an initial increase in shedding frequency with plates less than $\ell/D = 0.25$. Between $\ell/D = 0.25$ and $\ell/D = 1.0$ the Strouhal number, drag coefficient, and base suction all decreased, attaining minimum values at $\ell/D = 1.0$. The authors suggested that a distinction should be made between 'short' and 'long' plates with the division made at $\ell/D = 1.0$. Beyond $\ell/D = 1.0$ all three parameters demonstrated an increase up to $\ell/D = 2.0$ which was the longest plate used in the study.

A distinction must be made to avoid confusion or the appearance of contradiction regarding the effect a splitter plate has on wake width. Apelt et al. found that for even very short plates, the wake width decreased substantially. However, Roshko [1954] observed that for a given cylinder, a decrease in drag was accompanied by an increase in wake width, which implies that the splitter plate increased the wake width. The conclusions of both investigations are correct base on their respective definitions of wake width. Roshko determined the wake width from the free streamline theory which is a idealized model based on time average values of the base pressure and does not account for unsteady wake dynamics. For the drag to decrease, there must be a corresponding increase in base pressure which, in the idealized model, causes in the distance between the shear layers to increase. Apelt et al. [1973] base their wake width on time averaged mean and RMS velocity profiles of the wake. The time average measurements indicate a relatively wide wake for the plain cylinder configuration due to the shear layer oscillation. The splitter plate suppressed of the shear layer oscillation and, from a time average point of view, the wake width was significantly decreased. To summarize, suppression of the shear layer oscillations reduce the time average wake width, however the instantaneous wake width may increase due to the splitter plates effect of the base pressure. Apelt et al. concluded that the action of the splitter plate was to stabilize the separation points progressively, and reduce the wake width with increasing plate length. The wake envelope was evaluated

using mean velocity measurements and flow visualization. The results indicated that short plates produce a rather simple shaped wake envelope whereas long plates produce an envelope defined by the double curvature in the shear layer, see Figure 1.7.

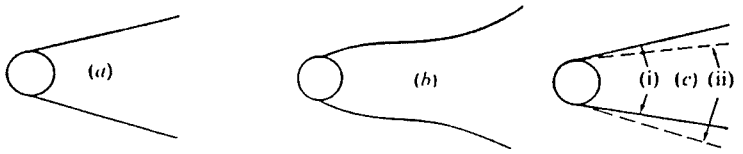

Figure 1.7. Wake envelope from flow visualization film, (a) 'short' plate, (b) 'long' plate (c) effect of movement of separation points. From Apelt et. al. [1973].

The author's suggested that the double curvature was due to the vortex forming before the end of the plate for $\ell/D > 1.0$ then, rolling over the trailing edge and convecting away with the flow. At longer plate lengths, the plate prevents the vortex from crossing the centerline altogether. That range corresponds to a progressive increase in the shedding frequency with increasing ℓ/D. For the long plates the shedding was slightly more irregular although the region near the cylinder was much more steady. In Part 2 of the paper, Apelt and West [1975], investigate the effects of long splitter plates, $2 < \ell/D < 7$, on the bluff body flow. They observed that the drag and vortex shedding were progressively modified up to $\ell/D = 5$. Beyond $\ell/D = 5$ there was no further change, C_d remained constant at 0.8 and vortex shedding was essentially eliminated. Results from their investigation of three different bluff bodies show the variation in Strouhal number as a function of splitter plate length in Figure 1.8.

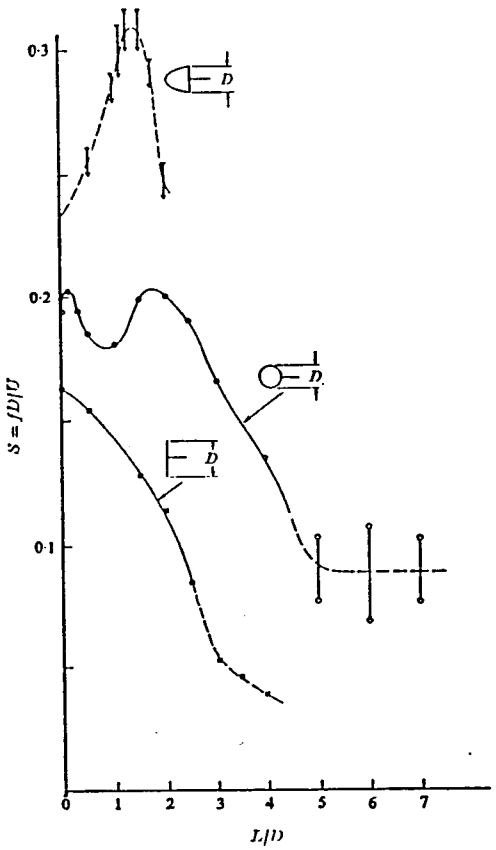

Figure 1.8. Variation in Strouhal number with ℓ/D. From Apelt and West [1975].

Unal and Rockwell [1987] investigated the vortex formation behind a circular cylinder with a splitter plate positioned so there was a gap between the trailing edge of the cylinder and the leading edge of the plate, similar to Roshko's [1955] configuration. The author's observed that when the large scale vortex formation was precluded by the edge of the plate, unstable disturbance growth at the Kármán frequency remained in the shear layer. They concluded that the effect of the intrusion of the leading edge of the plate into the formation region was to inhibit the formation of the Kármán vortices rather than to preclude the onset of the initial instability immediately downstream of the shear layer separation. As the plate was moved very close to the cylinder, impeding the large scale vortex formation the small scale shear layer transition vortices remained present. That suggested that the region of the shear layer immediately downstream of separation supports amplification of

the disturbance leading to the formation of the transition vortices and not Biot-Savart induction.

Bearman [1965] investigated the effect of splitter plates on the blunt trailing edge bluff body. He found that an increase in formation length caused by the splitter plate resulted in a decrease in the base drag. This also accompanied a reduction in the vortex strength consistent with Gerrard's [1966] observations.

1.5 Three-dimensional effects and end conditions

In recent years, the 3-dimensional aspects of the bluff body problem have received increased attention. Some of the failures of earlier analytic and numerical modeling in the prediction of separation point and drag have been traced to the 2-dimensional treatment of the problem. The formulations could be justified, in part because the flows they were modeling were nominally 2-dimensional. There the term 'nominal' is used to reflect the fact that from a time average point of view the flow is 2-dimensional or, in other words, the statistical averages of the flow parameters and their derivatives are zero in the spanwise direction. More recent experimental investigations have found that the bluff body wake is significantly more 3-dimensional than previously thought.

Roshko [1953] found a discontinuity in the Strouhal number - Reynolds number relation at approximately Re = 150. He described this as the transition point from a stable range to an irregular range where turbulent fluctuations accompany the periodic formation of vortices. Williamson [1989] found that the discontinuity was actually due to a transition from one oblique shedding mode to another oblique mode. By application of the formula, $S_o = S_\theta/\cos\theta$, where S_o is a universal Strouhal number, S_θ is the measured Strouhal number and θ is the oblique shedding angle, Williamson was able to eliminate the discontinuity from the S_o - Re curve. Konig et al. [1990] showed that the discontinuities in

the Strouhal number - Reynolds number relationship results from cells of different frequencies moving along the cylinder span as the Reynolds number varies. The oblique shedding modes were strongly influenced by the end boundary conditions. In some cases, where the flow over the span matched the end conditions, a chevron pattern was observed with symmetry about the center span. In the case where the flow could not match the end conditions a vortex discontinuity formed, resulting in spanwise cells of different frequency. Through flow visualization, Konig et al. [1992] found that when the oblique shedding angle varied across the span cells with different shedding frequency were produced. Application of Williamson's cosine law to the individual cells resulted in a constant Strouhal number across the span. Aspect ratio was also found to effect the spanwise shedding characteristics. Figure 1.9 shows the effect of aspect ratio on the cell arrangement and power spectra from a hot wire situated at the center of the span. The results indicate that the shedding frequency discontinuity between cells appears as side-band modulation in the power spectrum and its energy depends on the proximity of the sensor to the cell boundary.

Williamson [1989] also observed that through proper manipulation of the end plates, or by the use of base suction, parallel shedding could be accomplished. Others found a similar dependence of the oblique and parallel modes on the cylinder end conditions. Hammache and Gharib [1989] found that by placing control cylinders near the ends of the span, oriented perpendicular to the cylinder axis, they were able to attain parallel shedding. Eisenlohr and Eckelmann [1989] achieved parallel shedding by the use of end cylinders of slightly larger diameter than the primary cylinder. All of these studies confirm the significance of end conditions in determining the degree of 3-dimensionality in the wake.

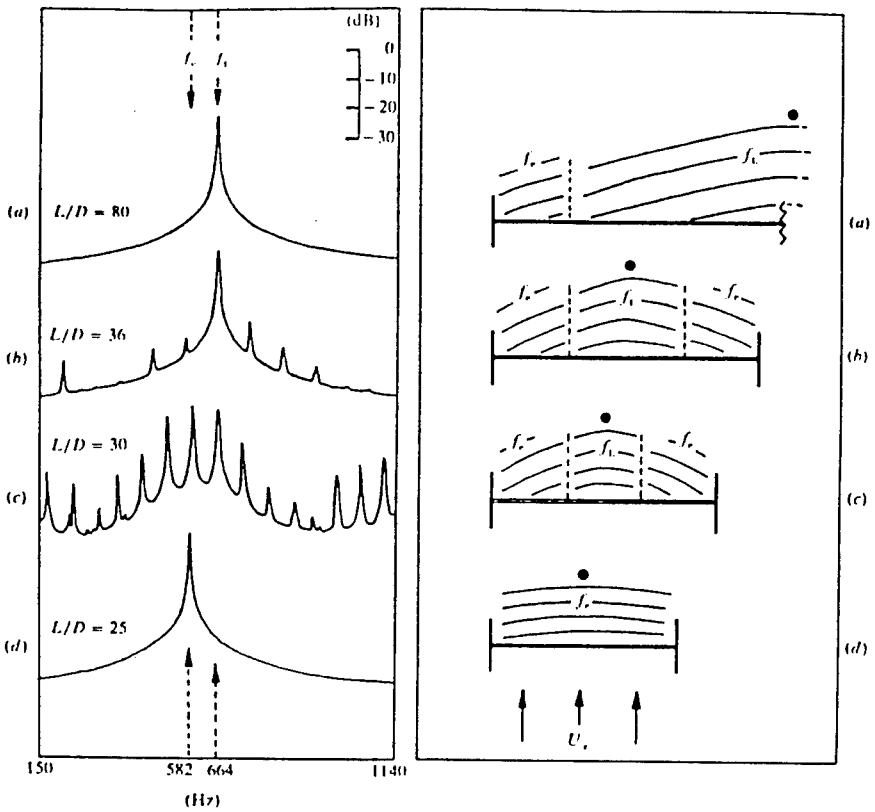

Figure 1.9. Effect of variation of aspect ratio on the spectra of the wake velocity fluctuations, and the cell arrangement along the span at Re = 101. From Williamson [1989].

Stansby [1974] for 16,000 < Re < 80,000, found, based on pressure measurements, that suitably designed end plates remove the tunnel wall effects and increase the degree of 2-dimensionality in the flow. Szepessy and Bearman [1992] investigated the optimal design of end plates for 4,000 < Re < 48,000. He concluded that a trailing edge distance from the cylinder greater than 3.5 D and leading edge distance of greater than 1.5 D is sufficient to prevent outside flow disturbances from effecting the vortex shedding. Eisenlohr and Eckelmann [1989] notice that for aspect ratios larger than 10, the shedding frequency near the end plates was approximately 10% lower than at the central locations. They attributed this decrease to an induced velocity, opposing the natural formation rate of

the vortices, caused by the curving of the horseshoe vortex which is generated by the interaction of the end plate boundary layer and the cylinder toward the center of the wake in the near downstream region of the flow. Eisenlohr and Eckelmann suggest that since the primary vortices cannot terminate in the fluid without violating the Helmholtz vortex laws, they must connect to the vortical structure generated by the horseshoe vortex at the cylinder ends. A conceptual view of this process is presented in Figure 1.10.

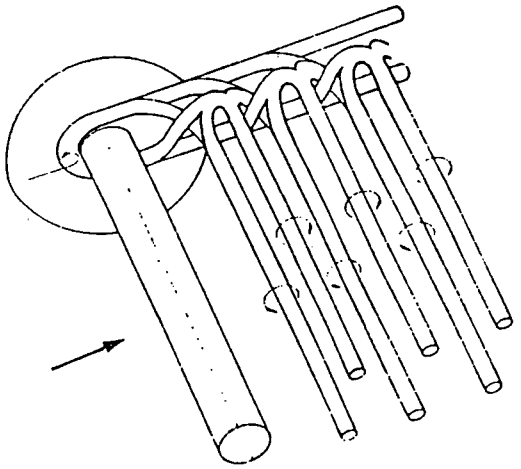

Figure 1.10. A perspective view of the horseshoe vortex, vortex street interaction. The strong curvature of the vortex axis leads to an induced velocity field opposing the mean stream. From Eisenlohr and Eckelmann [1989].

Two common phenomena associated with 3-dimensionality of the wake are vortex splitting and vortex looping. Vortex splitting can be caused by a difference in shedding frequency between neighboring spanwise cells. The higher frequency cell will produce more vortices than its lower frequency neighbor and since the vortex lines cannot terminate in the fluid, the extra vortex lines must be accommodated at the cell boundary. Figure 1.11 from Williamson [1989] shows a schematic of the vortex splitting process between two different constant frequency cells.

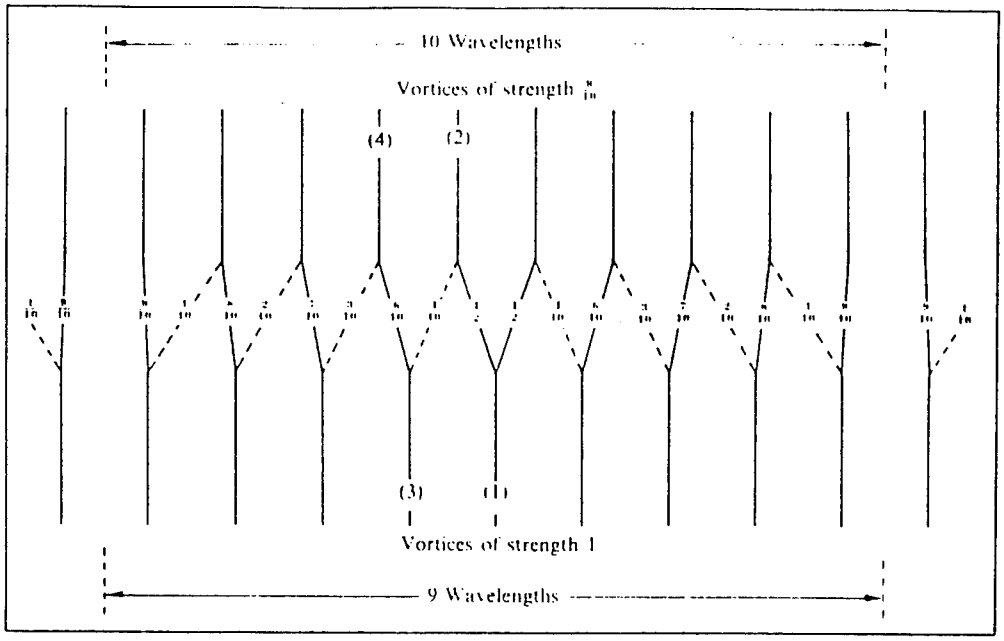

Figure 1.11. Idealized sketch of vortex splitting process. From Williamson [1989].

Vortex looping on the other hand, involves the linking of same sign vortices across the wake centerline and usually requires a higher degree of 3-dimensionality in the flow than the vortex splitting process. The linking of vortex lines shown in Figure 1.10 is an example of vortex looping. In general, vortex splitting accommodates the difference in shedding frequency between adjacent cells, and vortex looping accommodates a difference in the vortex strength in the adjacent cells.

Williamson [1991] used the term 'vortex dislocation' to identify the complex linking of vortex lines between adjacent cells of different frequency when the primary vortices in each cell move out of phase with each other. By placing a ring of slightly larger diameter than the cylinder at mid-span, he was able to experimentally produce at the vortex dislocations that are observed to occur naturally in bluff body wakes. The dislocations grow downstream into large-scale, low frequency, Λ structures which are inherently unstable and accompany the transition to 3-dimensionality. A flow visualization image of

the dislocations is shown on the left in Figure 1.12 and a schematic of the evolution of the dislocations is shown on the right.

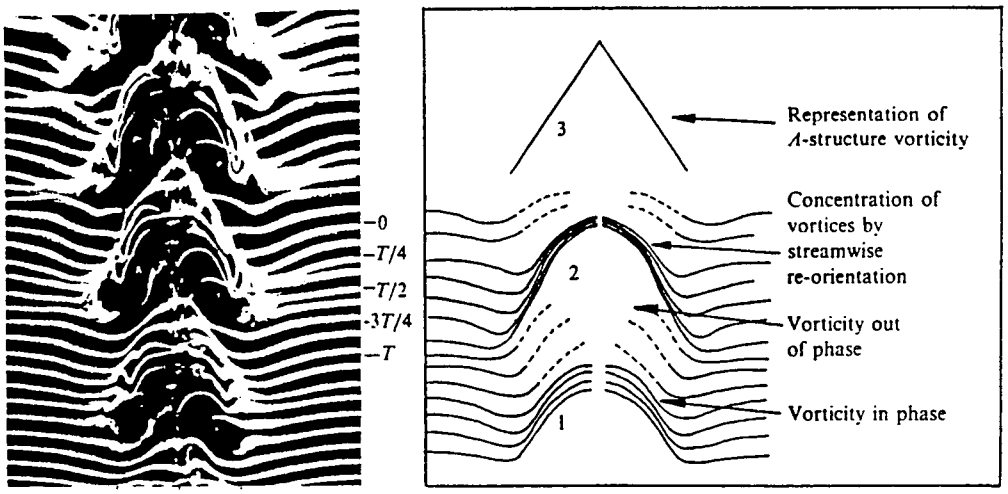

Figure x.12. Schematic of the evolution of dislocations, and their simplified representation. From Williamson [1992].

The dislocations are called 'two-sided' since they occur between two regions of constant shedding frequency which may or may not be in-phase with each other. A flow visualization image of the artificially produced vortex dislocations are shown in Figure 1.13. The image on the left (a) shows a transient (out-of-phase) two-sided dislocation. It is the result of a transient phase relation between the two dislocations, because the dislocation frequency on each side is different. The image on the right (b) shows the preferred stable (in-phase) symmetric two-sided dislocation. This appears when the dislocation frequency on each side of the ring is the same. Some of the prime characteristics of a dislocation are its relatively fast spanwise growth, a rapid breakdown to turbulence and a broad spectrum within several primary vortex wavelengths.

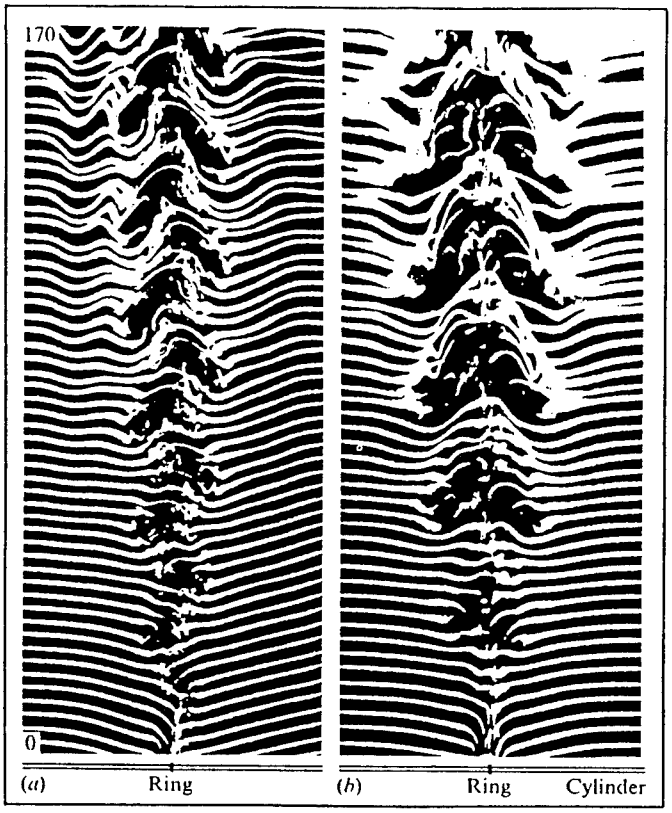

Figure 1.13. Two-sided dislocations: transient (a) versus stable (b). From Williamson [1992].

Breidenthal [1980] used a segmented, square wave, trailing edge splitter plate to produce spanwise cells with alternating shear layer and wake flow characteristics. The solid portion of the square wave had a sharp trailing edge that produced a local shear layer flow, and the indentation portion had a blunt trailing edge which formed a local wake flow. The shear layer regions rapidly formed the characteristic 2-dimensional vortex structures whereas, the wake regions formed closed vortex loops. The results confirmed the Brown-Roshko [1974] hypothesis which states that the asymptotic state for a shear layer containing vorticity of one sign is 2-dimensional, and for a wake, which contains both signs of vorticity, the asymptotic state is 3-dimensional. Figure 1.14 presents a flow

visualization image that shows the closed loop vortex structure found in the spanwise cells corresponding to the wake positions.

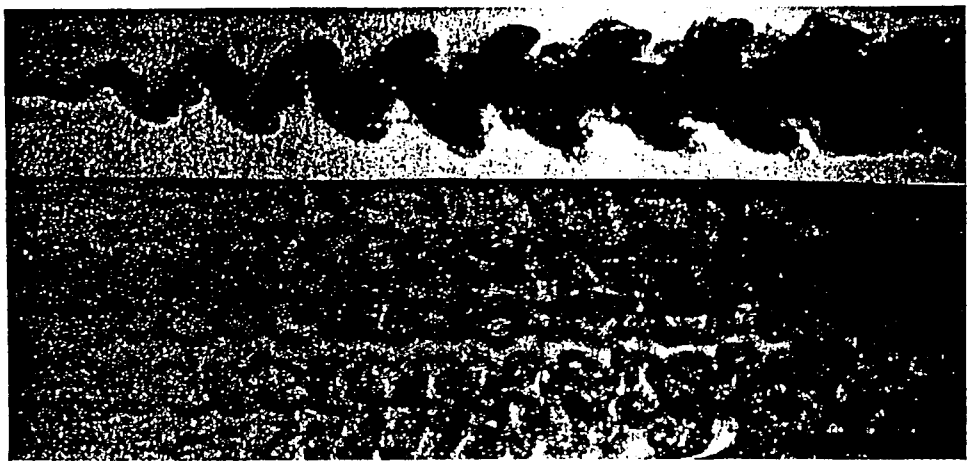

Figure 1.14. Spanwise wake and shear layer interaction. From Breidenthal [1980].

Meiburg and Lasheras [1988] conducted experimental and numerical investigations of the 3-dimensional transition in plane wakes. The 3-dimensionality was imposed using a transverse disturbance (corrugated splitter plate) or streamwise disturbance (sinuous trailing edge splitter plate) in the experiments and a periodic, transverse or streamwise, perturbation in the numerical model. Although their results were at a much lower Reynolds number than Breidenthal [1980], they observed a very similar structure of closed vortex loops aligned in the streamwise direction and suggested that the mechanisms causing the structures must be the same as at the higher Reynolds number. Spanwise Λ-structures similar to those described by Williamson [1989] were formed by the interaction of streamwise vorticity generated by the perturbations and the primary vortices. Figure 1.15 shows those structures in a comparison of the numerical and experimental results.

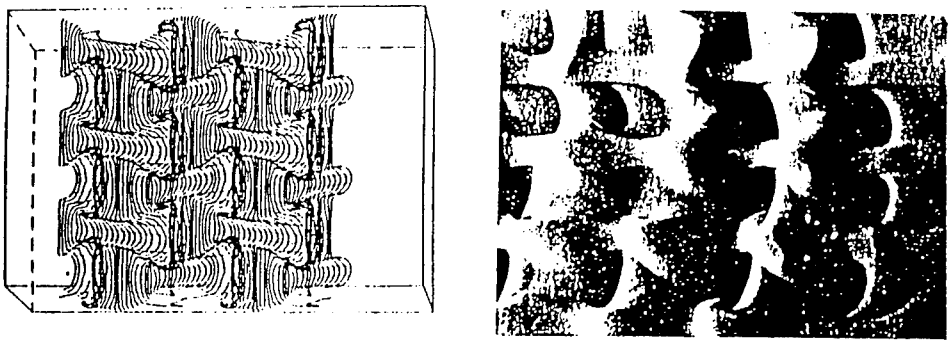

Figure 1.15. Numerical (left), and experimental wake visualization showing spanwise structures. From Meiburg and Lasheras [1988].

Petrusma and Gai [199x] investigated a segmented blunt trailing edge airfoil through low Reynolds number flow visualization with a laminar wake and measurements of Reynolds shear stresses in the turbulent wake. It was shown that the basic flow topology was consistent between the laminar (Breidenthal [1980]) and turbulent 3-dimensional wake. Rodriguez [1991] investigated the effect of a 3-D trailing edge consisting of alternate segments of blunt base and spanwise cavity on an airfoil type body. The results show a reduction in profile drag of more that 40% is possible by an optimization of trailing edge shape. The efficiency of the device was shown to be directly related to the presence of longitudinal vortices that formed at the discontinuities in the trailing edge.

Tombazis [1993] investigated the effects of 3-dimensional disturbances on the near wakes of D-shaped bluff bodies. He suggested that a convenient way of categorizing 3-dimensionality in flows was; mild, such as the oblique shedding typical in the laminar regime, strong, identified by the presence of vortex splitting and looping, smaller scale, such as occurs in the shear layers, and small scale, defined as turbulence. In Tombazis' investigation, a sinusoidal trailing edge on the D-shaped body was used to produced a periodic spanwise variation of the separation points. Spectral analysis indicated a dual

vortex shedding characteristic with the higher frequency existing at the valley and a coexistence of both frequencies at the peak. It could not be determined whether each one of the main two peaks in the power spectrum necessarily reflected the frequency of the vortex shedding. It could be possible that one of the peaks reflected induced velocities from a spanwise position some distance away and not the fluctuations of vorticity flux which accompanies vortex shedding. Furthermore, the two peaks could be produced from the sum effect of two modes occurring simultaneously, or two modes that occur independently at different times over the sample period. Tombazis explained that the reason for the existence of more than one shedding frequency could be traced to the tendency for the Kármán vortices to straighten out as they convect downstream. That meant that the formation length at the valley would be larger than at the peak. The increased entrainment by the longer shear layer would result in a reduced strength in the forming vortex and a reduced shedding frequency compared to the frequency of the cells formed near the peaks.

Flow visualization by Tombazis indicated that vortex splitting would occur regularly in the region of the peak. Water tunnel experiments indicated that two neighboring cells could experience in phase (symmetric mode) or out of phase (3-cell anti-symmetric mode) vortex shedding as shown in Figure 1.16. In both modes, a cell of lower frequency is situated in the region of the peak and dislocations occur on either side. These dislocations occur at a frequency equal to the difference between the two vortex shedding frequencies. A 2-cell anti-symmetric mode and an oblique shedding mode were also found in some of the water tunnel experiments although there was no evidence of their existence in the wind tunnel experiments. The flow visualization also indicated small streamwise vortices that linked the successive Kármán vortices in a fashion similar to that described by Meiburg and Lasheras [1988].

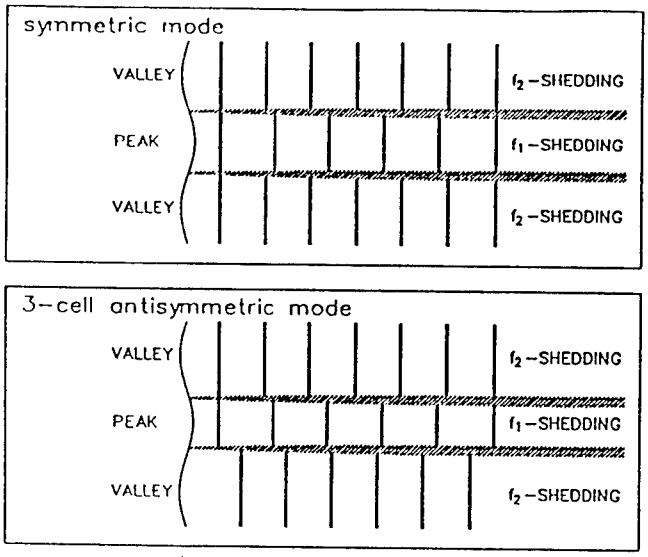

Figure 1.16. Schematic representation of various shedding modes. From Tombazis [1993].

Pearson and Szewczyk [1992] investigated the effect of 2-dimensional (straight trailing edge) and 3-dimensional (sinuous trailing edge) splitter plates on the circular cylinder bluff body. The results indicated that the wake produced by the sinuous trailing edge splitter plate differed for the straight splitter plate case. The introduction of a sinuous trailing edge splitter plate affects the base pressure along the span of the cylinder. As the base pressure increases, the vortex formation region is extended and the width of the wake decreases. Vortex shedding is altered, the drag force is reduced, and the base pressure is modified to produce spanwise cross-flow between the valleys and the peaks. Spanwise frequency variation, as well as the presence of two shedding frequencies at the location of a peak in the periodic splitter plate were observed. Based on these experimental measurements and flow visualization, the existence of vortex dislocations was also noted.

Borg and Szewczyk [1992] investigated the unsteady base pressure on a cylinder with a sinuous trailing edge splitter plate. Spanwise comparison of the base pressure

fluctuations showed strong correlation with the vortex shedding except for intermittent instances where the signals experienced a 90° phase shift. Correlation between the fluctuations on the stagnation line and the base region indicated that they were always in-phase.

Figure 1.17 contains data extracted from Borg [1992], showing that the base pressure fluctuation intensity is reduced substantially by the splitter plate and that its variation with ℓ/D is remarkably similar to that of the base pressure parameter and drag coefficient. Time average and instantaneaous pressure measurements by Rooney and Peltzer [1981] around the circumference of a circular cylinder also indicate good correlation between RMS pressure fluctuation intensity and mean pressure coefficient. Regions on the cylinder surface where with the highest suction, (near $\theta = 30°$ and 270°) also experienced the highest fluctuation intensity. These results suggest a direct relationship between bluff body drag reduction and suppression of the base pressure fluctuations.

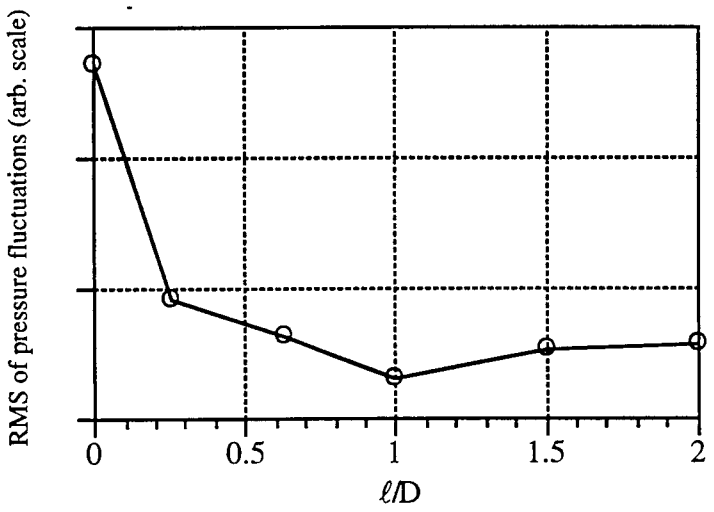

Figure 1.17. Variation in the RMS value of the base pressure fluctuations versus splitter plate length. Extracted from Borg [1992].

1.6 Tapered cylinders

The flow past a tapered cylinder introduces a spanwise variation in the local length scale of the bluff body problem. Slight variations in the spanwise scales can be accounted for in airfoils and other streamlined bodies using a simple strip theory. The bluff body however, includes large regions of separated flow and inherent unsteadiness that invalidate the strip theory approach. Gaster [1969] investigated the tapered cylinder flow at low Reynolds numbers and found that the vortex wake structure exists in a number of discrete spanwise cells having different shedding frequencies. The shedding frequency along a slightly tapered model adjusted so that it remained roughly compatible with the local length scales. When based on local diameter the Strouhal number remained near the 2-dimensional value of 0.20. The mean frequency in each cell depended on the local diameter and within each cell the shedding was regular and periodic. In a later study, Gaster [1971a] observed that there was a jump in frequency from one cell to its neighbor and a corresponding modulation of the flow at a frequency equal to the difference in the frequencies of the two cells.

At higher Reynolds numbers, $5{,}000 < Re < 50{,}000$, Gaster [1971b] observed that the signal generated by a hot wire in the flow past a straight cylinder was almost periodic while the tapered cylinder signals indicated increasing amounts of low frequency content and randomness as the taper increases. Compared to the straight cylinder at a similar Reynolds number, the taper substantially reduced the sectional drag coefficients by up to 20% and produced significant spectral broadening. Gaster suggested that the spectral broadening was essential if the vortices were to maintain any spanwise coherence. Correlation measurements indicated that the vortices shed at an oblique angle, with the point of detachment or formation traveling towards the larger diameter and lower frequency end. This pattern was convected downstream resulting in vortices that were slightly inclined to the cylinder axis.

Piccirillo and Van Atta [1992] investigated tapered cylinders in the laminar vortex shedding regime. They found that although the spanwise cells varied slightly in size, the mean size of the cells scaled well with taper ratio. The more tapered cylinders indicated a 'leaky' cell structure in which non-adjacent cells had a stronger influence over each other. However, the less tapered cylinders had a 'tight' cell structure in which only adjacent cells affected one another. Papangelou [1992] investigated the tapered cylinder at Reynolds number on the order of 100. The results indicated that the frequency jump between adjacent cells was constant along the cylinder's span and a function of air speed and taper angle only. The presence of simultaneous amplitude and phase modulation in the time signals was believed to be associated with the coupling between cells of different frequency. Figure 1.18 presents experimental results showing the spanwise variation in shedding frequency at low Reynolds number. The symbols indicate expreimental results and the line indicates the predicted shedding frequency based on the local diameter according to Roshko [1954].

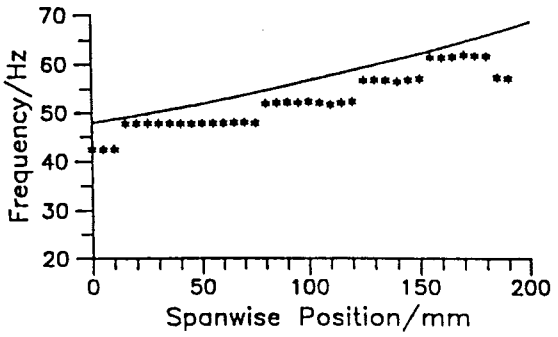

Figure 1.18. Experimental spanwise variation in shedding frequency from a tapered cylinder in uniform flow at Reynolds number of approximately 100. From Papangelou [1992].

1.7 Shear flow

Another common 3-dimensional bluff body flow is the interaction of a 2-dimensional cylinder with a mean shear freestream flow. These flows occur naturally in atmospheric boundary layers and ocean currents. The primary difference between a uniform flow and shear flow is the presence of vorticity normal to the plane of the shear flow. Maull and Young [1973] noted that as the shear flow approaches the body, the vorticity vector is bent toward the flow direction, forming longitudinal vortex filaments that interact with the primary shedding vortex. In their experiments, conducted on straight circular cylinders at a Reynolds number of 28,500 based on mid-span velocity, they observed that the shedding breaks down into a number of spanwise cells of constant shedding frequency. The division between the cells was thought to be marked by the longitudinal vortex in the stream direction. Figure 1.19 shows the spanwise variation in power spectra for the straight cylinder in shear flow.

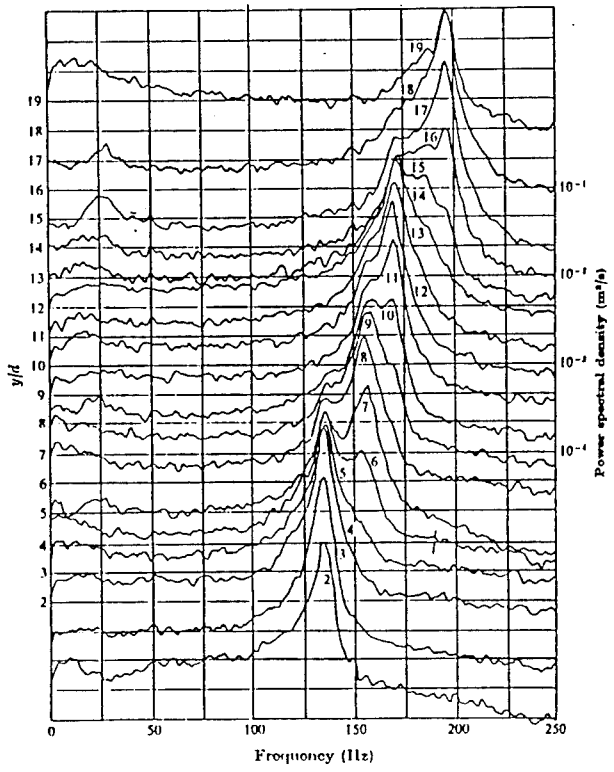

Figure 1.19. Spanwise variation in power spectrum for straight cylinder in shear flow. From Maull and Young [1973].

One explanation that the authors gave for the constant frequency cells was that the flow attempts to maintain a constant local Strouhal number, but that the coherence of the shed vortices requires a constant frequency over certain lengths. The local Strouhal number ranged between 0.24 and 0.27. The shear flow also altered the local base pressure coefficient from the uniform flow configuration. The base pressure coefficient became more negative with increasing shear velocity suggesting a base flow from high to low velocity sides of the span.

Rooney and Peltzer [1981] investigated the effect of shear flow on the wake of a circular cylinder in the transcritical Reynolds number regime. Their results indicated that discrete cells of constant shedding frequency were formed but from the data measured, it was impossible to determine a relationship between shear gradient and cell size. The fluctuations in pressures on the surface of the cylinder were significantly higher in sheared flow cases than for unsheared flow. Rooney and Peltzer [1982] concluded that any shear in the upstream velocity profile will trigger a cellular vortex shedding pattern at critical Reynolds numbers, with the cells becoming more distinct at higher shear levels further into the critical regime. In addition, there was a decrease in cell length with increasing upstream shear. Elsner [1982] further investigated the effects of shear flow on a rectangular cross section bluff body. A significant difference between the rectangular and circular cross section bluff body is that for the rectangle, the separation points are fixed at the trailing edge whereas, for the circular cross section the separation points are allowed to adjust to the flow characteristics. A spanwise structure of constant shedding frequency cells was observed for the rectangular cross section which was similar to that observed for the circular cylinder in shear flow.

Woo et al. [1989] measured the influence of shear flow on a circular cylinder in the Reynolds number range of 800 - 1,400. Their results indicated that for a constant steepness factor, $\beta = (dU/dz)(D/U_{ref})$, where U and U_{ref} are the local and mid-span velocities respectively, the Reynolds number had no significant effect on the Strouhal number. However, the increase in Reynolds number produced a decrease in vortex formation length, wake width, and base pressure coefficient. At a given Reynolds number, increased steepness factor did not cause significant change in the formation length although it resulted in an increase in wake width and decrease in base pressure and Strouhal number. The entrainment rate was greater on the high velocity end of the cylinder which the authors attributed to the higher local Reynolds number and therefore a more turbulent shear layer.

Griffin [1985] reviewed previous shear flow investigations and found some common characteristics. The vortex shedding takes place in spanwise cells with the shedding frequency constant in each cell. However, the number of cells, base pressure and drag force was strongly dependent upon aspect ratio and end effects. When the shear flow was highly turbulent (turbulent intensity greater than 5%) the critical Reynolds number was reduced by a factor of 10. Finally, in some cases with large aspect ratios, between 20 - 50, there was no discernible cell structure

1.8 Universal parameter

Dependent relationships between the various wake parameters indicate that there may be some form of similarity between wake characteristics of different bluff bodies. For instance Gerrard [1966] suggested that the size of the formation region is determined by a balance between various entrainment flows. He observed that the length and separation of the shear layers affected that balance which in turn, affected the rate at which vortices are shed. If a functional relationship between various length, width, velocity, frequency, and/or base pressure parameters remained constant for all bluff bodies, then similarity

would exist and could be described by a universal parameter. A practical application of that result would be to allow the prediction of the unsteady wake properties, drag, shedding frequency, etc., from a minimum of empirical data. In a more fundamental sense, the universal parameter's existence would provide significant insight into the mechanisms that control the bluff body wake.

Researchers have proposed various parameters expected to maintain a constant value for an arbitrary bluff body flow with varying degrees of success. The typical form of the universal parameter is that of the Strouhal number and therefore, it is commonly referred to as a universal Strouhal number. It generally consists of the shedding frequency, f_s, non-dimensionalized by the ratio of a characteristic length, L_c, and velocity scale, U_c. The characteristic length is typically the wake width, d', and the characteristic velocity the freestream value, U_m, or the shear layer velocity determined using Roshko's base pressure parameter, $U_s = KU_m$. The various proposed universal parameters can be divided into two categories depending on whether they are based on only empirical data, category 1, or some combination of empirical data and an analytic model, category 2. The following discussion represents a brief summary of some of the more well known universal parameters.

There are three category 1 universal parameters discussed herein. They were proposed by Fage and Johansen [1927], Simmons [1977], and Griffin [1981]. Fage and Johansen constructed their parameter using the freestream value for the velocity scale and the outer spacing of the shear layers as the characteristic length. This resulted in a parameter value of approximately 0.27 - 0.28 for a variety of bluff body shapes. For more slender bluff bodies, such as an airfoil at moderate angle of attack, or an ogive, the parameter was less reliable. Simmons [1977] took a similar approach, using the wake width as the characteristic length, however, he chose the shear layer velocity as the

characteristic velocity. The base pressure was measured and then the shear layer velocity determined following Roshko's [1955] derived relationship between the base pressure parameter, K, and the non-dimensional shear layer velocity, U_s/U_m. The wake width was defined as the distance between the maximum in the RMS of the velocity fluctuations in each shear layer at a streamwise location corresponding to the minimum static pressure measured along the wake centerline. This resulted in parameter values of approximately 0.16.

Griffin [1981] on the other hand proposed a parameter similar to Simmons, using the shear layer velocity and a wake width determined by the maximum RMS fluctuation intensity points in each shear layer. A different streamwise location for the wake width measurement was used though which was defined by the end of the formation region. The methods described above produce relatively constant values for certain bluff body shapes but broke down in cases of the more slender bluff bodies, and where the base pressure was altered through base bleed or by the incorporation of splitter plates.

Category 2 use a combination of empirical measurements along with idealized potential flow model predictions to produce a universal parameter. Roshko [1955] combined the measured shedding frequency and base pressure parameter with the wake width determined by using his modified free-streamline theory or, notched hodograph method. In the method, the flow is mapped into the hodograph plane through use of a complex potential function. The free streamlines representing the wake boundary map into a circle. A notch in the circle accounts for the difference in velocity between the freestream and the shear layer. The notched hodograph method was relatively successful in predicting the drag of bluff bodies although it relied on a measured base pressure to account for the difference between the shear layer and freestream velocity. By incorporating characteristic length and base pressure measurements in the notched hodograph method the wake width

used in Roshko's universal parameter was calculated. This method produced a universal parameter with a value of approximately 0.16 for a variety of bluff body shapes.

Bearman [1967] combined the measured shedding frequency and base pressure parameter with a calculated wake width. The wake width calculation was based on the von Kármán idealized potential flow model which predicts the wake drag of a bluff body. Combining the von Kármán model with the Kronauer [1964] stability criterion and Roshko's base pressure relation, three equations were obtained that could be solved simultaneously using the measured values of drag coefficient and Strouhal number. The solution predicted the transverse vortex spacing that was used as the characteristic length in Bearman's universal parameter. This method produced good collapse of the data to a value of approximately 0.18 however, its ability to predict the shedding frequency from measured values was not as reliable as some of the previously described methods. Table 1.1 summarizes the universal investigations described above.

method	freq., f_s	characteristic vel.,U_c	characteristic length, Lc
Strouhal	measured	U_m, measured	D, measured
Fage and Johansen	measured	U_m, measured	d', measured outer extent of shear layers.
Griffin	measured	$U_s=KU_m$, measured	d', measured at min. static pressure x/D.
Simmons	measured	$U_s=KU_m$, measured	d', measured at end of formation region.
Roshko	measured	$U_s=KU_m$, measured	d', calculated with notched hodograph.
Bearman	measured	$U_s=KU_m$, measured	d', calculated with von Kármán inviscid model and Kronauer stability criterion.

Table 1.1. Summary of universal parameter methods.

A common limitation of between the category 2 parameters is that they assume 2-dimensional flow in their idealized models. The category 1 parameters however, directly account for the 3-dimensional effects in the flow though the use of actual wake measurements. Both methods seem to break down though, when the near wake is modified by the use of a splitter plate.

1.9 Introduction to the present study

The current investigation is primarily experimental and focused on the near wake region of the circular cylinder bluff body in the subcritical Reynolds number regime. The experiments and analysis are separated into three major areas pertaining to uniform flow, mean shear approach flow, and shear layer characteristics. The investigation included both, 2 and 3-dimensional flow configurations. The 2-dimensional configuration was defined by a straight circular cylinder in uniform flow with a straight trailing edge splitter plate that could be varied in length. Those experiments were similar to the experiments conducted by Roshko [1955], Gerrard [1966], and Apelt et al. [1973]. The 3-dimensional configurations are defined by the use of a sinuous trailing edge on the splitter plate, cylinder taper, or mean shear flow. Hot wire anemometer and mean pressure measurements were performed to determine wake characteristics that included, base pressure, drag, shedding frequency, formation length, and wake width. These measurements were conducted in a low turbulence wind tunnel at Reynolds number of 20,000 - 40,000. Wind tunnel and water tunnel experiments were conducted and compared to the hot wire and pressure measurements. The water tunnel flow visualization experiments were conducted at Reynolds number of 4,700 - 7,500. A comprehensive set of wake parameters was generated from the experiments that allowed the dependent relationships between the various parameters to be investigated. The usefulness of this parameter set should not be underestimated, it provides, perhaps for the first time, a set of base pressure, wake width, formation length, shear layer velocity, and shedding frequency

measurements produced under consistent experimental and analysis conditions for a variety of 2 and 3-dimensional bluff body flows.

1.10 Purpose of the investigation

The bluff body problem has been studied extensively over the past century and the problem remains one of the more interesting and challenging in the field of fluid dynamics. The advances have come slowly and with them, a variety of new challenges. Over the past 40 years or so, advances in the area of wake control have allowed safer and more efficient designs for buildings, smoke stacks, dock pilings, drilling platforms, etc., which have justified the research efforts. The more recent investigations have determined the importance of 3-dimensionality in the processes that determine the wake characteristics. Increased control of the 3-dimensionality in the wake can be exploited in applications involving chemical and combustion mixing processes and heat transfer. Many of the these advances have yet not found their way into the practical world but their potential is promising.

The current investigation hopes to add to the understanding of the 3-dimensional aspects of the problem. Since flows are rarely 2-dimensional in nature, it is important to study the way the wake parameters interact under controlled, 3-dimensional circumstances. A significant difference between the current investigation and many of the other 3-dimensional type investigations is that the current work focuses on the subcritical regime while most others are performed in the laminar shedding regime. Data in the subcritical regime will be required for comparison and validation of numerical models that, due to increase computing power, are beginning to accommodate the higher Reynolds number flows. Similarities in the 3-dimensional characteristics between the laminar and subcritical regimes were also examined. Finally, it is hoped that the current investigation will provide useful data and ideas to other researchers in the bluff body field.

CHAPTER 2. EQUIPMENT

2.1 Wind Tunnels

Two subsonic wind tunnels, located at the Hessert Center for Aerospace Engineering at the University of Notre Dame were used for this research. The smaller of the two, a 2 ft. x 2 ft. x 6 ft. test section, indraft tunnel is shown in the schematic in Figure 2.1. This tunnel has a inlet contraction ratio of 20.6:1 with 12 anti-turbulence screens. The flow was driven by a eight-bladed fan connected to a 18.6 kW AC induction motor. To minimize vibrations, the motor was located on an isolated concrete floor in an adjoining room with a foam vibration insulator between the test section and the diffuser.

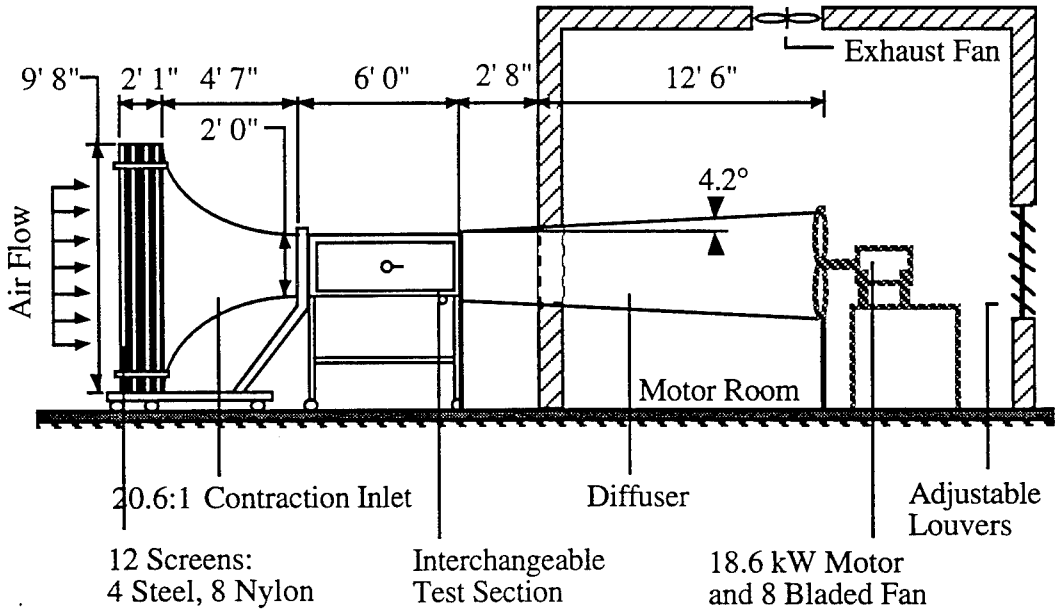

Figure 2.1. Schematic of the Subsonic Wind Tunnel located at the Hessert Center for Aerospace Research, University of Notre Dame

Speed capability of this tunnel ranged from 10 ft/s to 100 ft/s with most of the experiments run at a mean tunnel velocity of 36 ft/s. The turbulence intensity at this velocity was below 0.05%.

Cylinder models were mounted horizontally in a removable test section 6.0 feet long with a 2.0 ft. cross section. One side of the test section was constructed of glass to provide viewing access. A digitally controlled, three degree-of-freedom traverse mechanism was attached to the top of the test section. The traverse system was originally designed and used by Payne [1987] and had an overall probe positioning accuracy of ± 1 mm in the streamwise and spanwise directions and ± 0.1 mm in the transverse direction. Another test section measuring 2 ft. x 2 ft. x 8 ft. with windows on the top, bottom and one side was used for the flow visualization experiments described in Chapter 7.

A mean shear velocity profile could be generated in the tunnel by placing a curved, uniform screen, originally used by Fiscina [1977], upstream of the test section. The shape of the shear screen was determined using the method of Elder [1959]. A linear shear flow was produced with a velocity gradient, $dU/dz = 6.2\ sec^{-1}$ and turbulence intensity level of approximately 0.2%.

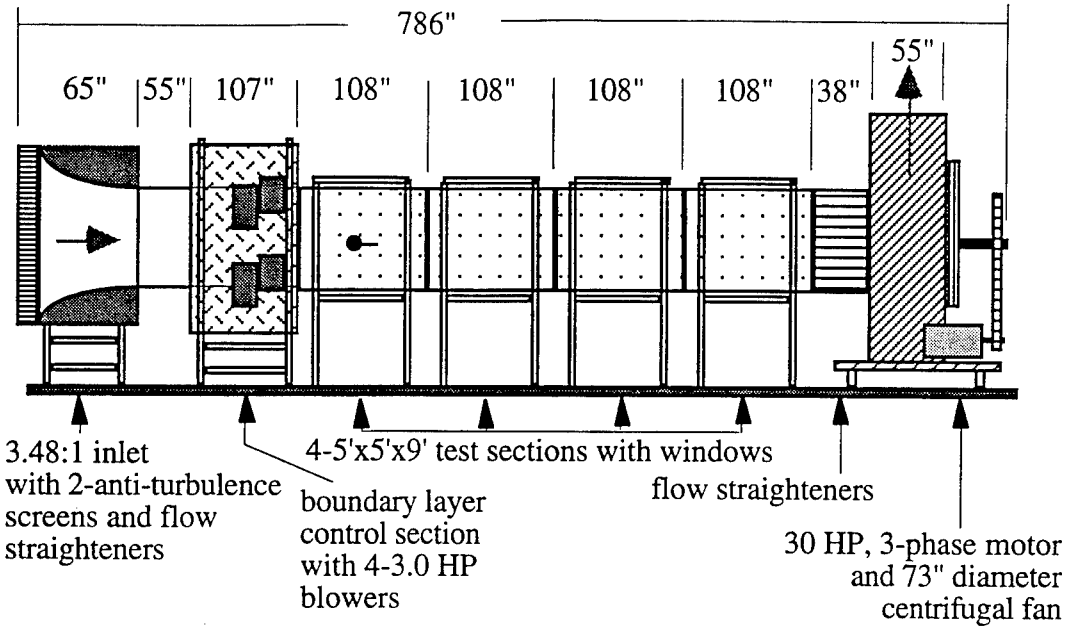

Figure 2.2. Schematic of atmospheric wind tunnel located in the Hessert Center for Aerospace Research at the University of Notre Dame.

A larger atmospheric wind tunnel, shown in Figure 2.2, was also used in this research. This wind tunnel was an indraft, open circuit type with an inlet contraction ratio of 3.24 : 1 and 5 x 5 x 36 ft. rectangular test section. A 30 HP, 3-phase induction motor powered a 73 inch diameter centrifugal fan to produce flow velocities from 10 - 40 ft/s with a turbulence intensity of 0.5% at the model location.

2.2 Models

The straight cylinder model used in the 2 ft. x 2 ft. tunnel was constructed from 2.0 inch outside diameter (OD), aluminum pipe with a 0.5 inch wall thickness and length of approximately 30 inches. A slot 1/16 inch wide and 1/8 inch deep was machined along the span to provide a mount for the splitter plates. A spanwise series of 15, 1/8" holes were machined into the cylinder, spaced 1.0 inches apart, to provide access for base pressure measurements. The ports were offset by 10° from the base to avoid interference with the

splitter plate. Tygon tubing of 1/16 inch inside diameter (ID), was inserted through the 15 holes and then out the end of the cylinder and cut flush with the cylinder surface to produce mean pressure measurement ports. Two tapered cylinder models with different taper ratios, dD/dL = 0.031 and 0.042 were also produced. The cylinder with the higher taper ratio was constructed from 2.0 inch diameter solid aluminum rod and did not contain base pressure ports. The model had a minimum diameter of 1.0 inches at one cylinder end that increased linearly to a maximum diameter of 2.0 inches over a span of 24.0 inches. The model with the smaller taper, dD/dL = 0.031, was machined from 2.0 inch OD aluminum pipe with a 0.5 inch wall thickness. The linear taper extended from a minimum diameter of 1.25 inches at one end, to a maximum diameter of 2.0 inches over a 24.0 inch span. Fifteen base pressure ports were mounted on the dD/dL = 0.031 model, spaced 1.0 inch apart, with the same dimensions and materials as those used on the straight cylinder model. All three models were polished to a smooth surface finish.

The end plates used with the models were constructed from 0.25 inch thick Plexiglas 11.5 inches long and 6.0 inches wide. The leading edge of the end plate was rounded off with a radius of 3.0 inches. The inboard side of the leading edge was chamfered to help eliminate flow separation on the end plate. A schematic of an end plate is presented in Figure 2.3. The smaller diameter of the tapered cylinder was accommodated by an insert that fit into the 2.0 inch diameter hole in the end plate to effectively reduce the hole diameter to the size required by the taper.

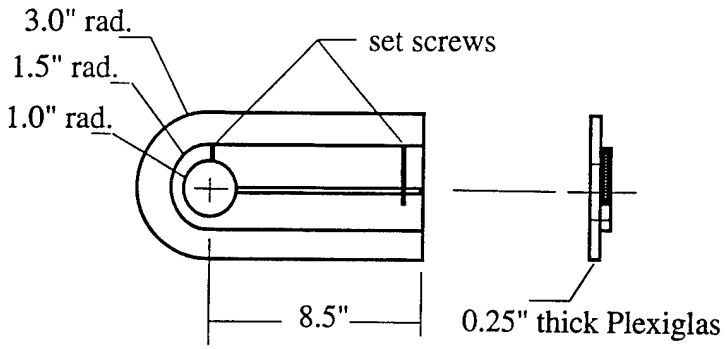

Figure 2.3. Schematic of cylinder end plates.

Various splitter plates were constructed from 1/16 inch aluminum plate for use with the straight cylinder model. Eleven, straight trailing edge, plates were used in the experiments and ranged in length from $\ell/D = 0.125$ to 2.0. In addition, five sinuous trailing edge splitter plates of $\lambda/D = 3.0$ and $\ell/D = 0.5$ - 1.5, and two plates each of $\lambda/D =$ 1.5 and 6.0 with $\ell/D = 0.625$ and 1.0 were used. All the sinuous trailing edge splitter plates had an amplitude, $a/D = 0.5$. The blunt trailing edges of the splitter plates were not sharpened or rounded off although they were filed and polished to remove edge imperfections and roughness. A schematic of a sinuous trailing edge splitter plate with the geometric parameter convention denoted is shown in Figure 2.4.

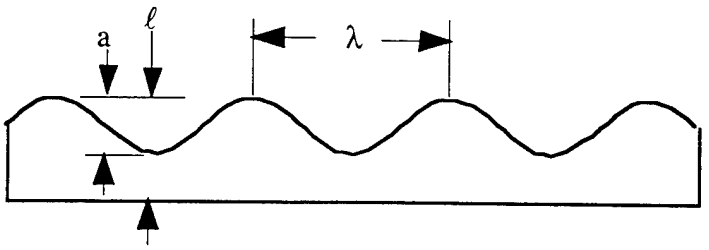

Figure 2.4. Schematic of sinuous trailing edge splitter plate with parameter convention.

Photographs of the straight and dD/dL = 0.031 taper models with end plates and a splitter plate are shown in figures 2.5 a and 2.5 b.

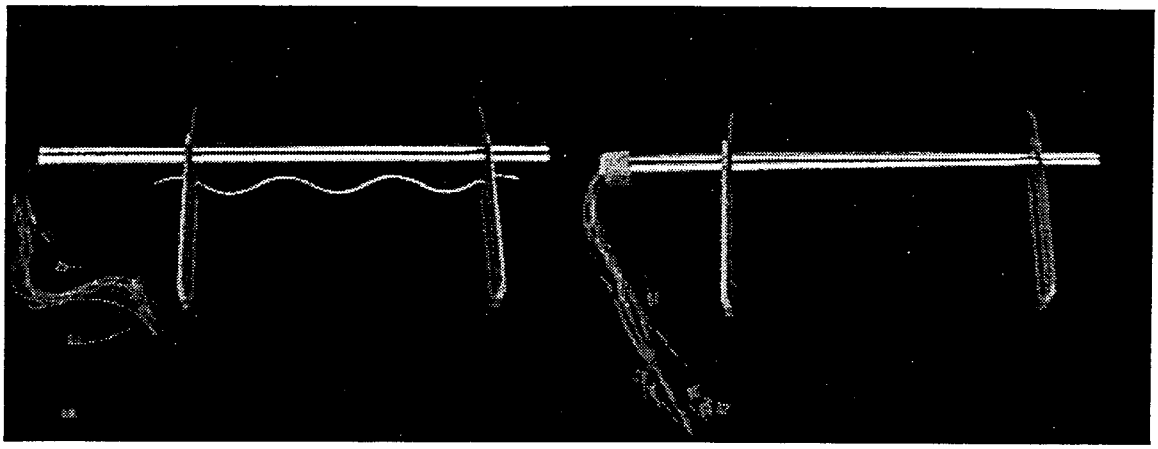

(a) (b)

Figures 2.5. Photographs of cylinder models used in hot wire and mean pressure measurements. a) Straight cylinder with end plates and periodic trailing edge splitter plate. b) dD/dL = 0.031 tapered cylinder model with end plates.

A larger, 3.5 inch diameter straight cylinder model was used in the experiments conducted in the atmospheric tunnel. The model was constructed of 3.5 inch OD aluminum pipe with a 0.25 inch wall thickness and length of approximately 72 inches. A series of 1/8 inch diameter holes were drilled through the cylinder around the mid-span circumference. The holes started 10° above the stagnation point and continued, past the stagnation point, around the circumference spaced 10° apart, skipping the base point and ending 10° above the base point. This configuration resulted in 20 holes around 200° of the circumference. As with the smaller models, 1/16 inch ID Tygon tubing was inserted into the holes and cut flush with the cylinder surface to create the pressure ports. The large diameter of the cylinder was chosen to allow a mechanism to be inserted inside it that could slide a splitter plate in and out of the cylinder, thereby providing infinite length adjustment capability for the splitter plate. A schematic of the splitter plate adjustment mechanism is shown in

Figure 2.6. The mechanism consisted of two steel shafts, for adjustment and tension, that ran the length of the cylinder. The adjusting shaft had two pinion gears that were matched by gear racks attached to the splitter plate near both ends. Rotation of the adjusting shaft resulted in radial movement of the splitter plate. The second, tension shaft was located below the splitter plate between the adjusting shaft and the cylinder wall. Two bearings were positioned on the shaft adjacent to, and below the rack. Transverse adjustment of the tension shaft allowed pressure to be applied to the bottom of the plate to maintain contact between the pinion gears and the racks. The adjusting shaft extended out through the end cap of the model to allow adjustment of the splitter plate from outside the wind tunnel.

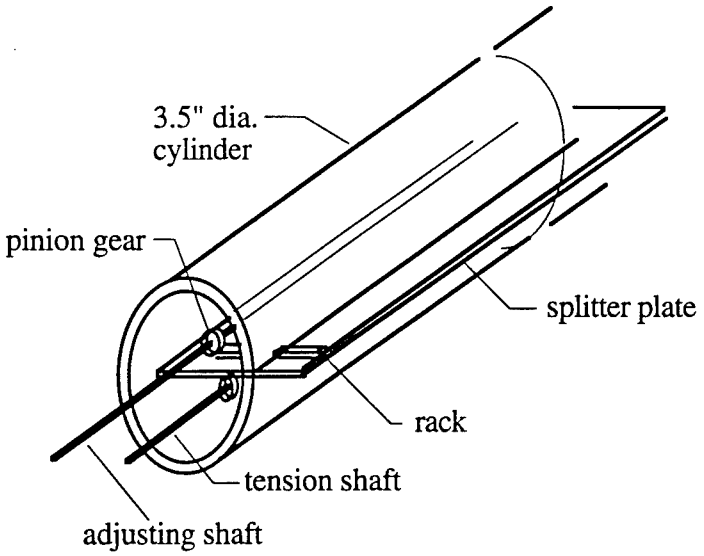

Figure 2.6. Schematic of splitter plate adjustment mechanism for 3.5" diameter atmospheric tunnel model.

The end plates used on the large model had the same basic construction as the smaller model end plates except they measured 23.0 inches long, 18.0 inches wide, 0.25 inches thick, and had a leading edge radius of 9.0 inches. The end plates had streamwise slots cut in them that the splitter plate could slide through. This design eliminated unwanted transverse movements in the splitter plate but still allowed spanwise adjustment

of the end plates for aspect ratio control. Three interchangeable splitter plates were designed for the large cylinder from 1/8 inch aluminum plate. Two straight trailing edge splitter plates were required to cover the desired length range resulting in a short plate covering $\ell/D = 0.00$ to 0.82 and a longer plate for $\ell/D = 0.82$ to 1.57. A sinuous trailing edge splitter plate of $\lambda/D = 3.0$, $a/D = 0.5$, and an ℓ/D range of 0.5 to 1.25 was also constructed. The 1/8 inch thick plate allowed 1/16 inch ID brass tubes to be imbedded in the surface of the sinuous trailing edge splitter plate to provide access for surface mean pressure measurements. A series of 5 equally spaced pressure ports were manufactured which spanned the distance between two peaks of the sinuous trailing edge. The ports were positioned 0.25 inches from the trailing edge of the splitter plate. An image of the 3.5 inch diameter cylinder model with a straight trailing edge splitter plate is presented in Figure 2.7.

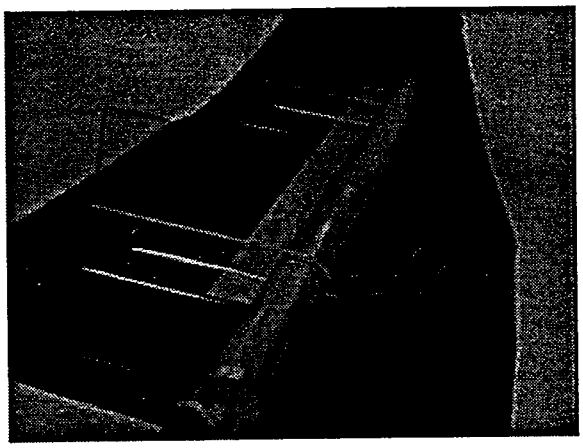

Figure 2.7. Photograph of 3.5 inch diameter cylinder with adjustable splitter plate and end plates attached.

2.3 Data Acquisition Equipment

Hot wire measurements were conducted using a Dantec 55P01 single wire probe. This probe had a tungsten wire sensor of 5 μm diameter and 1.0 mm length and operated in a constant temperature mode with an overheat ratio of 1.8. The analog signal from the hot

wire was processed with a TSI Intelligent Flow Analyzer (IFA 100). The IFA 100 was equipped with a TSI model 157 signal conditioner that provided 10 DC offset settings between 0 - 9 volts, 27 possible gain settings between 1-900 and 49 possible low-pass filter settings between 1 Hz - 500 kHz using a third-order, -18 dB/octave roll-off, Sallen-Key type anti-alias filter. The unit included AC coupling capability with high pass filter settings of 0.1, 3, and 10 Hz and filter roll-off of -6 dB/octave.

The gained and filtered analog signal from the IFA 100 was converted to a digital format using either of two National Instruments A/D conversion boards. One, a AT-MIO-16X, 16-bit board had a maximum sustained sample rate of 100 kHz with pretrigger and posttrigger sampling capability. This board could scan up to 8 channels sequentially and was used in the ±5 volt signal range. The other, a EISA-A2000, 12-bit board had a maximum sustained sample rate of 1 MHz with programmable AC/DC coupling and pretrigger and posttrigger capability. This board could sample 4 channels simultaneously with a voltage range of ±5.12 V.

The A/D conversion boards were controlled with LabVIEW software installed on a Macintosh IIfx computer with 5 Mb RAM. LabVIEW is a software language that provides graphical representations of virtual instruments that can be 'wired' together in much the same manner as their hardware counterparts. The software package provides a large quantity of pre-coded virtual instruments such as fast-Fourier transforms (FFT's), digital filters, statistical analysis tools, etc. that can be combined in various configurations to custom design a data acquisition and processing system. To ensure proper operation, all pre-coded functions used in the experiments were validated using input/output relationships from a signal generator or known analytic functions. The LabVIEW programs were also used to control the probe traverse system through the use of digital I/O ports on the A/D boards. That feature allowed the design of automated data acquisition and processing

systems that were capable of traversing the wake of the cylinder and storing, not only the raw data but also processed data such as mean velocities, RMS of velocity fluctuations, and power spectrum representations for each traverse point. The LabVIEW programs greatly increased the efficiency of data acquisition and analysis over previous methods. Also, LabVIEW's ability to process and display the data in real time made it possible to detect errors as they occurred so they could be corrected without significant time loss.

Differential pressure measurements from the pitot-static tube and mean pressure ports were made through the use of Setra Systems model 339B electronic manometers with a range of -0.5 to 0.5 in.H_2O and an analog signal output range of -5 to 5 volts. The electronic manometers were calibrated against a Betz model 2500 micro-manometer with a range of -50 to 2500 Pa and resolution of $\pm$0.1 Pa. The analog output from the Setra manometer was digitized by an A/D conversion board and processed by the LabVIEW computer program.

A 48 channel Scanivalve and solenoid controller model CTLR2P/S2-S6 was used in conjunction with the electronic manometers to obtain the mean differential pressure measurements from the various surface pressure ports. Controlled through LabVIEW software and an A/D board, the Scanivalve was able to connect any of up to 48 pressure ports to the electronic manometer automatically.

2.4 Signal analysis methods

Most of the digital signal analysis was performed using LabVIEW software programs which contained the various pre-coded analysis subroutines or, virtual instruments. These subroutines were verified in various ways. For example, the LabVIEW FFT routine was checked by having it process a digital representation of an analytic Sine function. The result was compared with the output produced from a simple

FORTRAN DFT code using an identical function. In addition, the subroutine was checked by sampling a real, analog Sine wave of known frequency produced by a function generator and verified by an oscilloscope. All the subroutines used in the analysis of the experimental data have been verified in a similar manner.

Mean and RMS or, root mean square, statistical values of a time varying signal were important not only in the direct measurement of wake parameters, but also in the initial calibration of the hot wire and validation of the wind tunnel flow characteristics. The term 'mean' will be used imply the arithmetic mean of a set of N values $x_1, x_2, x_3,...,x_N$ denoted by the upper case X, and defined by,

$$X = \frac{1}{N}\sum_{i=1}^{N} x_i \tag{2.1}$$

The RMS value of a set of N values will be denoted by a subscript, lower case character, x_{rms}, and imply use of the quadratic mean defined by,

$$x_{rms} = \sqrt{\frac{1}{N}\sum_{i=1}^{N} x_i^2} \tag{2.2}$$

In many cases an ensemble average was used and will be defined as the mean value of a set of mean or RMS values. The ensemble averaging technique was used as an efficient method of obtaining a very long time average of a signal without requiring storage of the total number of values in the computer memory at any one time.

The use of a fast Fourier transform allowed the major frequency components of a periodic signal to be analyzed. The Fourier transform is defined as,

$$X(f) = \int_{-\infty}^{\infty} x(t)e^{-i2\pi ft}dt \tag{2.3}$$

In order to implement this formula on a digital, finite signal the discrete Fourier transform (DFT) is introduced,

$$X_k = X(k\Delta f) = X(f_k) = \sum_{n=0}^{N-1} x_n e^{-i2\pi kn/N}\Delta t \tag{2.4}$$

The smallest frequency difference that can be resolved or, sampling resolution of this formula is $\Delta f = f_s/N$. Since $N = f_s T$, it follows that the frequency resolution only depends upon the sample period, T,

$$\Delta f_s = \frac{1}{T} \tag{2.5}$$

To increase computational efficiency of the calculation of the Fourier coefficients, LabVIEW implements a fast Fourier transform (FFT) routine based on the Split-Radix algorithm, National Instruments [1990].

The average power spectrum used in LabVIEW is defined as,

$$S_{xx}(f_k) = X^*(f_k)X(f_k) = |X(f_k)|^2 \tag{2.6}$$

where, $X^*(f)$ is the complex conjugate of X(f). Depending on the reference, the exact definition of the DFT and therefore, the FFT and power spectrum will vary. The various methods usually only vary by a scaling constant though and the differences only effect the magnitude of the Fourier coefficients. As an example the average power spectrum method

implemented in the LabVIEW algorithm differs from the two-sided autospectral density function defined by Bendat and Piersol [1986] by a factor equal to the sample period. Since in the present study the magnitude of a frequency peak was only evaluated in terms of a difference relative to some other peak, and all results are based on the same algorithm, the differences between various DFT definitions have no significant effect on the results. As a consequence, arbitrary scales were used for the presentation of all power spectrum data in this study.

FFT routines work on an assumption that the discrete time sample contains an integer number of periods and, to model it as an infinite time series, the routine essentially lines up copies of the time series end to end. Since real samples do not contain an integer number of periods, sharp discontinuities form where the ends of the series join and give rise to spectral leakage. To reduce the amount of spectral leakage a smoothing window function was applied to the digital time series. The Hanning window was chosen for the present study although there are many window functions available that effectively accomplish the same task. The Hanning function is defined by,

$$w_n = 0.5\left(1-\cos\left(\frac{2\pi n}{N-1}\right)\right) \qquad \text{for } 0 \le n \le N\text{-}1 \tag{2.7}$$

This function reduces to zero at the ends and therefore minimizes the transition edges of the sampled signal to reduce leakage. Applying the Hanning window also results in a loss of power compared to a non-windowed formula. The total loss in power is proportional to the ratio of the area of the window to that of a rectangular window (no window function). For the Hanning window that ratio turn out to be 0.5 so, to recover the power loss due to the window function the DFT is multiplied by 2.0. The form of the DFT then, after including the window function and the power loss factor is,

$$X(f_k) = 2.0 \sum_{n=0}^{N-1} w_n x_n e^{-i2\pi kn/N} \Delta t \tag{2.8}$$

Cross-correlation analysis was used in the hot wire experiments to determine vortex convection velocities. This is explained by considering two periodic, zero-mean signals, x(t) and y(t), with variances σ_x and σ_y respectively, sampled over a time period T. The cross-correlation coefficient is defined,

$$\rho(\tau) = \frac{\frac{1}{T} \sum_{t=-T/2}^{T/2} x(t) y(t+\tau) dt}{\sigma_x \sigma_y} \tag{2.9}$$

The value of the cross-correlation coefficient is bounded by $-1 \leq \rho(t) \leq 1$ and gives a measure of the linear dependence between x(t) and y(t) for a displacement of τ in y(t) relative to x(t).

The cross-correlation was used in this research to measure streamwise vortex convection velocities. To accomplish the measurement, two probes were located near the shear layer at identical spanwise positions but with a streamwise separation of Δx. The probe signals were sampled simultaneously, digitized, and processed by the cross correlation algorithm. The time displacement corresponding to the maximum value of the cross-correlation coefficient $\tau_{\rho max}$, gave the time required for a flow disturbance to travel the distance between the probes. The convection velocity of the vortex, U_{cv}, was then computed by the relationship $U_{cv} = \Delta x/\tau_{\rho max}$.

2.5 Hot wire calibration

The hot wire probe was calibrated in the wind tunnel test section and referenced to the pitot-static tube and electronic manometer that were to be used in the experiments. For the calibration, the pitot-static tube was positioned in close proximity (within one inch) of the hot wire sensor and both were aligned to the flow. The tunnel was run at various motor speed settings and the freestream tunnel velocity computed from the pitot-static tube measurements. The hot wire and electronic manometer signals were sampled at 1000 Hz for 4 seconds. The mean voltage from the electronic manometer output sample was computed and converted to in.H_2O through the manometer calibration. Bernoulli's equation was used to compute the mean velocity of the flow from the differential pressure measurement and the ambient conditions of the laboratory air. For each tunnel speed setting a mean velocity from the pitot-static tube and a mean voltage from the hot wire was recorded. A fourth order polynomial curve fit was used to produce a conversion relationship between mean velocity and hot wire mean voltage such as that shown in Figure 2.8. The coefficients for the curve fit were used in the computer data acquisition programs for real time conversion of the hot wire signal to velocity.

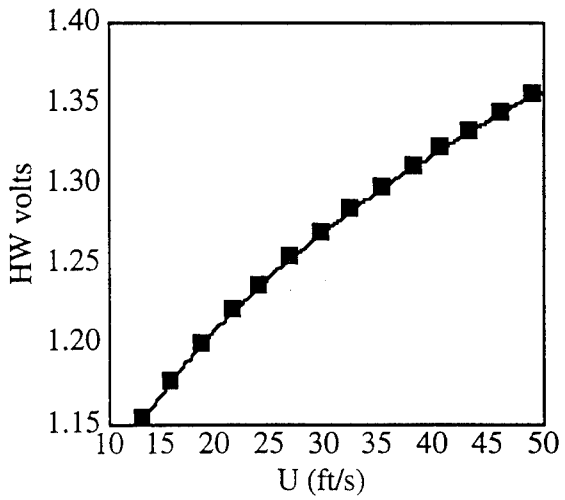

Figure 2.8. Typical hot wire calibration data and curve fit.

The fourth order polynomial fit used in the hot wire calibration allowed convenient calculation of the RMS value of the velocity fluctuations, u_{rms}. Let E and e_{rms} be defined as the mean DC voltage and the RMS value of the AC coupled hot wire signal respectively. Then u_{rms} is calculated by,

$$u_{rms} = e_{rms}\left[\frac{dU}{dE}\right]_{E_o} \tag{2.10}$$

where, the bracketed quantity can easily be determined from the derivative of the polynomial fit evaluated at the mean voltage experienced by the sensor, E_o. The RMS of the velocity fluctuations is typically presented in non-dimensional form, normalized by a characteristic mean velocity, U. In the data pertaining to the turbulence level of the empty tunnel test section this parameter will be identified as the turbulence intensity and be presented as a percentage of the mean freestream velocity computed from the reference pitot-static tube measurements. For measurements in the periodic cylinder wake, where it may not be appropriate to call this parameter a turbulence intensity, it will be identified as the RMS of the velocity fluctuation to avoid misunderstanding.

2.6 Wind tunnel flow quality

Measurements were made with a calibrated hot wire to determine the uniformity and turbulence level of the flow in the wind tunnel test section. A series of probe traverses were performed that covered the majority of the empty tunnel cross section at the location where the model was to be placed. This procedure was performed for both the wind tunnels used including the wind tunnel configured with the shear flow generator.

The data presented in the following figures describing the mean velocity and turbulence characteristics of the wind tunnels used in the experiments were obtained by performing ten ensemble averages of 2048 samples acquired at a sample rate of 1000 Hz.

The analog signal was low-pass filtered at 500 Hz to avoid aliasing. The AC coupled component of the signal was obtained at a high pass filter setting of 0.1 Hz. The filter settings were checked against power spectra for data obtained at various sample rates and filter settings to prevent the filtering out of any significant turbulent energy scales.

Figure 2.9 shows the mean velocity profiles for the atmospheric wind tunnel at a reference tunnel velocity of 21 ft/s. This flow velocity corresponds to a Reynolds number for the 3.5 inch diameter cylinder of 30,000. The charts indicate a gradual deficit in mean velocity, symmetric about the tunnel centerline, reaching approximately 90% of the reference velocity at the center of the tunnel. This slight curvature of the velocity profile was not considered to have a significant effect on the experiments since the profile near the model location was fairly uniform and the measurements conducted were all located at the center of the span. Spanwise traverses, which would be affected the most by the profile curvature, were not performed on the large model. Figure 2.10 shows the turbulence intensity profiles obtained at the same time as the mean velocity profiles. The charts indicate a uniform profile for most of the area near the model location with a turbulence intensity level of approximately 0.5%.

Mean velocity and turbulent intensity profiles for the 2 ft. x 2 ft. cross section wind tunnel are presented in Figure 2.11. The reference velocity of 38.4 ft/s corresponds to a Reynolds number for the 2.0 inch diameter cylinder of approximately 32,000. These charts show that the mean velocity and turbulence intensity profiles are uniform across the majority of the wind tunnel cross section. The turbulence intensity level is relatively low, below 0.04% for most of the section. The high turbulence intensity and slight mean velocity deficit measured near z = -7 inches was due to the wake from the reference pitot-static tube.

Figure 2.12 presents the mean velocity and turbulence intensity profiles for the shear flow configuration. The reference velocity is based on pitot-static tube measurements located at a fixed position near mid-span. The turbulence intensity though, in normalized by the local mean velocity obtained from the hot wire . The mean velocity profile shows strong linearity between the tunnel span positions of z = -8 to 6 inches with a gradient of $dU/dz = 6.2\ sec^{-1}$. Beyond z = 6 inches the profile deviated from the linear gradient, with a greater reduction in velocity, to the end of the span. The region of higher gradient beyond z=6 inches, corresponds to an increase in the turbulence intensity which, up until that point was at a low and uniform level of approximately 0.20%. For comparison, the shear profile generated in the present study shows lower turbulence and better linearity than Maull and Young [1973], and comparable turbulence with slightly less linearity than Woo et al. [1989]. Experiments demonstrated the normalized velocity gradient, $d(U/U_{ref})/dz$ remained constant over the different reference velocities used in this investigation. Various parameters have been used to characterize shear flows, the following, calculated for the present study are typical of those most commonly found in the literature (e.g. Woo et al. [1989] and Griffin [1985]),

shear gradient, $dU/dz = 6.2\ sec^{-1}$

steepness parameter, $\beta = dU/dz(D/U_{ref}) = 0.03$

shear parameter, $\Lambda = \beta W/D = 0.34$

where, W is the tunnel width, U_{ref} is the mid-span velocity, and D = 2.0 in.

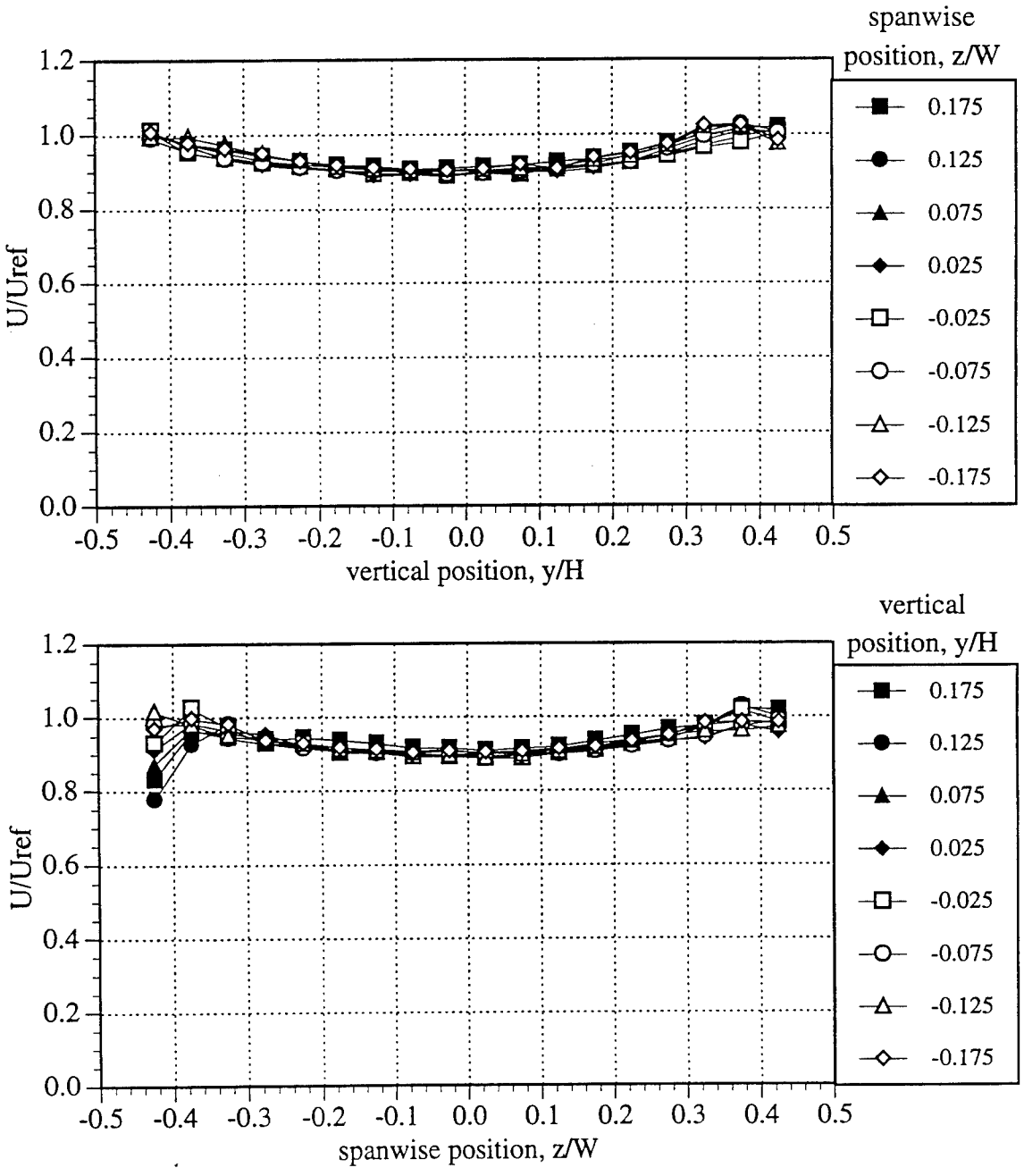

Figure 2.9. Mean velocity profiles for the atmospheric tunnel.
Uref = 21 ft/s, sample rate = 1000 Hz, # samples = 2048, # ensembles = 10.

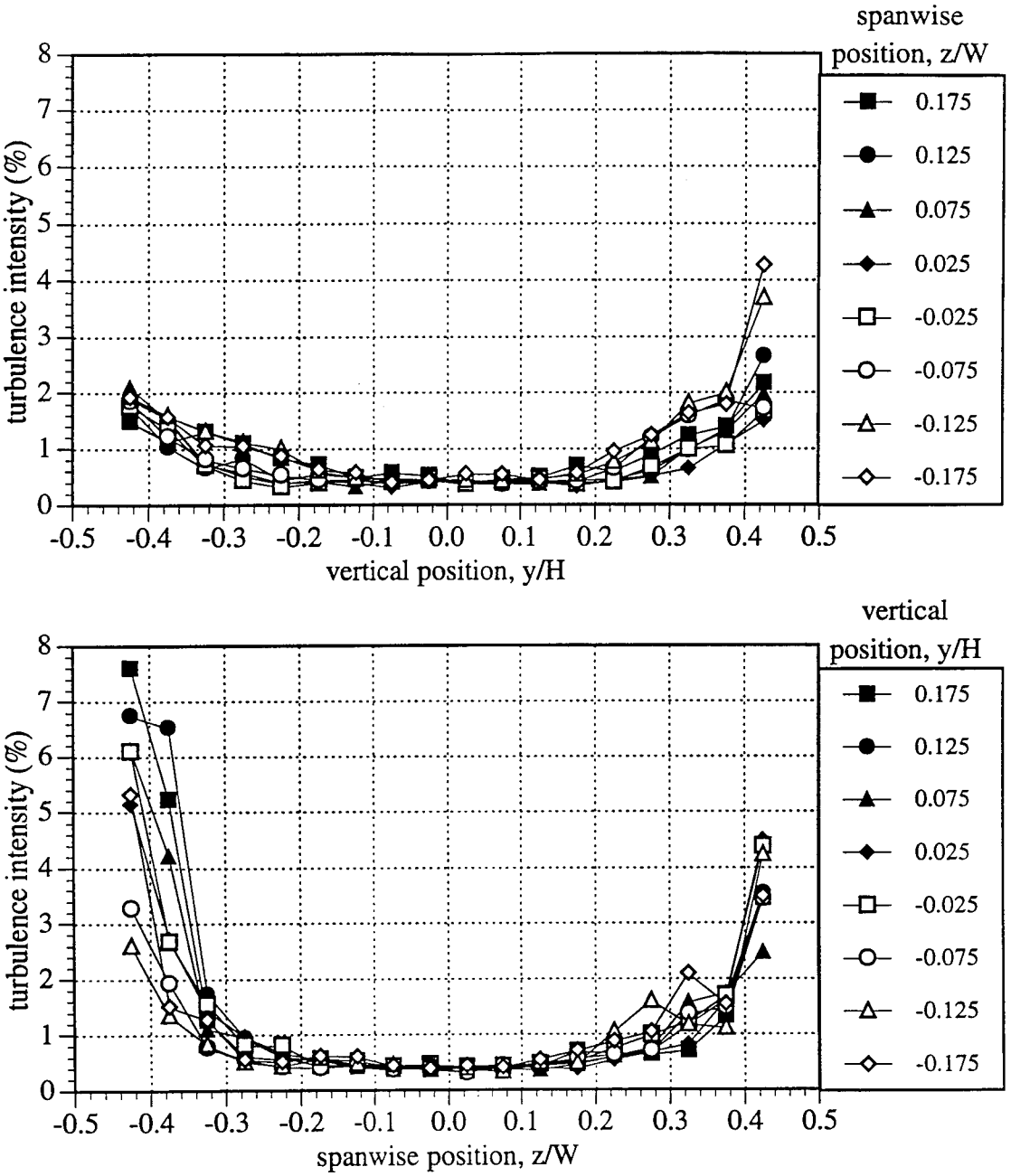

Figure 2.10. Turbulence intensity profiles for the atmospheric tunnel.
Uref = 21 ft/s, sample rate = 1000 Hz, # samples = 2048, # ensembles = 10.

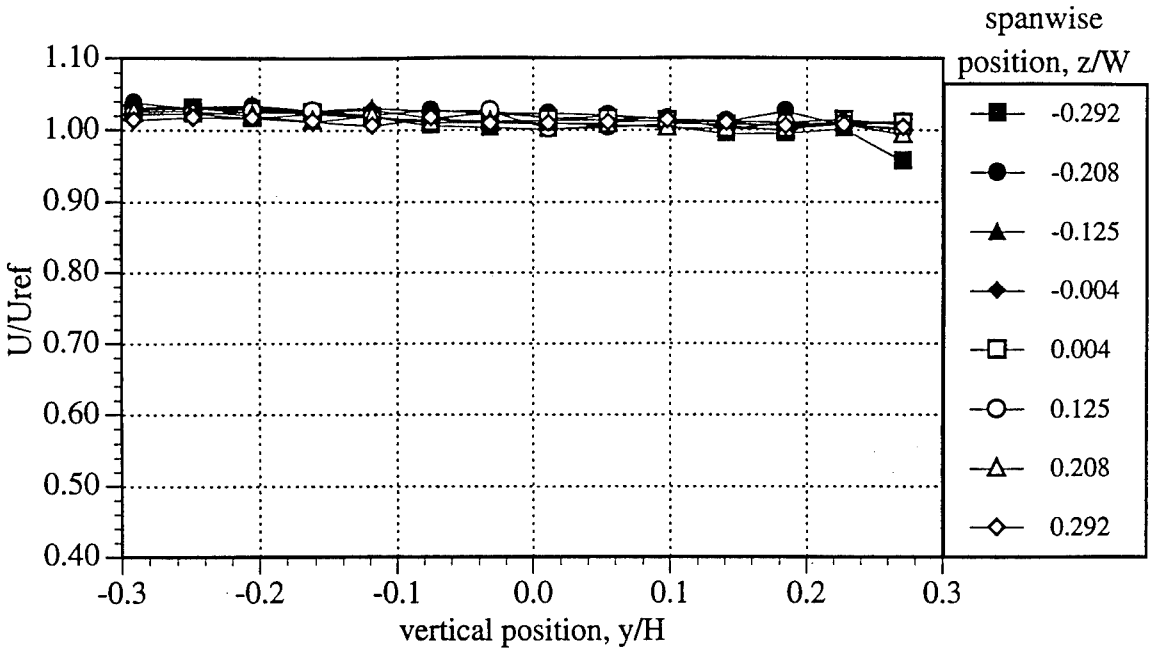

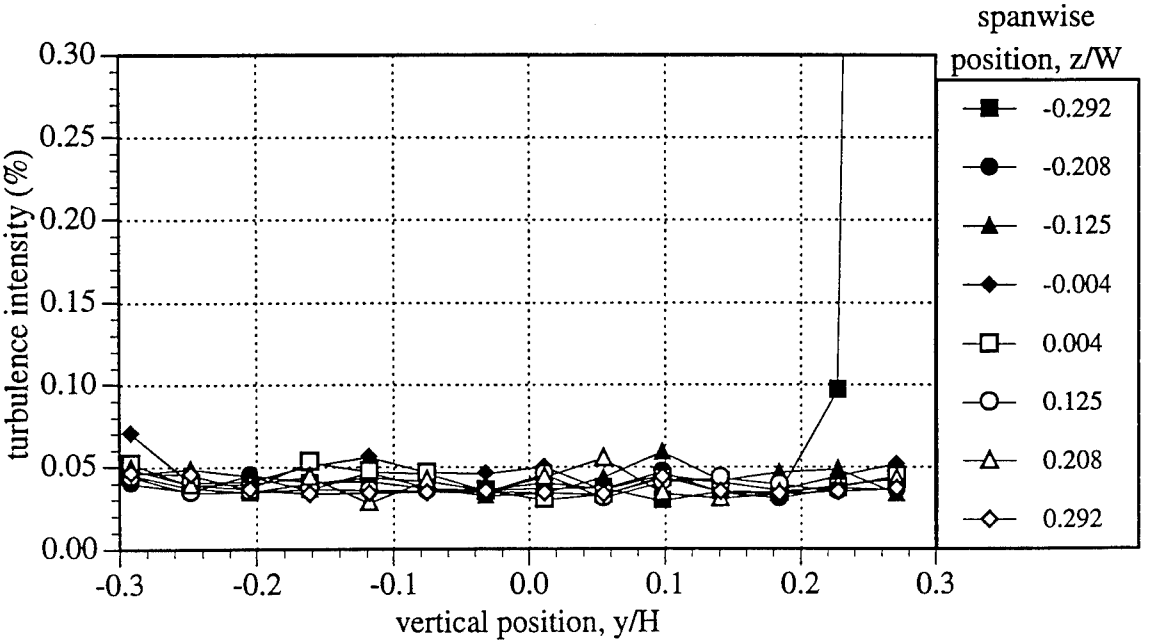

Figure 2.11. Mean velocity and turbulence intensity profiles for uniform flow in low speed tunnel. Uref = 38.4 ft/s, sample rate = 1000 Hz, # samples = 2048, # ensembles = 10.

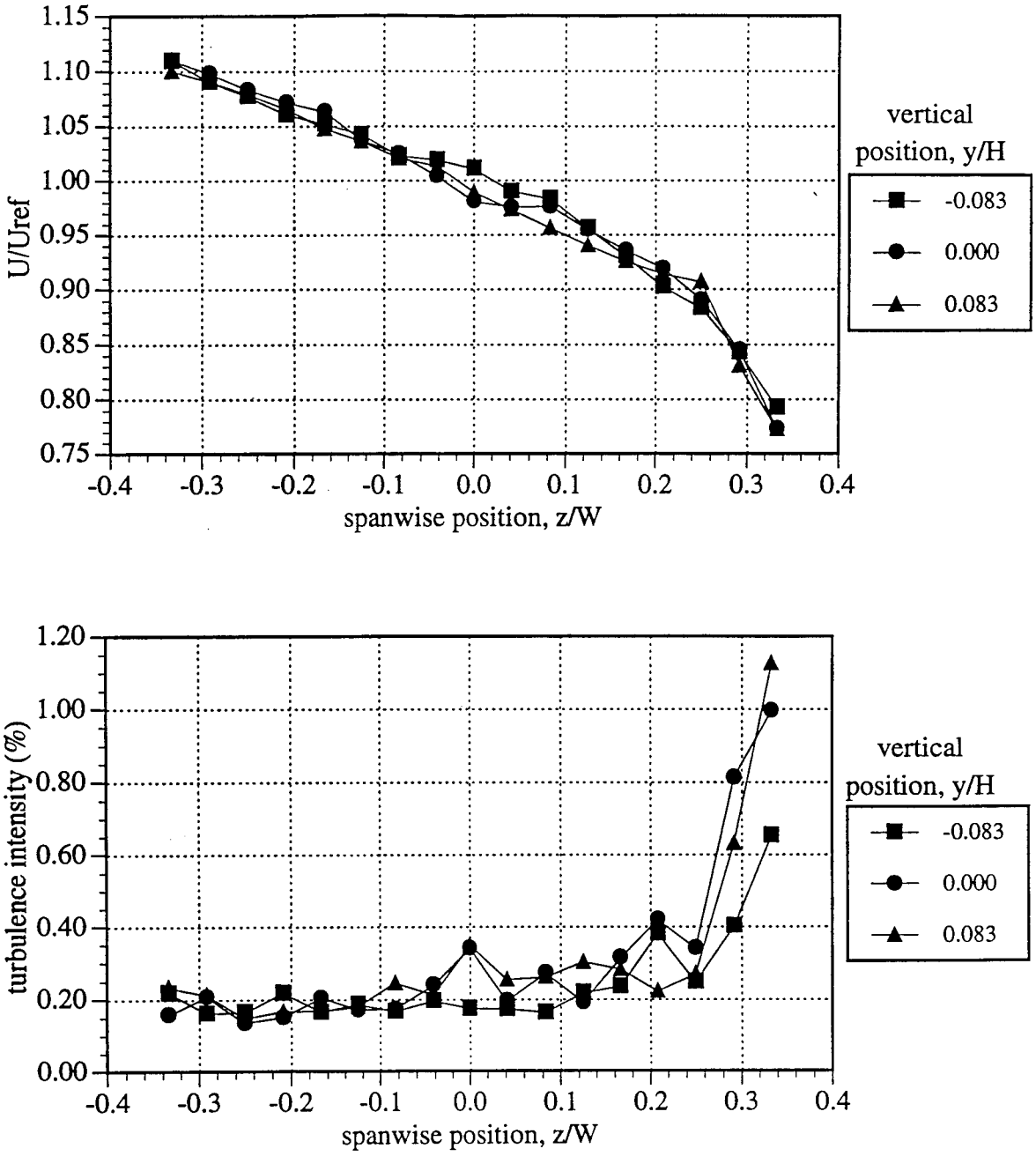

Figure 2.12. Mean velocity and turbulence intensity profiles for shear flow in low speed tunnel. Uref = 36 ft/s, sample rate = 1000 Hz, # samples = 2048, # ensembles = 10.

CHAPTER 3. RESULTS FOR A STRAIGHT CYLINDER IN UNIFORM FLOW

The following is a presentation of the hot wire and mean pressure experiment results for a straight cylinder in uniform flow. The experiments include mean velocity, RMS fluctuation intensities, and power spectrum measurements obtained from single-sensor hot wire probes, and base pressure and drag measurements from surface pressure ports. The investigated configurations include straight and sinuous trailing edge splitter plates. The experiments were conducted at Reynolds number of 30,000 based on the cylinder diameter.

3.1 RMS fluctuation intensity maps

Figures 3.1 - 3.9 present color contour maps that indicate the variation in RMS fluctuation intensities in the near wake region behind the circular cylinder with splitter plate. The variation in RMS magnitude give an indication of the distribution of energy in the near wake for the various splitter plate configurations. The maps were produced by measuring the RMS value of the hot wire voltage fluctuations at a series of locations or, grid points in the wake and then displaying the results on color contour plots with each color representing a different range of RMS values. Table 3.1 presents the relevant sampling parameters and grid spacing used to generate the maps.

	Figures 3.1 - 3.3	Figures 3.4 - 3.9
$\Delta x/D$	0.20	0.25 (0.125)
$\Delta y/D$	0.10	0.20
$\Delta z/D$	-	(0.10)
sample frequency, Hz.	200	200
sample size	2048	1024
ensembles	5	5

Table 3.1. Sampling parameters and grid spacing for RMS of fluctuations maps. Values in parenthesis apply to Figure 3.9 only.

The RMS values presented in Figures 3.1 - 3.3 are based on RMS voltage fluctuation measurements that have been converted to RMS fluctuation intensity through the hot wire calibration. The conversion cannot be considered reliable though in regions of 3-dimensionality such as those within the formation region. The plots still serve their purpose though and give an indication of the distribution of energy in the wake, provided the comparisons are made between consistent data. The remainder of the maps presented in Figures 3.4 - 3.9 are based on RMS values of the voltage fluctuations.

Figures 3.1 and 3.2 present maps for a circular cylinder in uniform flow with splitter plates of $\ell/D = 0.0$, 0.5, 1.0, and 1.9. The cross-section schematic of the cylinder and splitter plate shown, indicates the approximate scale and location of the model to the measurement grid. Figure 3.3 omits the cylinder schematic to allow room for direct comparison of the four configurations on a single page. The results clearly show a difference in the time average energy distribution between the cylinder without a splitter plate and the various splitter plate configurations. Most noticeable is the considerable area occupied by high RMS values in Figure 3.3 (a) compared to those shown in Figure 3.3

(b), (c), and (d). With a splitter plate, the near wake energy is distributed in a smaller transverse region than without the plate, indicating a more narrow wake. The areas of highest energy, shown by the red contours, move downstream with increasing plate length corresponding to an increase in the length of the formation region. There is also a decrease in the size of the area occupied by high energy for the cases with a splitter plate compared to that with no splitter plate. The reduction in size of the high energy region is interpreted as an increase in the organization of the near wake.

Figures 3.4 - 3.6 show RMS intensity maps of the region behind a straight circular cylinder with splitter plate, $\ell/D = 0.0, 0.125, 0.25$, and 0.5, using the same format as in Figures 3.1 - 3.3. In addition to the previously described difference in data processing between the results in these figures and those in Figures 3.1 - 3.3, there are the effects of a coarser grid spacing and shorter sample times that contribute to explain the waviness of the contour lines. The maps indicate the effect of very short splitter plates on the wake and describe a region closer to the cylinder than in the previous cases, up to $x/D = 1.0$. The results show that the presence of even a very short splitter plate can alter the energy distribution significantly. The orange contours that surround the highest energy, red contours, are smaller in all of the splitter plate configurations than in the no splitter plate configuration indicating that the energy becomes more localized. The highest energy, red contours move downstream with increasing plate length corresponding to an increase in length of the formation region as also indicated previously. The contours in the very near wake region, around $x/D = 1$, show a substantial reduction in wake width with the splitter plate configurations over the no splitter plate case.

Figures 3.7 and 3.8 present RMS maps for a straight cylinder in uniform flow with a sinuous trailing edge splitter plate. The maps presented in the left column correspond to a spanwise location adjacent to a peak on the sinuous splitter plate and those in the right

column, a valley. In Figure 3.7, the contour maps show the effect of sinuous splitter plate length by comparing the $\ell/D = 0.5$, 0.625, and 0.75 configurations at a constant wavelength, $\lambda/D = 3$. Figure 3.8 examines the effect of plate wavelength on the wake by comparing the $\lambda/D = 1.5$, 3, and 6 configurations at a constant plate length, $\ell/D = 0.625$. Examination of Figure 3.7 shows that the region of highest energy, denoted by the red contours, moves downstream with increasing plate length for both the peak and valley locations, similar to the effect observed for the straight splitter plates. Comparison of the peak position to the valley position for constant plate length did not indicate significant differences except for, possibly in the downstream area along $y/D = 0$. That region seemed to show a slight increase in the centerline energy levels at the valley compared to those at the peak. Figure 3.8 indicates that the wavelength of the sinuous splitter plate had an effect on the near wake energy distribution. Examination of the orange contours show that the regions of moderate energy moved closer to the cylinder with increasing wavelength. The regions of highest energy, the red contours, remained essentially stationary though, with respect to wavelength changes. Again, the only noticeable peak to valley effect was the reduction in magnitude of the downstream energy at locations corresponding to peaks on the splitter plate trailing edge at $y/D = 0$.

Figure 3.9 shows a x-z plane view of the RMS distribution along the centerline, $y/D = 0$, of a straight cylinder with sinuous trailing edge splitter plate, $\ell/D = 0.625$, $\lambda/D = 3$, $a/D = 0.5$. The map illustrates the 3-dimensionality introduced to the flow field by the sinusoidal trailing edge. The length of the formation region, denoted by the red contours, remained relatively constant along the span. Downstream, between $x/D = 3.5$ to 4, there appears a definite 3-dimensional distribution of energy. The minimum energy location corresponded to the peak span position of the sinuous splitter plate.

Figure 3.10 shows mean velocity contours for the circular cylinder with splitter plates of ℓ/D = 0.0, 0.5, 1.0, and 1.9. It should be noted that the single sensor hot wire does not measure accurate u-velocity magnitudes in the wake region, approximately y/D = -0.5 to 0.5, where the flow angles and fluctuations are large. However, the figure indicates that the splitter plate has a significant effect on the flow external to the wake. With increasing splitter plate length the regions of high velocity in the outer flow extend downstream. The velocity gradient in the shear layer was much greater for the splitter plate configurations. Without the splitter plate the mean velocity experiences little change in the streamwise direction whereas, with the splitter plate, there was a substantial deceleration of the outer flow between x/D = 2.0 - 4.6. Figure 3.11 presents data from the mean velocity contour maps showing the mean profiles at selected streamwise wake positions. As with the previous figure, the data within y/D = -0.5 - 0.5 does not reflect accurate u-components of the mean flow. The results indicate that by x/D = 4.6 the profiles have relatively similar shapes, regardless of splitter plate length. In the near wake region however, the external flow increases in velocity with increasing ℓ/D. The profiles for ℓ/D = 0.5 at x/D = 2.0 and 3.4 were almost identical to the profiles for ℓ/D = 1.0 at x/D = 3.4 and 4.6. That indicated that between ℓ/D = 0.5 and 1.0 the flow characteristics were only translated in the streamwise direction due to the increased splitter plate length. Comparison between ℓ/D = 1.0 and 1.9 show that the profiles matched at similar streamwise locations suggesting that the increase in plate length had less of an effect on the mean profile.

3.2 Power spectra and Strouhal number

Figures 3.12 -3.17 compare power spectra from the near wake of a straight circular cylinder in uniform flow with various splitter plate configurations. The measurements were obtained at two streamwise positions, x/D = 2 and 4, and at a transverse position of y/D = 0.5. The primary shedding frequency for all configurations was approximately 50 Hz therefore, the flow was sampled at a frequency of 200 Hz with an analog low-pass filter

set at 100 Hz to prevent aliasing. The spectra are based on 100 ensemble averages of 1024 samples resulting in a total sample time per configuration of 8.53 minutes. All experiments were conducted at a Reynolds number of 30,000 and cylinder aspect ratio, AR = 8.

Figures 3.12 and 3.13 present the power spectra results for straight splitter plates of ℓ/D = 0.0 - 1.75 at streamwise probe locations of x/D = 2 and 4 respectively. Both figures illustrate the splitter plate length effect on the primary shedding frequency and the shape of the primary peak in the power spectrum. Variation in splitter plate length between ℓ/D = 0 - 1.75 resulted in primary shedding frequency measurements that varied from 44 - 51 Hz, the minimum occurring for ℓ/D = 0.0, and the maximum with ℓ/D = 1.5. Between ℓ/D = 0.0 and ℓ/D = 0.125 the primary peak became more narrow-band and higher in frequency. The bandwidth remained narrow up to ℓ/D = 0.375 and then gradually became more broad-band with increasing plate length. Measurements beyond ℓ/D = 1.25 show a return to the narrow-band shedding and the introduction of lower frequency, secondary peaks and apparent side-band modulation. Between ℓ/D = 1.5 and ℓ/D = 1.75, the secondary peak increased in magnitude and decreased in frequency (from 11.5 to 9 Hz). The ℓ/D = 1.75 spectrum clearly shows side-band components offset from the primary peak by the secondary frequency of 9 Hz. Careful analysis of Figure 3.12 shows that low frequency components were also measured at plate lengths of ℓ/D = 1.25 - 1.75. Although weak in magnitude, those secondary peaks appear to increase in frequency with decreasing plate length. There was a reduction in the magnitude of the secondary and side-band peaks with increasing downstream distance as indicated by comparison of results at streamwise positions x/D = 2 and x/D = 4.

Figures 3.14 and 3.15 present the power spectra for sinuous trailing edge splitter plates, λ/D = 3, at streamwise probe locations of x/D = 2 and 4 respectively. Both peak and valley probe positions were analyzed for each configuration. The spectra trends were

similar to those for the straight trailing edge splitter plates, indicating narrow-band primary frequency peaks at the short plate lengths that became more broad-band at the intermediate lengths. For the longest splitter plate, $\ell/D = 2$, the primary peak was very narrow and accompanied by a secondary low frequency peak at 9.5 Hz. The primary peak varied in frequency between 46 - 50 Hz depending upon the splitter plate length. Comparison of Figure 3.14 with 3.15 show that the low frequency peak at $\ell/D = 2$ became smaller when the probe was moved from x/D = 2 to 4, consistent with the straight trailing edge results. The comparisons did not suggest any significant differences in the spectra between the peak and valley spanwise positions.

Examination of Figures 3.12 - 3.15 indicate similarities between the power spectra obtained for the straight and sinuous trailing edge splitter plates. Figures 3.16 and 3.17 are presented to better describe those similarities. The figures present results for a combination of straight and sinuous splitter plates of consistent average length. The average length of a sinuous trailing edge splitter plate of amplitude, a/D = 0.5 is defined as the plate length, ℓ/D, reduced by half the sine wave amplitude or, 0.25. Figures 3.16 and 3.17 each present four groupings having average splitter plate lengths of, $\ell/D = 0.25, 0.75, 1.25$, and 1.75. These average lengths correspond to sinuous trailing edge lengths of, $\ell/D = 0.5, 1.0, 1.5$, and 2.0. Results from both the peak and valley probe locations were included. The results show strong similarities between the power spectra for plates of similar average length. The shape and frequency of the primary peaks are nearly identical. For the longest plate length, the low frequency and side-band peaks vary in magnitude but occur at the same frequency.

Strouhal number versus splitter plate length results were obtained from experiments conducted in the atmospheric tunnel with the 3.5 inch diameter model at Re = 33,000 and 40,000, and computed from the data presented in Figures 3.12 - 3.15 for the 2.0 inch

diameter model at Re = 30,000. The data for the 3.5 inch model reflect 30 ensemble averages of 1024 samples at a sample rate of 100 Hz where the maximum shedding frequency was approximately 20 Hz. A mechanism in the 3.5 inch model allowed the splitter plate length to be adjusted from outside the wind tunnel. Two plates were required to cover the full ℓ/D range, a shorter plate covered ℓ/D = 0.0 to 0.82 and a longer plate, from ℓ/D = 0.821 to 1.57. Results were obtained at 0.25 inch length increments or $\Delta\ell$/D = 0.0714. To avoid hysteresis, large length adjustment increments were employed between successive measurements.

Figure 3.18 shows the results of the Strouhal number experiments conducted in the atmospheric tunnel. Three sets of data are presented with Reynolds number = 33,000, 40,000, and 40,000 and aspect ratio = 16, 16, and 8 respectively. The variation in Strouhal number with ℓ/D was similar for all sets and show an initial increase in Strouhal number from ℓ/D = 0.0 that reached a local maximum near ℓ/D $\approx$ 0.2 - 0.3. The Strouhal number then decreased with increasing plate length to a local minimum near ℓ/D $\approx$ 0.6 - 0.7. Beyond ℓ/D = 0.7 the data show a linear increase in Strouhal number with increasing plate length to a maximum near ℓ/D = 1.5. Reynolds number did not appear to have a significant influence on the data, as indicated by similar results for Re = 33,000 and 40,000 at an aspect ratio of 16. A reduction in aspect ratio though, from 16 to 8 produced an increase in the Strouhal number and shifted the data to a lower ℓ/D, although the general trend in the data remained consistent with the higher aspect ratio cases.

Figure 3.19 combines Strouhal number versus ℓ/D results for the 3.5 inch model at AR = 8 (see Figure 3.18) with those for the 2 inch model computed from the power spectrum data presented in Figures 3.12 - 3.15. The comparison illustrates a strong correlation between the results of both straight trailing edge experiments. The local minimum and maximum Strouhal numbers occur near similar ℓ/D, and a comparable

variation in Strouhal number was observed over the entire ℓ/D range. The results also indicate that beyond ℓ/D = 1.5 the Strouhal number began to decrease suggesting a maximum Strouhal number near ℓ/D = 1.5. The closed symbols on the plot represent sinuous trailing edge data for peak and valley locations. The results are similar to those for the straight trailing edge plates except that they are shifted by -0.25 ℓ/D, thus supporting the concept of similar shedding characteristics for plates of similar average length. Results from similar investigations by Gerrard [1966] and Apelt et al. [1973] indicate the Strouhal number continues to increase beyond ℓ/D = 2.0, whereas the present investigation shows a maximum Strouhal number at ℓ/D = 1.5. This discrepancy could be a result of the relatively sparse number of discrete plate lengths analyzed in the previous studies. Gerrard [1966] show one data point between ℓ/D = 1.2 - 2.0 and Apelt et al. show one point between ℓ/D = 1.0 - 2.0. In a later study however, Apelt and West [1975] show the Strouhal number to be decreasing at ℓ/D = 2.0. In the current investigation, measurements were obtained for every 0.036 ℓ/D between ℓ/D = 0.0 - 1.57 in the atmospheric wind tunnel and every 0.25 ℓ/D between ℓ/D = 0.0 - 2.0 in the smaller wind tunnel.

3.3 Wake parameters

Figure 3.20 presents the pressure distribution around the 3.5 inch model in uniform flow for various straight splitter plate lengths at Re = 30,000 and AR = 16. The freestream velocity of 6.4 m/s resulted in shedding frequency of approximately 15 Hz. A sample frequency of 100 Hz was used to obtain 10 ensembles of 512 samples for a total sample time of 51.2 seconds per pressure port. A settling time of 10 seconds was incorporated between each successive port measurement to minimize transient effects. The profiles agree well with the previous investigation of Apelt et al. [1973] and show a significant reduction in base suction with the introduction of the splitter plate. The base suction continued to decrease with increasing plate length up to ℓ/D = 0.64 at which point its variation with ℓ/D became difficult to detect. The figure indicates that the pressure

distribution over the first 40 - 50 degrees of the circumference was essentially unaffected by the presence of the splitter plate, furthermore, the results gave no indication that the separation point was affected by the splitter plate length.

Figure 3.21 shows the relationship between section drag coefficient, C_d, base pressure parameter, K, and ℓ/D. The results of Figure 3.21(a) indicate a linear relationship between K and C_d. A linear regression of the data produced the expression,

$$C_d = 1.96\ K - 1.64 \qquad (3.1)$$

Figure 3.21(b) shows a significant, initial reduction in drag and base suction with ℓ/D, reaching minimum values at approximately ℓ/D = 1.0, which agreed with the results of Gerrard [1966] and Apelt et al. [1973]. The effect of aspect ratio on C_d and K can be determined from a comparison of the open symbols, AR = 16 , to the closed symbols, AR = 8. The reduction in aspect ratio produced an increase in drag and base suction although the effect was primarily related to the splitter plate configurations and not apparent for ℓ/D = 0.0.

The pressure coefficient distribution near the trailing edge of a sinuous splitter plate is indicated by Figure 3.22. Consistent with the circumference C_p measurements, the splitter plate surface C_p was referenced to freestream flow properties corrected for pitot-static tube position error. The results indicate a C_p variation from valley to peak that was similar regardless of plate length, showing maximum suction at the peak that decreased to a minimum at the valley. The variation in C_p suggest, at least for regions near the plate surface, a spanwise flow away from the valleys and toward the peaks. Figure 3.23 presents the surface C_p data plotted versus ℓ/D and shows that for all port locations, C_p became less negative with increasing ℓ/D. Also included on the chart and denoted by the

dash line is the base pressure coefficient at a peak location. The results show a difference in the magnitude between C_{pb} and C_p at different span positions, but similar behavior with respect to ℓ/D. The maximum measured suction occurred at the shortest ℓ/D and decreased to an apparent minimum near ℓ/D = 1.25. Consistent with power spectrum results, the sinuous plate and straight plate minimum suction locations agree if the average plate length (ℓ/D - 0.25) is used for the comparison.

Figure 3.24 shows the length of the formation region as a function of splitter plate length. The results indicate a substantial initial increase in formation length from the plain cylinder case to the shortest splitter plate of ℓ/D = 0.125. Between ℓ/D = 0.25 - 0.75 there was a linear increase in formation length with increasing ℓ/D. Beyond ℓ/D = 0.75 the formation region remained at a relatively constant length of ℓ_f/D = 2.5. Results from Pearson and Szewczyk [1992] show a similar trend in formation length with ℓ/D.

Figures 3.24 and 3.25 show the spanwise variation in near wake parameters for straight trailing edge splitter plates of ℓ/D = 0.0, 0.25, 0.5 and 1.0, and a sinuous trailing edge plate of ℓ/D = 1.0, λ/D = 3, a/D = 0.5, in uniform flow at Re = 30,000 and AR = 8. The results are based on the data presented for each configuration in Appendix A along with the corresponding sampling parameters. The near wake parameters considered were formation region length, ℓ_f/D, wake width, d'/D, shear layer velocity U_s/U, and base pressure parameter, K. Figure 3.24(a) shows the variation in ℓ_f/D and indicates an increase in formation length with increasing ℓ/D. The formation length of the sinuous ℓ/D = 1.0 plate fell between the lengths measured for the straight ℓ/D = 0.5 and 1.0 configurations, consistent with the concept of using an average length in comparisons between straight and sinuous splitter plates. Figure 3.24(b) compares the spanwise variation in wake width for the various splitter plate configurations. The wake width increased with increasing ℓ/D and indicates the significant effect a small splitter plate can have. These results also support the

average splitter plate length concept previously discussed. Figures 3.25(a) and (b) show the splitter plate effect on U_s/U and K respectively. The variation with ℓ/D was similar for both parameters and indicated a significant reduction in shear layer velocity and base suction with the introduction of the splitter plate. The spanwise variation was fairly uniform for both parameters.

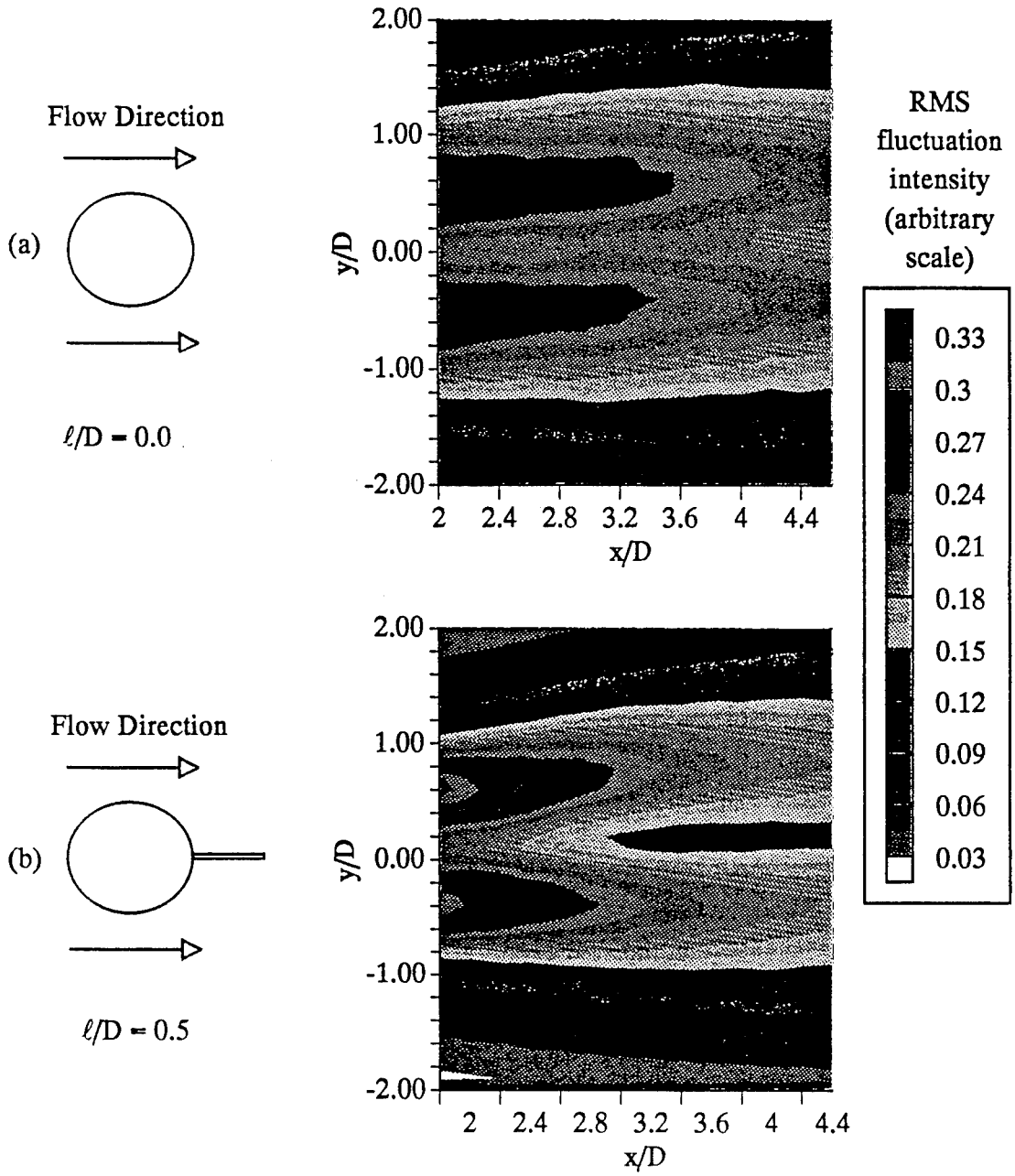

Figure 3.1. RMS fluctuation intensity for straight cylinder in uniform flow with splitter plate, (a); $\ell/D = 0.0$, (b); $\ell/D = 0.50$. Re = 30,000.

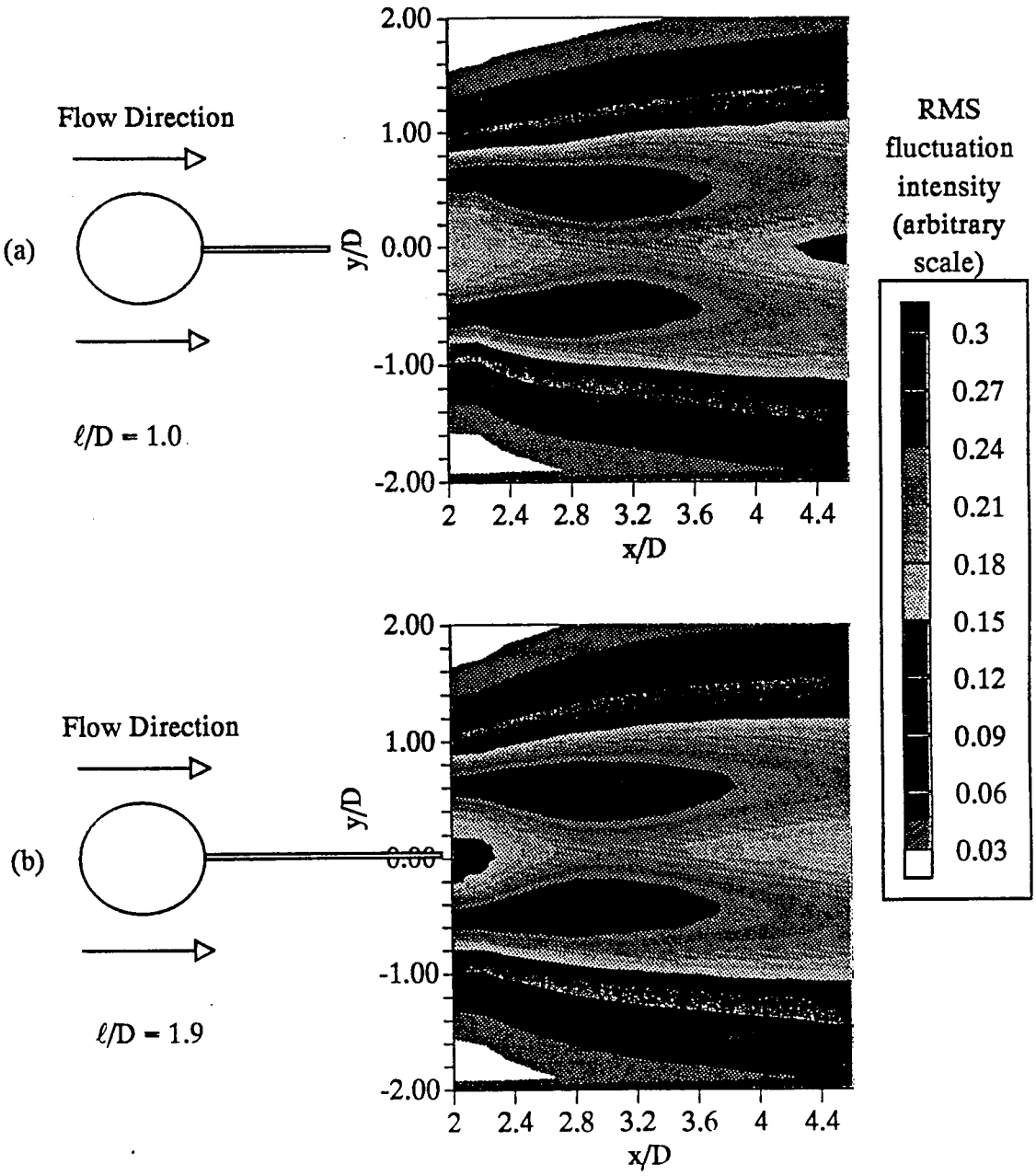

Figure 3.2. RMS fluctuation intensity for straight cylinder in uniform flow with splitter plate, (a); $\ell/D = 1.0$, (b); $\ell/D = 1.9$. Re = 30,000.

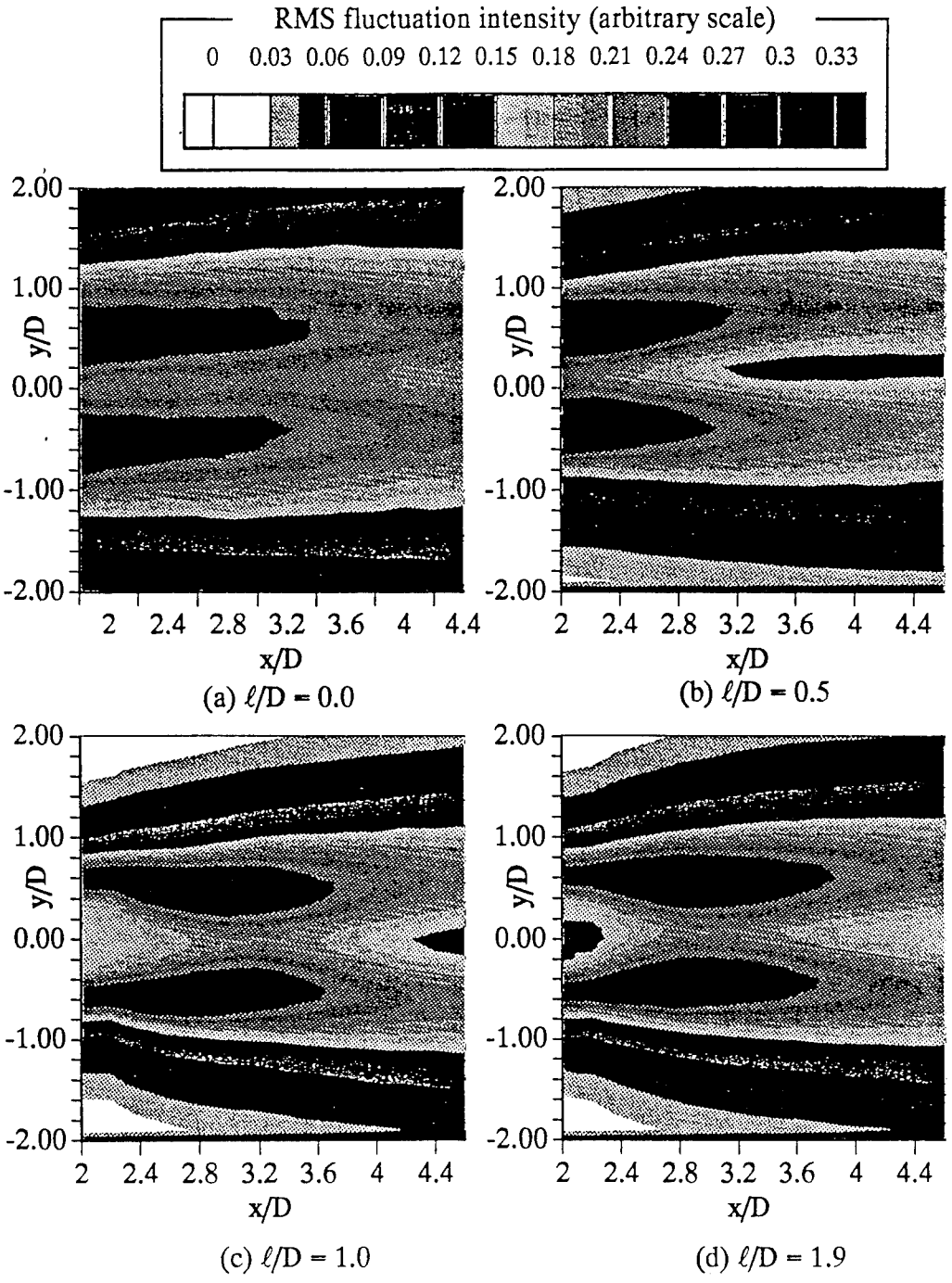

Figure 3.3. RMS fluctuation intensity for straight cylinder in uniform flow with splitter plate, (a); $\ell/D = 0.0$, (b); $\ell/D = 0.5$, (c); $\ell/D = 1.0$, (d); $\ell/D = 1.9$. Re = 30,000.

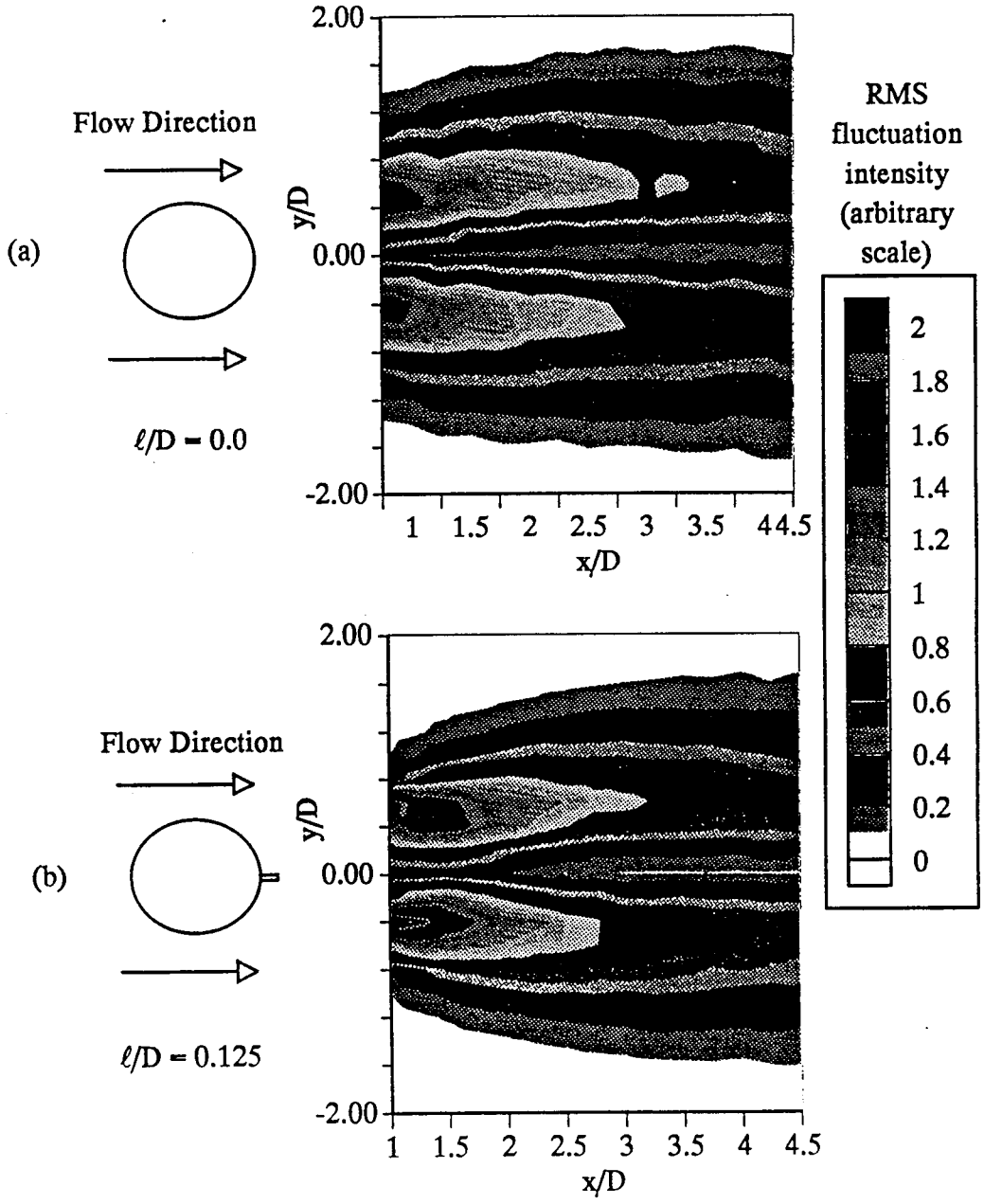

Figure 3.4. RMS fluctuation intensity for straight cylinder in uniform flow with splitter plate, (a); $\ell/D = 0.0$; (b); $\ell/D = 0.125$. Re = 30,000.

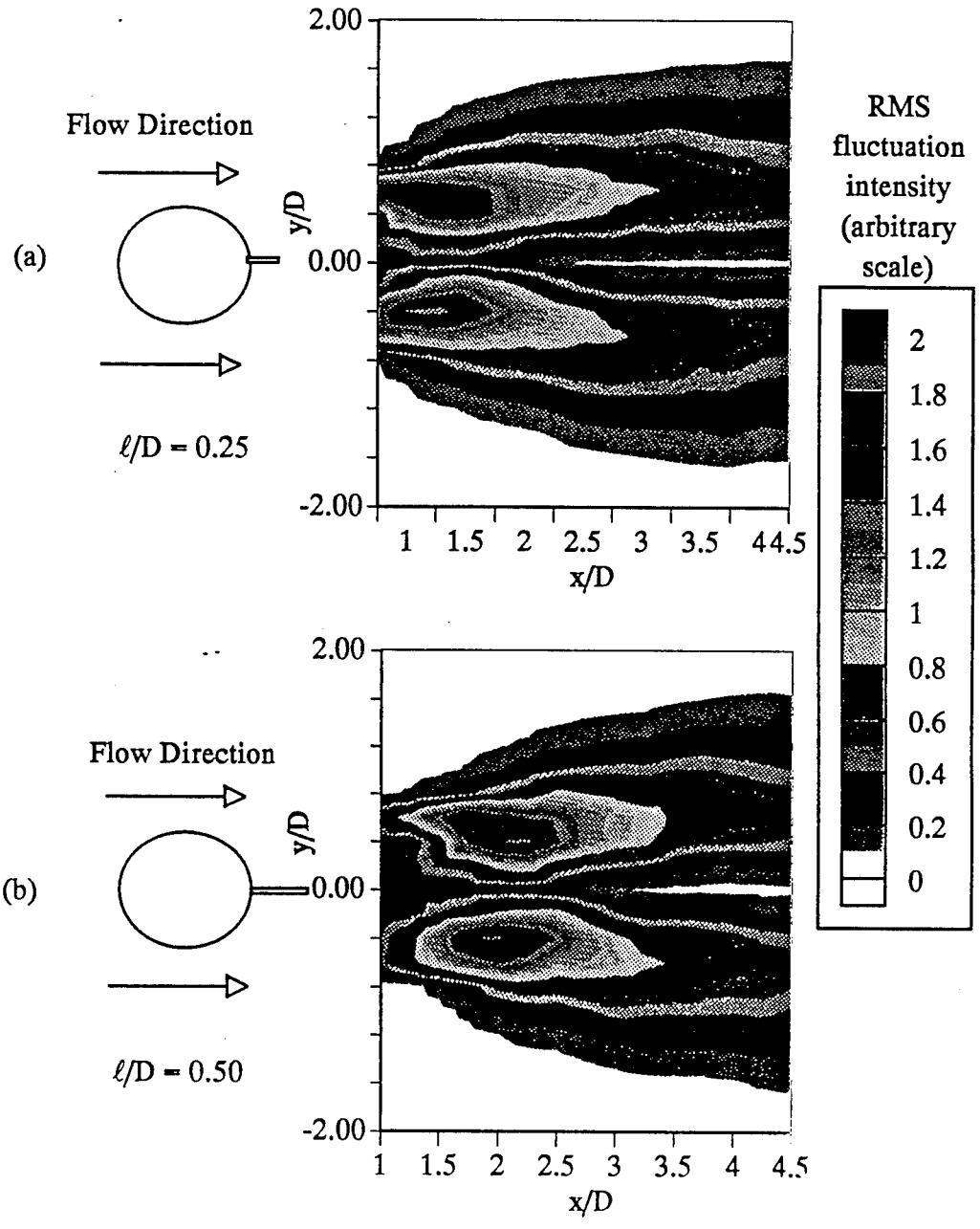

Figure 3.5. RMS fluctuation intensity for straight cylinder in uniform flow with splitter plate, (a); $\ell/D = 0.25$, (b); $\ell/D = 0.50$. Re = 30,000.

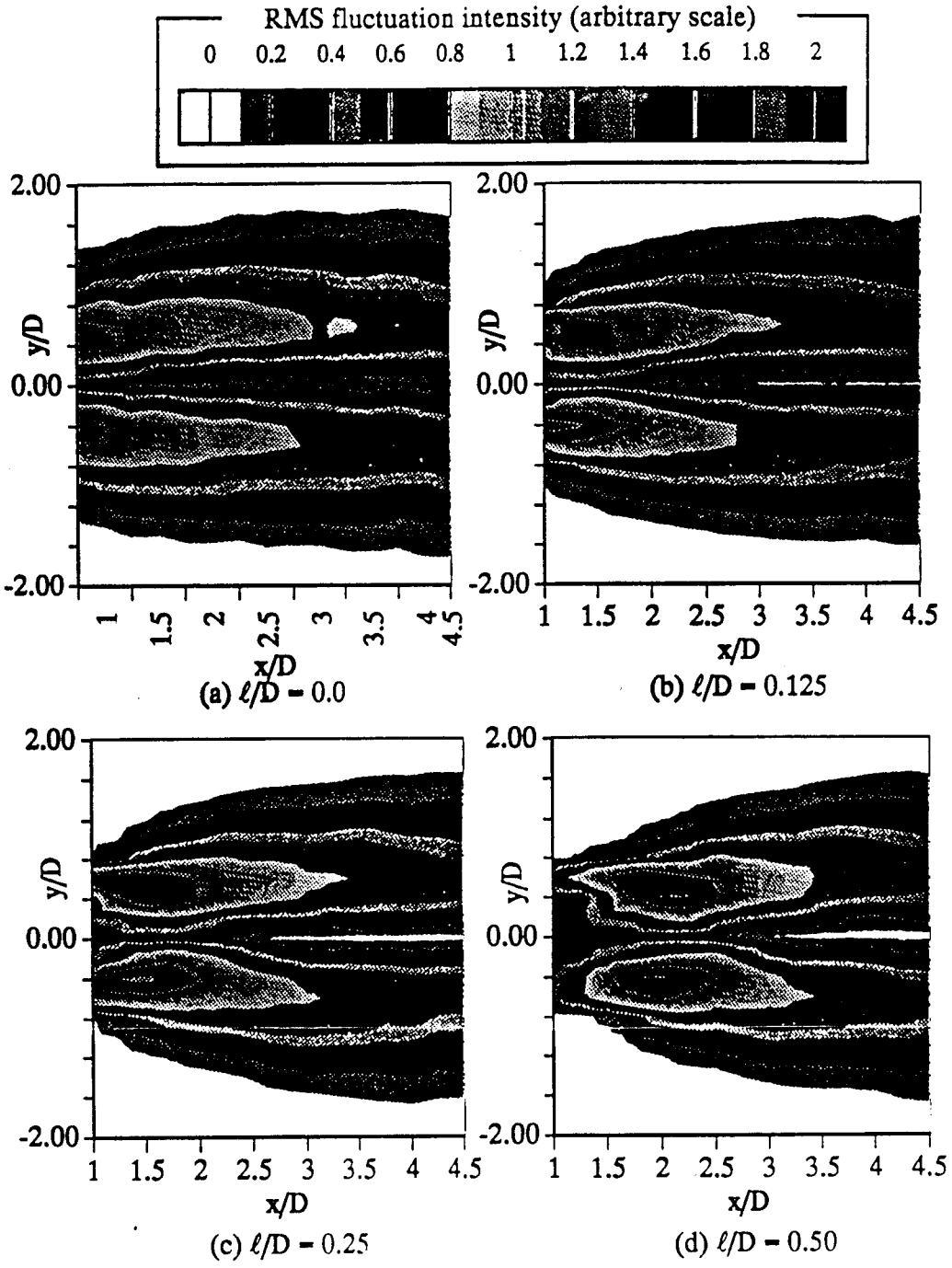

Figure 3.6. RMS fluctuation intensity for straight cylinder in uniform flow with splitter plate, (a); $\ell/D = 0.0$, (b); $\ell/D = 0.125$, (c); $\ell/D = 0.25$, (d); $\ell/D = 0.50$. Re = 30,000.

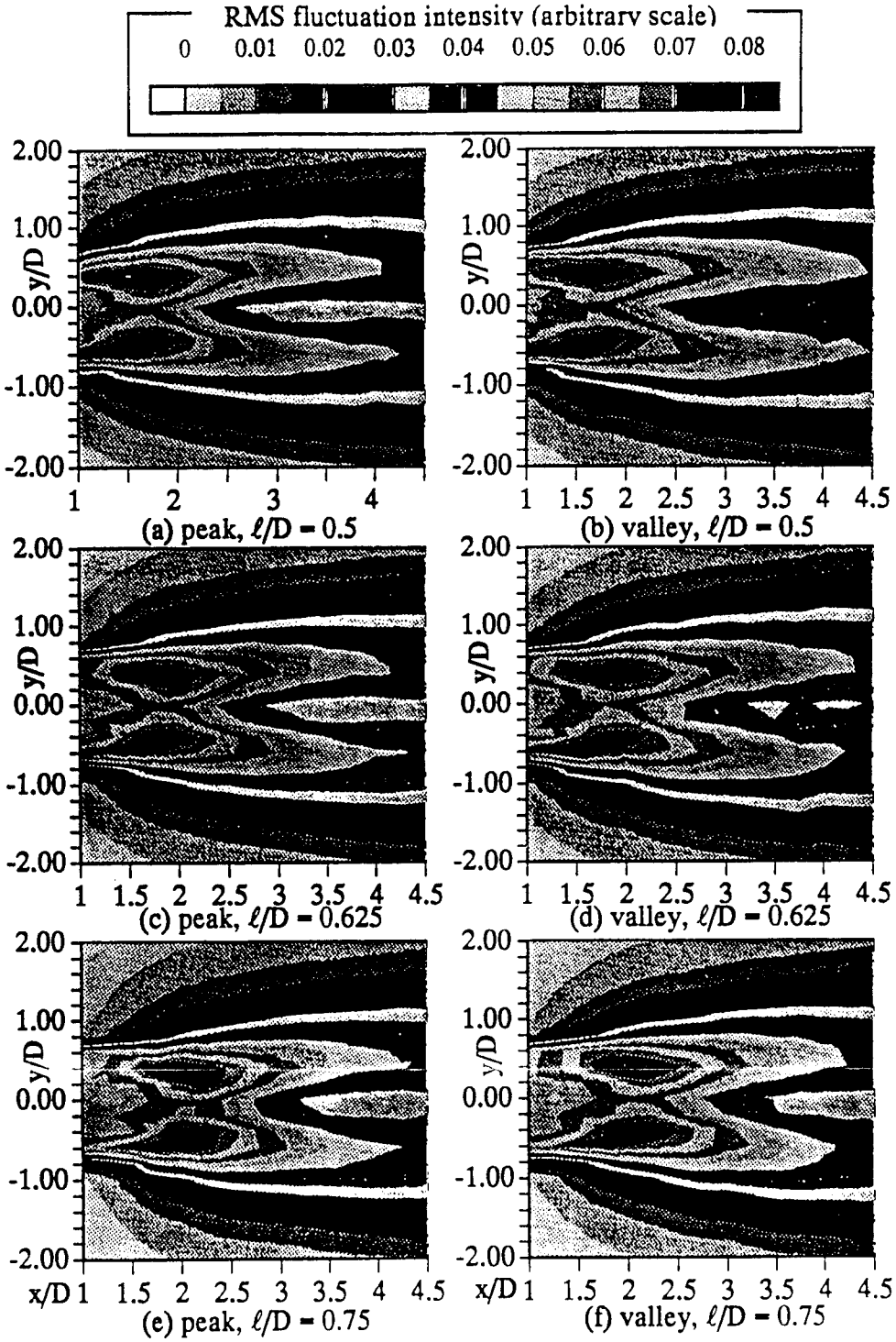

Figure 3.7. RMS fluctuation intensity for straight cylinder in uniform flow with sinuous trailing edge splitter plate, $\lambda/D = 3$. Re = 30,000. a; peak $\ell/D = 0.5$, b; valley $\ell/D = 0.5$, c; peak $\ell/D = 0.625$, d; valley $\ell/D = 0.625$, e; peak $\ell/D = 0.75$, f; valley $\ell/D = 0.75$.

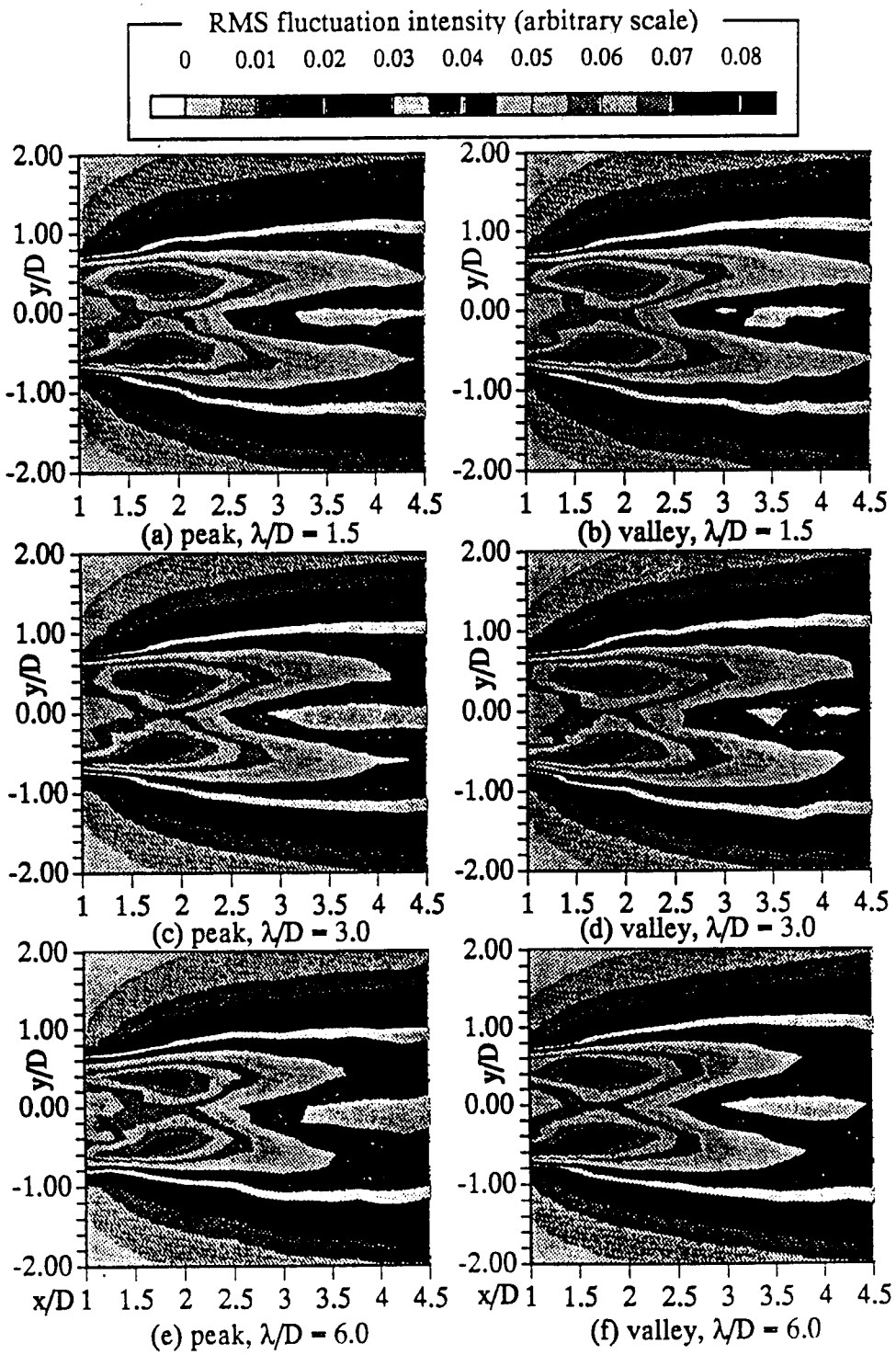

Figure 3.8. RMS fluctuation intensity for straight cylinder in uniform flow with sinuous trailing edge splitter plate, $\ell/D = 0.625$. Re = 30,000. a; peak $\lambda/D = 1.5$, b; valley $\lambda/D = 1.5$, c; peak $\lambda/D = 3$, d; valley $\lambda/D = 3$, e; peak $\lambda/D = 6$, f; valley $\lambda/D = 6$.

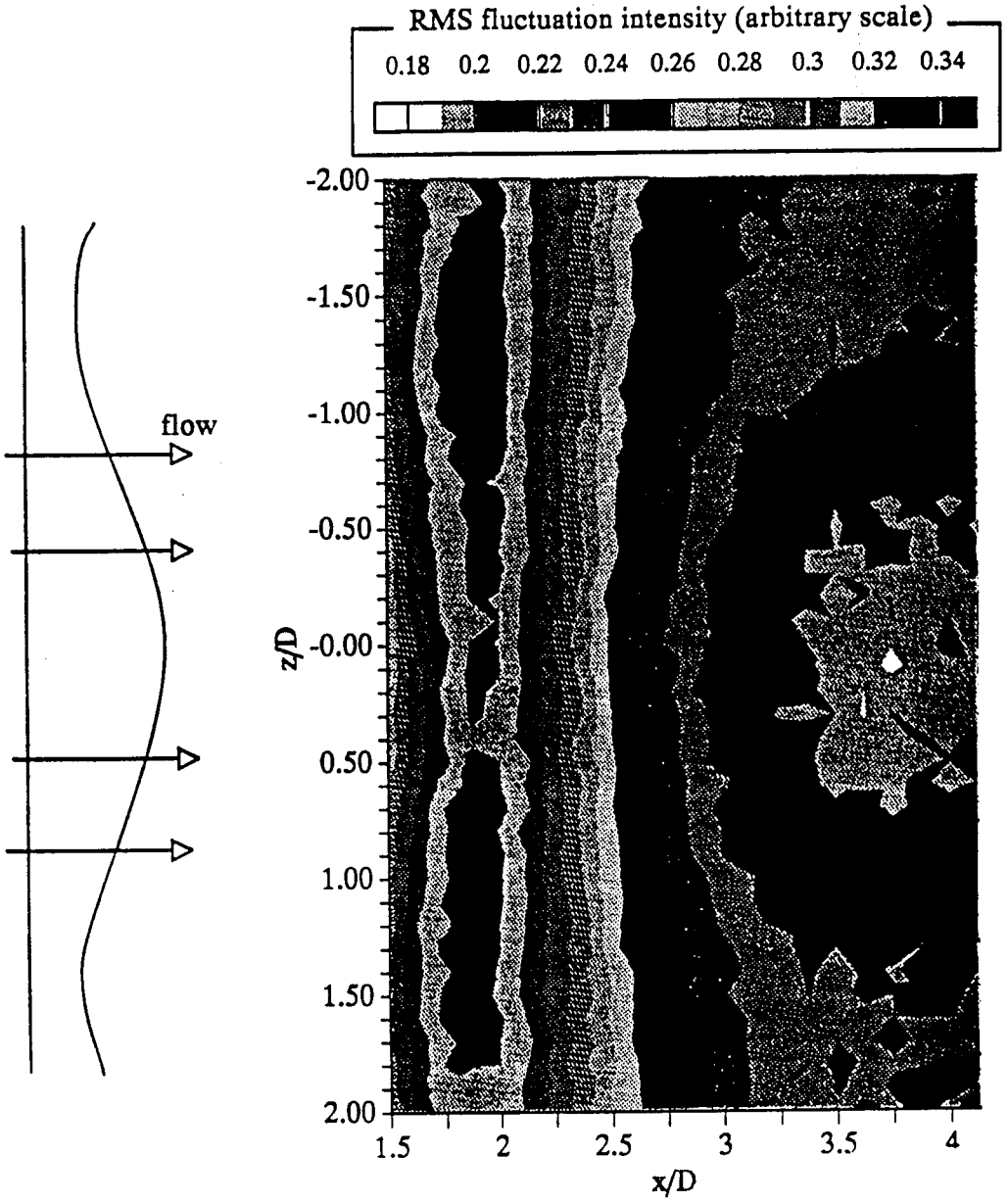

Figure 3.9. RMS fluctuation intensity for straight cylinder in uniform flow with sinuous trailing edge splitter plate, $\ell/D = 0.625$, $\lambda/D = 3$. Probe located along centerline of cylinder, $y/D = 0$. $Re = 30{,}000$.

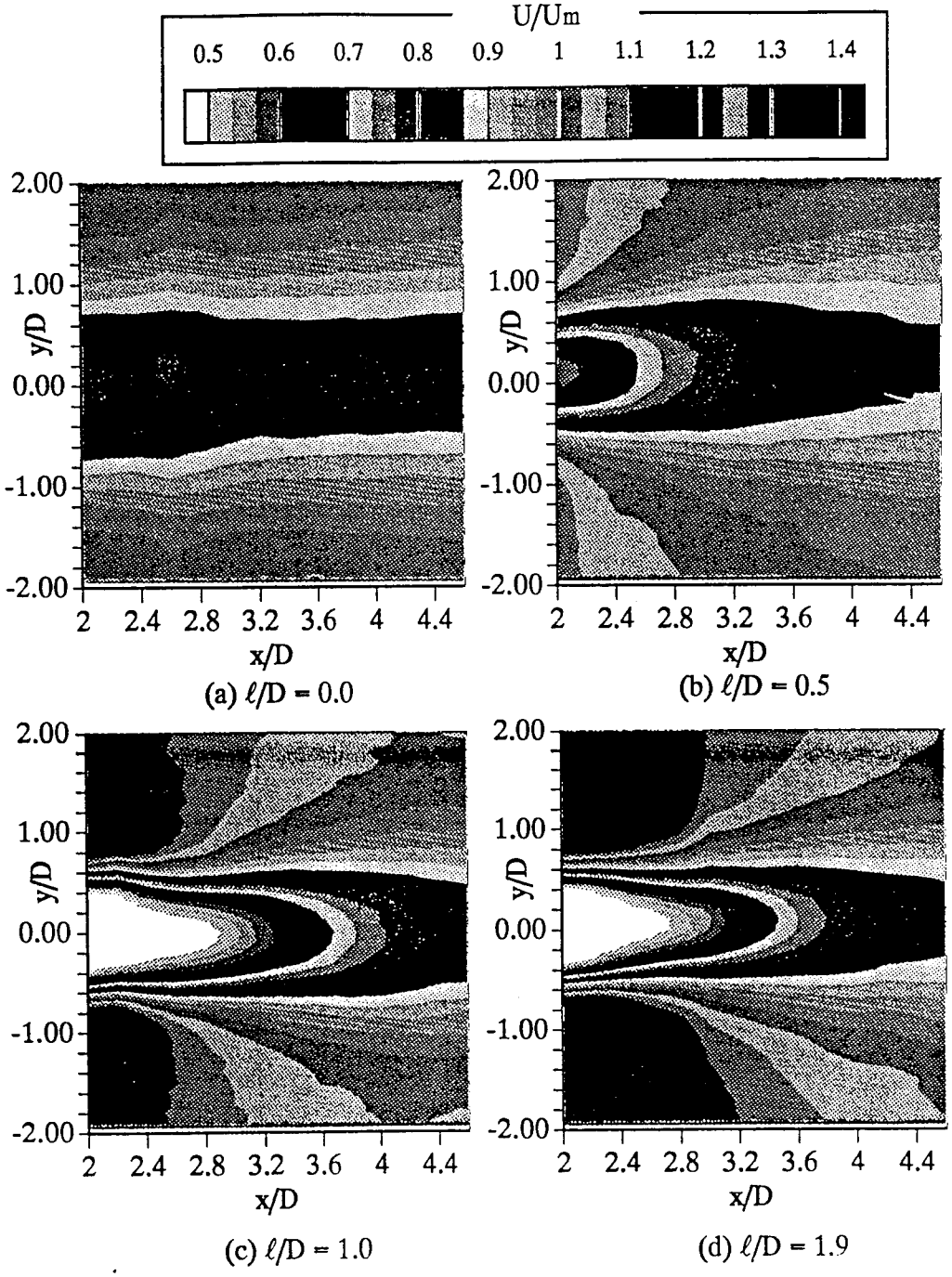

Figure 3.10. Mean velocity contours for straight cylinder in uniform flow with splitter plate, (a); $\ell/D = 0.0$, (b); $\ell/D = 0.5$, (c); $\ell/D = 1.0$, (d); $\ell/D = 1.9$. Re = 30,000. Note: single sensor hot wire cannot measure u-velocity component inside formation region, approximately $-0.5<y/D<0.5$.

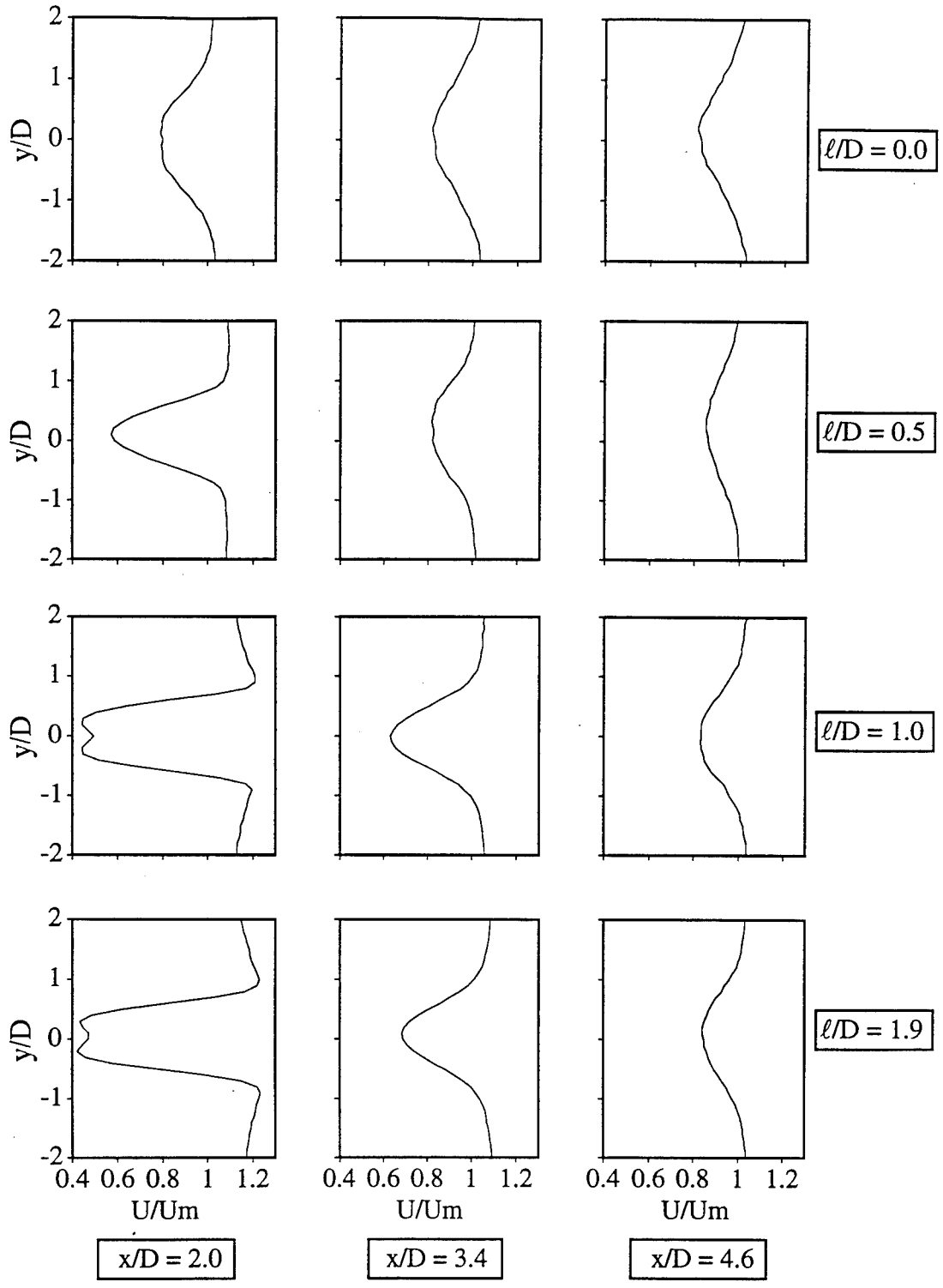

Figure 3.11. Mean velocity profiles for straight cylinder in uniform flow with splitter plate. Note: single sensor hot wire can not measure u-velocity component inside formation region, approximately -0.5<y/D<0.5.

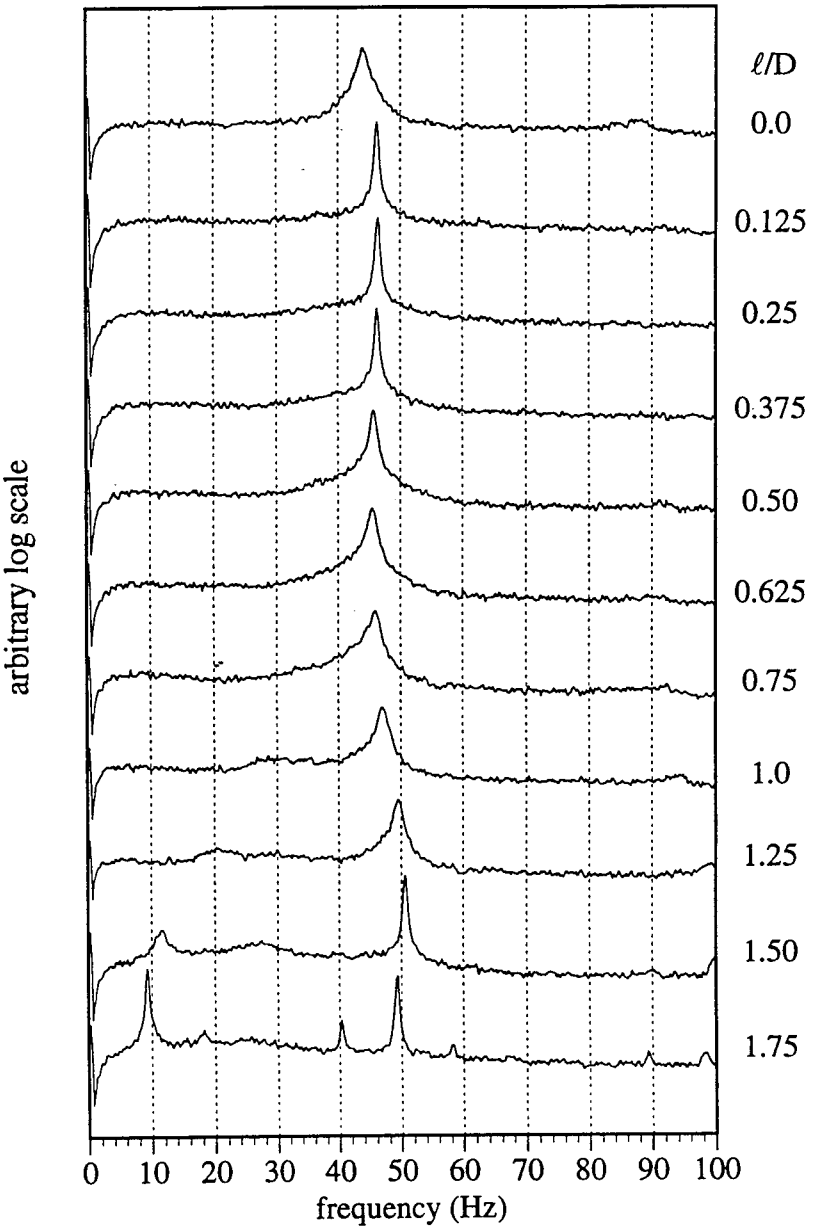

Figure 3.12. Power spectrum for straight trailing edge splitter plates. x/D = 2, y/D = 0.5, Re = 30,000. 100 ensembles of 1024 samples at 200 Hz sample rate.

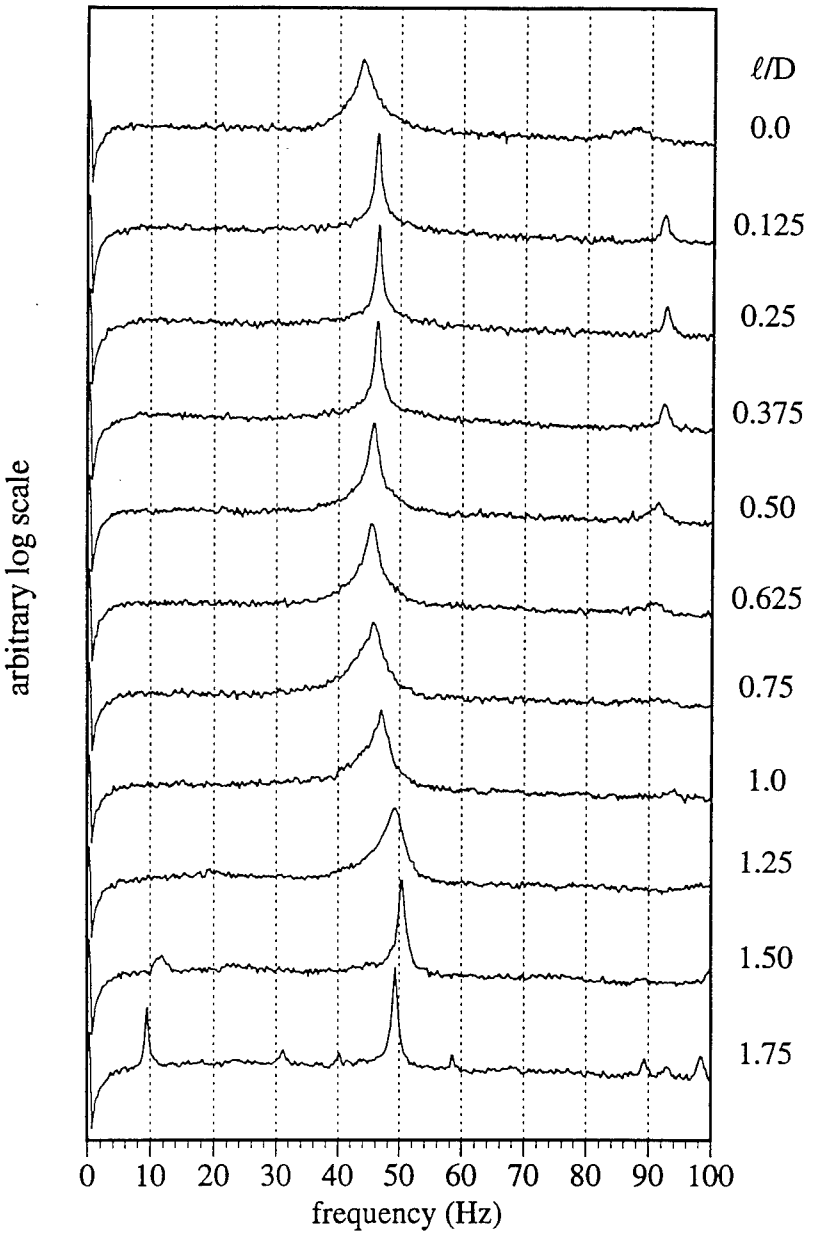

Figure 3.13. Power spectrum for straight trailing edge splitter plates. x/D = 4, y/D = 0.5, Re = 30,000. 100 ensembles of 1024 samples at 200 Hz sample rate.

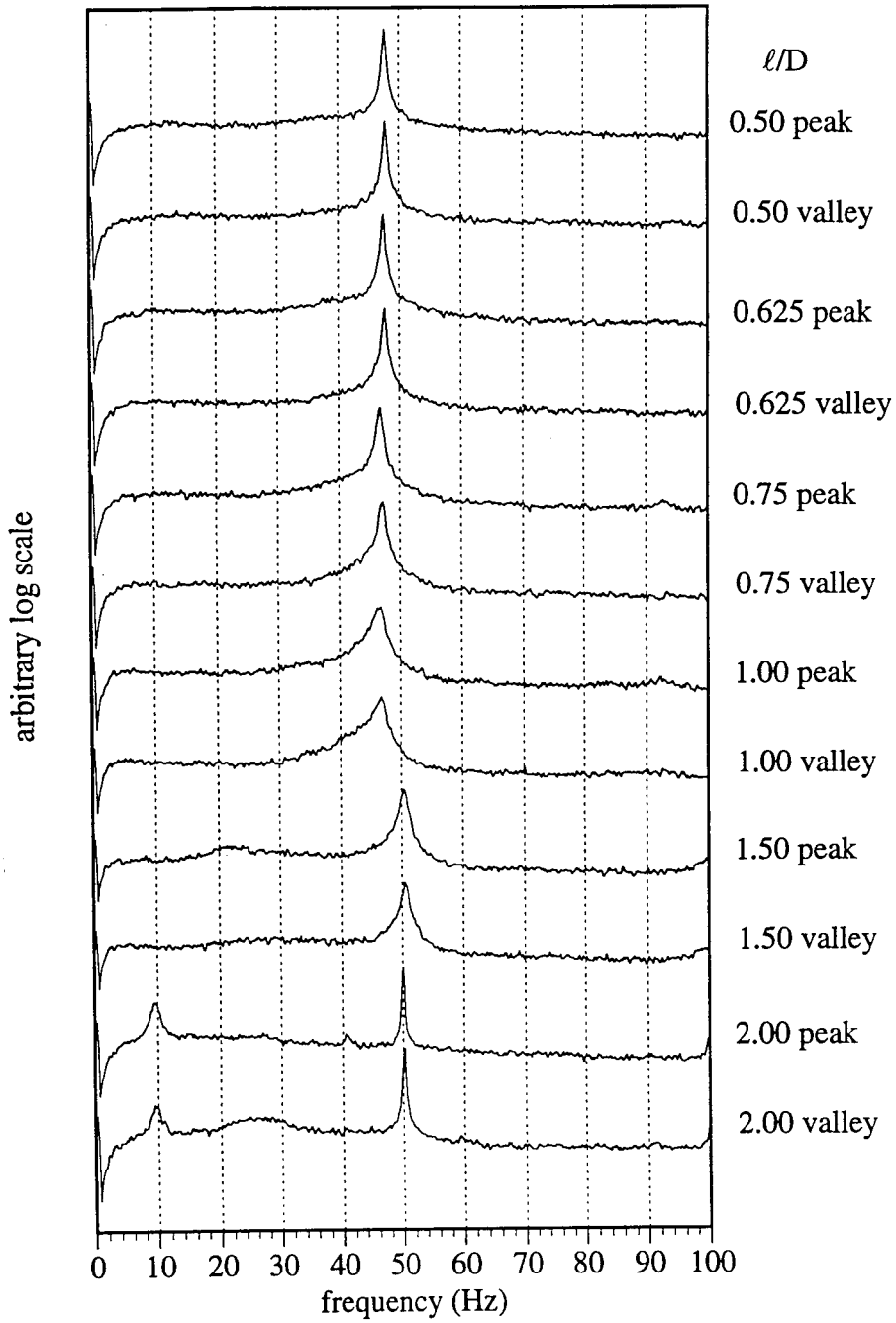

Figure 3.14. Power spectrum for sinuous trailing edge splitter plates. $\lambda/D = 3$, $x/D = 2$, $y/D = 0.5$, $Re = 30{,}000$. 100 ensembles of 1024 samples at 200 Hz sample rate.

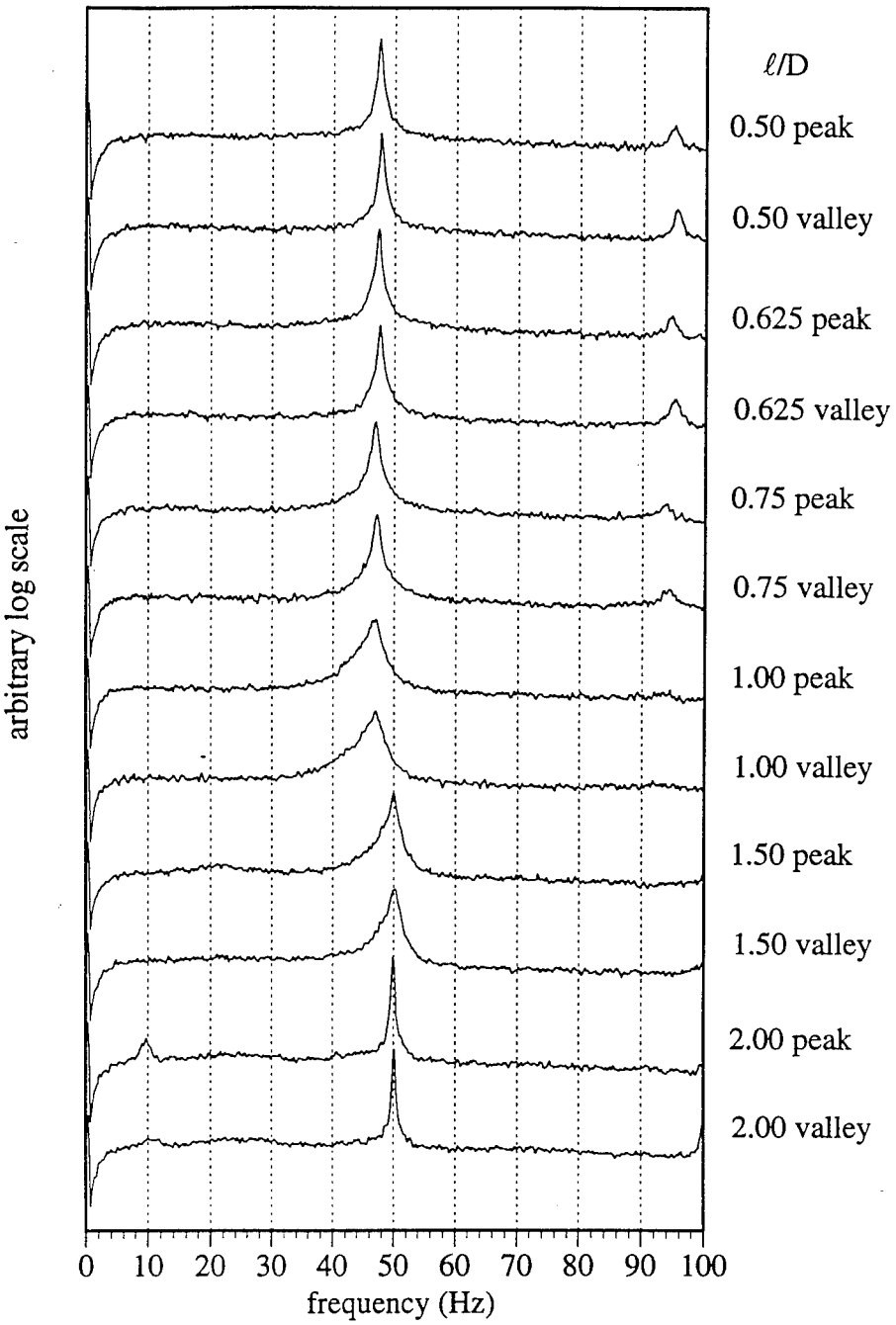

Figure 3.15. Power spectrum for sinuous trailing edge splitter plates. $\lambda/D = 3$, $x/D = 4$, $y/D = 0.5$, $Re = 30{,}000$. 100 ensembles of 1024 samples at 200 Hz sample rate.

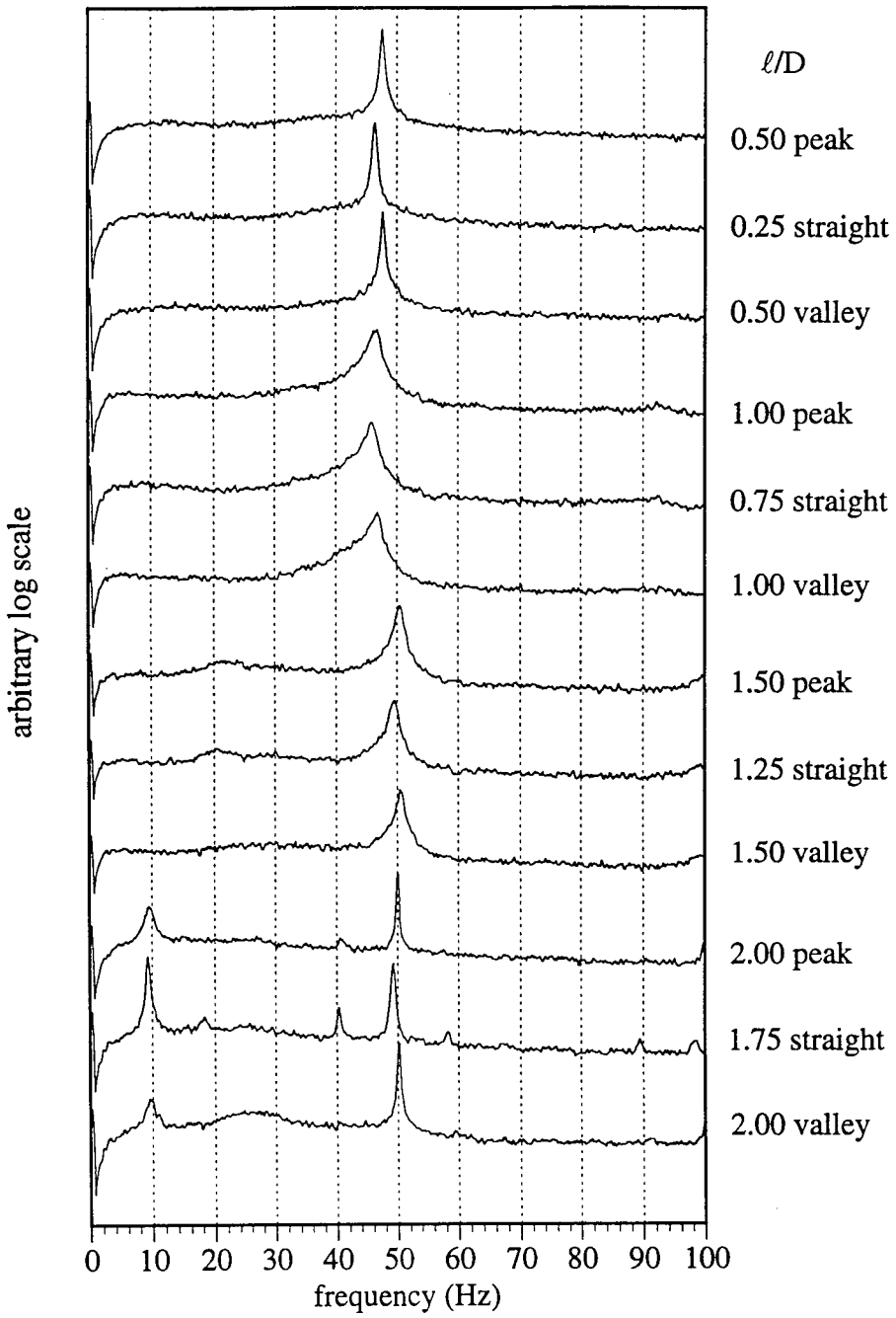

Figure 3.16. Power spectrum comparison for sinuous and straight trailing edge splitter plates. $\lambda/D = 3$, $x/D = 2$, $y/D = 0.5$, $Re = 30{,}000$. 100 ensembles of 1024 samples at 200 Hz sample rate.

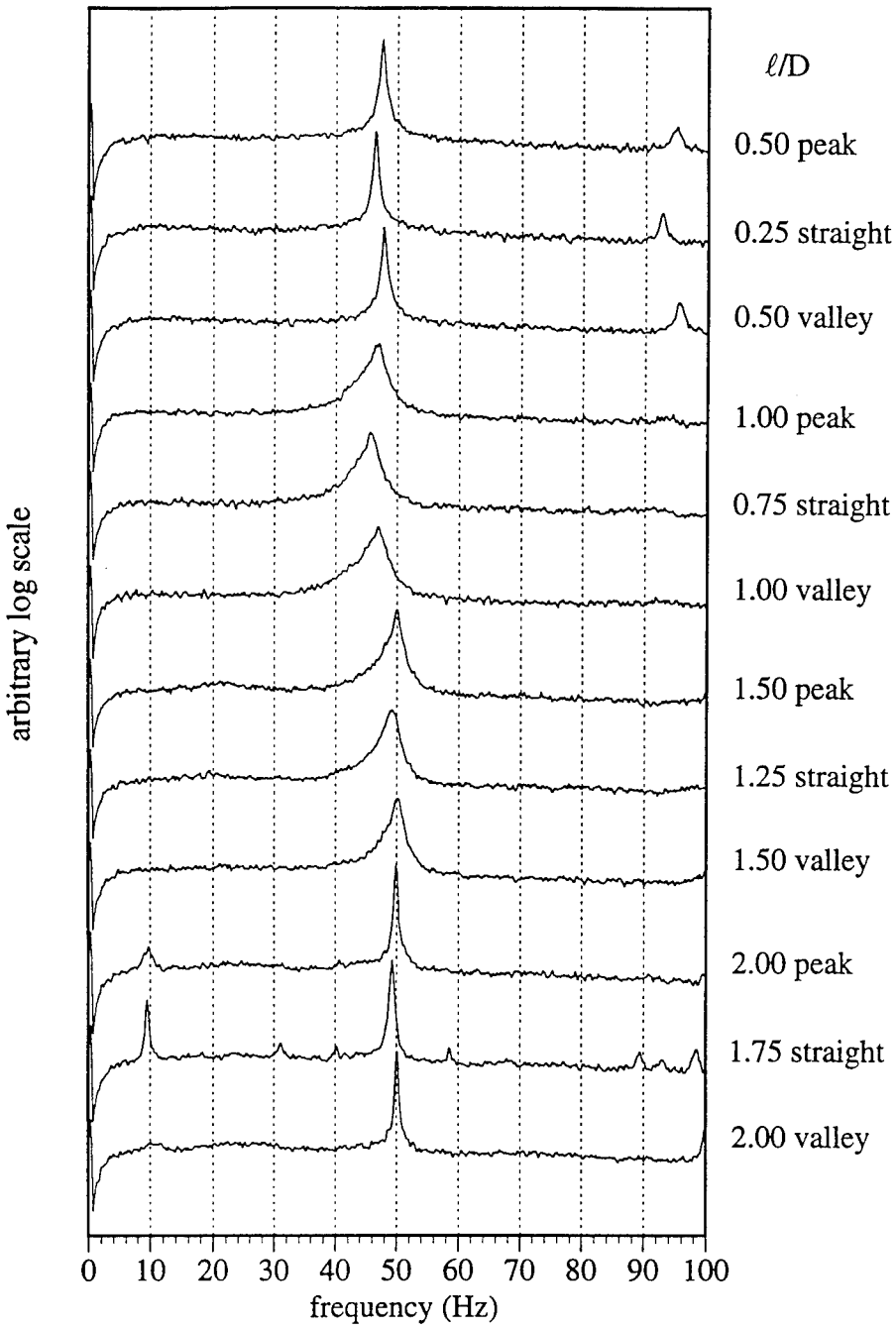

Figure 3.17. Power spectrum comparison for sinuous and straight trailing edge splitter plates. $\lambda/D = 3$, $x/D = 4$, $y/D = 0.5$, Re = 30,000. 100 ensembles of 1024 samples at 200 Hz sample rate.

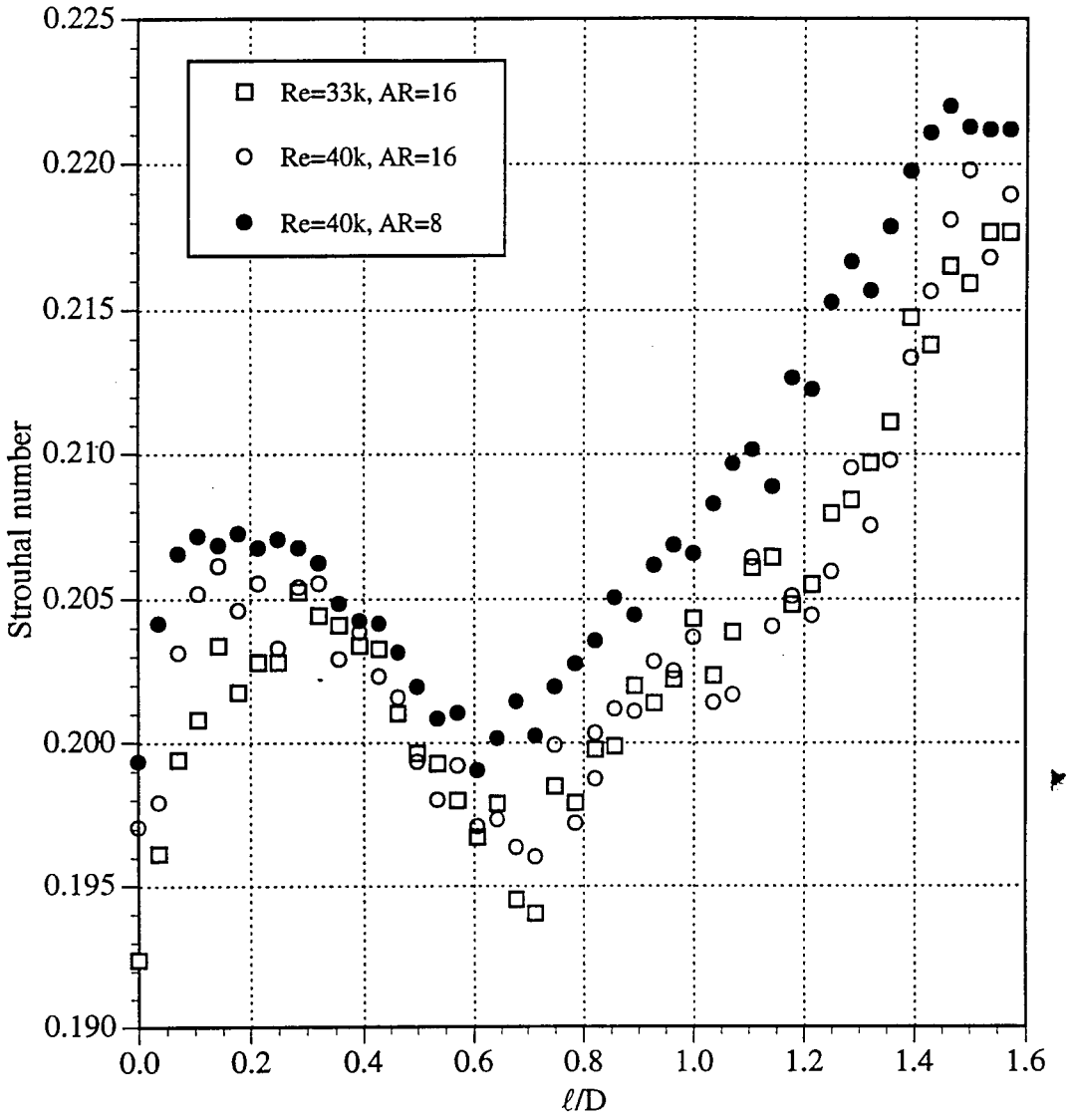

Figure 3.18. Strouhal number vs. straight trailing edge splitter plate length 30 ensembles of 1024 samples at 100 Hz sample rate. x/D = 3.5, y/D = 1.0.

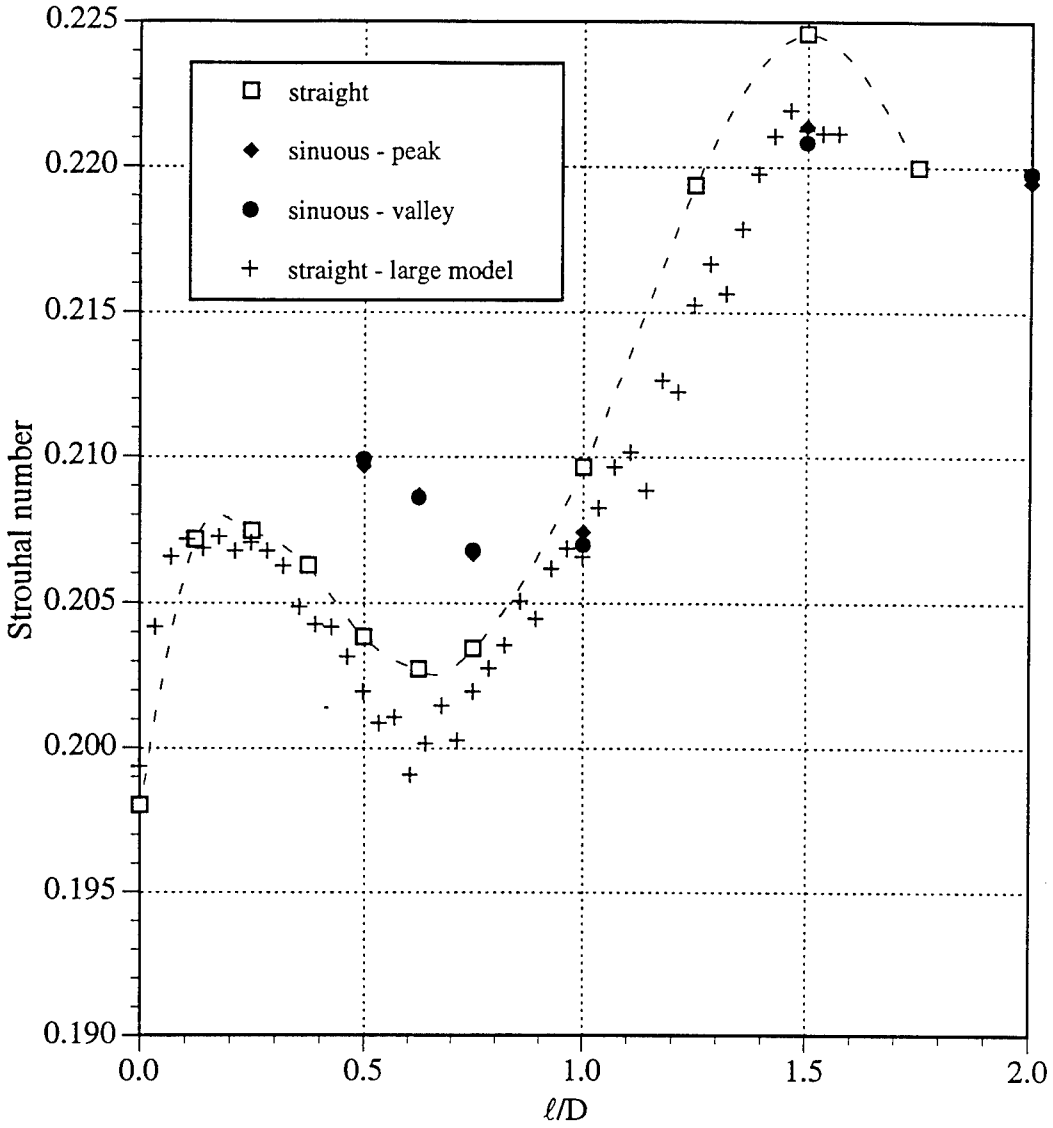

Figure 3.19. Strouhal number vs. straight and periodic trailing edge splitter plate length, AR = 8. □, ◆, ●; D = 2.0 in., Re = 30,000, x/D = 2, y/D = 0.5. +; D = 3.5 in., Re = 40,000, x/D = 3.5, y/D = 1.0.

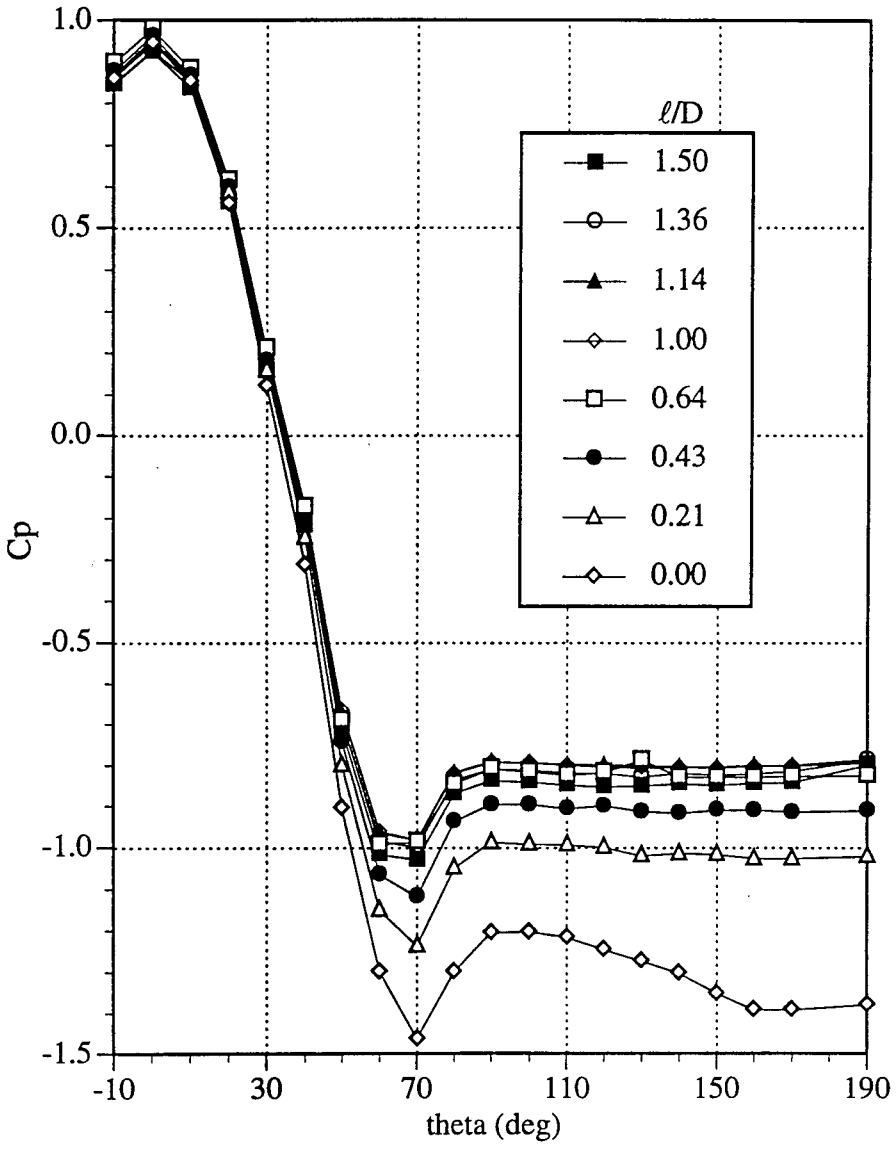

Figure 3.20. Pressure distribution around circular cylinder in uniform flow with splitter plate. Re = 30,000, AR = 16.

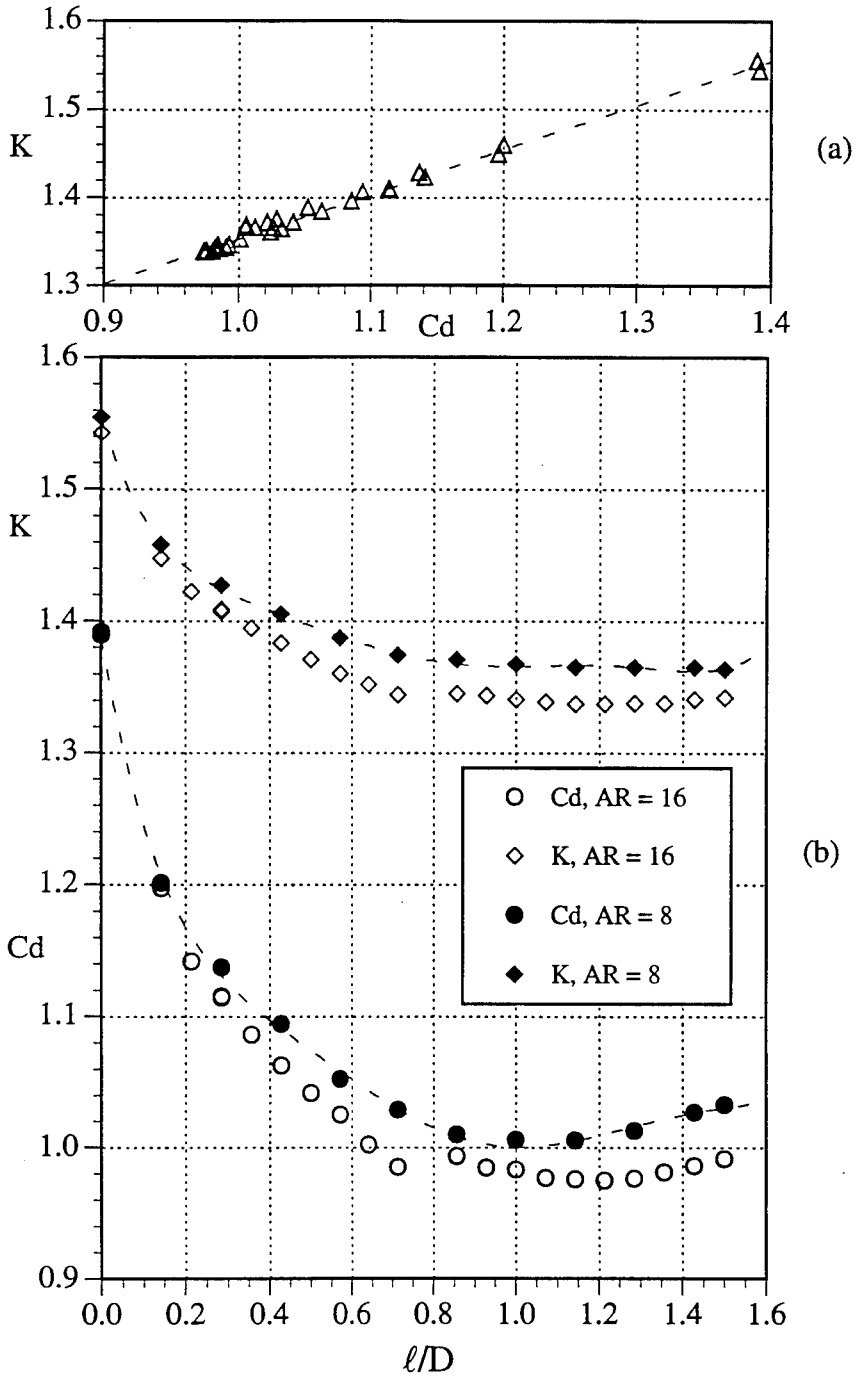

Figure 3.21. Section drag coefficient and base pressure parameter versus splitter plate length for circular cylinder in uniform flow. Re = 30,000

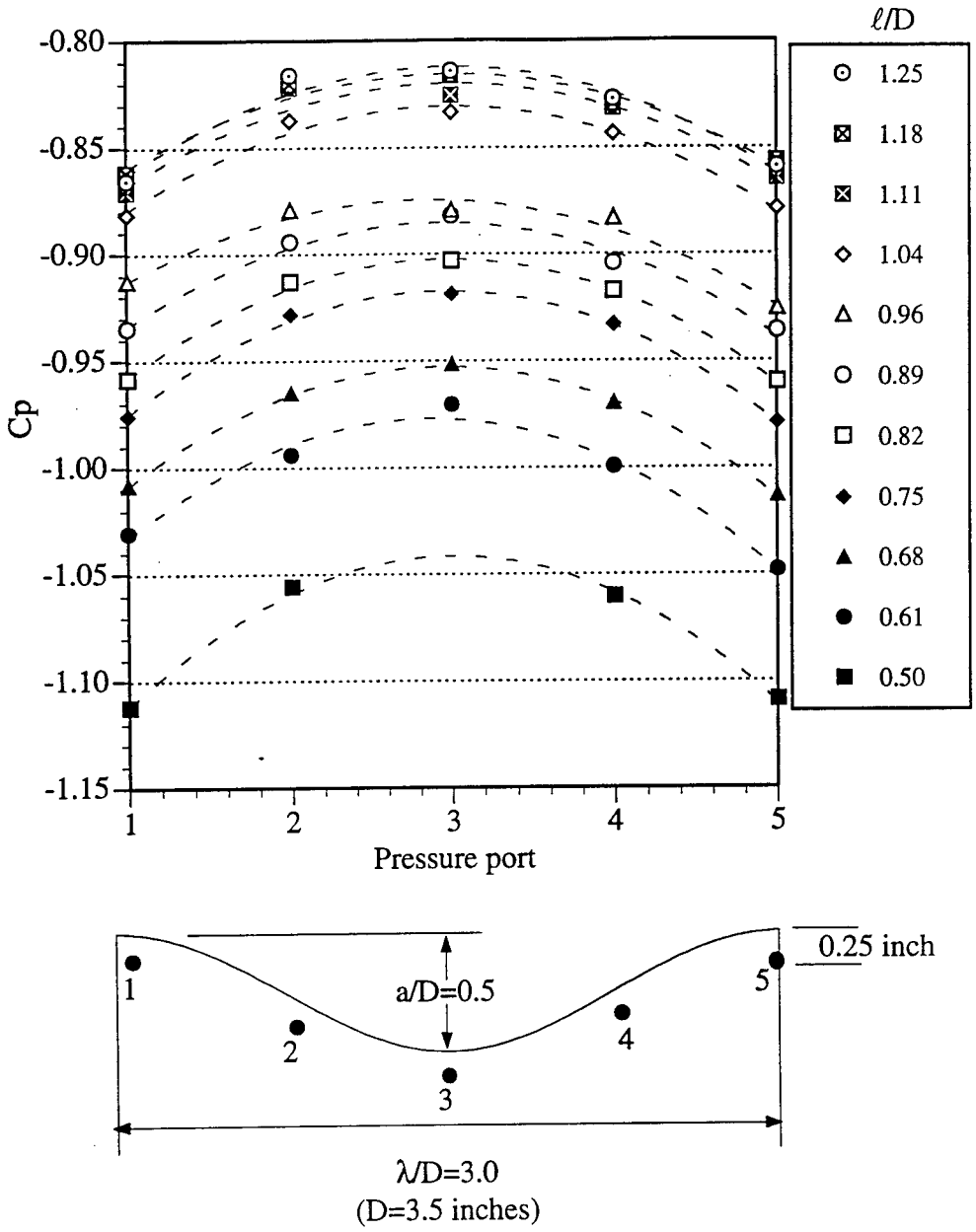

Figure 3.22. Pressure variation on surface of sinuous trailing edge splitter plate. Re = 30,000, AR = 16.

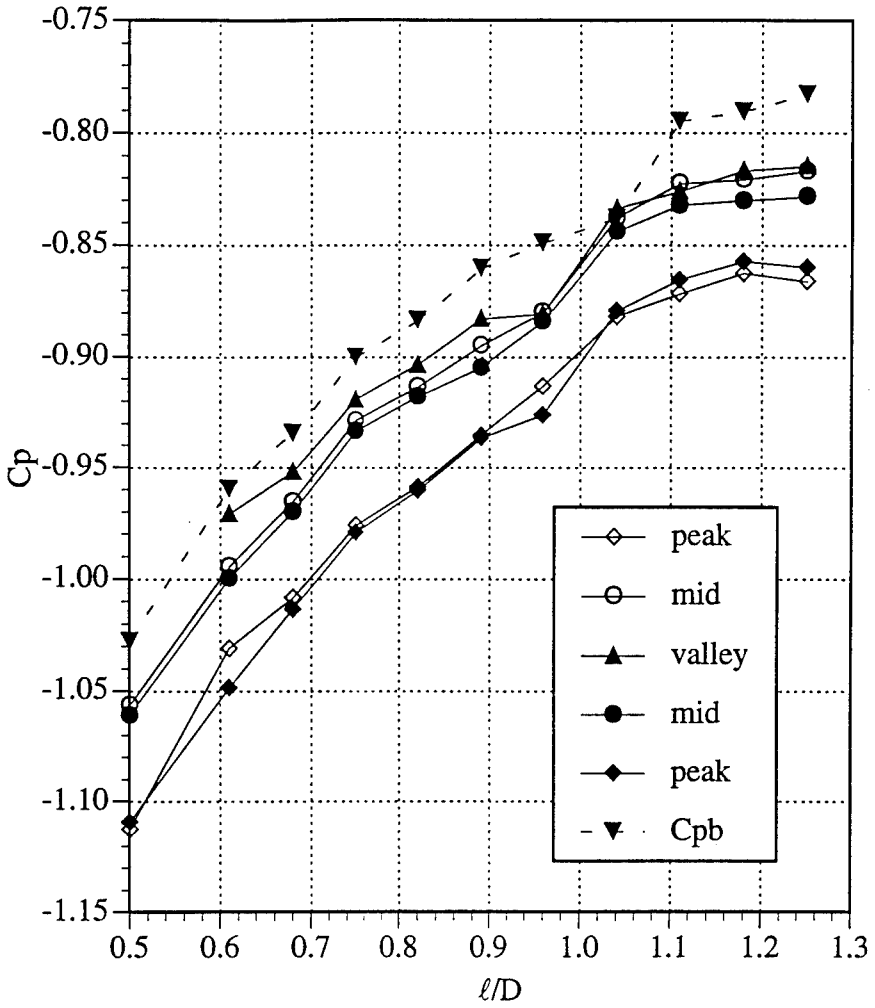

Figure 3.23. Sinuous trailing edge splitter plate surface Cp distribution versus ℓ/D. AR = 16, Re = 30,000.

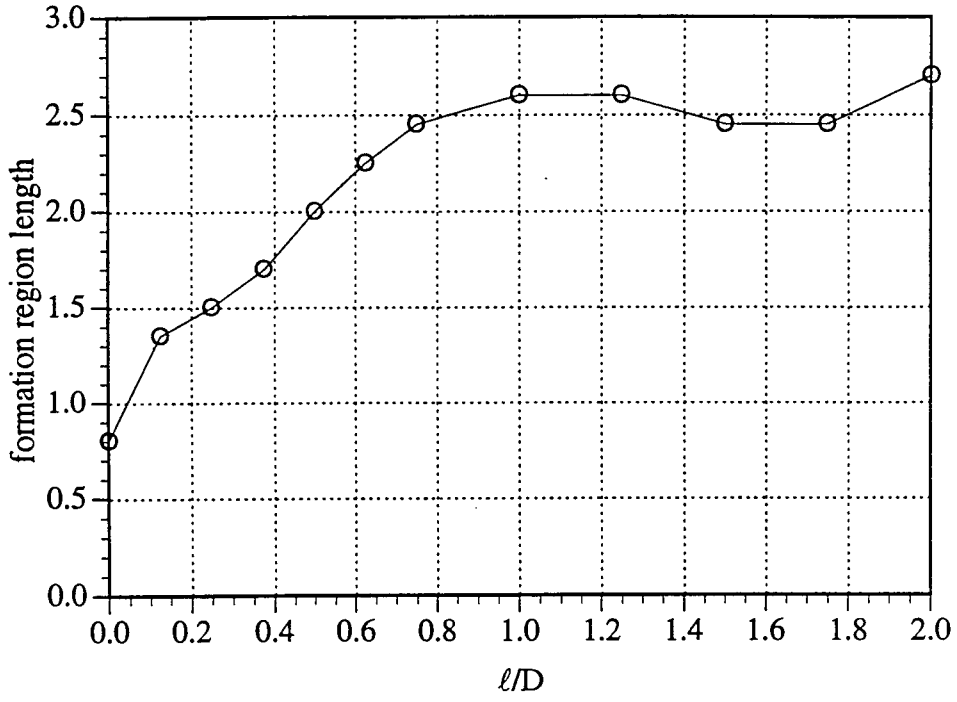

Figure 3.24. Formation region length versus splitter plate length for straight circular cylinder in uniform flow. Re = 30,000, AR = 8.

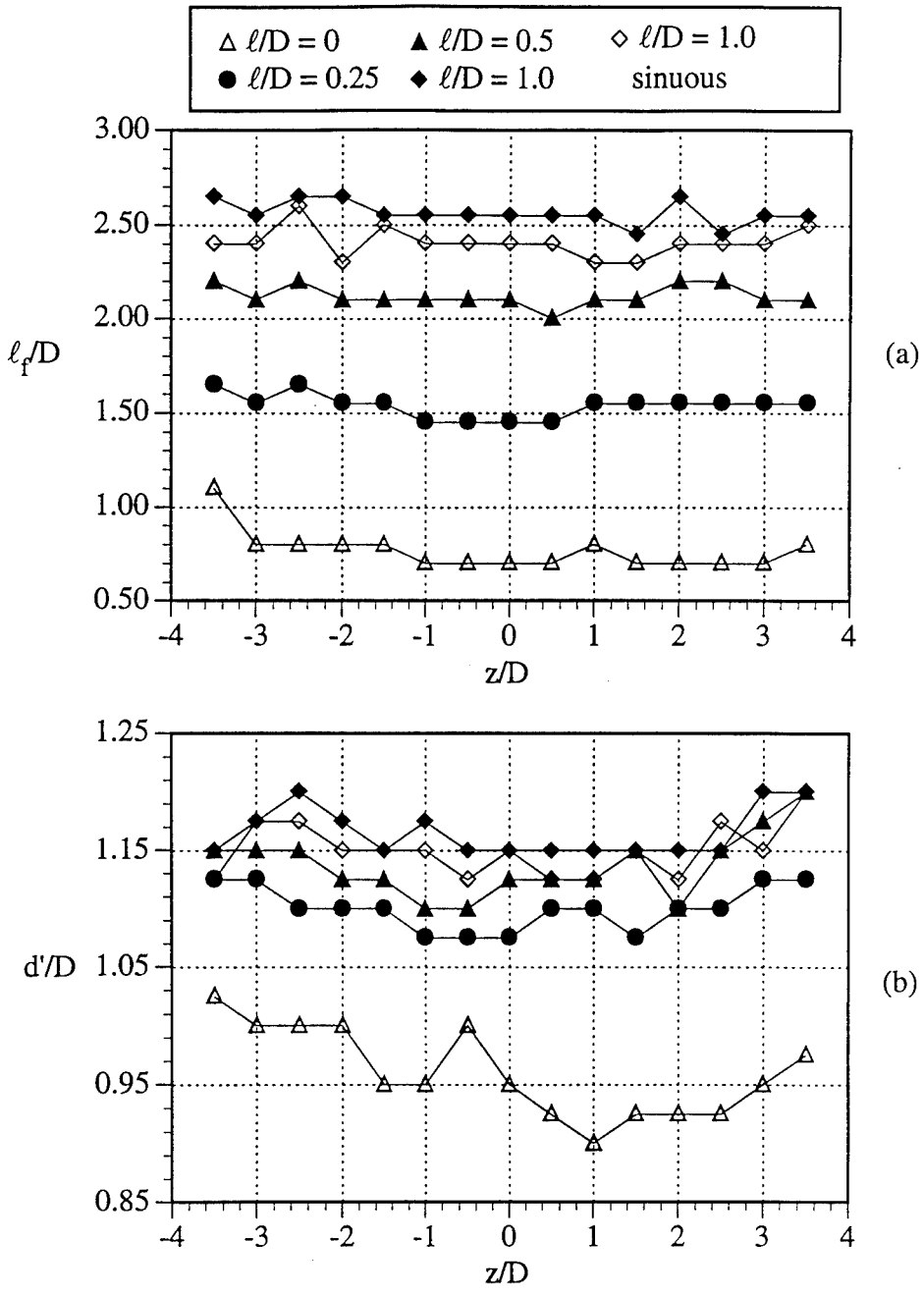

Figure 3.25. Formation region length and wake width versus span for straight cylinder in uniform flow.

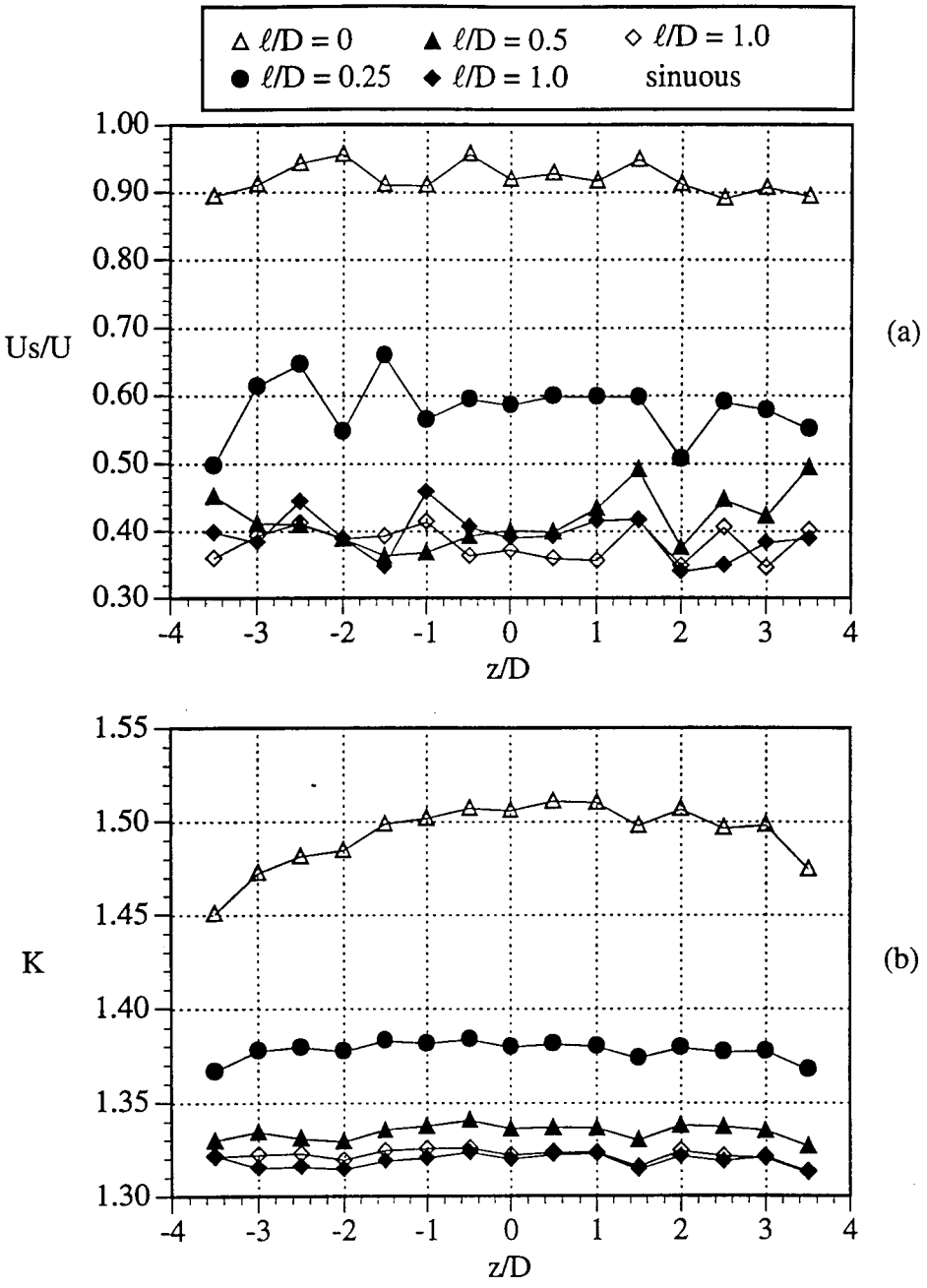

Figure 3.26. Shear layer velocity and base pressure parameter versus span for straight cylinder in uniform flow.

CHAPTER 4. RESULTS FOR A STRAIGHT CYLINDER IN SHEAR FLOW

The following results pertain to experiments conducted on straight circular cylinders in shear flow at Reynolds number based on midspan velocity (U_{ref} = 36 ft/s) of 30,000 and AR = 8 unless otherwise noted. The shear velocity gradient, dU/dz = 6.2 sec^{-1}, the steepness parameter, $\beta = 0.03$, and the shear parameter, $\Lambda = 0.34$. The power spectrum results were based on 20 ensembles of 1024 samples acquired at a sample rate of 200 Hz for a total sample time of 102.4 seconds.

4.1 Power spectra and Strouhal number

Spanwise variation in the power spectra for a straight circular cylinder in shear flow is presented in Figure 4.1. Spectra obtained with the shear generating screen in opposite orientations i.e., with the shear gradient from high to low velocity, and the reverse orientation (rotated 180° along longitudinal axis) with the shear gradient from low to high velocity across the width of the test section are compared. The experiments were run for the two orientations to confirm that the shear screen produced consistent velocity profiles that were independent of screen orientation or wall effects. The results show the typical spanwise cells of constant shedding frequency consistent with previous investigations, Maull and Young [1973], Woo et al. [1981] and Griffin [1985]. For the present investigation, the relatively small aspect ratio limited the number of spanwise cell to approximately 2-4. More cells would be expected at a larger aspect ratio, for example in the investigations of Woo et al. [1981], no fewer than 7 constant frequency cells were detected with AR = 36 and $\beta = 0.032$. For comparison, the shedding frequency produced for the cylinder in a uniform flow at U = 36 ft/s was 44 Hz. Results indicate that constant

frequency cells in the shear flow were centered about that frequency with the low and high frequency cells at about 38 and 50 Hz respectively or, 44 ± 6 Hz. In addition, the Strouhal number based on local velocity at the center of each spanwise cell was approximately equal to the expected uniform flow value of 0.20.

Spanwise variation in power spectra for four straight and sinuous splitter plate combinations of similar average length, ℓ/D_{avg} = 0.25, 0.50, 0.75, 1.25 are compared in Figures 4.2 - 4.5. Examination of the spectra in these figures suggest that although the shape of the power spectrum differs in some of the comparisons, the dominant shedding frequency and its spanwise variation was consistent between plates of the same average length in all comparisons. Figure 4.2 indicates that for ℓ/D_{avg} = 0.25 both configurations produced two constant frequency cells, a low frequency cell of 44 Hz at the low speed side of the span and high frequency cell of 49 Hz at the high speed side. The frequency difference of 5 Hz compares to a difference of 12 Hz measured in the ℓ/D = 0.0 case. The average of the high and low frequency, about 46.5 Hz, was approximately equal to the frequency measured for ℓ/D = 0.25 in uniform flow. The span position where the transition to the higher frequency occurs, appeared to be approximately 1D closer to the high speed side for the sinuous plate than for the straight plate.

Comparison of the spectra for a straight ℓ/D = 0.50 and sinuous ℓ/D = 0.75 splitter plate configuration is made in Figure 4.3. The straight plate results indicate a nearly constant primary frequency across the span of about 47 Hz with some lower frequency modes clearly present at the low speed side. The sinuous plate results show a very similar spanwise variation to the straight plate although the lower frequency mode, 44 Hz, appeared to dominate at some of the midspan positions and then became absorbed in the broad-band spectra near the low speed end. As with the previous comparisons, the average

of the two dominant frequencies present was equal to the frequency detected for a straight plate of similar length in uniform flow.

Comparison of the spectra for a straight plate of $\ell/D = 0.75$ and a sinuous plate of $\ell/D = 1.0$ shown in Figure 4.4 indicates one dominant frequency mode of 46 Hz apparent in both configurations that was located at the high speed side of the shear for approximately 4D of span. The dominant frequency at the high speed side was more narrow-band than those near the low speed side and its frequency was consistent with that measured for a straight, $\ell/D = 0.75$ plate in uniform flow. Near the low speed side of the span, the dominant modes increased in frequency slightly with decreasing shear velocity to a maximum of 51 Hz, higher than the primary mode at the high velocity side. Also, weaker low frequency modes of 32 - 39 Hz, were evident at the low speed side that decreased in frequency with decreasing shear velocity across the span.

For a straight plate of $\ell/D = 1.25$ and sinuous plate of $\ell/D = 1.5$ shown in Figure 4.5 the spectra indicate a slight variation in the primary shedding frequency across the span from 50 Hz at both ends to approximately 46 Hz near midspan for both configurations. The lower frequency modes found for the $\ell/D_{avg} = 0.75$ configurations were no longer present in the spectra.

Data for the two straight splitter plate configurations, $\ell/D = 1.0$ and 1.5, that did not have corresponding average length sinuous plate configurations for comparison are presented in Figure 4.6. Both configurations indicate one relatively large spanwise cell of constant shedding frequency extending from the high speed side for approximately 4D of the span. For the $\ell/D = 1.0$ configuration the frequency of the cell was approximately 47 Hz, consistent with the shedding frequency measured for that plate in uniform flow. Beyond $z/D = 1$ the dominant mode increased in frequency with increasing span position to

about 51 Hz at z/D = 3. There was evidence of low frequency components similar to those measured at ℓ/D = 0.75 although lower in relative magnitude to the dominant mode. The ℓ/D = 1.5 configuration indicated a dominant frequency for the high velocity span positions of approximately 50 Hz. Beyond z/D = 1 there was a slightly lower frequency, 46 Hz, spanwise cell that extended to the low speed end. The spectra at z/D = 2.5 and 3 show a very low frequency mode of about 16 Hz. Of all the splitter plate configurations investigated in shear flow, the ℓ/D = 1.5 configuration demonstrated the least spanwise variation in dominant frequency and is probably indicative of what occurs for higher ℓ/D.

Power spectrum results for the investigation of Reynolds number effect on the spanwise variation in shedding frequency for a circular cylinder in shear flow with splitter plate, ℓ/D = 0.0 and 1.0 are presented in Figures 4.7 - 4.9. The tunnel speed was varied to produce a midspan velocity that ranged from U_{ref} = 31 - 59 ft/s resulting in Reynolds numbers based on midspan velocity of Re_{ref} = 26,500 - 49,100. Comparison of Figures 4.7 - 4.9 show that the ℓ/D = 0.0 configuration, at all tested reference velocities, demonstrated the characteristic, two constant frequency spanwise cells observed in the previous results for U_{ref} = 36 ft/s, except scaled in frequency. At all velocities, the ℓ/D = 1.0 configuration indicated the identical spanwise variation found at the U_{ref} = 36 ft/s case. A relatively large spanwise cell at the high velocity side and the highest frequency dominant mode corresponding to the lowest velocity span position were observed.

In Figure 4.10 the results taken from Figures 4.7 - 4.9 are presented in the form of Strouhal number based on U_{ref} versus ℓ/D for the extreme positions at the low and high velocity sides of the span, z/D = 3 and -3 respectively. The results indicate that although the shedding frequency shifted depending on U_{ref}, the Strouhal number based on U_{ref} remained essentially constant regardless of Reynolds number. The data also indicates the relationship between the shedding frequency of the low and high velocity side cells and its

variation with ℓ/D. A curve fit through the data shows that the two cells should be at approximately the same frequency for plates of ℓ/D = 0.4 and somewhere above ℓ/D = 1.0. A higher frequency crossover point occurred between ℓ/D = 1.25 and 1.5 for the data presented in Figures 4.5 and 4.6.

In Figures 4.11 and 4.12 the effects of aspect ratio on a straight circular cylinder in shear flow with Re_{ref} = 30,000 are presented. Figure 4.11 shows the spanwise variation in the power spectrum at AR = 9 and 5. The results for AR = 9 identify three constant frequency cells at 36, 45, and 51 Hz. For AR = 5 only two modes, 44 and 48 Hz, were observed in the power spectra at all evaluated span locations. The low frequency mode was more prominent at the low speed span positions and likewise, the high frequency mode dominated the high speed span positions. The results support conclusions drawn in previous investigations, Fiscina [1977], and Davies [1976], that the number of spanwise cells are strongly dependent upon aspect ratio. The effect of aspect ratio on the dominant shedding frequency at a fixed span position is shown in Figure 4.12. Two cases were considered, corresponding to fixed probe positions at z/D = -3 (high speed side) and z/D = 3 (low speed side). The aspect ratio was controlled by moving the end plate at the opposite side of the span relative to the probe to produced a range of aspect ratios from AR = 3.0 - 8.5. The results show that the shedding at the high velocity side was not affected significantly by the changes in aspect ratio. The shedding at the low velocity side however, indicated a significant modification of the dominant frequency depending upon aspect ratio, from 39 Hz to 44 Hz. The results for the probe fixed at the low speed side also indicated two modes in the spectrum for aspect ratios larger than AR = 4. The frequency difference between the two peaks increased with increasing aspect ratio. There was no evidence in the spectra of a low frequency peak equal to the difference in frequency between the two primary peaks that would indicate modulation between the two modes. The results of

Figure 4.12 suggest that the low speed side of the span was more sensitive to changes in aspect ratio than the more narrow-band, more energetic, high speed side.

4.2 Wake parameters

Figures 4.13 - 4.15 present the various wake parameters calculated from the data detailed in Appendix A pertaining to the straight cylinder in shear flow splitter plate configurations.

Spanwise variation of RMS fluctuation intensity obtained from traverses along the cylinder centerline of a straight cylinder with $\ell/D = 0.0$, 0.5, and 1.0 is shown in Figure 4.13. The streamwise location at which the maximum RMS value was detected was defined as the length of the formation region, ℓ_f/D. The results indicate an increase in ℓ_f/D as the shear velocity increased across the span. The difference in ℓ_f/D at the low speed end compared to the high speed end became greater with increasing plate ℓ/D. For $\ell/D = 0.0$, the magnitude of the maximum RMS intensity remained relatively constant across the span. The $\ell/D = 0.5$ and 1.0 configurations however, show a gradual decrease in the maximum RMS intensities with decreasing shear velocity across the span. The splitter plate also affected the shape of the RMS profiles, producing flatter curves with less well defined peaks with increasing ℓ/D, especially at the high velocity span positions. Comparison of the data for all three configurations showed that the maximum RMS intensities decreased with increasing ℓ/D at all spanwise positions.

Spanwise variation in formation region length and wake width for splitter plate configurations of $\ell/D = 0.0$, 0.25, 0.5, 1.0, and sinuous $\ell/D = 1.0$ are shown in Figure 4.14 (a) and (b). The length of the formation region varies linearly with increasing shear velocity for all configurations. Also, the ℓ_f/D increased with ℓ/D for all configurations. For the sinuous $\ell/D = 1.0$ plate, the formation lengths fell between the straight $\ell/D = 0.5$

and 1.0 results, consistent with the concept of using an average length in comparisons between straight and sinuous plates. The wake width results show trends which are similar to the formation length results i.e., increased wake width with increased shear velocity and ℓ/D. The increase in wake width across the span became smaller with increasing ℓ/D as indicated by the more shallow slope of the profiles at higher ℓ/D.

In Figure 4.15 (a) and (b) the spanwise variation in shear layer velocity, U_s/U and base pressure parameter, K for the various splitter plate configurations are presented. Both parameters were based on the local flow velocity, U as opposed to the midspan reference velocity, U_{ref}. Strong similarities between the two parameters were indicated by their spanwise and ℓ/D trends. An increase in shear velocity corresponded to an increase in base suction and both parameters decreased with increasing shear velocity and ℓ/D. The spanwise trend in base suction was consistent with the results of Griffin [1985] at Re_{ref} = 20,000 and β = 0.015, and AR = 36, and Maull and Young [1973] for a D-shaped body. The results for Us/U and K support the average splitter plate length concept.

4.3 Vortex convection velocity

A Kármán vortex convection velocity and its spanwise variation for a straight circular cylinder in shear flow with splitter plate configurations of ℓ/D = 0.0, 0.5, and 1.0 is considered next. Two single sensor hot wire probes were used to determine the convection velocity. First measurements were made at various transverse locations (y/D's) to determine the best location to site the probes. In reviewing the RMS profiles it was first thought that the position y/D = 0.5 would be preferred since it corresponds to the approximate center of the vortex. However, measurements indicated that the position y/D = 0.25 was preferred because it produced the strongest correlations and most repeatable data. Hence, the probes were located at y/D = 0.25 and spaced 1.4375 inches apart in the streamwise direction with the upstream probe positioned at x/D = 3.0. Typical time series

from the two hot wires is indicated in Figure 4.16 (a). Also shown in Figure 4.16 (b) is the cross-correlation coefficient for the two signals as a function of phase lag, τ. The hot wire probes were sampled at a frequency of 10,000 Hz for 20 ensembles of 2000 points resulting in a total sample period of 4.0 seconds. To increase the time resolution of the cross-correlation and thereby improve the accuracy of the velocity measurements (equal to 1/sample rate or 0.0001 seconds) a high sample rate was selected. The vortex convection velocity was determined by dividing the probe spacing, Δx by phase lag, τ that corresponded to the maximum correlation coefficient, $\tau_{\rho max}$. In the present study the vortex convection velocity, U_c was referenced to the midspan velocity or, U_c/U_{ref}. The presence and prominence of the smaller peaks gave an indication of the periodicity of the disturbance. For example, multiple peaks of the same magnitude represent the case of both probes sensing identical periodic disturbances separated by some phase lag equal to the time from $\tau = 0$ to the nearest peak or, $\tau_{\rho max}$. Conversely, the absence of multiple peaks represent the case of a single, non-periodic disturbance convecting past the sensors.

Variation in correlation coefficient across the span for a straight cylinder with no splitter plate, $\ell/D = 0.0$ indicates that the correlation curves were fairly uniform in shape and consistent in magnitude across the span except for a noticeable decrease in periodicity at the low speed side of the span as shown in Figure 4.17. The value of $\tau_{\rho max}$ increased slightly from the high to low speed span locations consistent with a reduction in vortex convection velocity. Cross-correlation results for the $\ell/D = 0.5$ configuration are shown in Figure 4.18. A significant reduction in periodicity near the low speed span positions was measured. Also a reduction in $\tau_{\rho max}$ was measured in the low speed portion of the span that would correspond to an increase in the vortex convection velocity in that region. Results for the $\ell/D = 1.0$ configuration are shown in Figure 4.19 and indicate a further decrease in the periodicity of the disturbance in the low speed region of the span. As with the $\ell/D = 0.5$ case $\tau_{\rho max}$ decreased in the low speed region indicating an increase in the

vortex convection velocity. All configurations demonstrate strong periodicity in the high speed region of the span.

From the results of the data presented in Figures 4.17 - 4.19 the vortex convection velocities were calculated and are shown in Figure 4.20. The data for the $\ell/D = 0.0$ configuration shows a linear increase in convection velocity from low to high speed span positions. The convection velocity measured for the $\ell/D = 0.5$ and 1.0 configurations show similar, relatively low convection velocities of approximately $U_c/U_{ref} = 0.61$ over the span from $z/D = -3.0$ to 0.5. Beyond $z/D = 0.5$ though, the splitter plate configurations experienced an increase in U_c/U_{ref} to levels above those recorded on the high speed side.

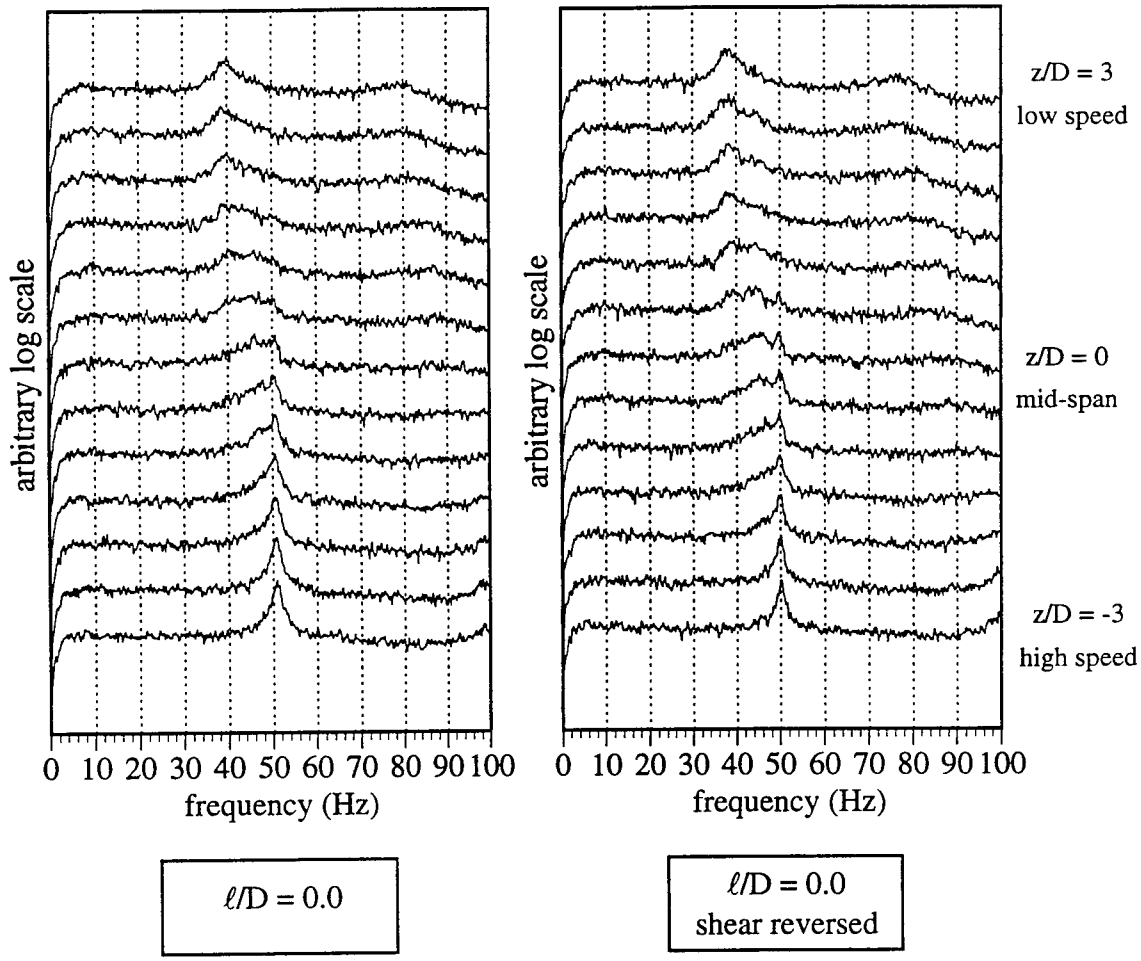

Figure 4.1. Power spectra for straight circular cylinder in shear flow. x/D = 3, y/D = 0.5.

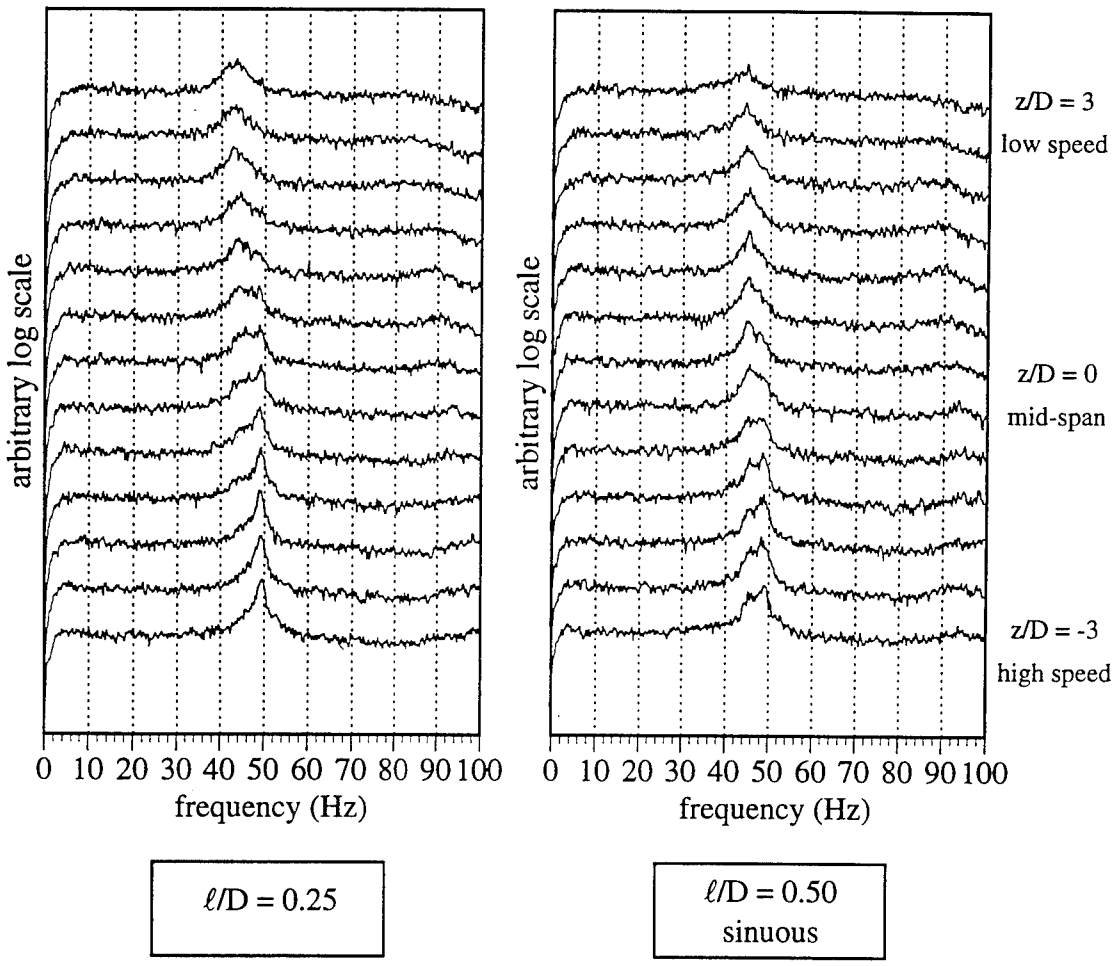

Figure 4.2. Power spectra for straight circular cylinder in shear flow.
x/D = 3, y/D = 0.5.

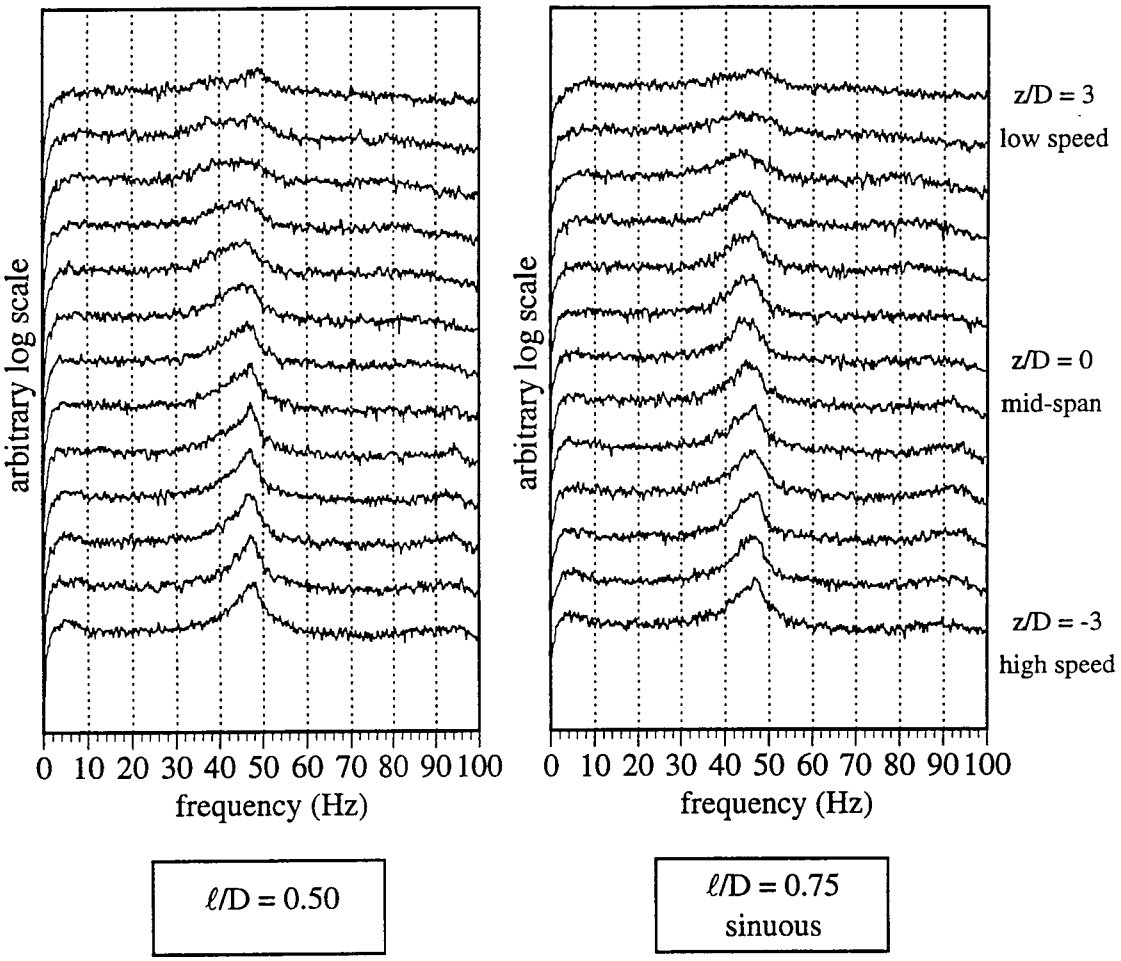

Figure 4.3. Power spectra for straight circular cylinder in shear flow. x/D = 3, y/D = 0.5.

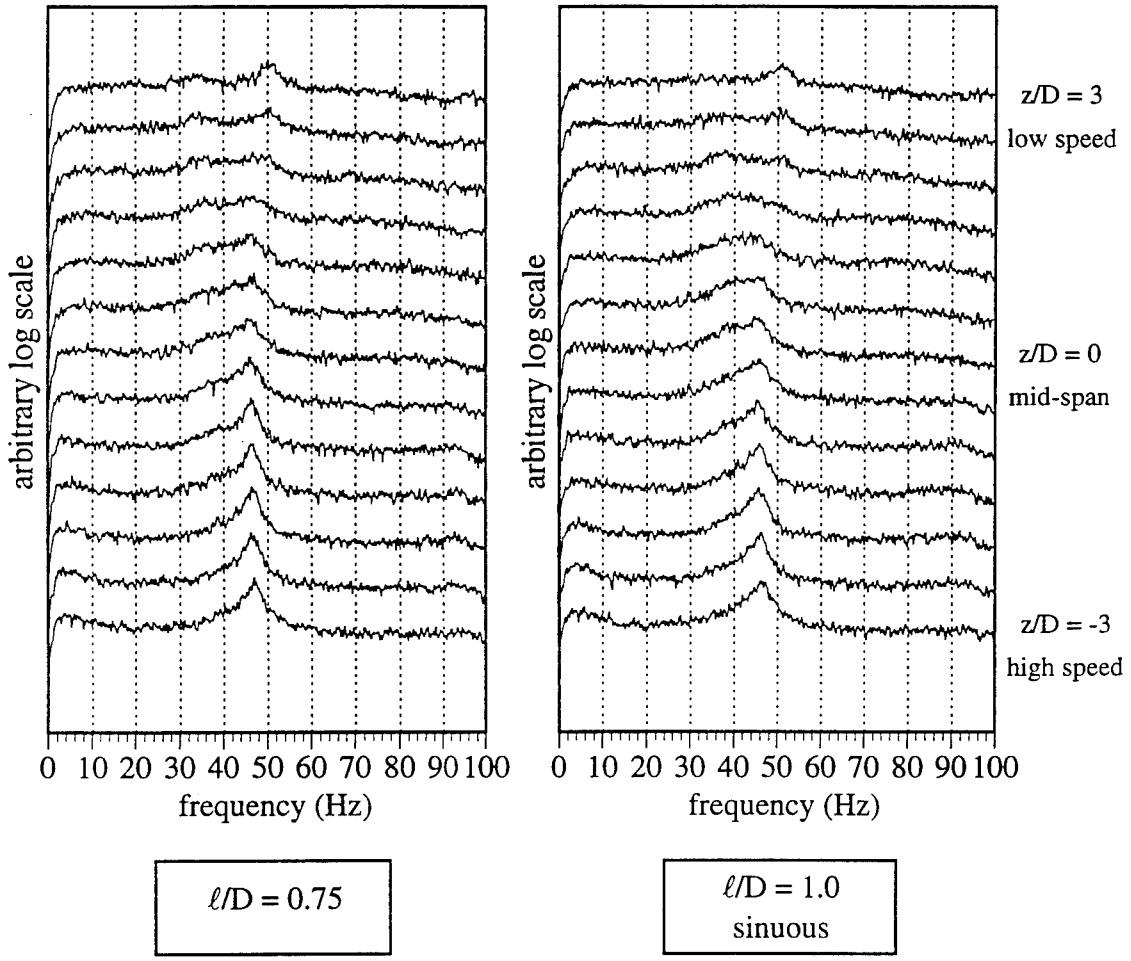

Figure 4.4. Power spectra for straight circular cylinder in shear flow.
x/D = 3, y/D = 0.5.

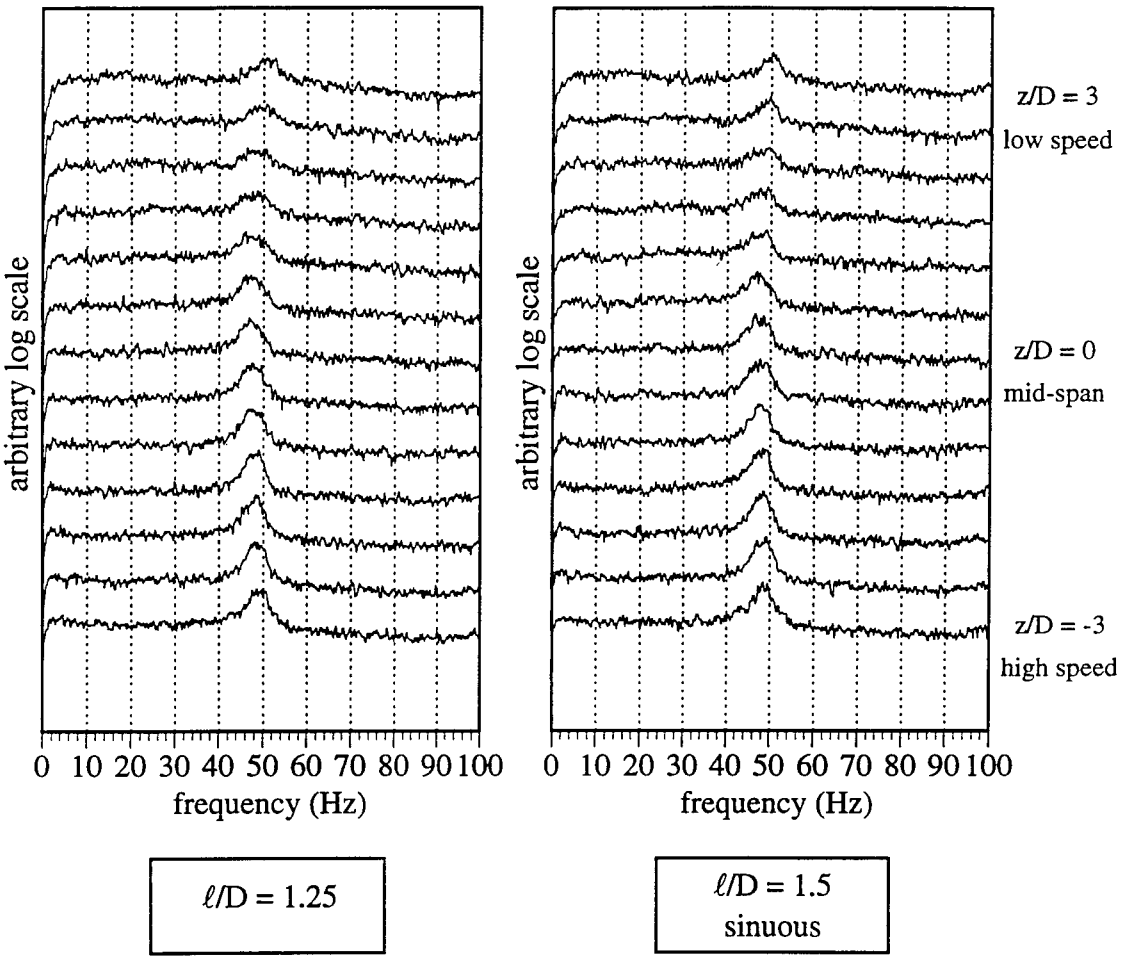

Figure 4.5. Power spectra for straight circular cylinder in shear flow.
x/D = 3, y/D = 0.5.

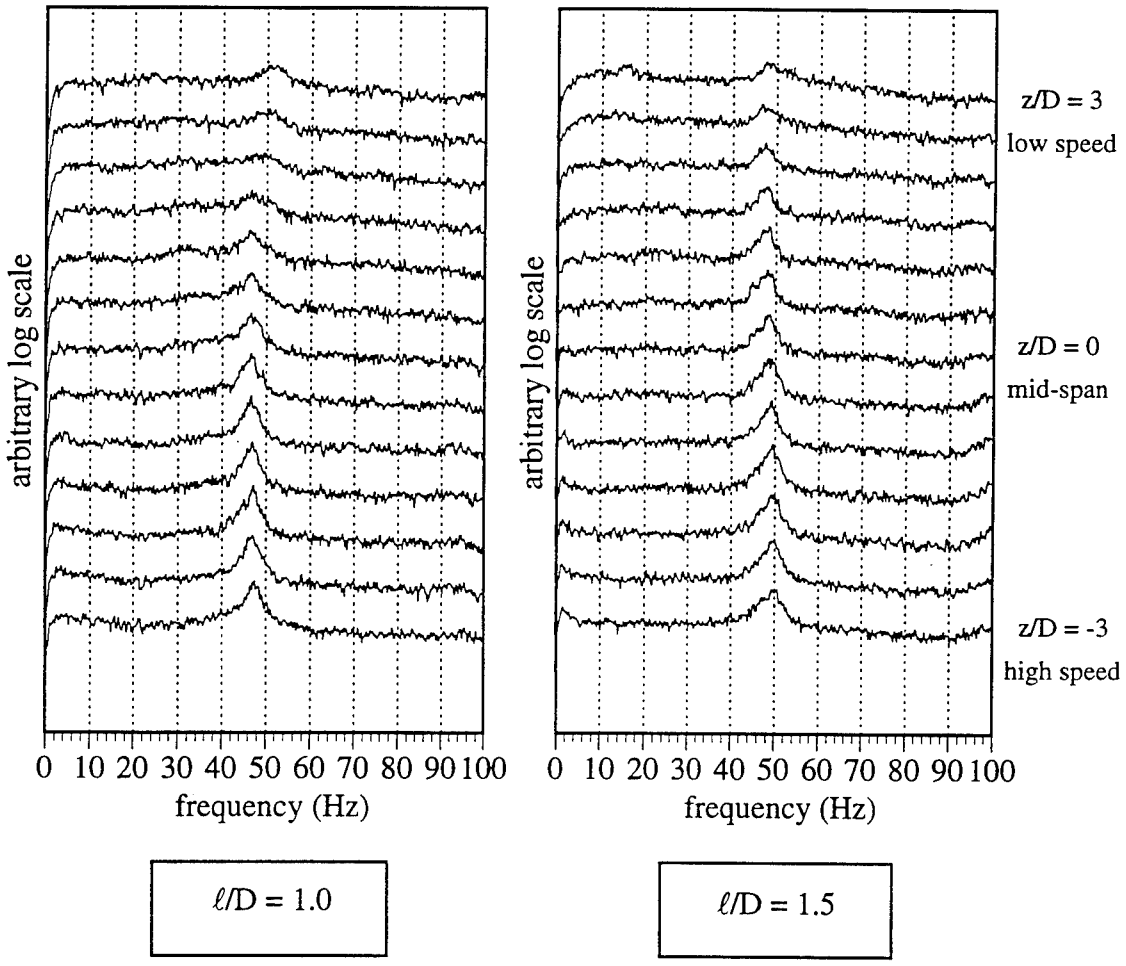

Figure 4.6. Power spectra for straight circular cylinder in shear flow. x/D = 3, y/D = 0.5.

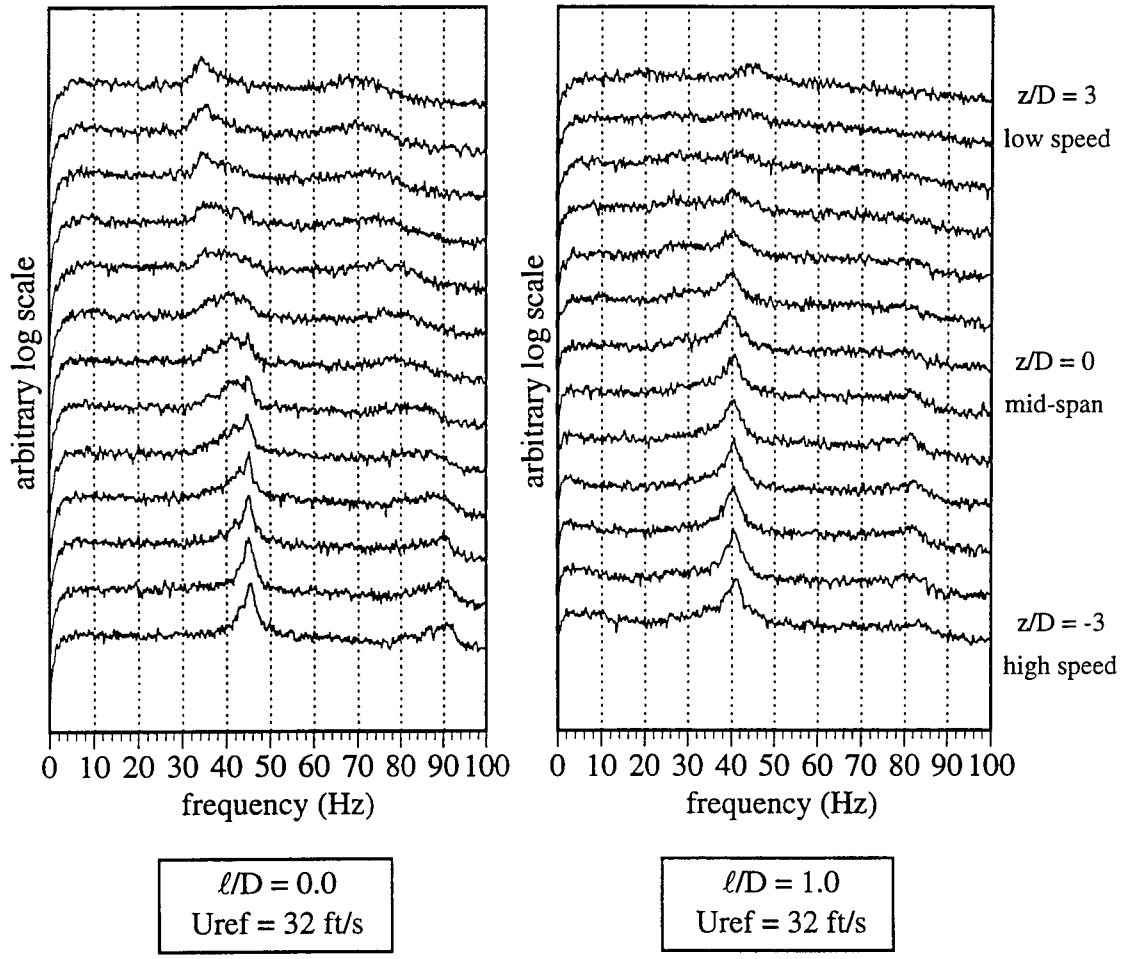

Figure 4.7. Power spectra for straight circular cylinder in shear flow. x/D = 3, y/D = 0.5, Re_{ref} = 26,500.

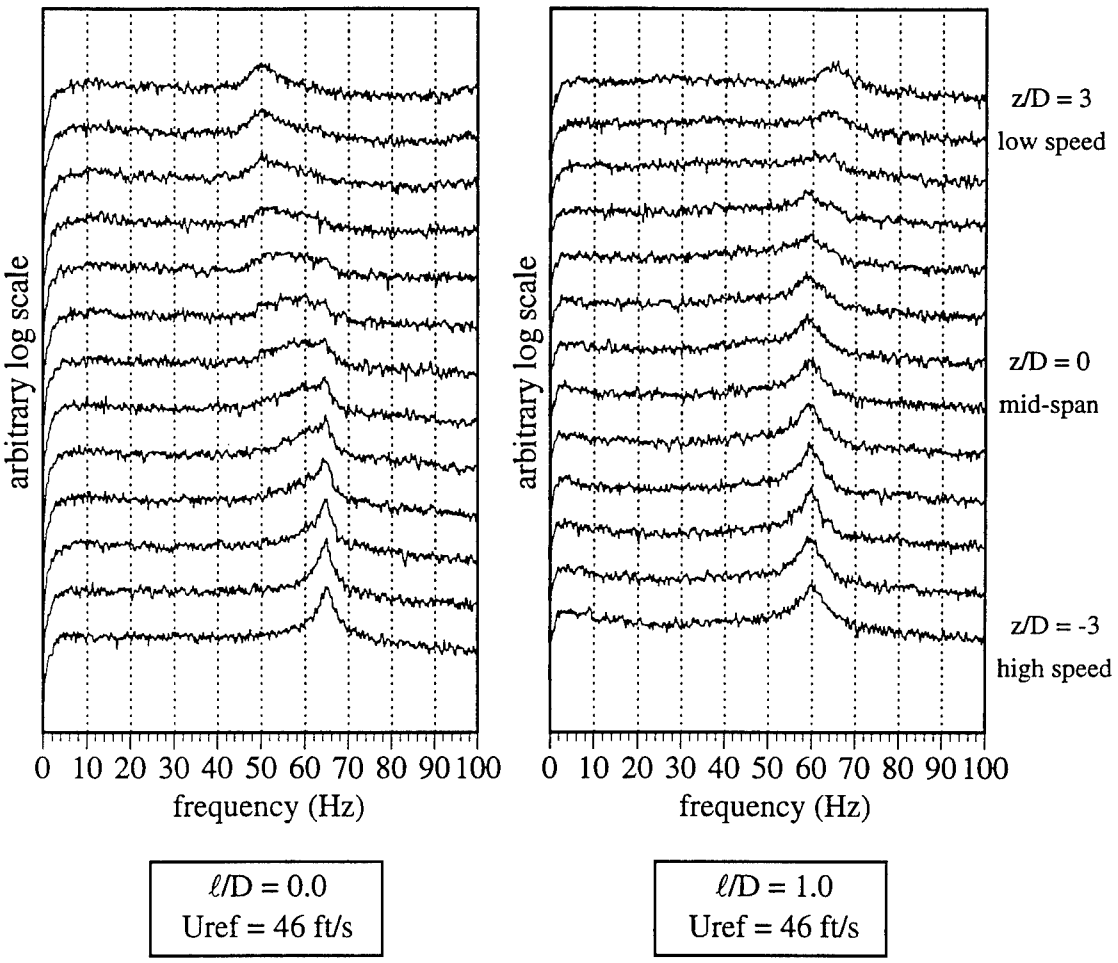

Figure 4.8. Power spectra for straight circular cylinder in shear flow.
x/D = 3, y/D = 0.5, Re_{ref} = 38,200.

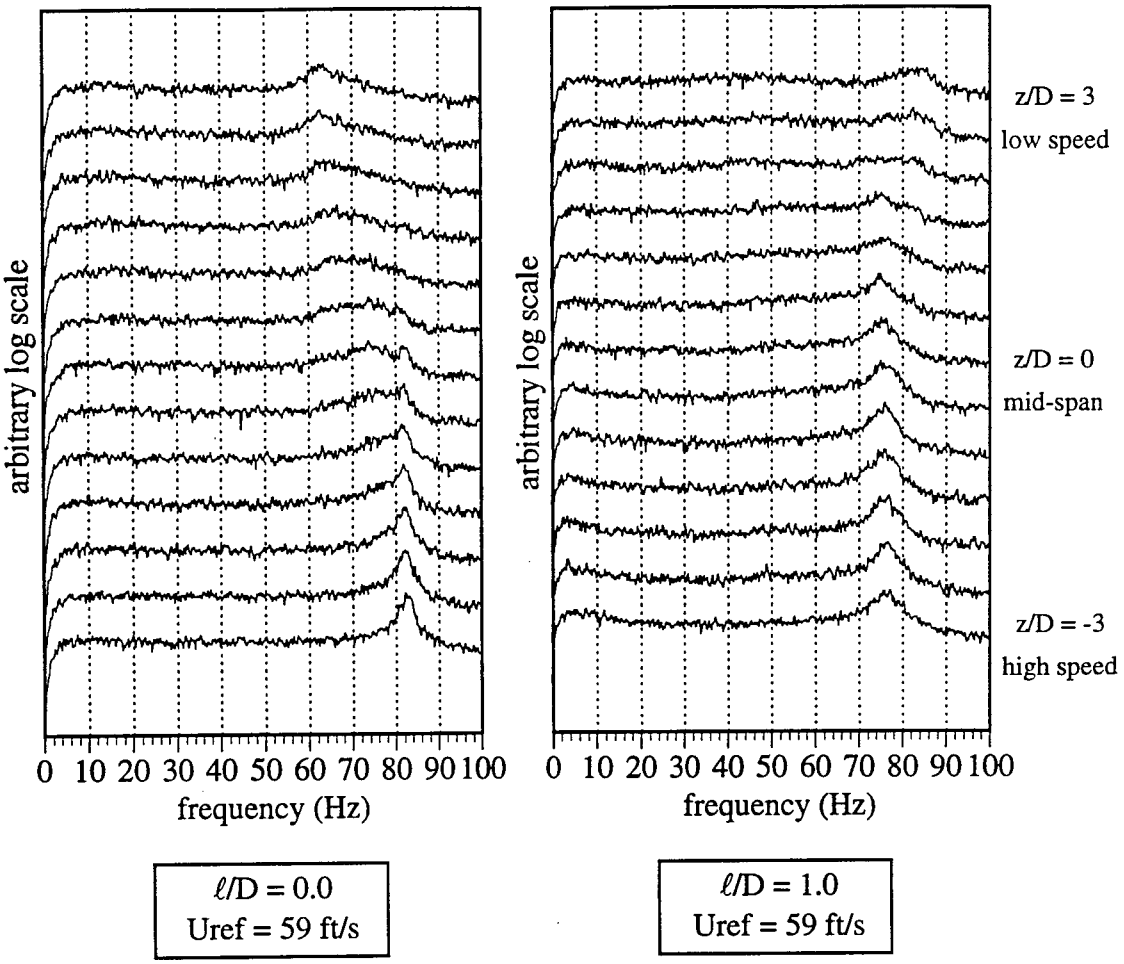

Figure 4.9. Power spectra for straight circular cylinder in shear flow.
x/D = 3, y/D = 0.5, Re_{ref} = 49,100.

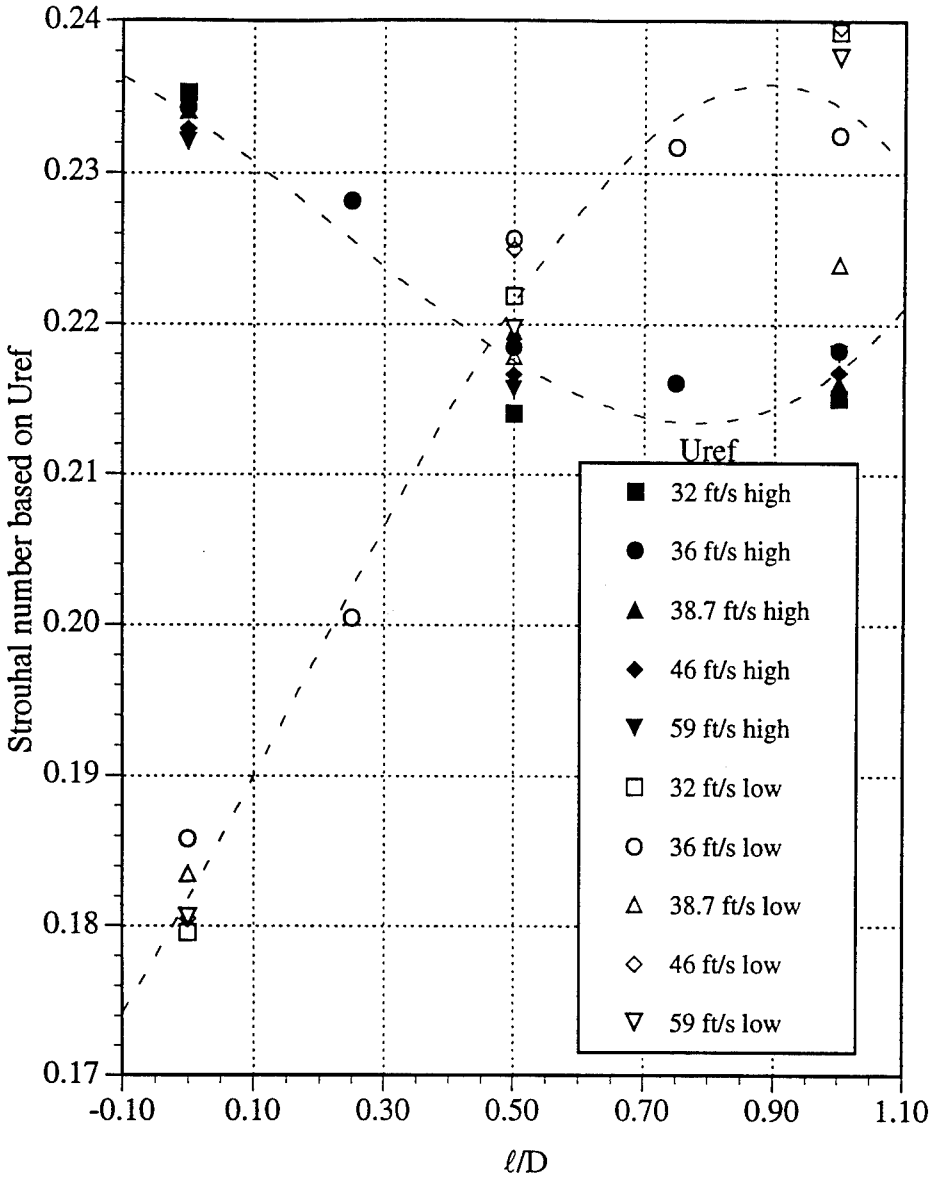

Figure 4.10. Strouhal number based on reference velocity versus splitter plate length. High = probe at z = 6 (high velocity side), Low = probe at z = -6 (low velocity side).

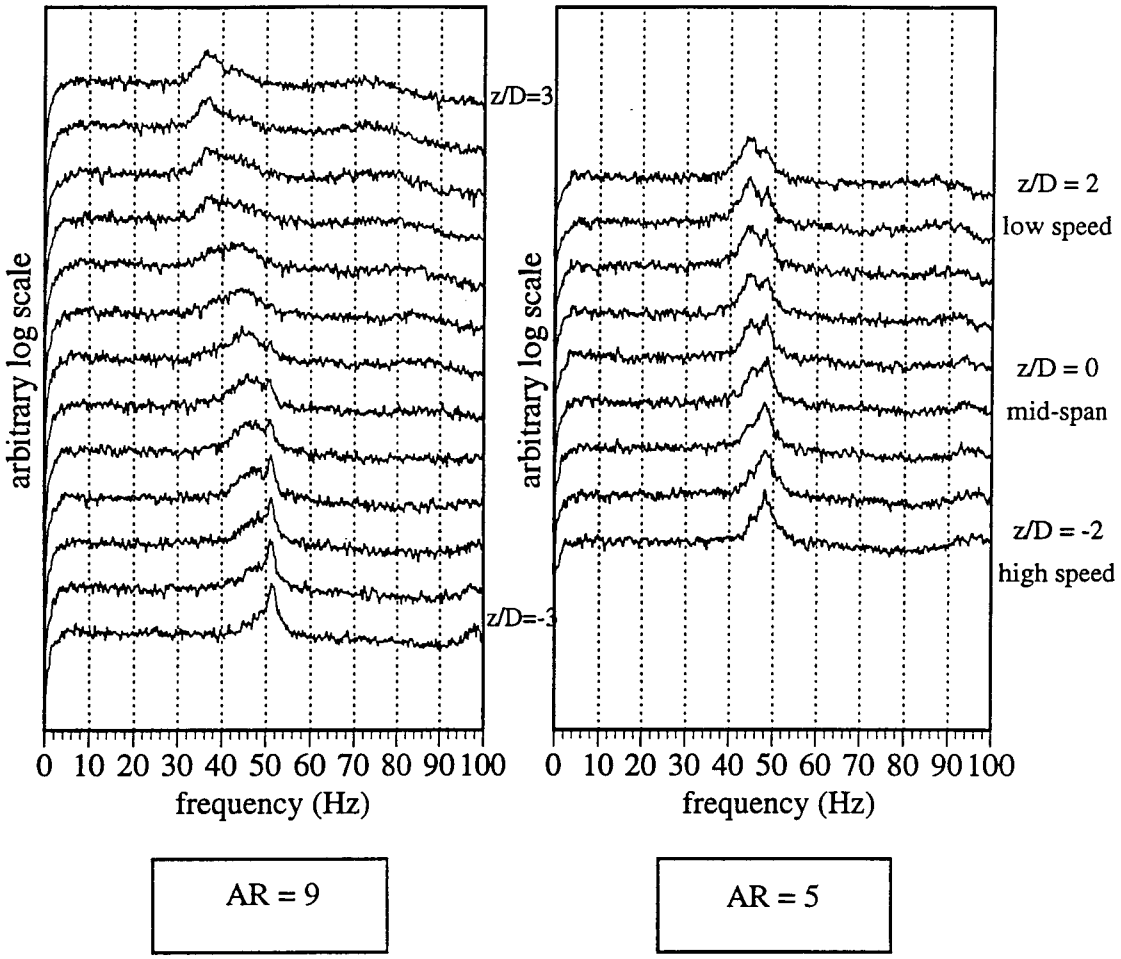

Figure 4.11. Aspect ratio effect on power spectra for straight circular cylinder in shear flow. x/D = 3, y/D = 0.5, ℓ/D = 0, Re_{ref} = 30,000.

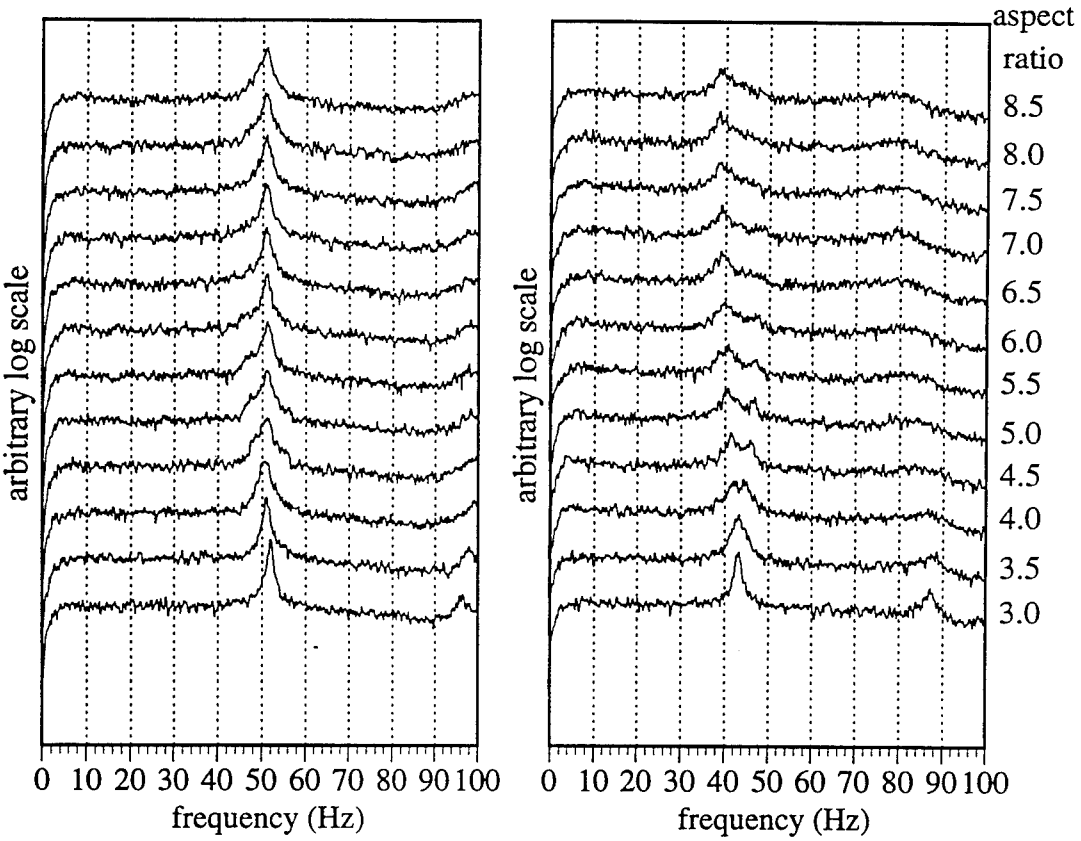

Probe fixed at high velocity side, z/D=-3. End plate on low speed side adjusted to vary aspect ratio.

Probe fixed at low velocity side, z/D=3. End plate on high speed side adjusted to vary aspect ratio.

Figure 4.12. Power spectra for straight circular cylinder in shear flow. x/D = 3, y/D = 0.5, ℓ/D = 0, Re_{ref} = 30,000.

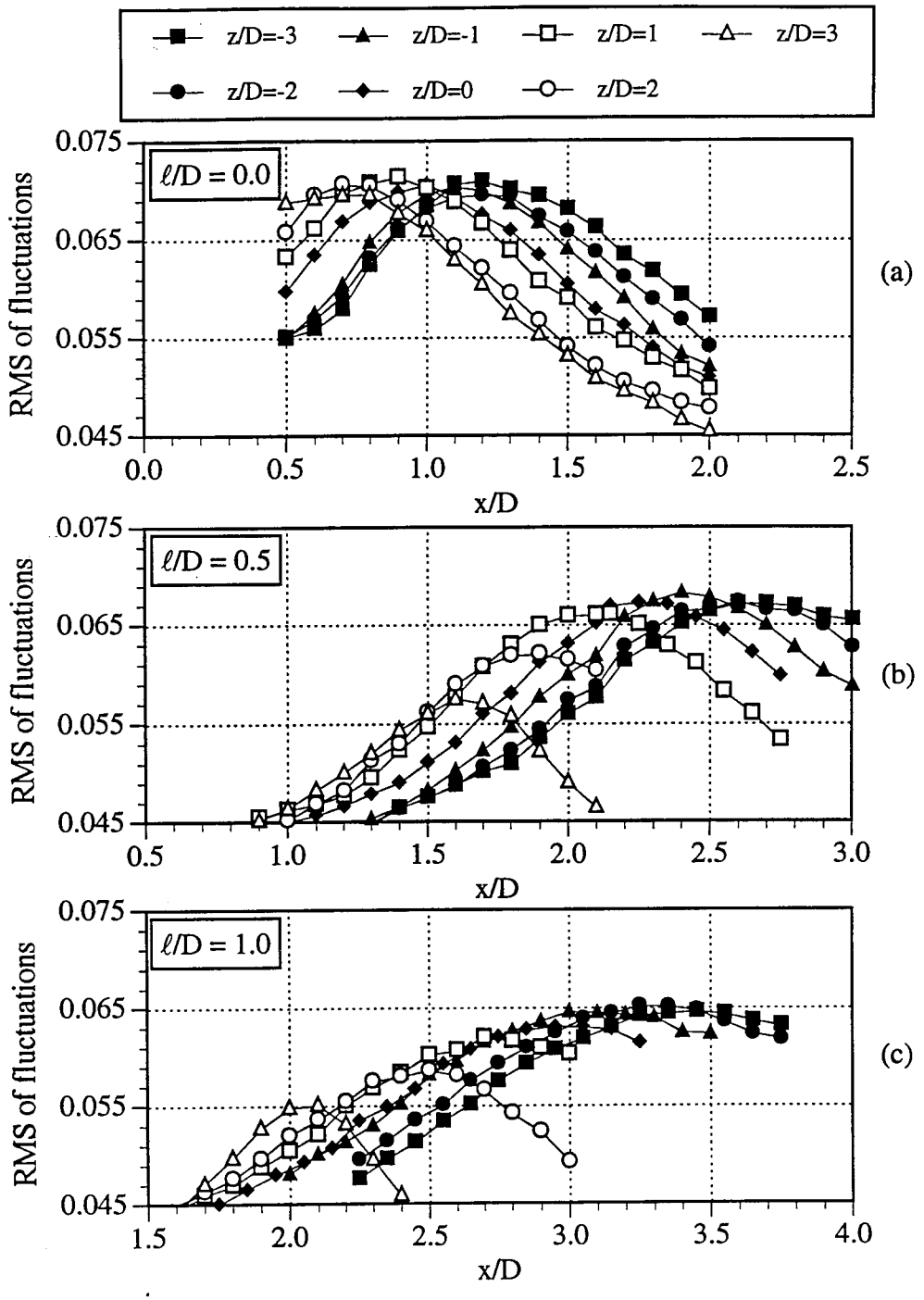

Figure 4.13. RMS of fluctuations versus x/D. Shear flow, Uref = 11 m/s, y/D = 0. Velocity increases with decreasing z/D.

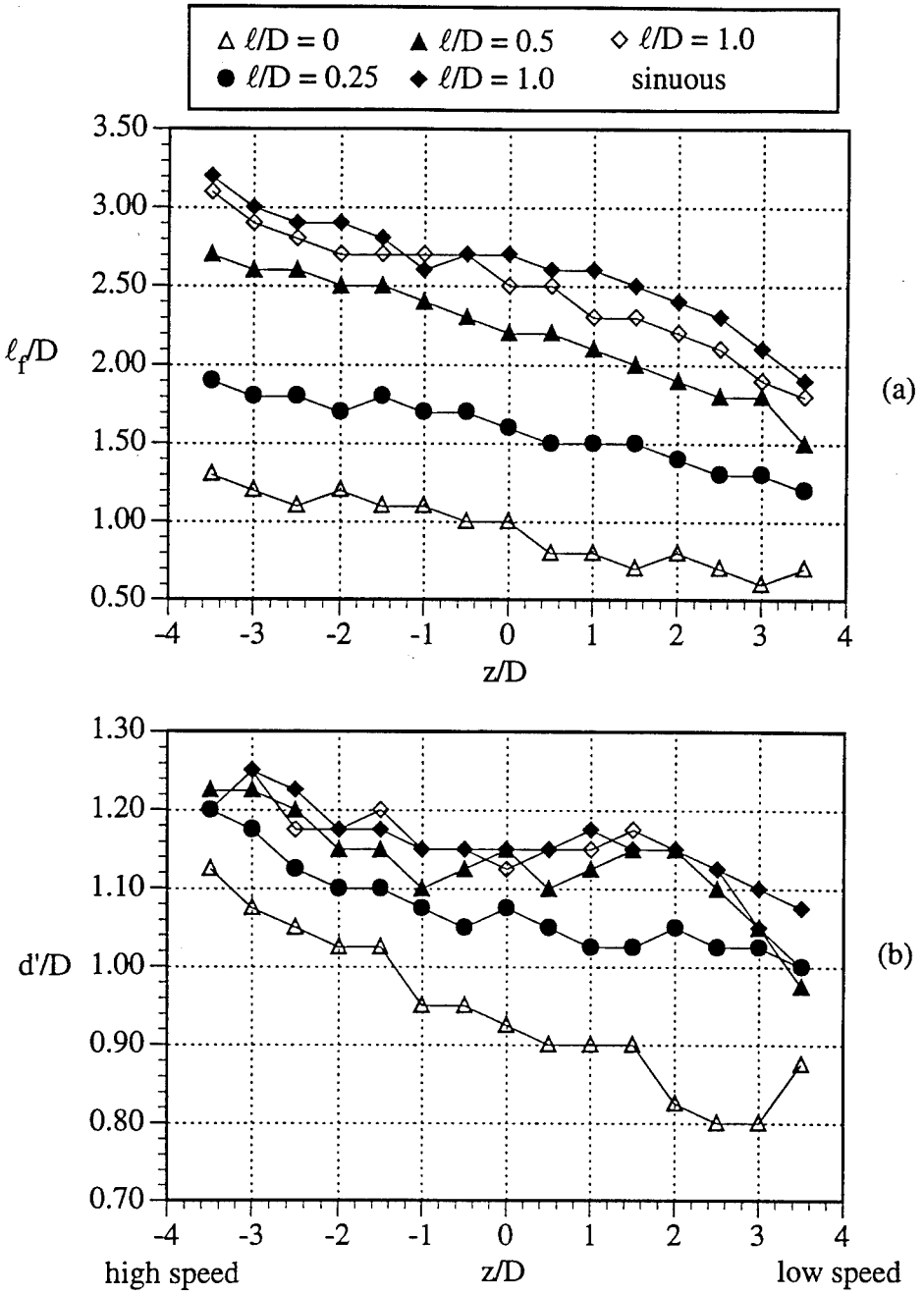

Figure 4.14. Formation region length and wake width versus span for straight cylinder in shear flow.

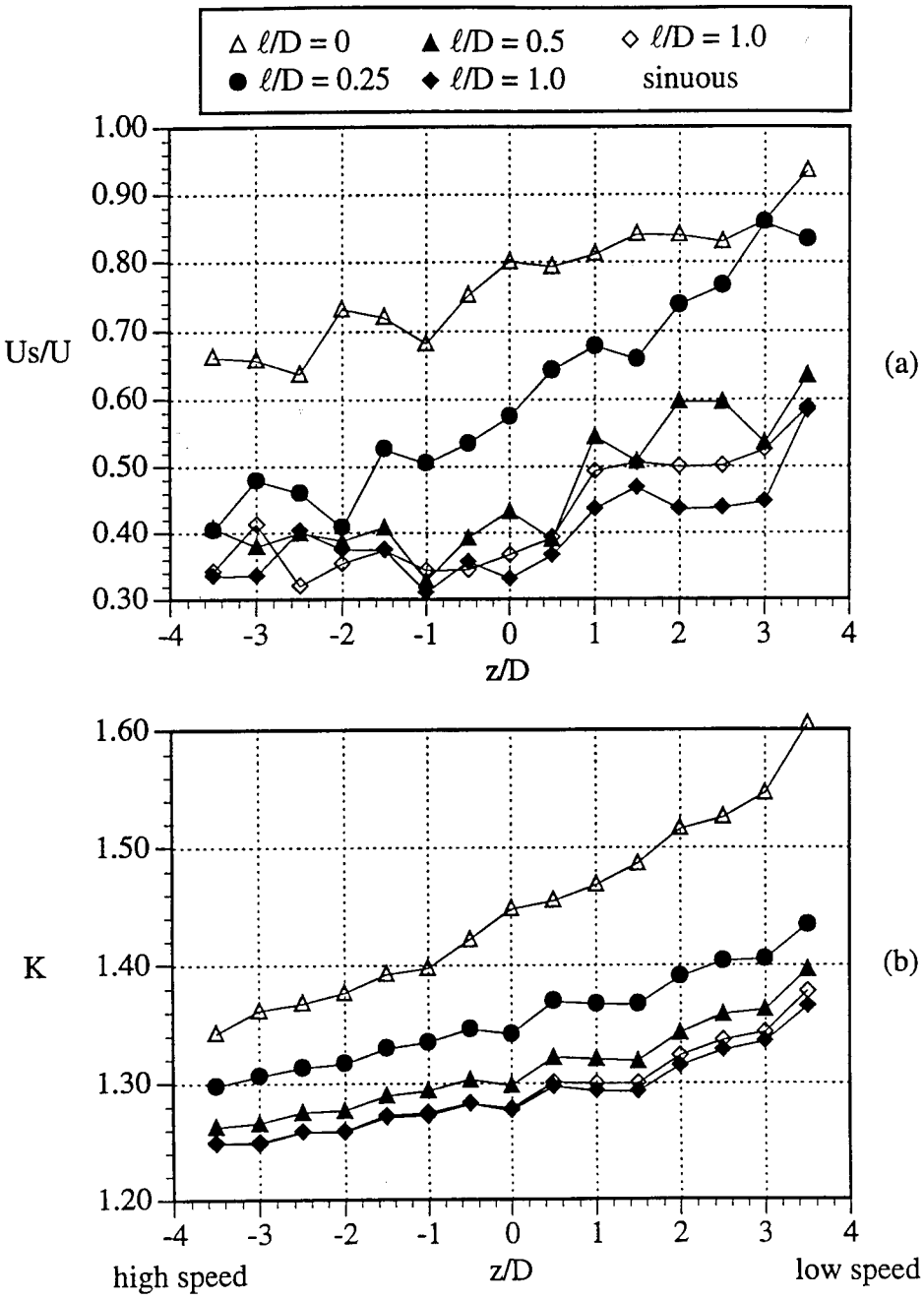

Figure 4.15. Shear layer velocity and base pressure parameter versus span for straight cylinder in shear flow.

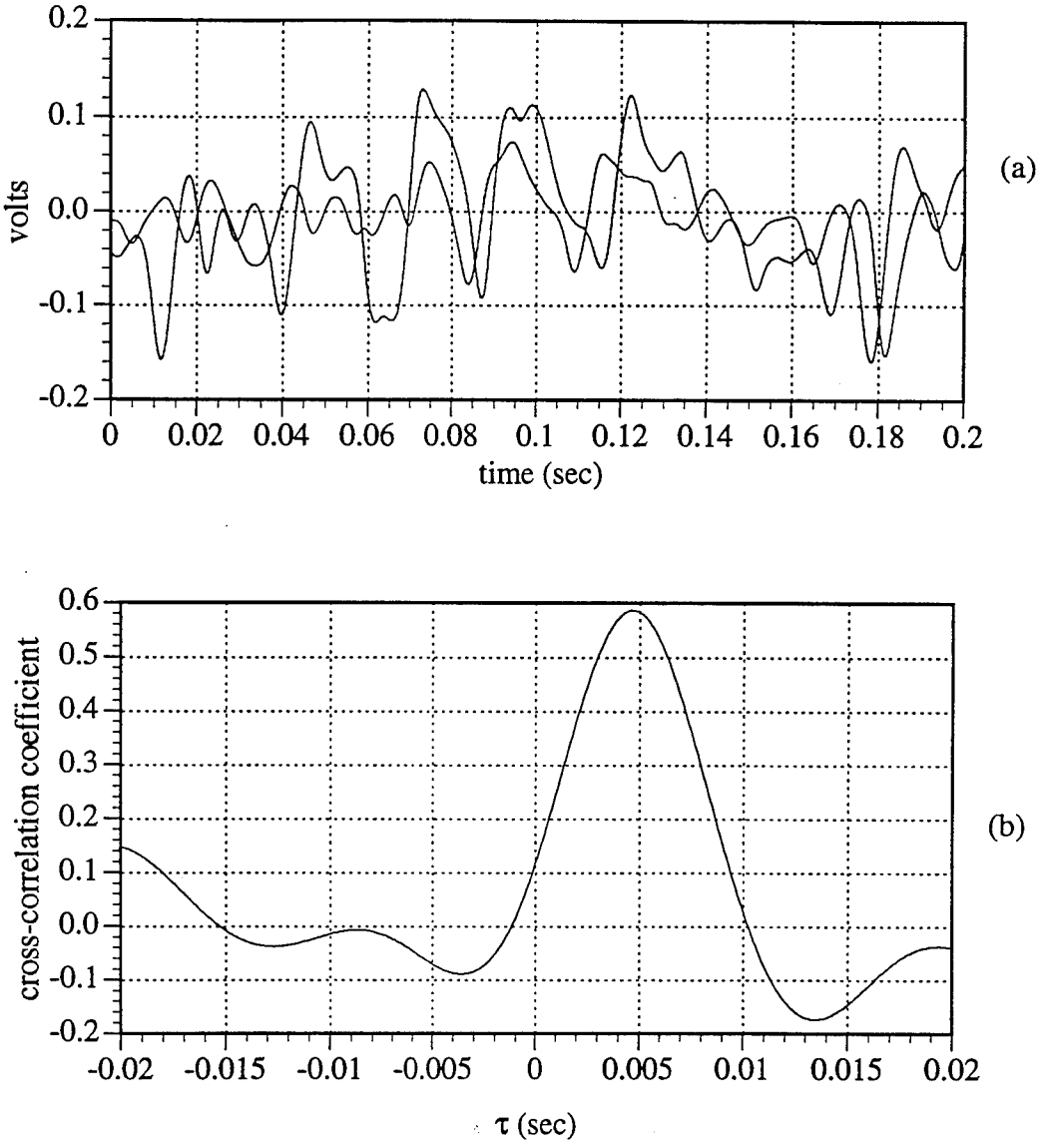

Figure 4.16. Typical time series and cross-correlation coefficient data for calculation of vortex convection velocity. Probe spacing, Δx = 1 7/16 inches

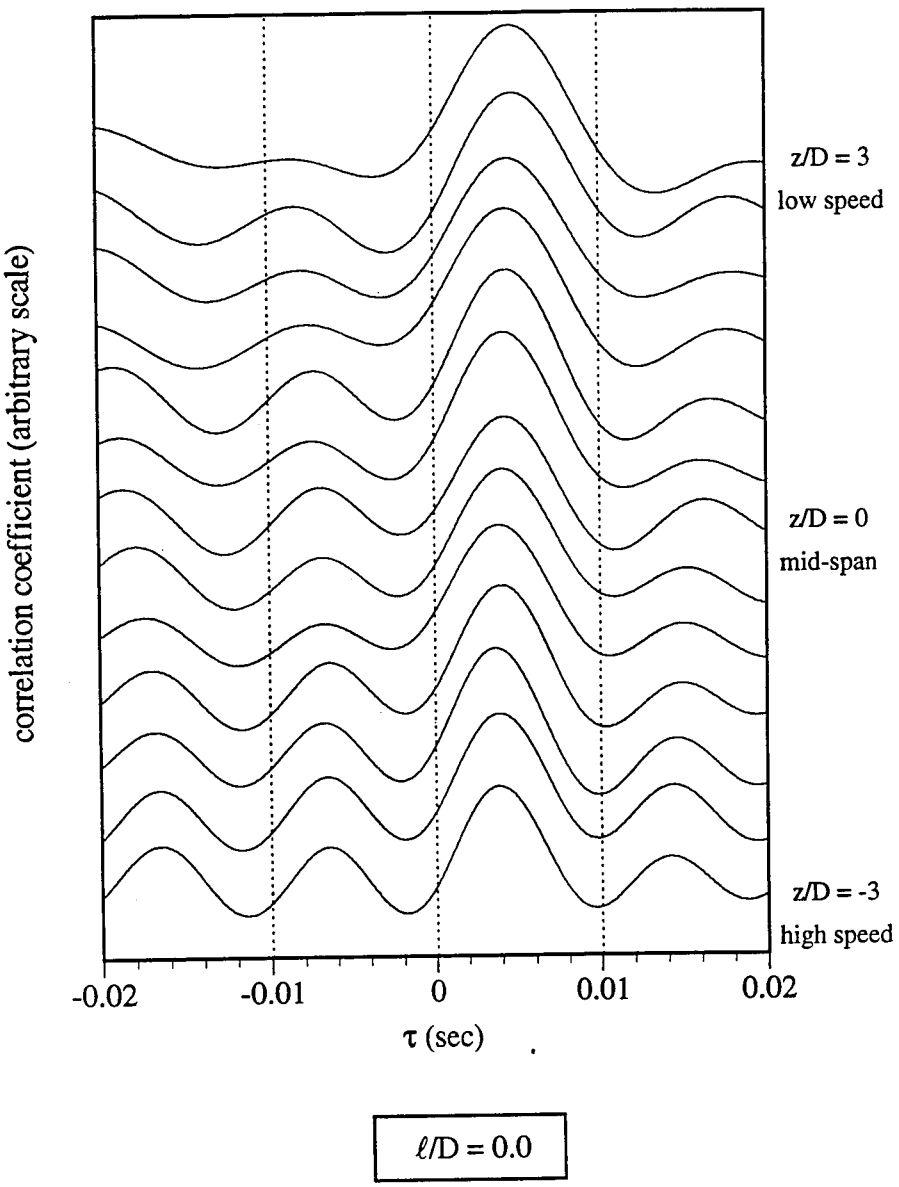

Figure 4.17. Cross-correlations for straight circular cylinder in shear flow.

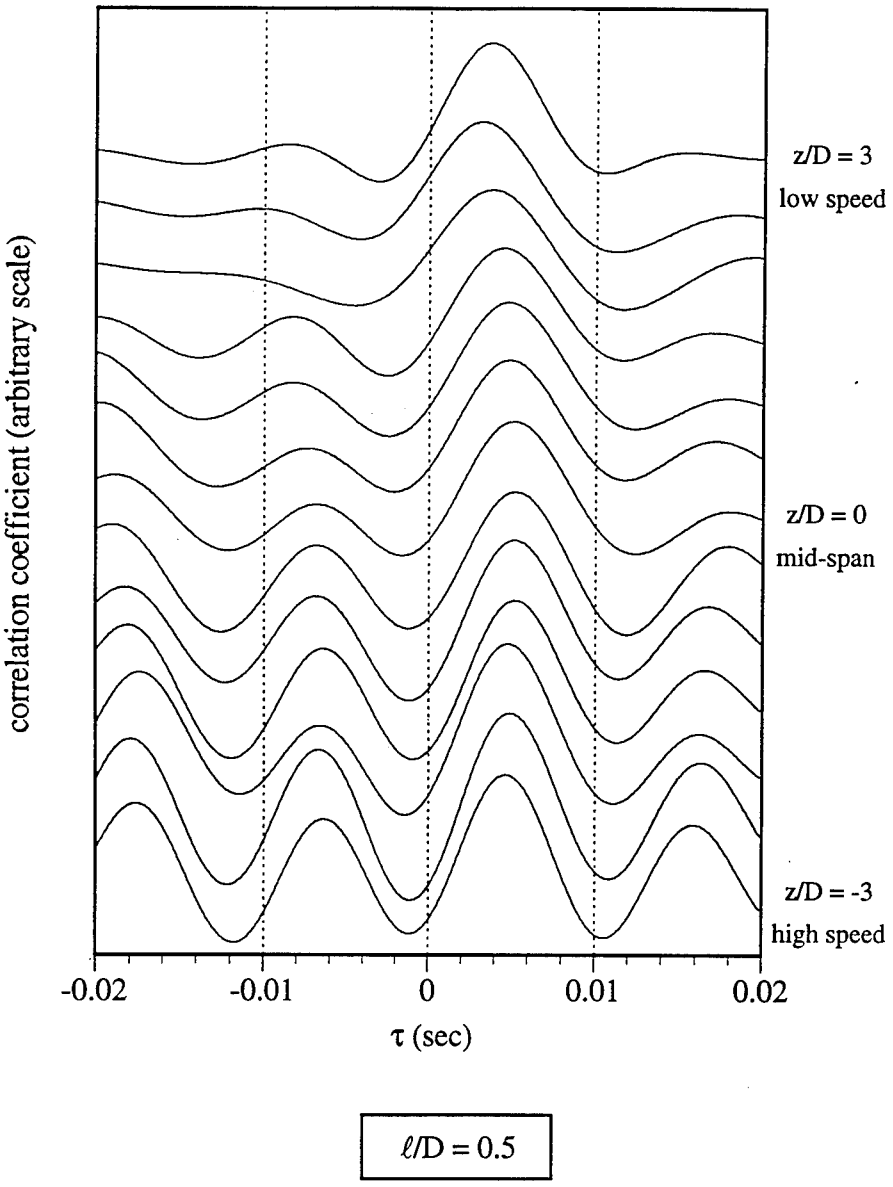

Figure 4.18. Cross-correlations for straight circular cylinder in shear flow.

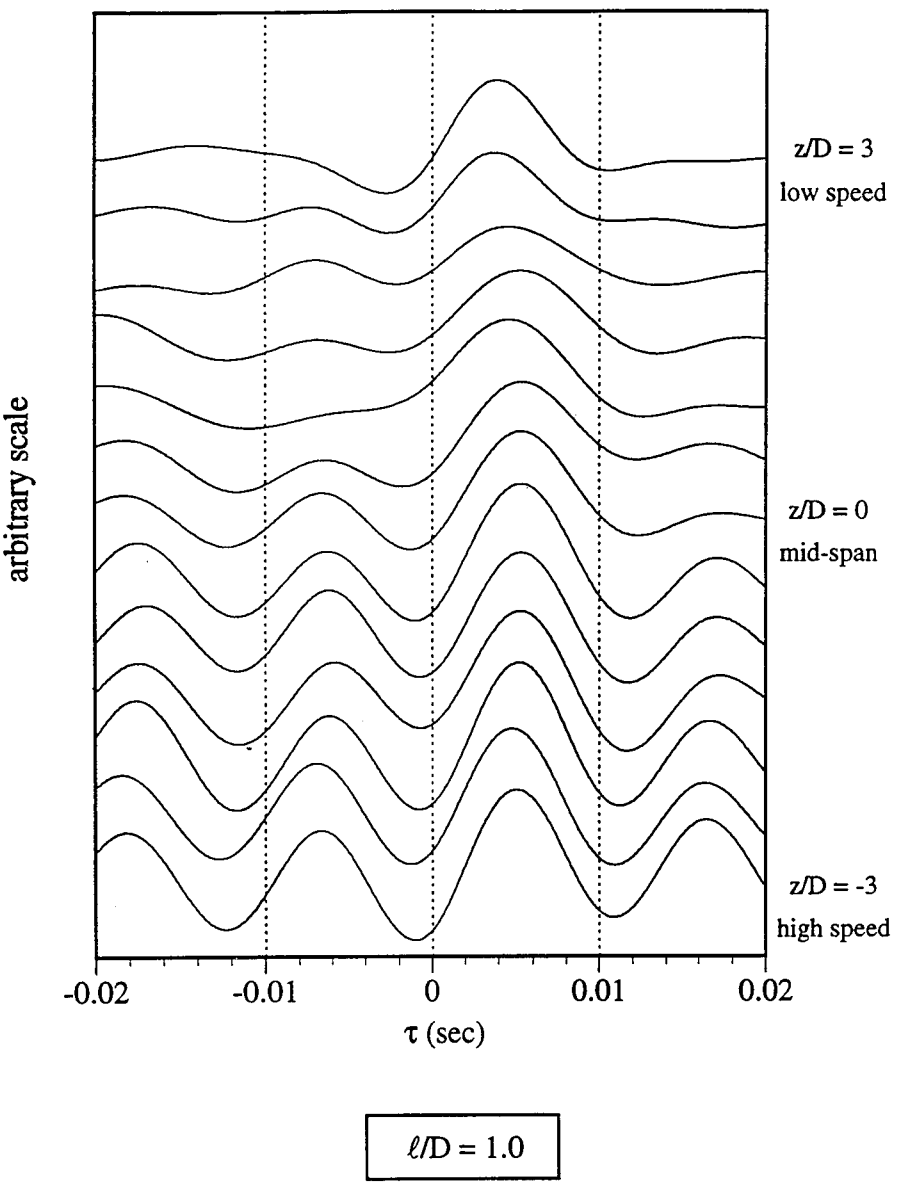

Figure 4.19. Cross-correlations for straight circular cylinder in shear flow.

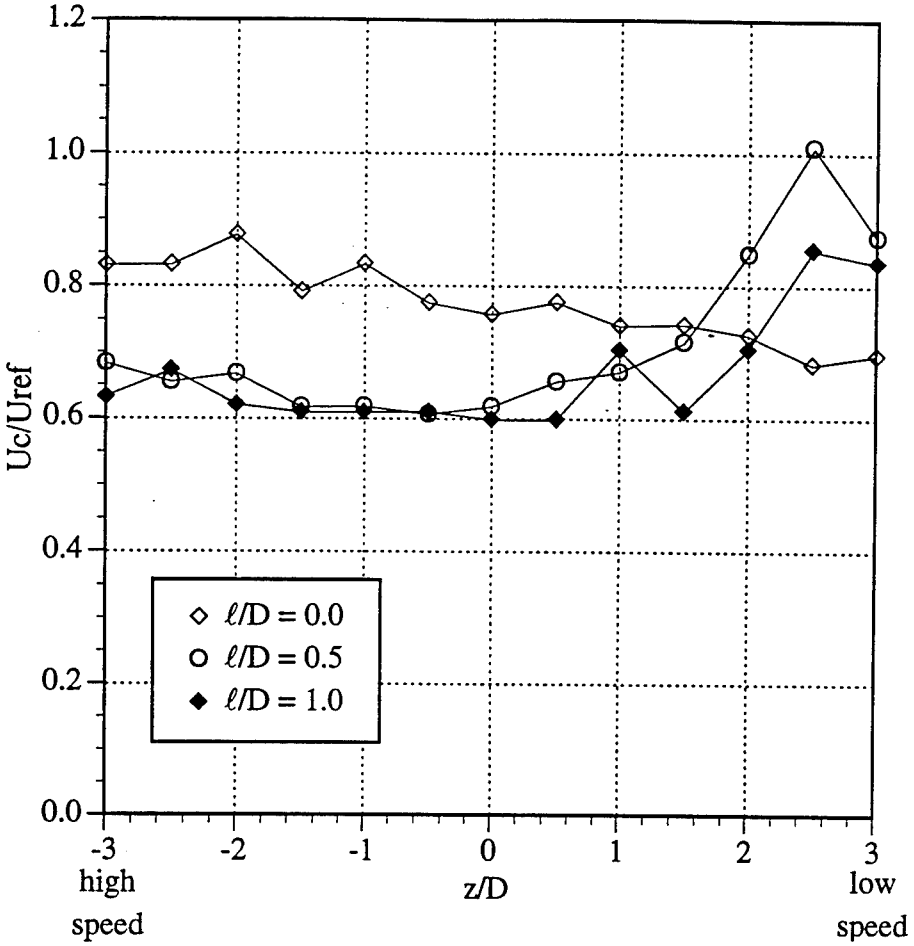

Figure 4.20. Vortex convection velocity versus span for straight circular cylinder in shear flow. Uref = 36 ft/s

CHAPTER 5. RESULTS FOR A TAPERED CYLINDER IN UNIFORM AND SHEAR FLOW

Results of experiments conducted on the tapered cylinder models in uniform and shear flow are presented below. For the tapered cylinder in shear flow experiments, the models were oriented with their large diameter end corresponding to the high velocity side of the shear. The power spectrum results were based on 25 ensembles of 1024 samples acquired at a sample rate of 200 Hz for a total sample time of 128 seconds.

5.1 Power spectra

The spanwise variation in power spectra for a tapered cylinder in uniform flow is compared to that for a straight cylinder in shear flow in Figure 5.1. The results indicate a similarity between the two flows by the appearance of three spanwise cells of constant shedding frequency. The tapered cylinder case shows cells with frequencies of 49, 60, and 68 Hz and the straight cylinder case, cells of frequencies 38, 46, and 51 Hz. The higher frequency cells correspond to the high velocity side of the shear for the straight cylinder and the small diameter end of the cylinder for the tapered case. The spanwise cells indicated in the tapered cylinder results have been observed in previous investigations, Gaster [1971a] and Papangelou [1992], at Reynolds number based on local diameter of 80 - 200 and Gaster [1971b] for local Reynolds number up to 60,000.

Power spectra results for two different tapered cylinders, dD/dz = 0.031 and 0.042, in shear flow, $\beta = 0.03$ are compared. The dD/dz = 0.031 taper ratio was selected so that when positioned in the shear flow the expected shedding frequency based on a local Strouhal number of 0.20 would be constant. That relationship can be described by U/D =

constant across the span. The results shown in Figure 5.2 indicate that when the taper ratio was matched to the shear profile the shedding frequency maintained a constant value across the span. The magnitude and width of the primary peak in the spectra was also consistent across the span. The case of the higher taper ratio cylinder, dD/dz = 0.042 indicated a shift in the shedding frequency across the span beyond the constant condition to an arrangement of four constant frequency cells, 56, 60, 64, and 68 Hz with the highest frequency cell located at the small diameter, low velocity side of the span.

5.2 Wake parameters

The spanwise variation of near wake parameters calculated from the data presented in Appendix A for a tapered cylinder, dD/dz = 0.031 in uniform and shear flow is shown in Figures 5.3 and 5.4. The results for a straight cylinder in uniform and shear flow are included for comparison purposes. All the wake parameters are referenced to the local conditions namely, the local diameter for the formation length and wake width, the local mean velocity for the Strouhal number and shear layer velocity, and the local dynamic pressure for the base pressure coefficient. In Figure 5.3 (a) opposite trends in the spanwise variation of formation region length between the tapered cylinder in uniform flow and the tapered cylinder in shear flow are observed. For the uniform flow case the formation length increased across the span from ℓ_f/D = 1.1 to 1.4 with decreasing diameter. For the shear flow case, the formation length decreased toward the small diameter, low velocity side of the span from ℓ_f/D = 1.2 to 0.6. The trend for the taper-shear configuration was similar to that of the straight cylinder in shear flow configuration. Wake width results, Figure 5.3 (b), are similar for the taper-uniform and taper-shear configurations which show a decrease in the wake width with decreasing diameter and shear velocity respectively. The results are similar to those for the straight cylinder in shear flow configuration which also indicated a decrease in wake width from the high to low velocity side of the span.

Spanwise variation in shear layer velocity for the tapered cylinder configurations are shown in Figure 5.4 (a). The results indicate a relatively uniform shear layer velocity across the span for the taper-uniform configuration. The taper-shear results indicate a slight increase in U_s/U across the span toward the low velocity, small diameter side. Although the spanwise frequency variation between the taper-uniform and the straight-shear configurations were similar, see Figure 5.1, the straight-shear case indicated a much larger variation in U_s/U. Figure 5.4 (b) shows that the variation in base pressure parameter correlated well with the shear velocity trends in Figure 5.4 (a). The shear flow configurations show an increase in base suction from the high to low velocity positions while the uniform flow configurations remained relatively constant across the span.

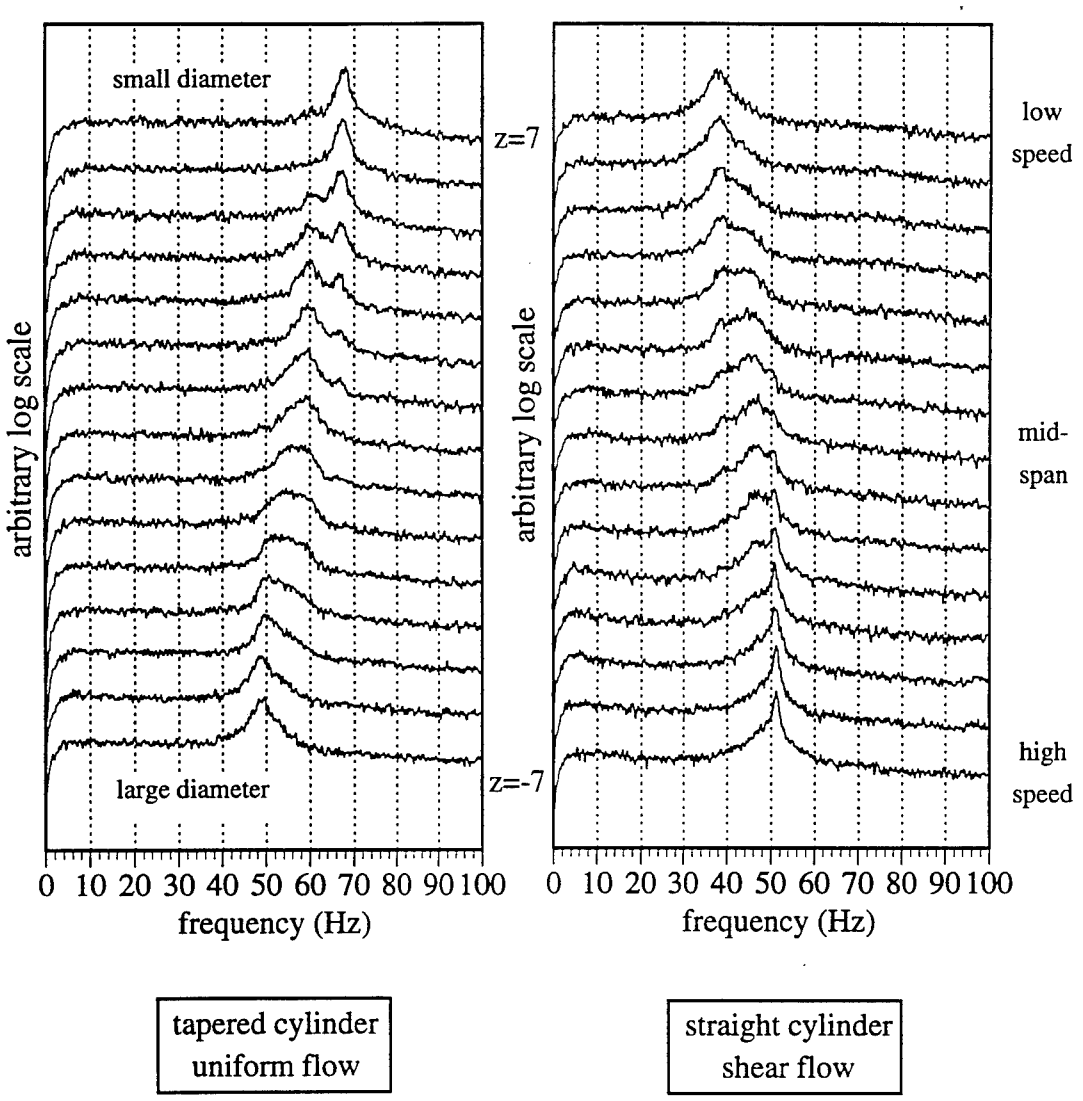

Figure 5.1. Power spectra for tapered circular cylinder in uniform flow and straight cylinder in shear flow. U and Uref = 36 ft/s, z in inches.

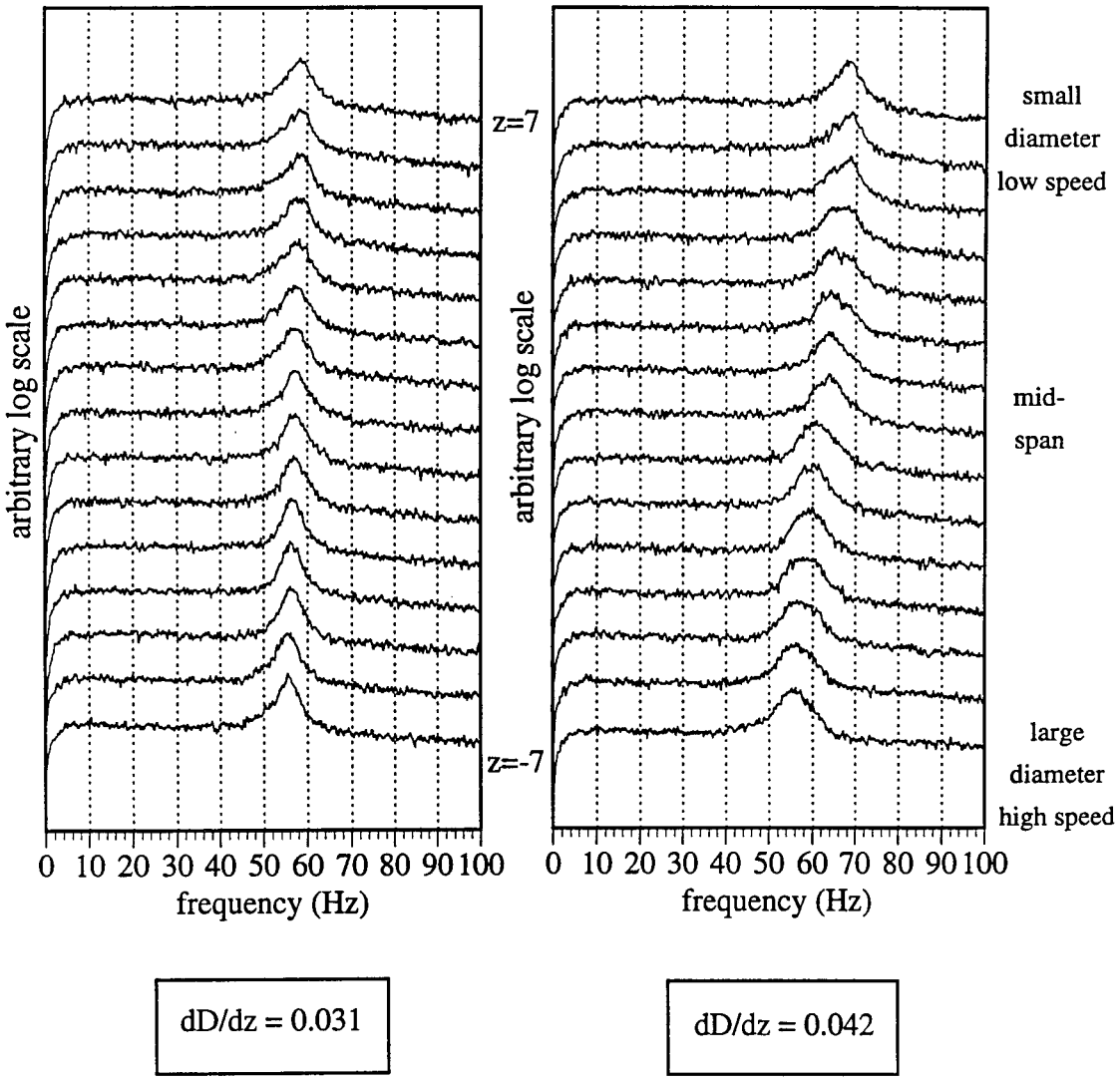

Figure 5.2. Power spectra for tapered circular cylinder in shear flow.
Uref = 36 ft/s, z in inches.

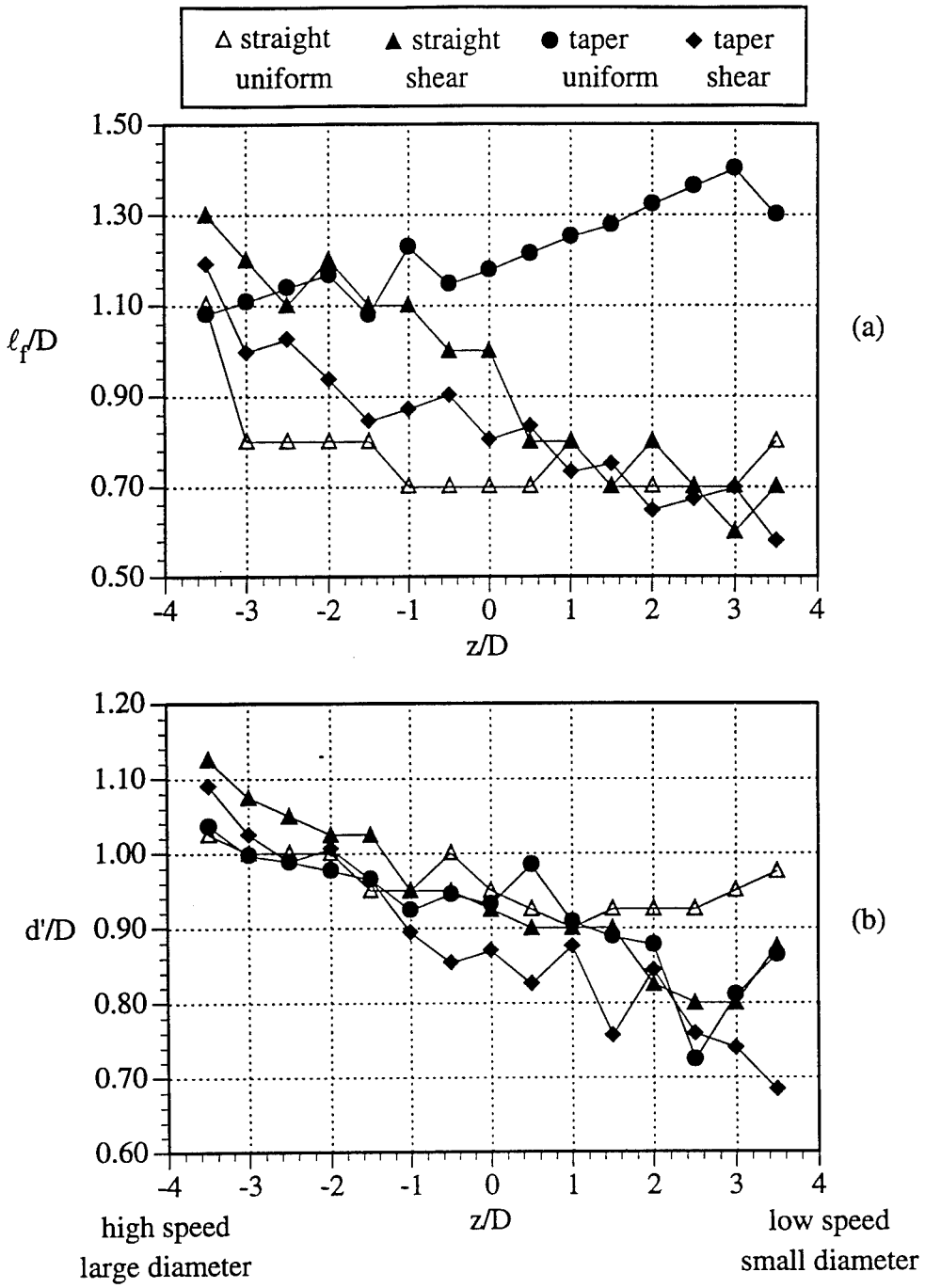

Figure 5.3. Length of the formation region and wake width versus span for straight and tapered cylinder in uniform and shear flow, D= 2.0 inches.

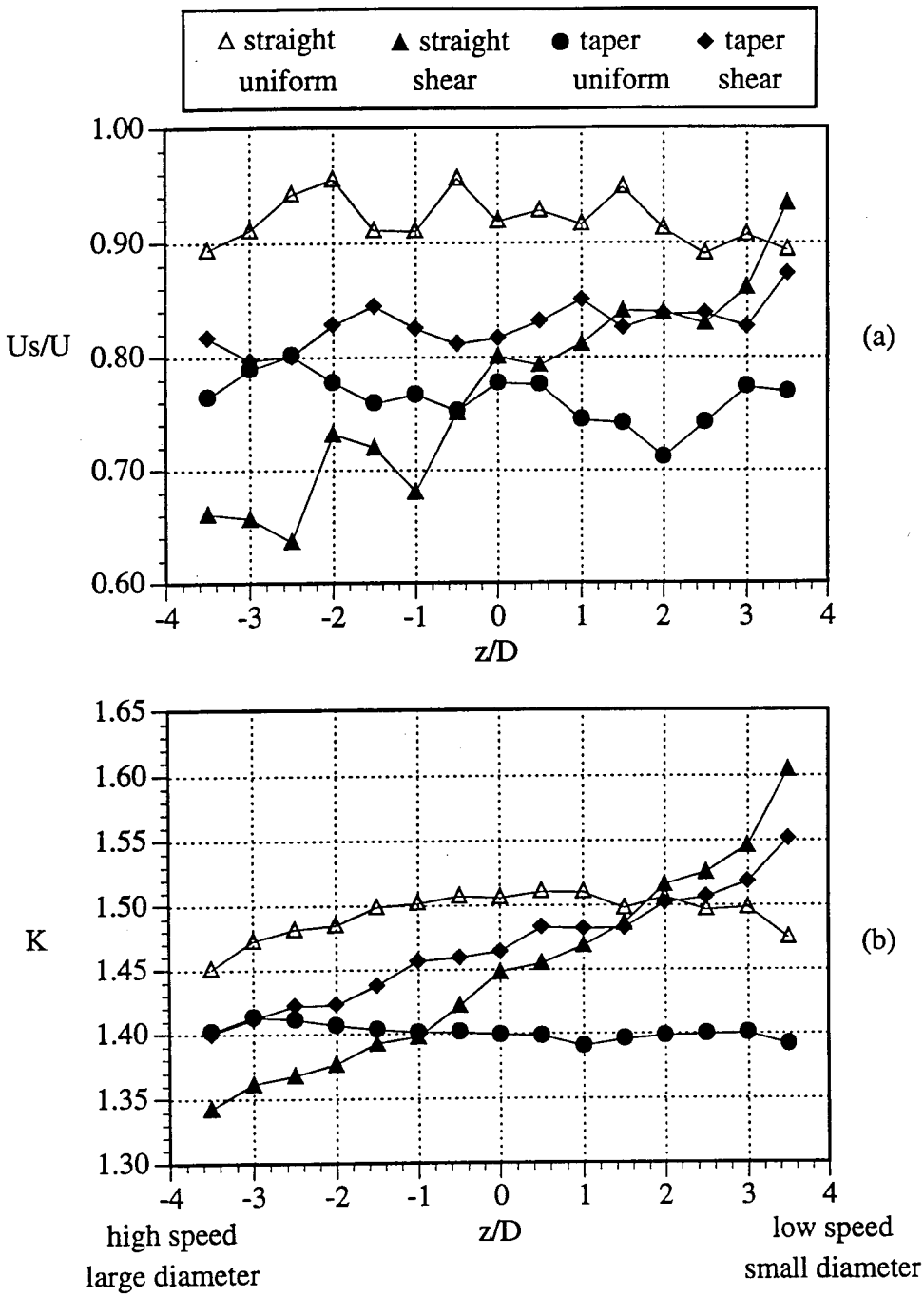

Figure 5.4. Shear layer velocity and base pressure parameter versus span for straight and tapered cylinder in uniform and shear flow, D = 2.0 inches.

CHAPTER 6. RESULTS FOR THE UNIVERSAL STROUHAL NUMBER INVESTIGATION

The results presented in Figures 6.1 - 6.24 were used to evaluate the concept of a universal Strouhal parameter. Such a parameter would predict the shedding frequency of a bluff body from various measured quantities in the near wake. The data used to generate the various parameters are presented in Appendix A and were acquired at flow velocities of $U = U_{ref} = 11$ m/s. Four basic cylinder-flow arrangements were considered in the study,

1) Uniform flow	Straight cylinder with splitter plates
2) Uniform flow	Tapered cylinder
3) Shear flow	Straight cylinder with splitter plates
4) Shear flow	Tapered cylinder

The splitter plates considered were $\ell/D = 0.0$ (no plate), 0.25, 0.5, 1.0, and sinuous $\ell/D = 1.0$, $\lambda/D = 3$, $a/D = 0.5$. For each configuration, data was acquired at 15 equally spaced spanwise positions over the 16 inches between the endplates. The experiments produced 180 sets of wake parameters with each set representing a particular configuration and spanwise position. The wake parameters considered in the present study are presented in Table 6.1. All parameters were based on local diameter and velocity measurements and corrected for tunnel blockage (see Appendix B).

parameter	dimensional	non-dimensional
shedding frequency	f_s	$St = f_sD/U$
formation region length	ℓ_f	ℓ_f/D
wake width	d'	d'/D
shear layer velocity	U_s	U_s/U
base pressure parameter	-	$K = sqrt(1-C_{pb})$

Table 6.1. Near wake parameters considered in evaluation of universal parameter.

A summary of the results for each configuration and all parameters with the exception of shear layer velocity which was omitted for clarity are presented in Figures 6.1 - 6.12. The shear layer velocity results are presented in subsequent figures. In addition to the parameters the power spectrum for each spanwise location is presented. For the nominally 2-dimensional cases, Figures 6.1 - 6.5 (including sinuous splitter plate case) the results indicate the expected spanwise uniformity in the parameters. Figures 6.6 - 6.12 clearly reflect the 3-dimensionality imposed by the shear flow and cylinder taper on the wake parameters and power spectra.

Comparisons between the various configurations for each parameter are presented for uniform flow in Figures 6.13 - 6.16 and shear flow in Figures 6.17 - 6.20. A linear least squares curve fit, represented by a dashed line, was used to clarify and compare spanwise trends in the parameters. The results indicate that the concept of using the average length of the sinuous splitter plate in comparisons with the straight splitter plate was supported by all the considered parameters. In general, the length of the formation region and wake width increased with increasing ℓ/D and the base pressure parameter and shear layer velocity decreased with increasing ℓ/D. The tapered cylinder results compared well to those of $\ell/D = 0.0$ configuration for all parameters. Table 6.2 provides a qualitative

summary of the influences that ℓ/D, and spanwise variations in mean velocity and cylinder diameter have on the wake parameters.

	increasing ℓ/D shear & unif.	increasing U shear	increasing Dia. uniform	increasing Dia. shear
ℓ_f/D	increases	increases	increases	decreases
d'/D	increases	increases	increases	decreases
K	decreases	decreases	decreases	no change
U_s/U	decreases	decreases	no change	no change

Table 6.2. Effect of ℓ/D and spanwise variations in mean velocity and cylinder diameter on wake parameters, from Figures 6.13 - 6.20.

Figures 6.21 - 6.23 compare the relationship between pairs of the wake parameters for all configurations. Figure 6.21 (a) indicates that an increase in formation length was generally accompanied by an increase in wake width. An exception occurred for the tapered cylinder in uniform flow configuration that demonstrated an opposite trend. Figure 6.21 (b) it is observed that an increase in base suction is accompanied by an increase in shear layer velocity. This trend supports the formulation of Roshko [1954] in which he equated the base pressure parameter to the shear layer velocity although, in the present investigation the magnitude of the shear layer velocity differed significantly from K. This discrepancy may be attributed to the difficulty encountered in defining an appropriate transverse location for the measurement of U_s. Despite that discrepancy the results indicate a strong correlation between the two parameters. The relationship between the shear layer velocity and wake width indicates that increasing wake width corresponded to a decrease in shear layer velocity as shown in Figure 6.22 (a). In Figure 6.22 (b) it is observed that shear layer velocity and formation length are strongly correlated and that an increase in formation length was accompanied by a decrease in shear layer velocity. Figure 6.23 (a)

shows that, with the exception of the tapered cylinder data, the wake width decreased with increasing base suction and in Figure 6.23 (b) an increase in base suction was accompanied by a decrease in formation length. The results from Figures 6.21 - 6.23 indicate consistent relationships between the wake parameters that are useful in determining the most suitable way of combining the parameters to construct a universal parameter.

The relationship the local Strouhal number to the various other wake parameters is shown in Figures 6.24 and 6.25. The results indicate a rather random distribution of the data that suggests that the shedding frequency is not directly related to the local length and velocity scales of the formation region. However, the local Strouhal number does remain relatively constant ($0.17 < St < 0.25$) for all the configurations.

In Figure 6.26 three non-dimensional shedding frequencies calculated for all of the configurations are investigated. The traditional Strouhal number that is based on the local diameter and velocity is presented in Figure 6.26 (a). The results show an average value of $St = 0.204$ and standard deviation of $\sigma = 0.012$. Figure 6.26 (a) also shows the parameter, St* calculated from the equation,

$$St^* = \frac{St}{K}\frac{D}{d'} \tag{6.1}$$

The resulting data scatter shows an improvement over the traditional Strouhal number with a mean of $St^* = 0.142$ and standard deviation of $\sigma = 0.011$. The results presented in Figure 6.24 (b) were based on the Roshko [1954] universal parameter,

$$St' = \frac{St}{K}\frac{d'}{D} \tag{6.2}$$

Although Roshko's parameter has proved useful in predicting near wake characteristics for a wide variety of bluff bodies, it produced a large variation when calculated from the data in the current study. The mean value of St' = 0.161 was consistent with Roshko's results, but the standard deviation of $\sigma = 0.028$ was more than twice that encountered using the traditional Strouhal number or St*. The relatively large variation in St_R was due primarily to the taper and shear or, 3-dimensional configurations. The problem can be clearly understood by consideration of Figure 6.23 (a) which presents the relationship between wake width and base pressure parameter. Since wake width decreased with increasing base suction, and both over similar ranges, the ratio (d'/D)/K diverged while the product, (d'/D)*K, which was used in the calculation of St*, produced a fairly constant result.

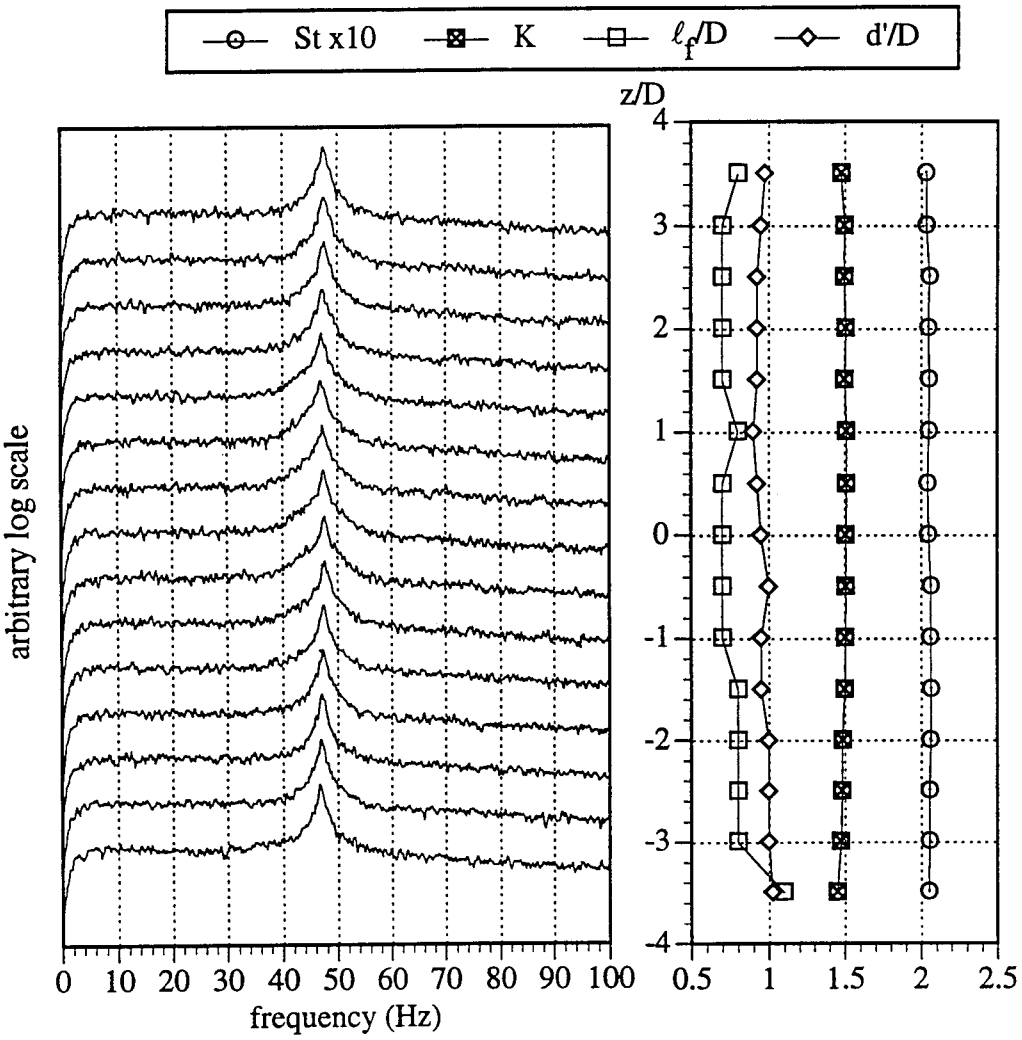

Figure 6.1. Power spectra and wake parameters for straight circular cylinder in uniform flow. Re=30,000, AR=8

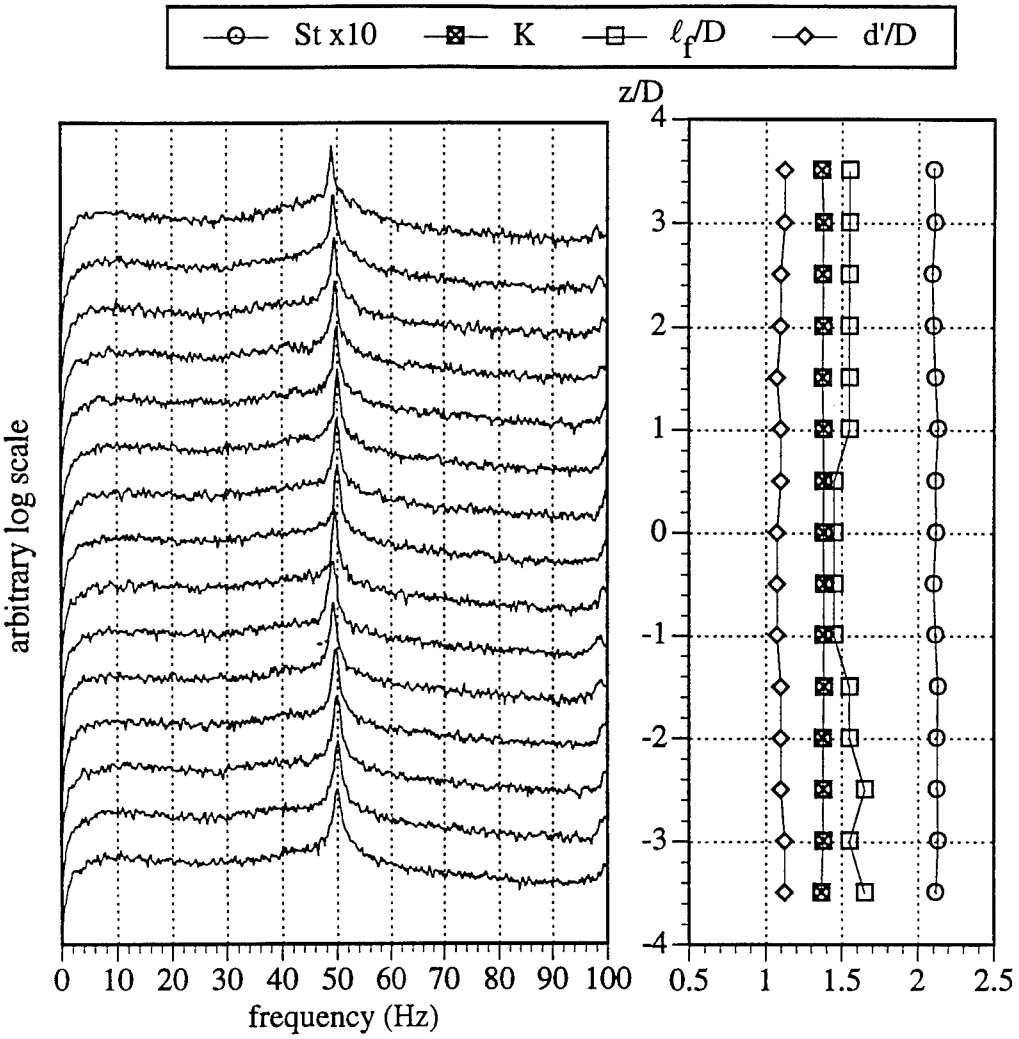

Figure 6.2. Power spectra and wake parameters for straight circular cylinder with splitter plate, ℓ/D = 0.25 in uniform flow. Re=30,000, AR=8

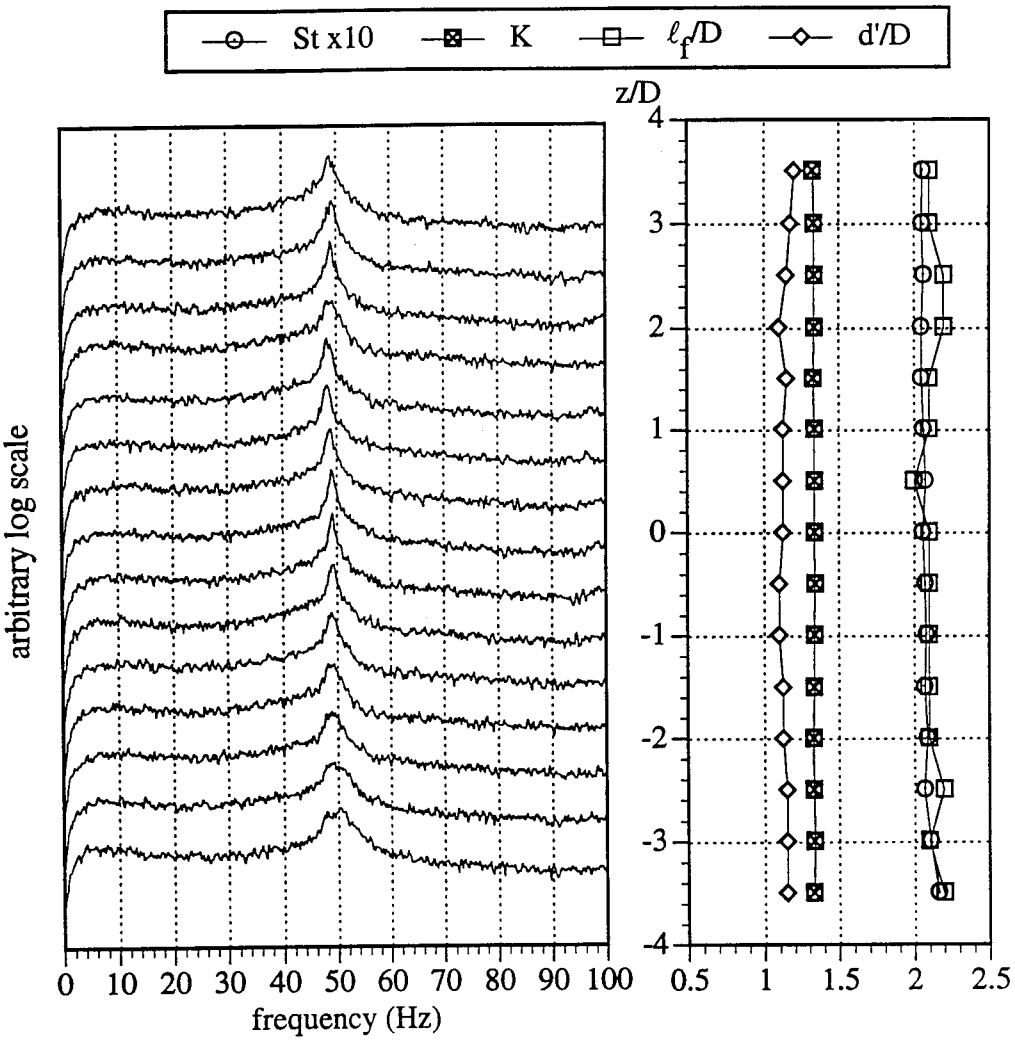

Figure 6.3. Power spectra and wake parameters for straight circular cylinder with splitter plate, ℓ/D = 0.50 in uniform flow. Re=30,000, AR=8

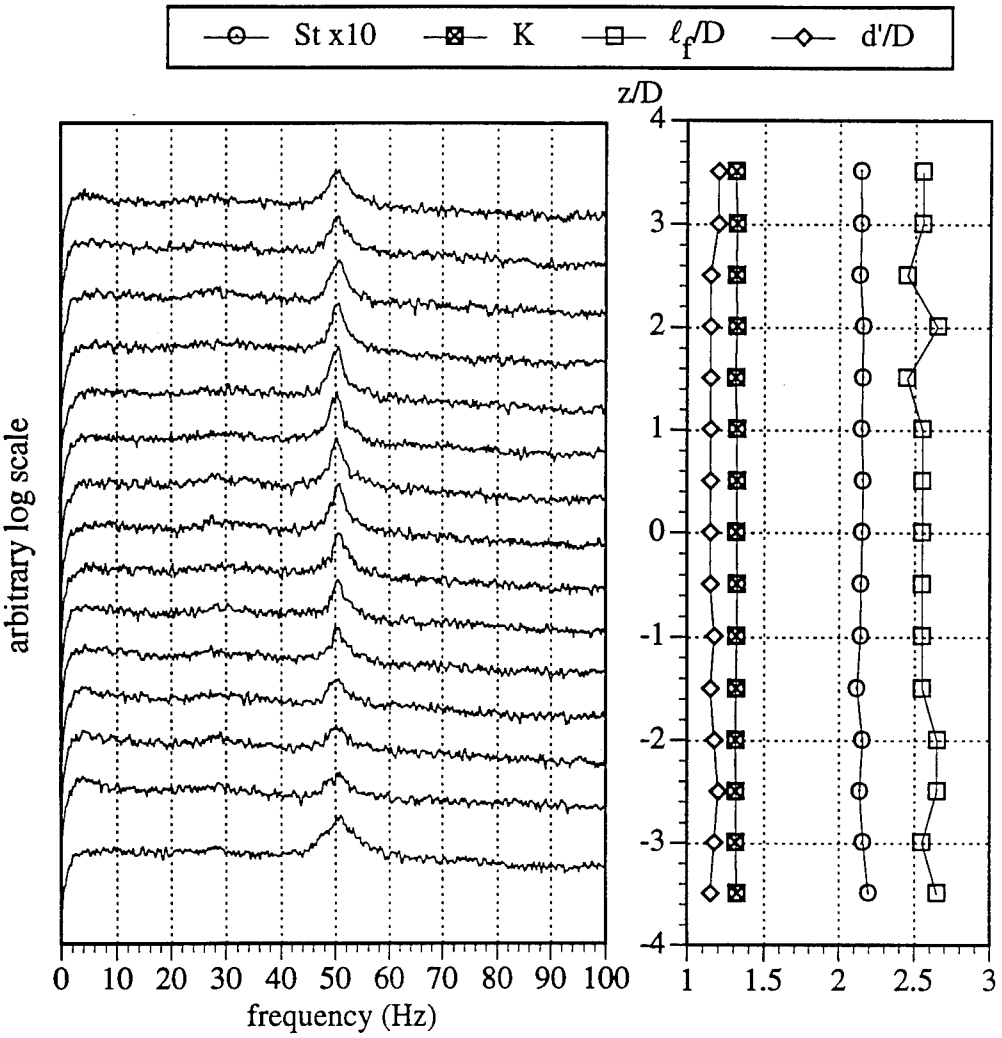

Figure 6.4. Power spectra and wake parameters for straight circular cylinder with splitter plate, ℓ/D = 1.00 in uniform flow. Re=30,000, AR=8

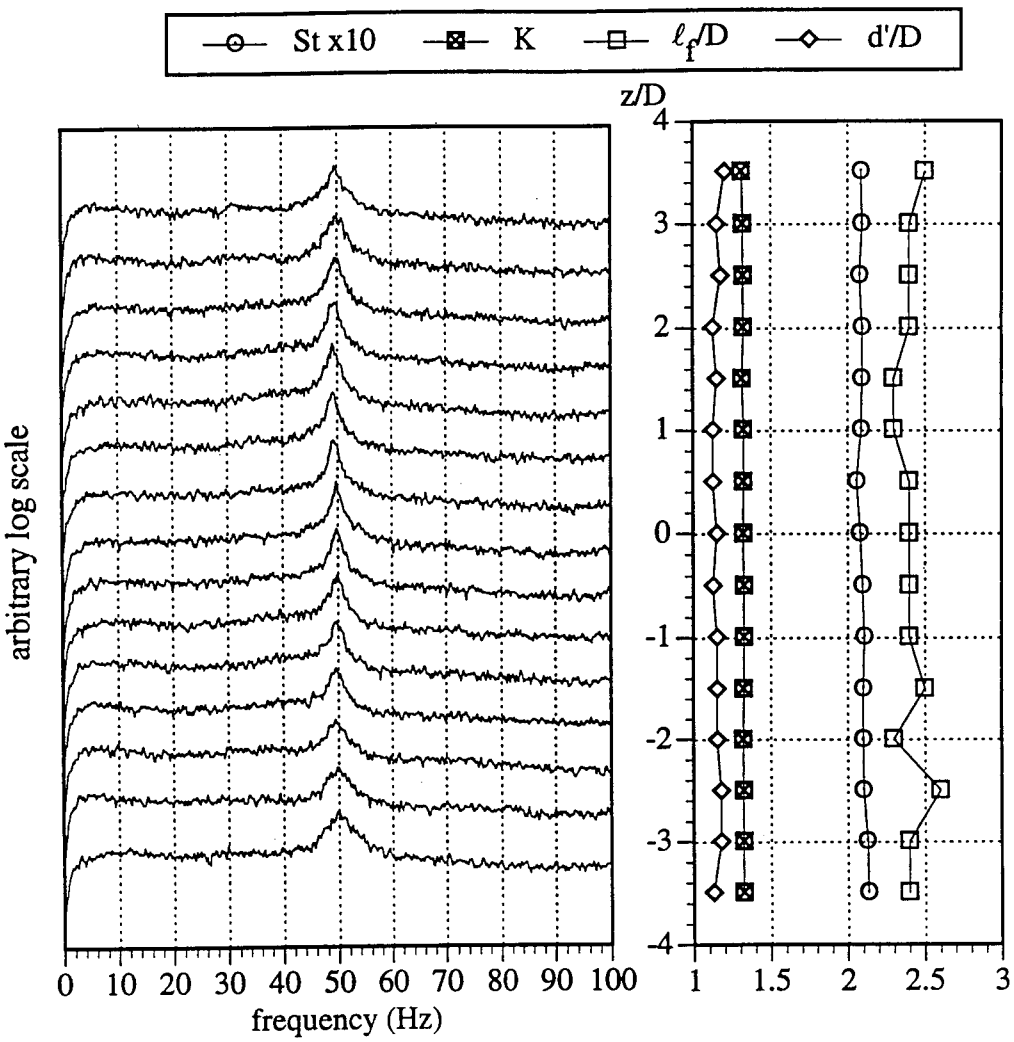

Figure 6.5. Power spectra and wake parameters for straight circular cylinder with sinuous trailing edge splitter plate, ℓ/D = 1.00, λ/D = 3, in uniform flow. Re=30,000, AR=8

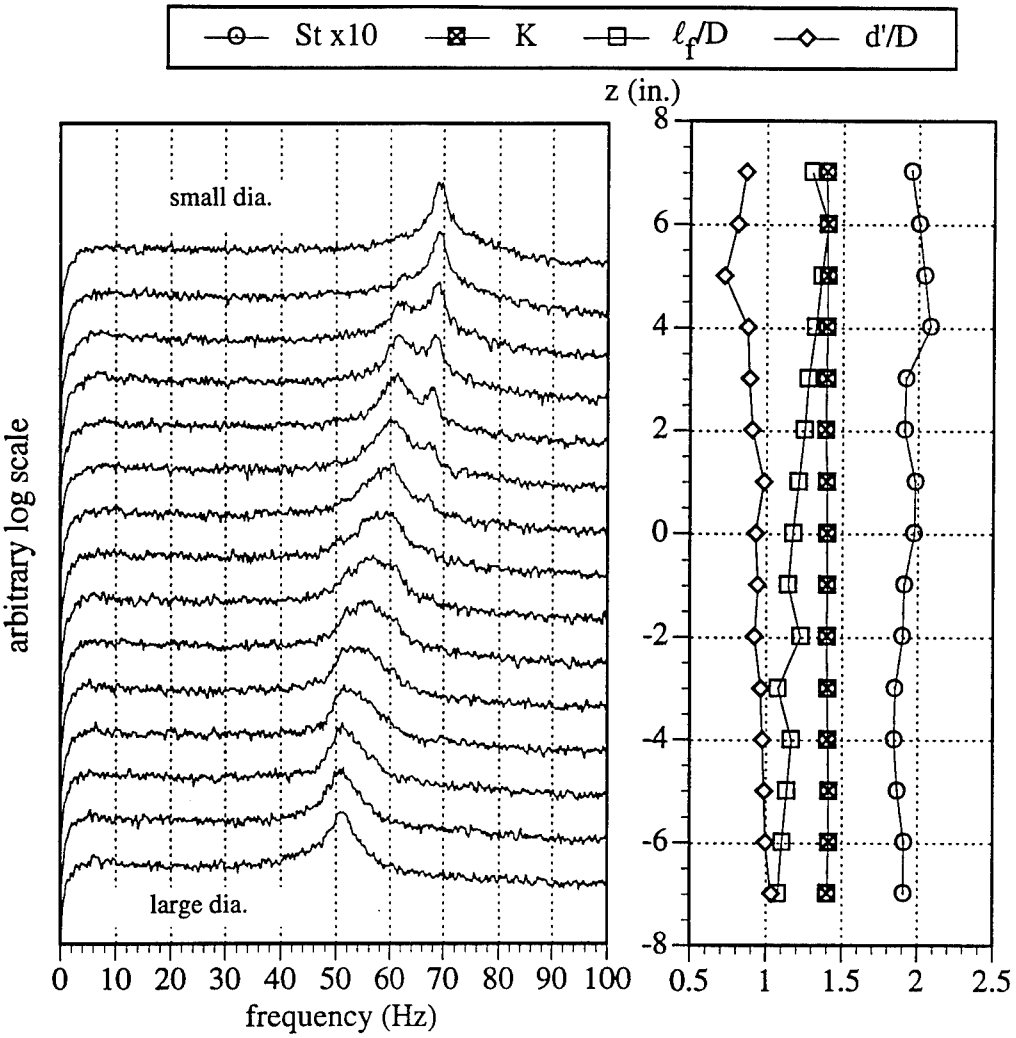

Figure 6.6. Power spectra and wake parameters for tapered circular cylinder in uniform flow. Re=21,000 - 25,000.

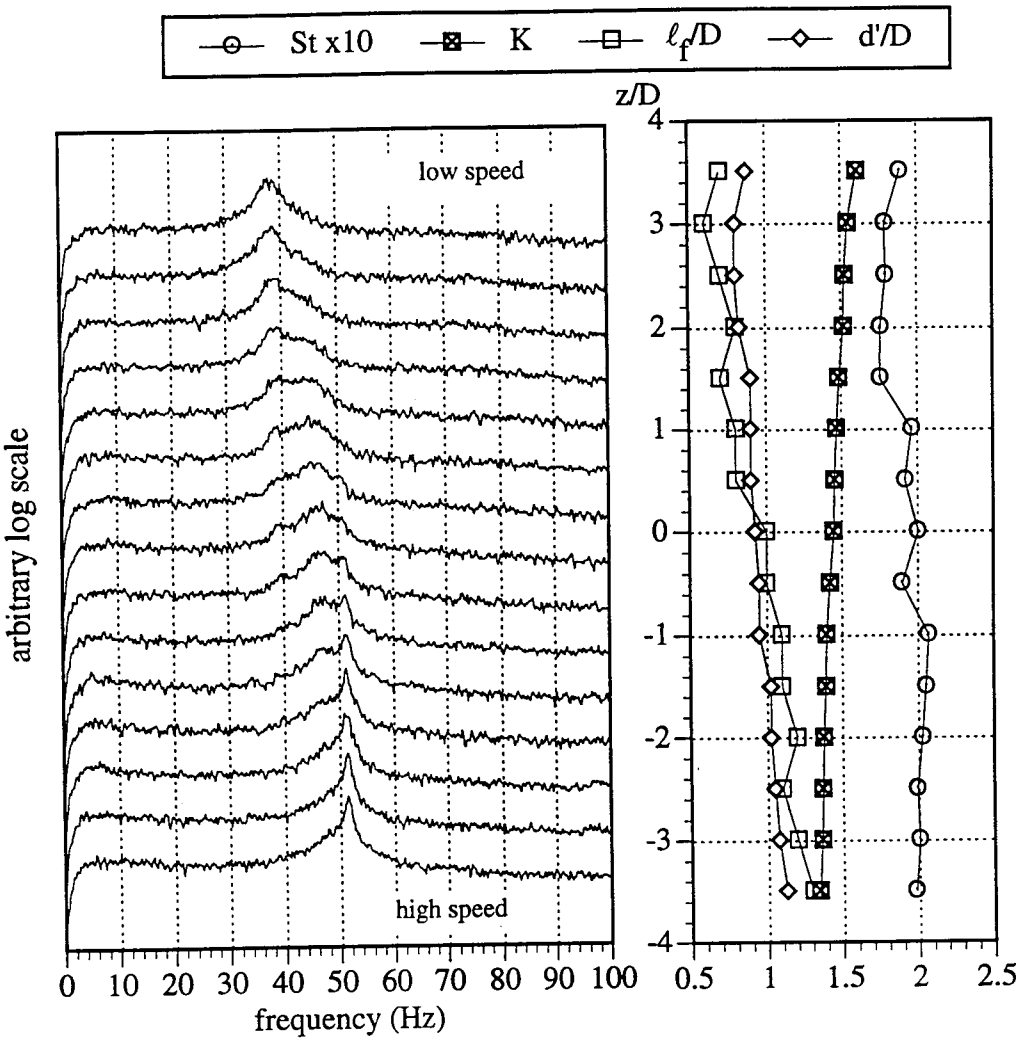

Figure 6.7. Power spectra and wake parameters for straight circular cylinder in shear flow. Re=28,000 - 36,000

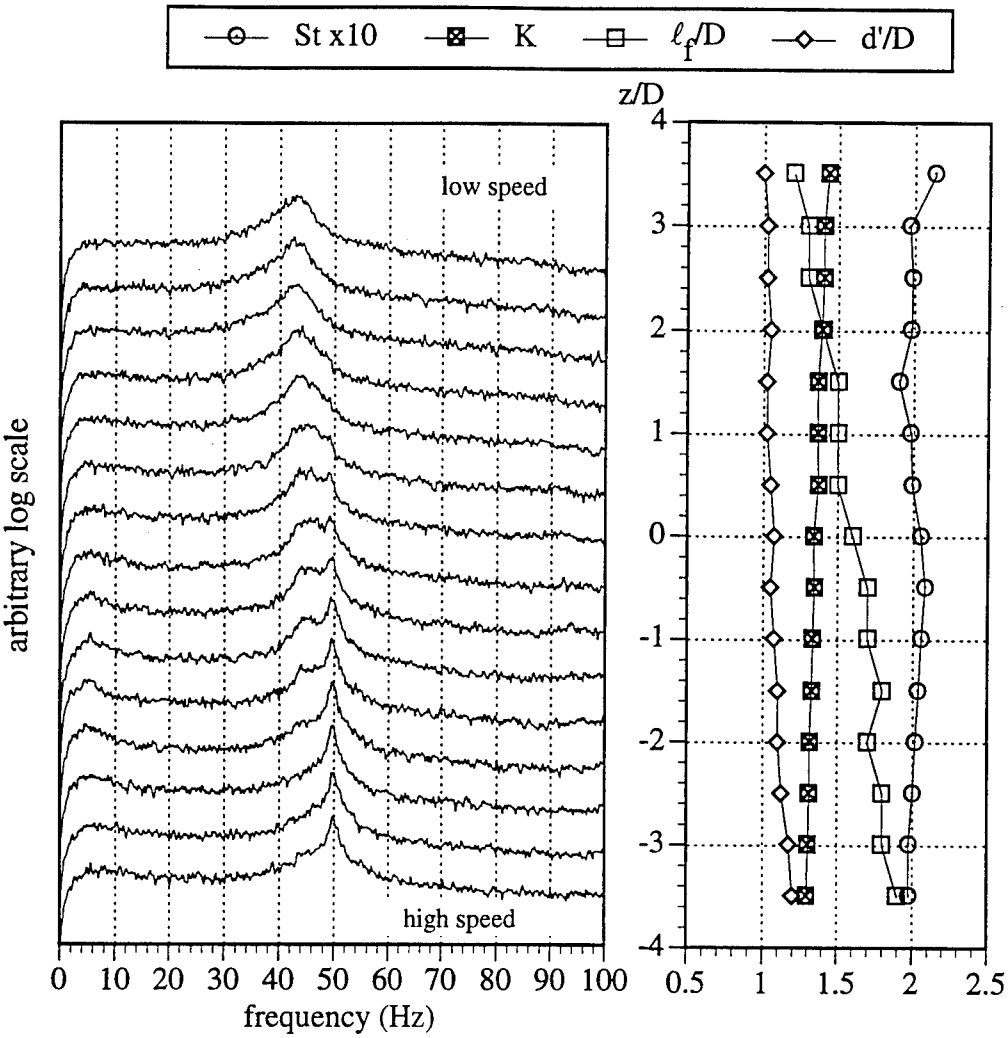

Figure 6.8. Power spectra and wake parameters for straight circular cylinder in shear flow with splitter plate, ℓ/D = 0.25. Re=28,000 - 36,000

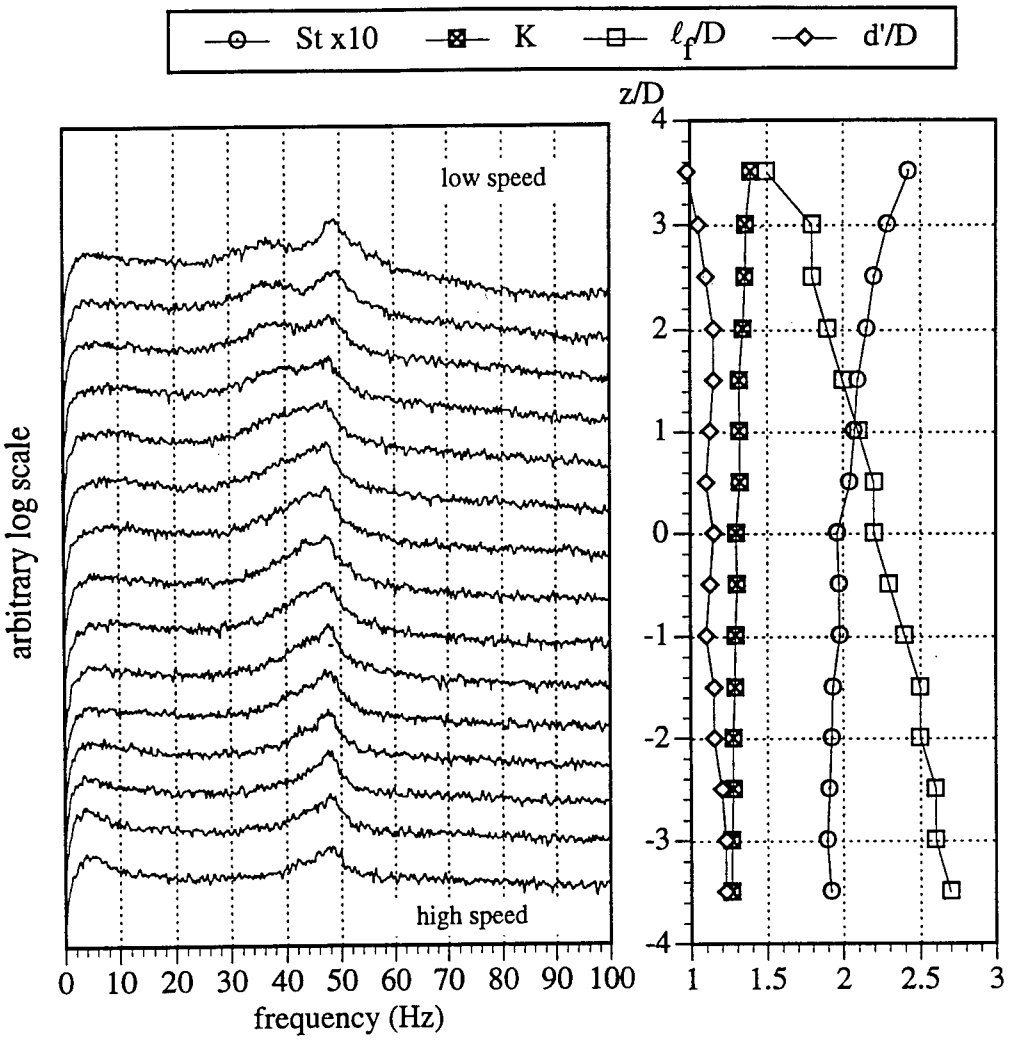

Figure 6.9. Power spectra and wake parameters for straight circular cylinder in shear flow with splitter plate, ℓ/D = 0.50. Re=28,000 - 36,000

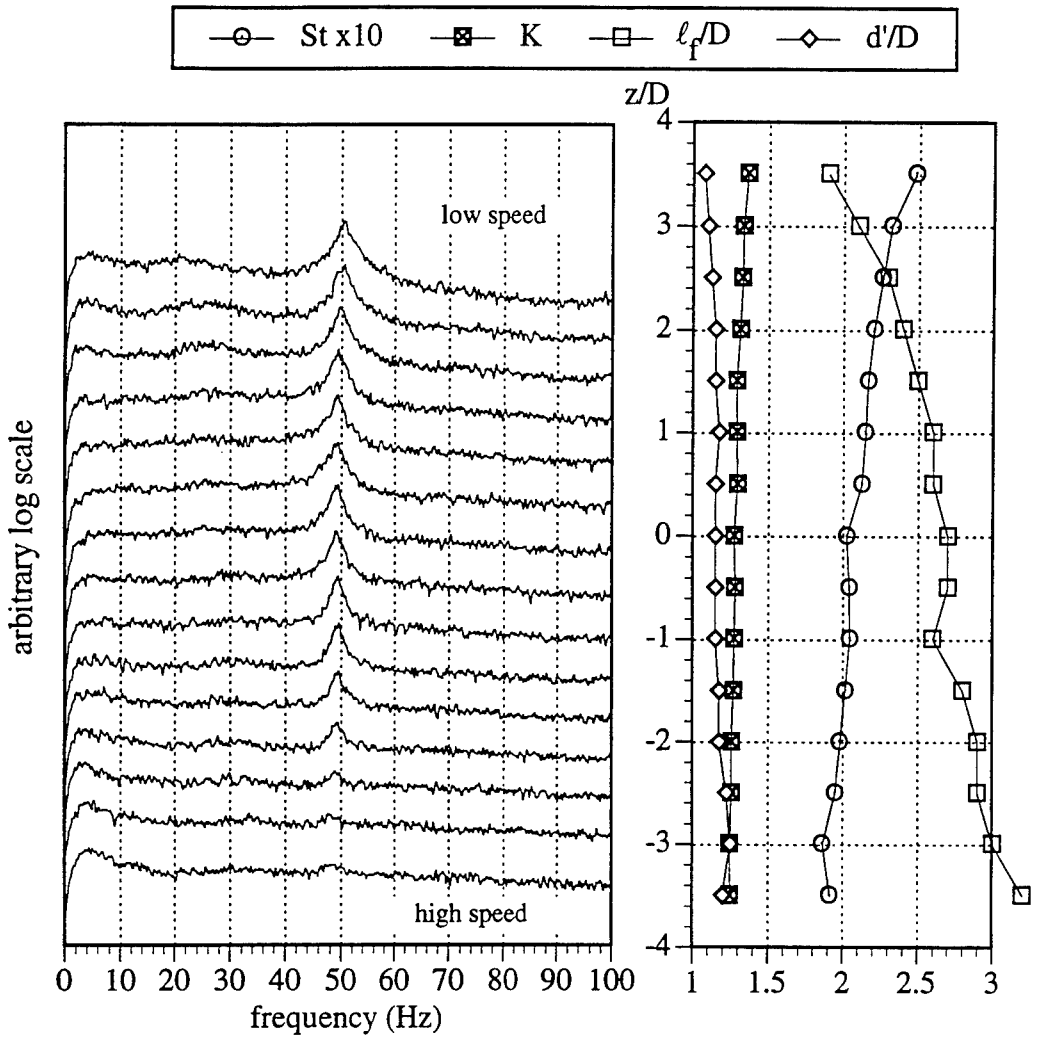

Figure 6.10. Power spectra and wake parameters for straight circular cylinder in shear flow with splitter plate, ℓ/D = 1.00. Re=28,000 - 36,000

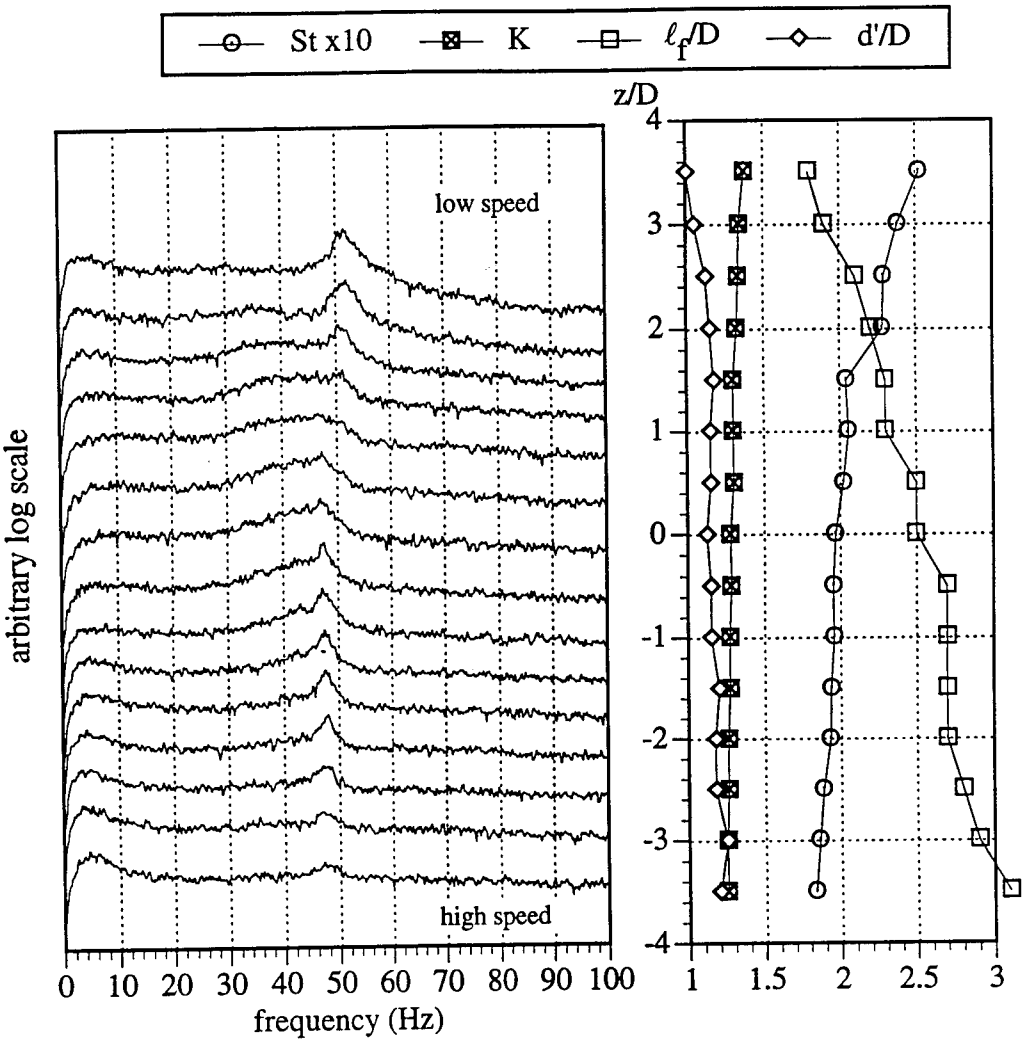

Figure 6.11. Power spectra and wake parameters for straight circular cylinder with sinuous trailing edge splitter plate, ℓ/D = 1.00, λ/D = 3, in shear flow. Re = 28,000 - 36,000, AR=8

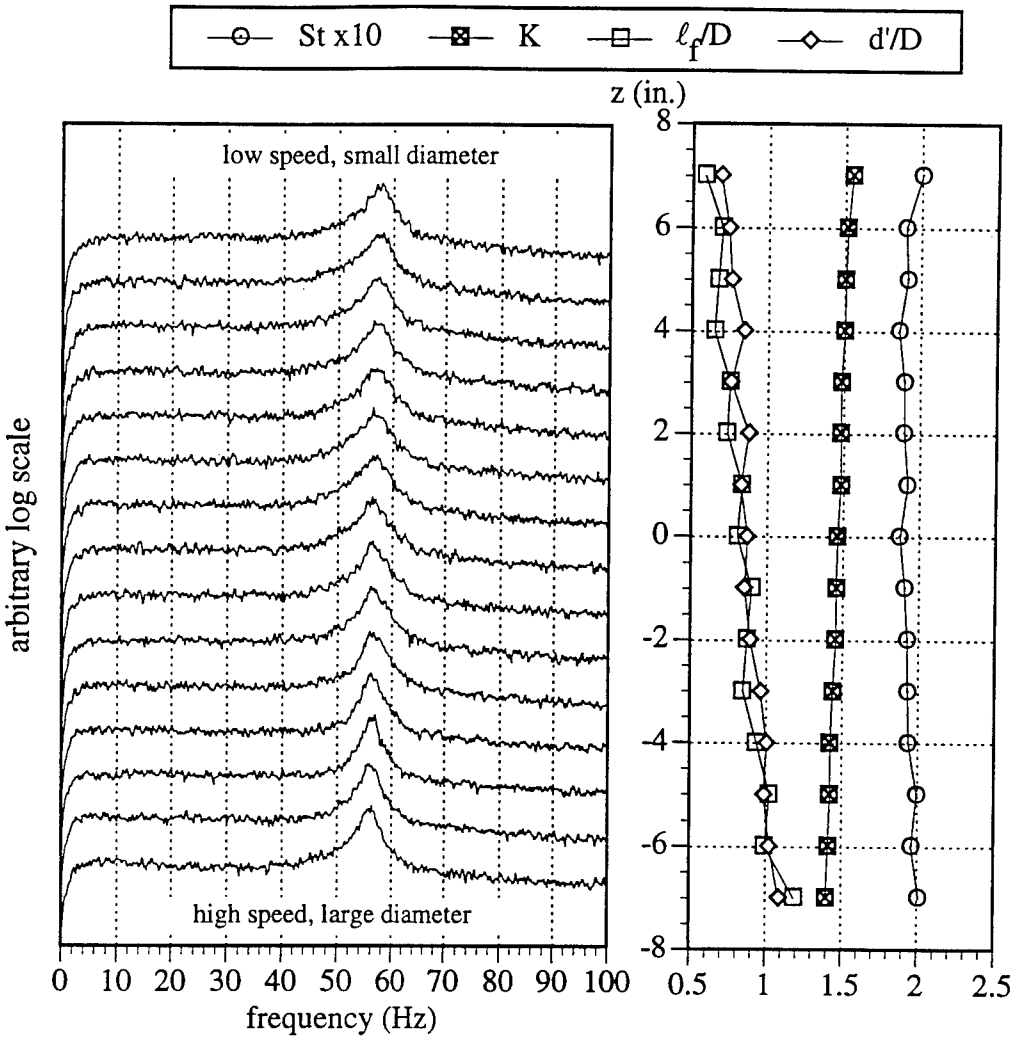

Figure 6.12. Power spectra and wake parameters for tapered circular cylinder in shear flow. Re=19,000 - 33,000

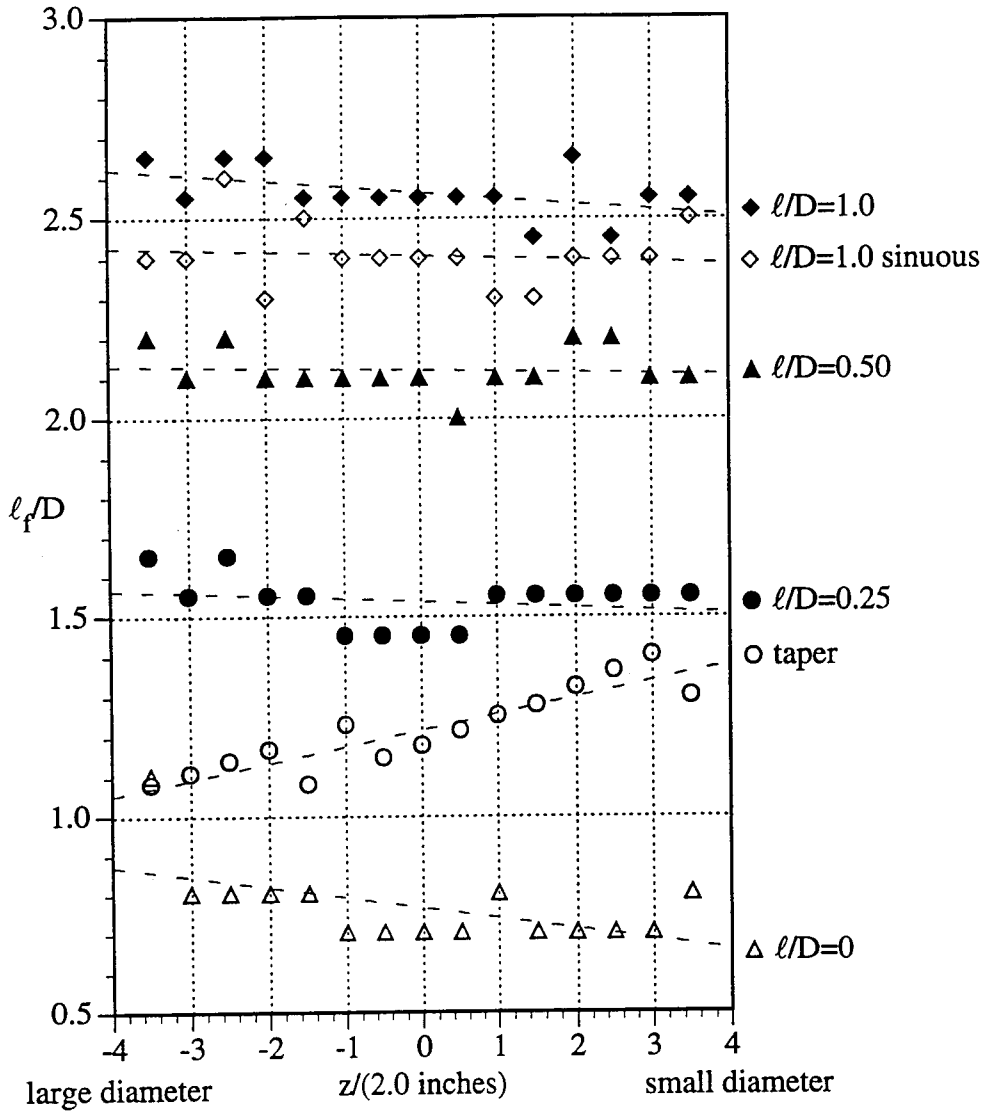

Figure 6.13. Length of the formation region length versus span for cylinder in uniform flow.

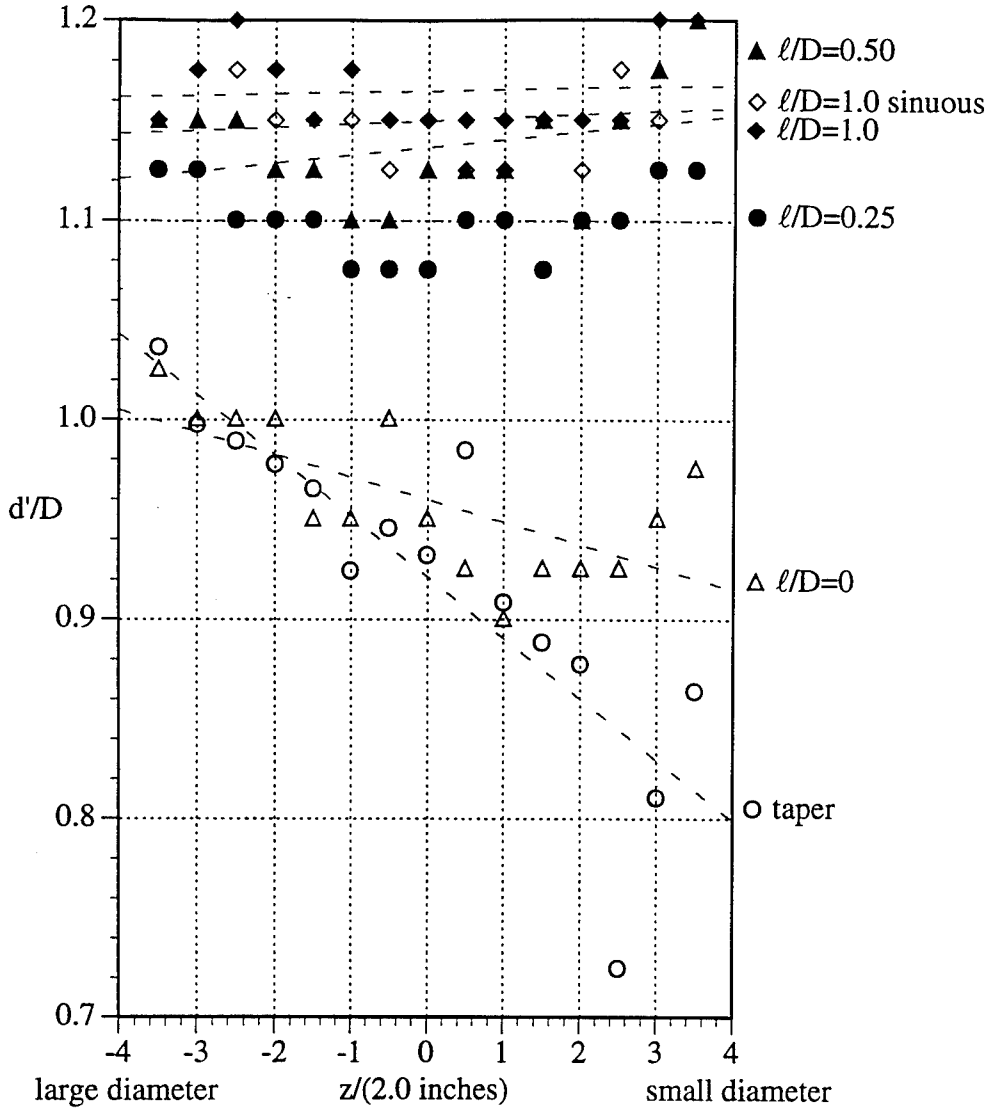

Figure 6.14. Wake width versus span for cylinder in uniform flow.

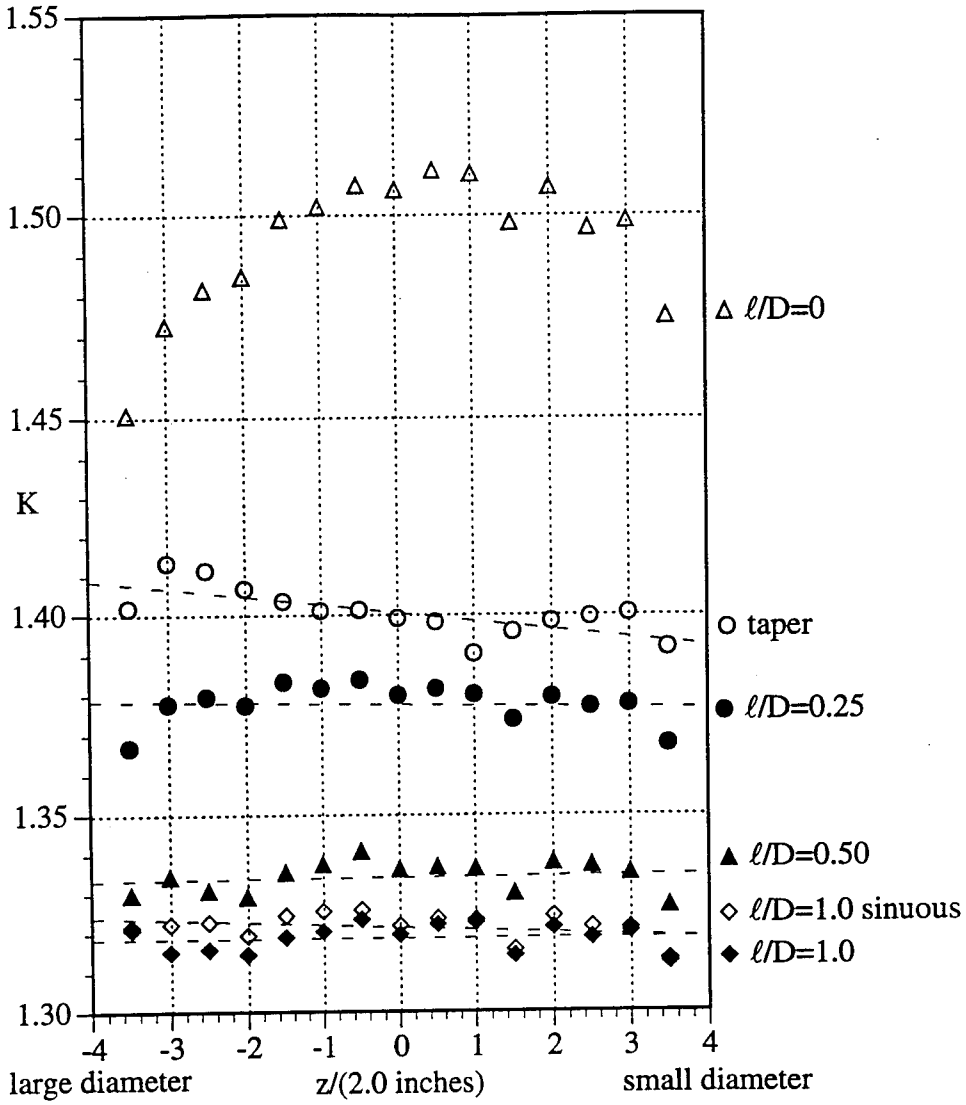

Figure 6.15. Base pressure parameter versus span for cylinder in uniform flow.

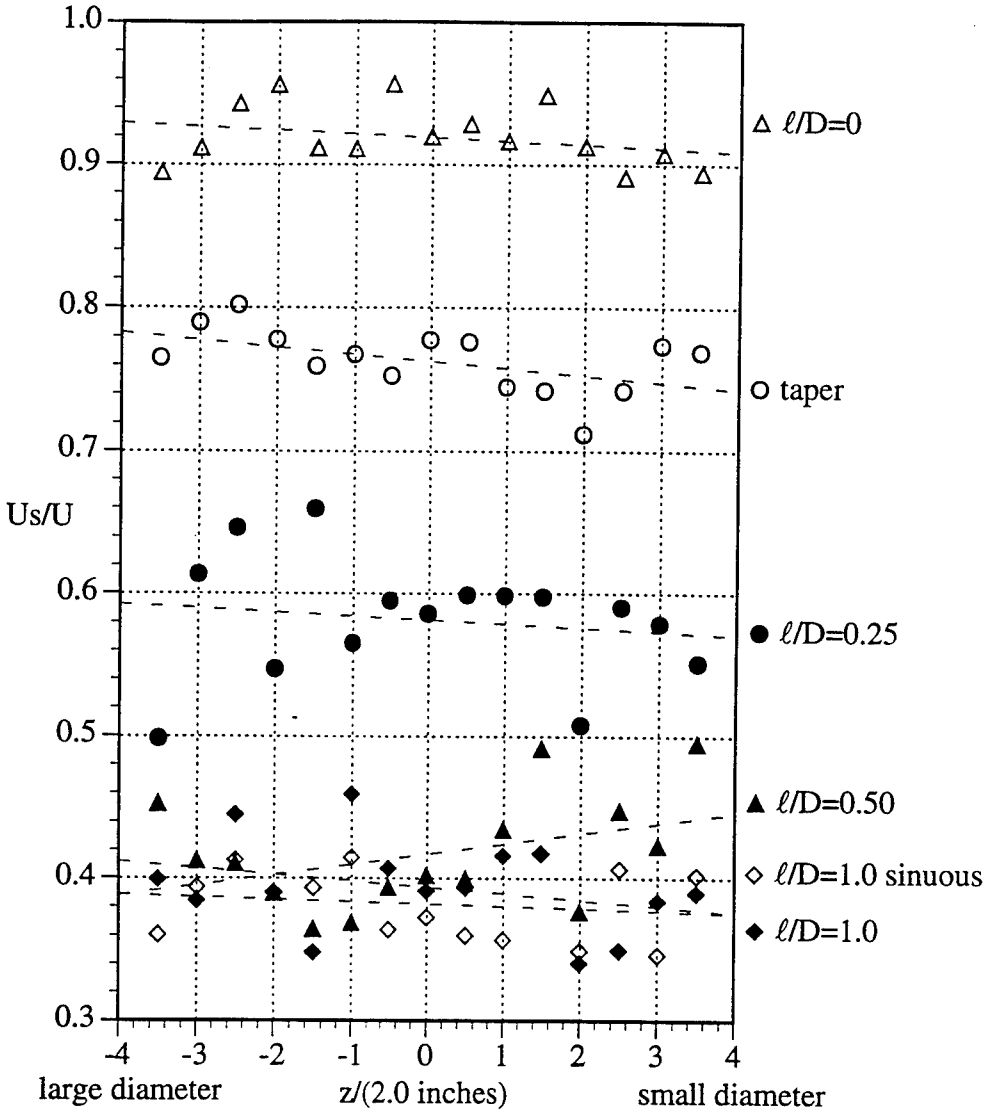

Figure 6.16. Shear layer velocity versus span for cylinder in uniform flow.

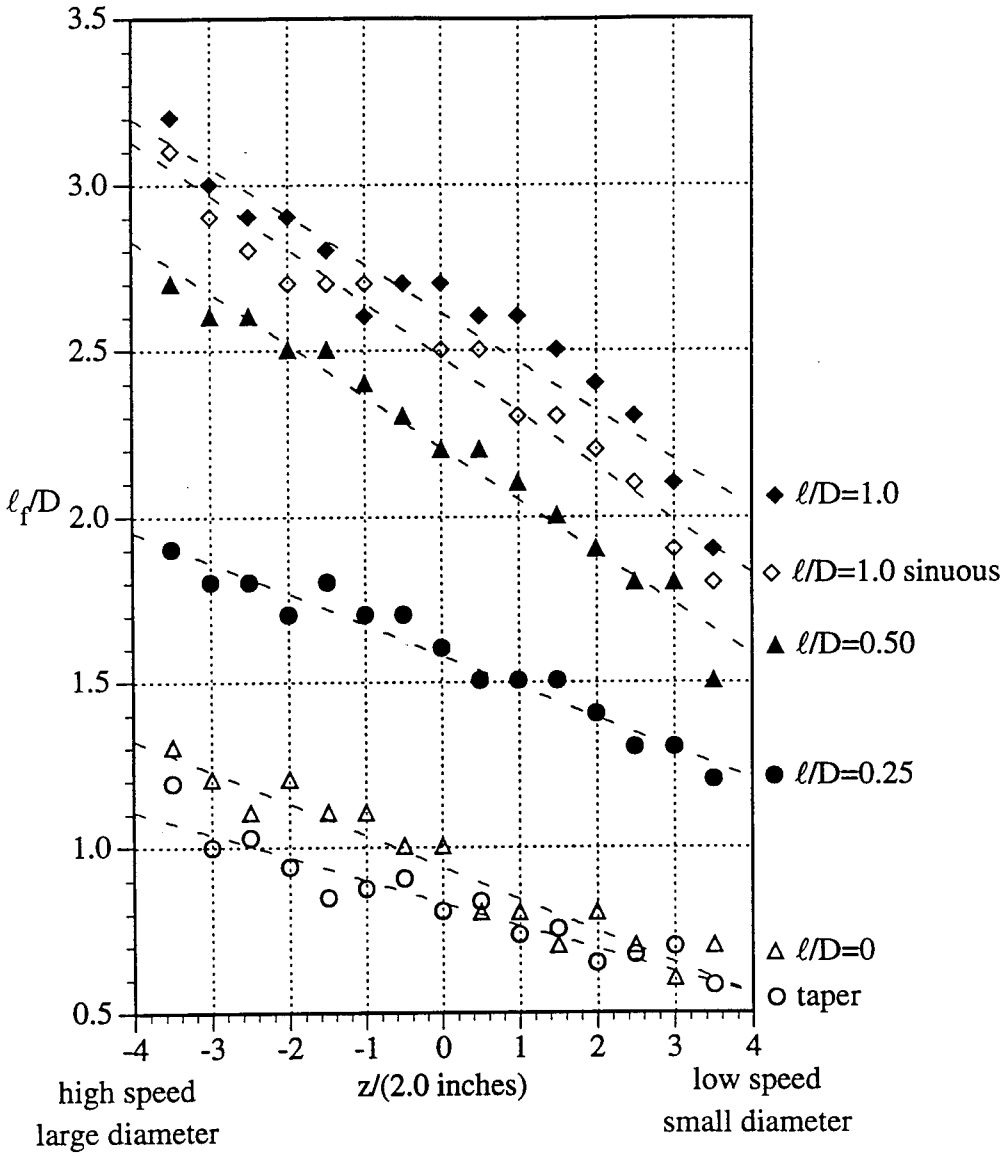

Figure 6.17. Length of the formation region versus span for cylinder in shear flow.

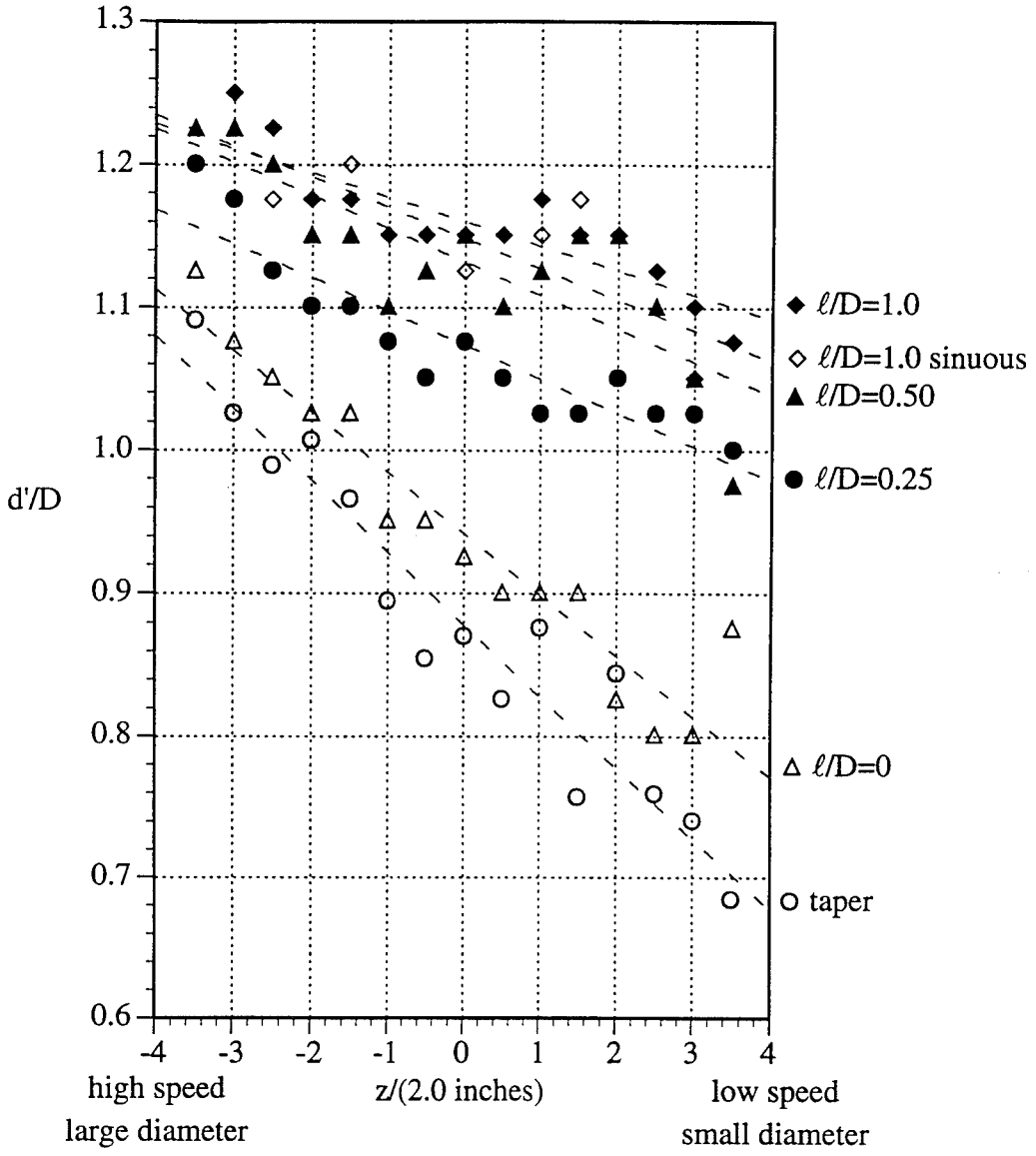

Figure 6.18. Wake width versus span for cylinder in shear flow.

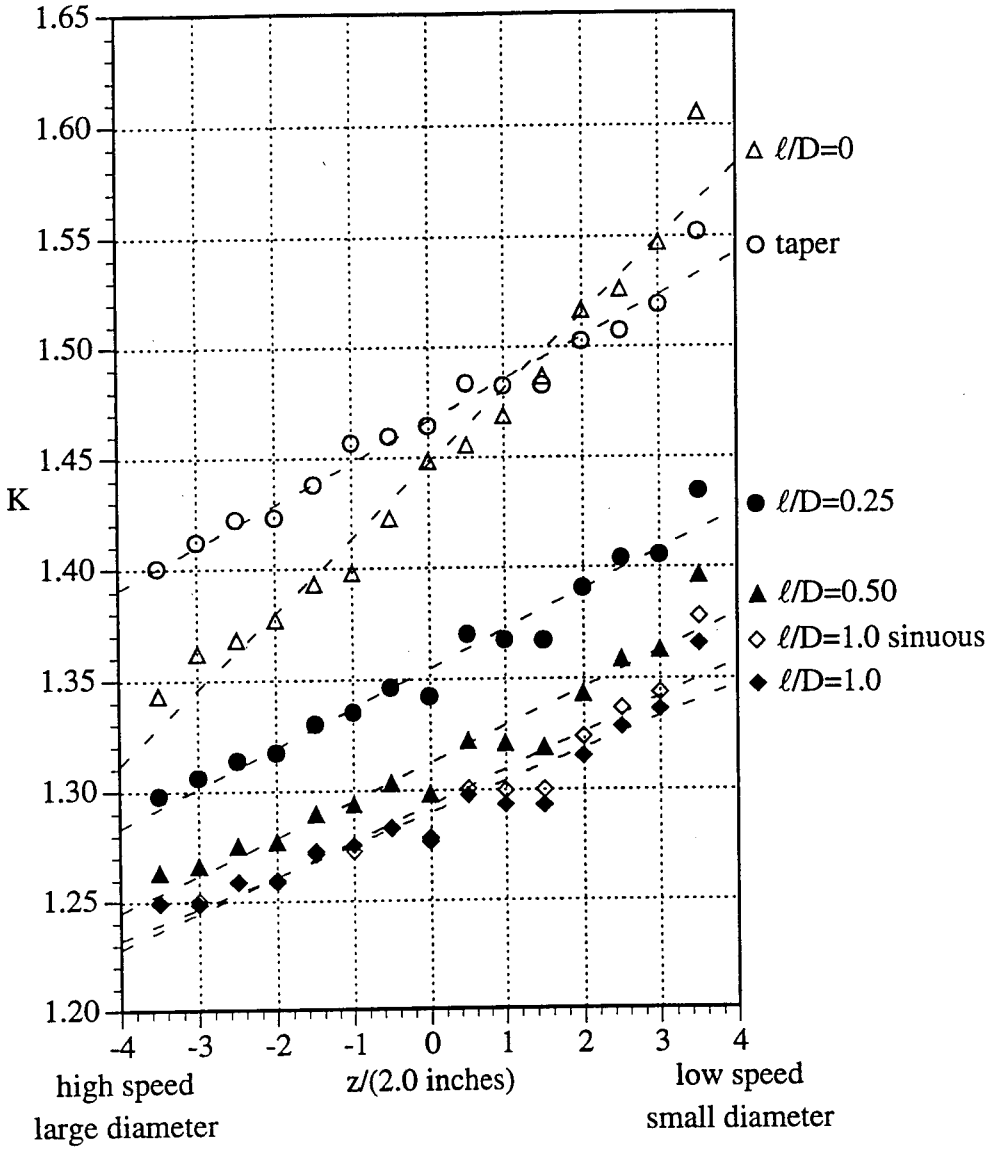

Figure 6.19. Base pressure parameter versus span for cylinder in shear flow.

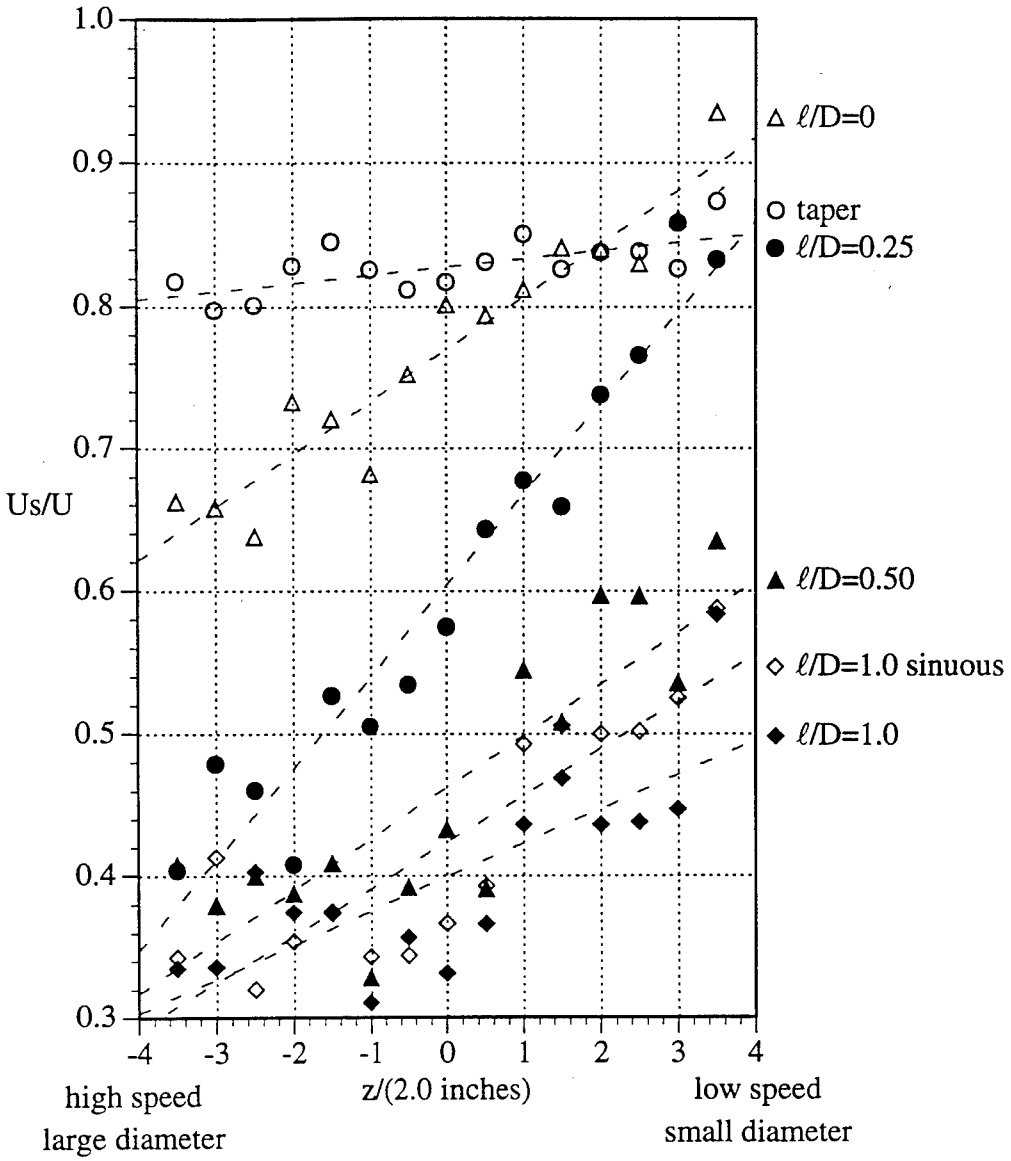

Figure 6.20. Shear layer velocity versus span for cylinder in shear flow.

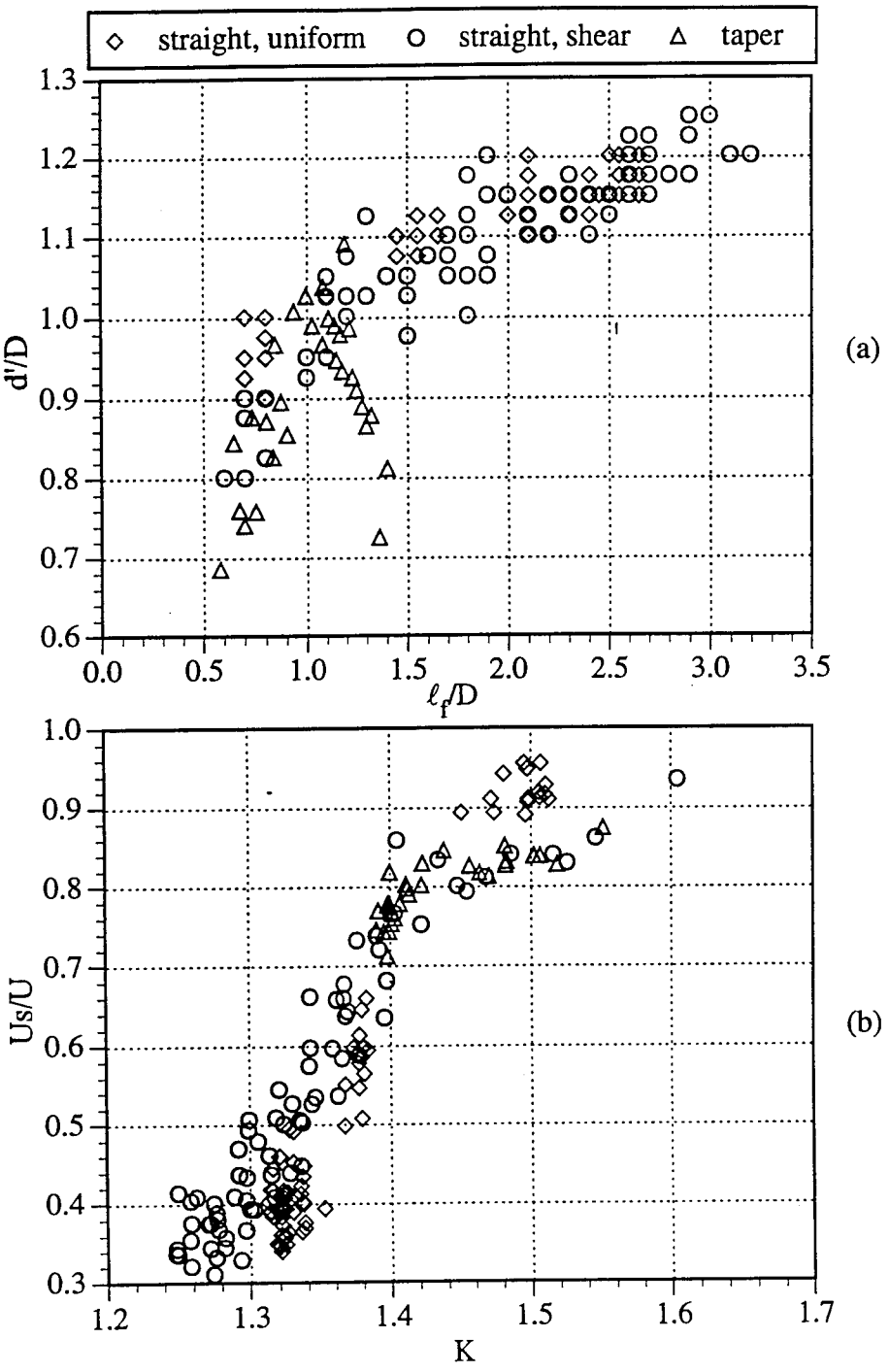

Figure 6.21. Comparison of wake parameters for all configurations

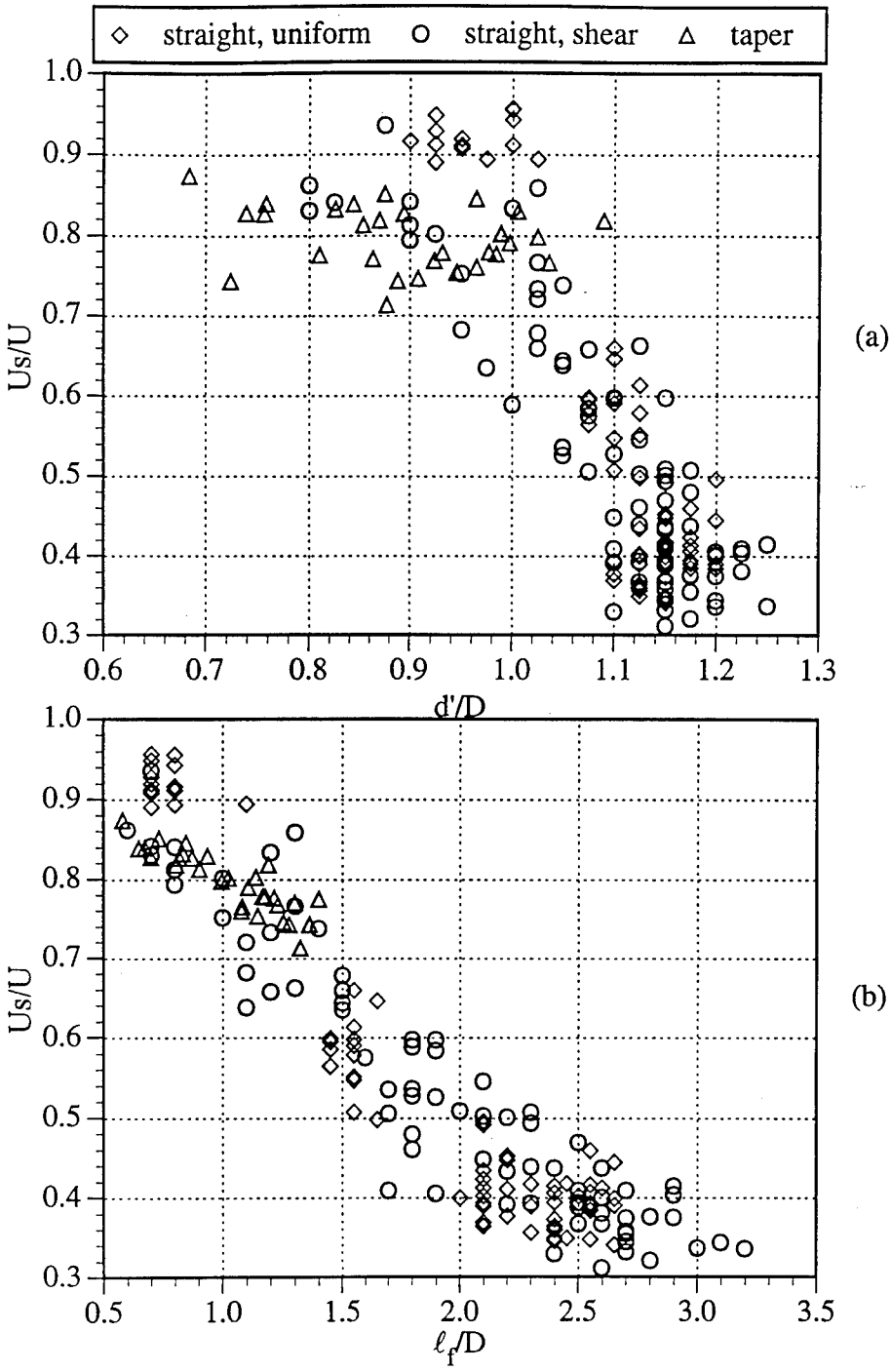

Figure 6.22. Comparison of wake parameters for all configurations

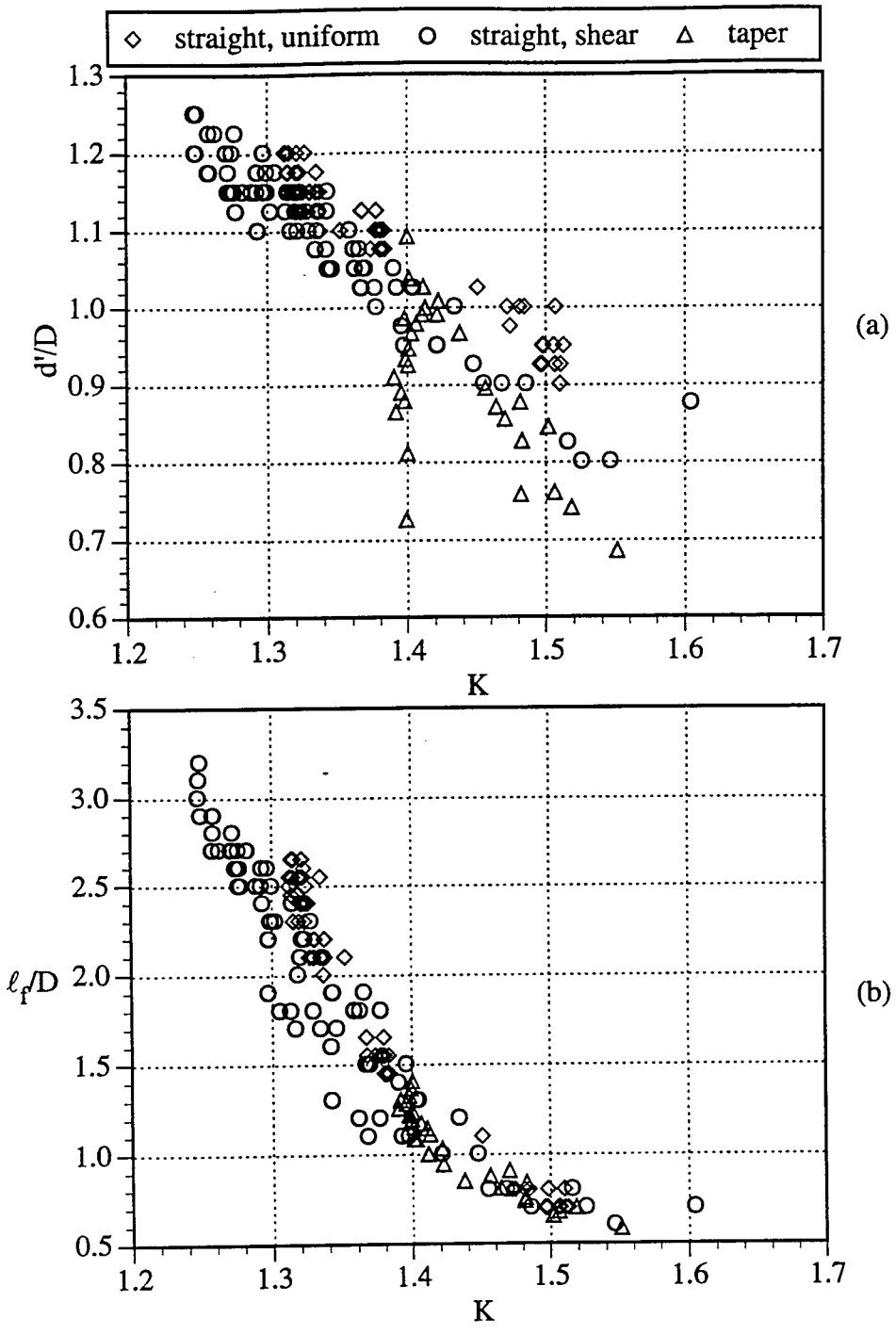

Figure 6.23. Comparison of wake parameters for all configurations

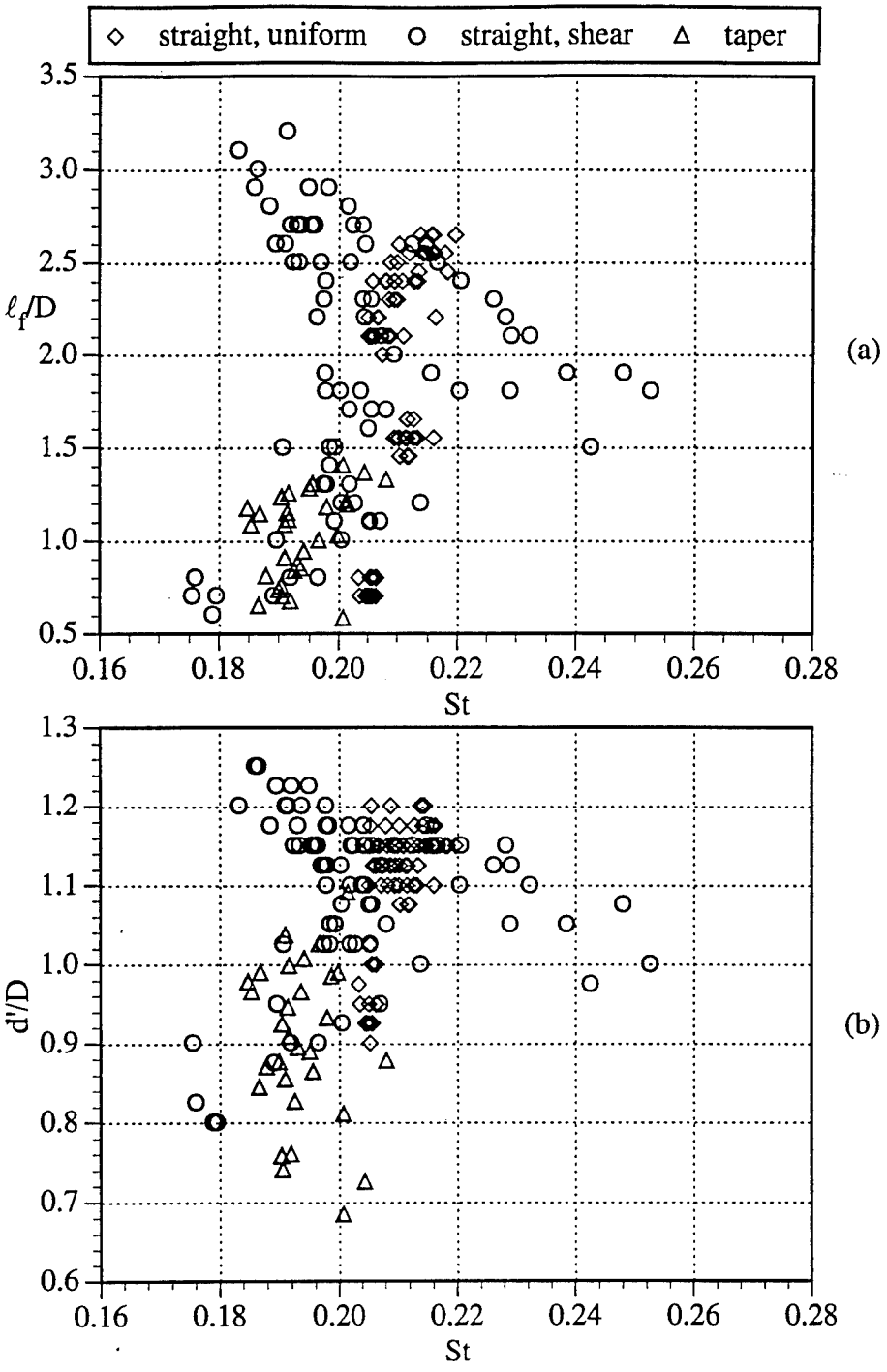

Figure 6.24. Comparison of wake parameters for all configurations

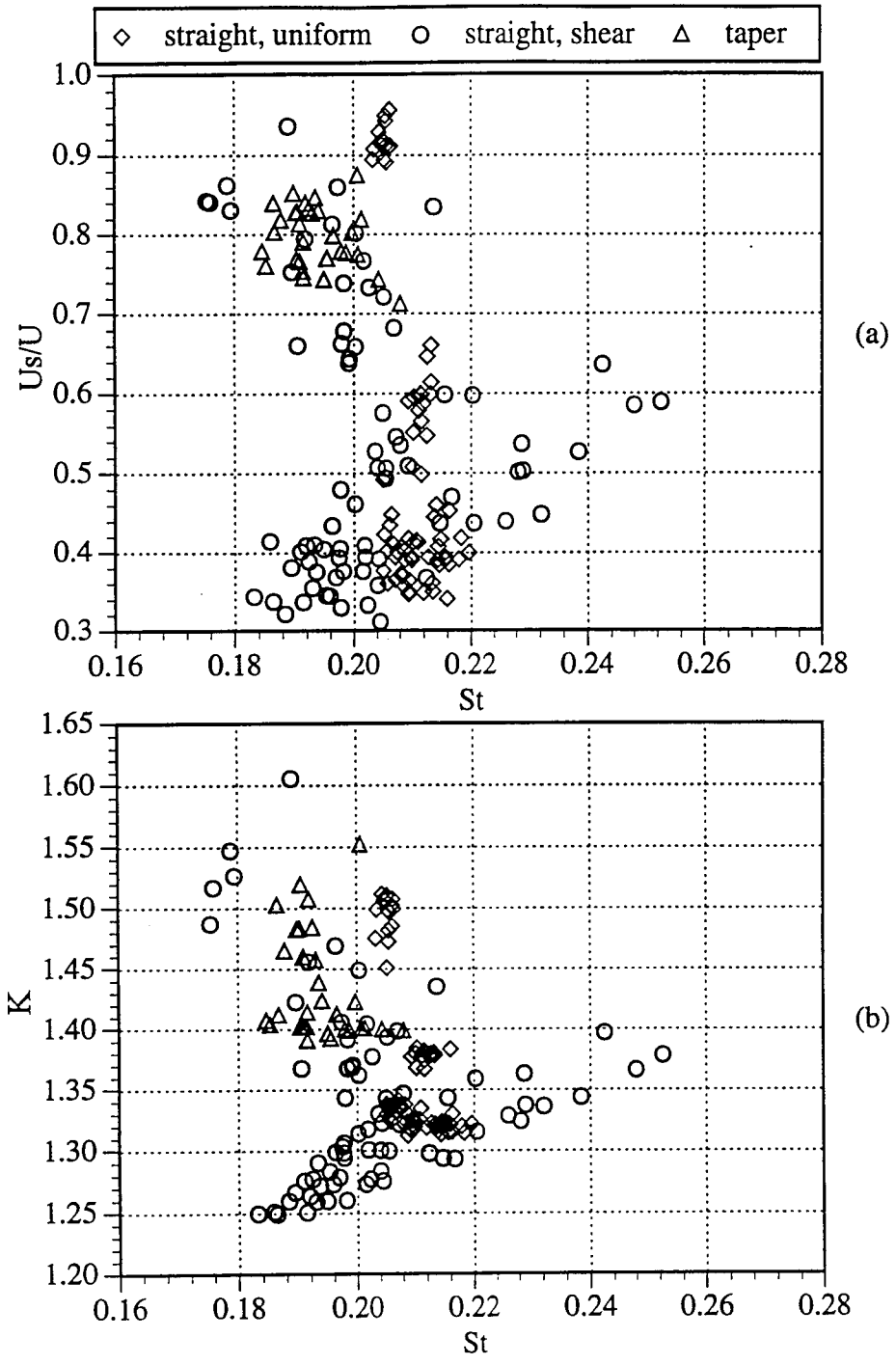

Figure 6.25. Comparison of wake parameters for all configurations

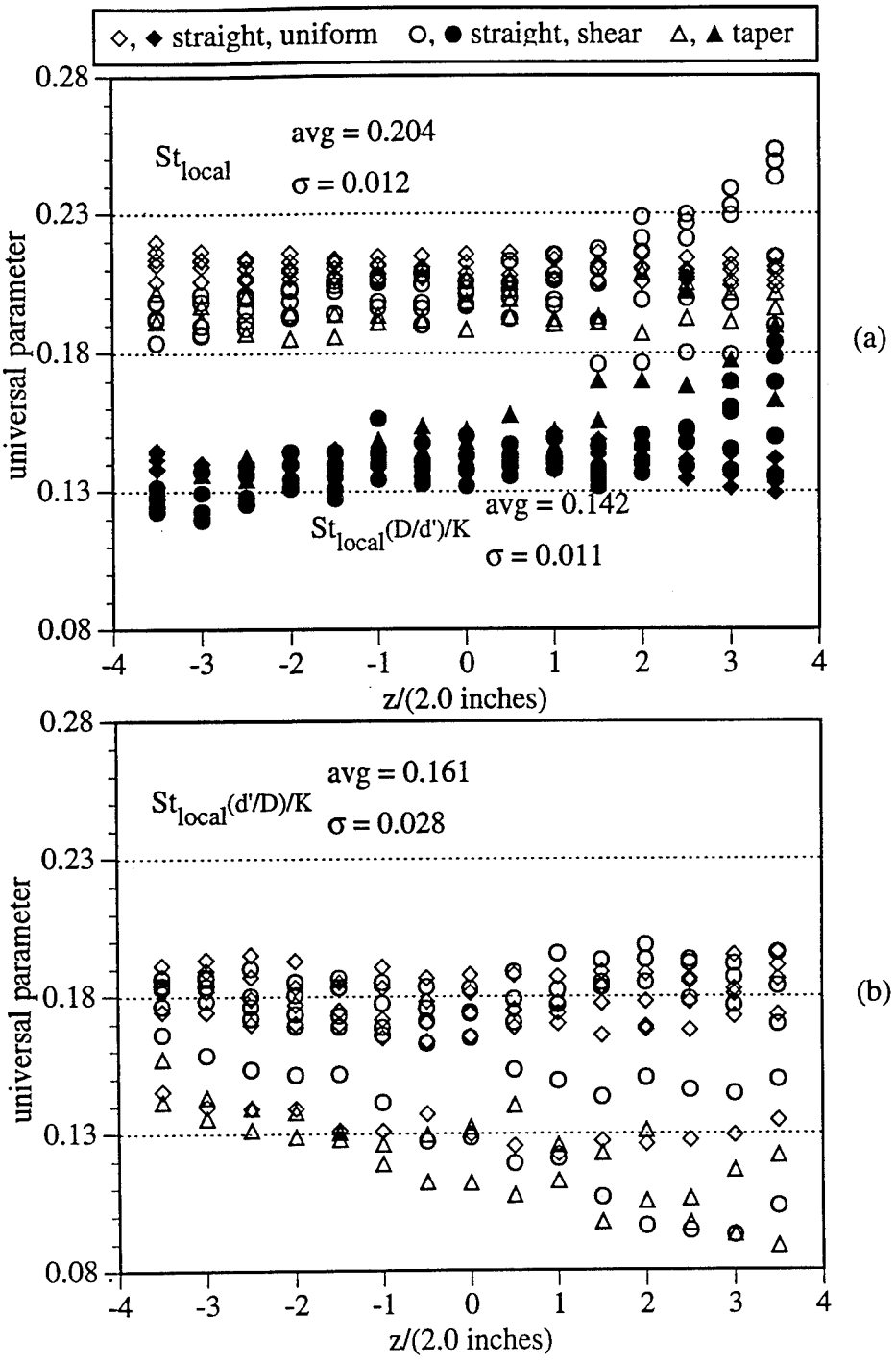

Figure 6.26. Comparison of universal wake parameters for all configurations

CHAPTER 7. FLOW VISUALIZATION

7.1 Introduction

In this section the equipment, procedures and results of the flow visualization experiments are presented. Three techniques were utilized, smoke filament in air, hydrogen bubble in water, and lead particle precipitation in water. The experiments covered Reynolds numbers from 2700 - 7550 in the water channel and 30,000 in the wind tunnel experiments. The flow visualization images presented in this section were captured from video tape sequences using a video card and Global Image Lab software on a IBM 486 PC system. The images were then processed using Adobe Photoshop software on a Macintosh system. Although the lead precipitation flow visualization experiments were conducted at both, Imperial College in London, and at the University of Notre Dame, the images presented in this section come only from the Notre Dame experiments. The reason for this is that most of the experiments conducted earlier in the program at Imperial College were subsequently recreated when a water channel facility became available at Notre Dame. Much of the credit though for the quality of the final images is due to the guidance of Professor Peter Bearman and his colleagues at Imperial College in perfecting this technique. Every attempt was made to prevent bias in the selection of the still images presented in this section and to show images that indicate typical and repeatable flow characteristics.

7.2 Lead Precipitation Technique

A lead precipitation flow visualization technique similar to that used by Tombazis [1993] was used to observe the structure of the shear layer instabilities in a water channel. The procedure requires the mounting of a thin lead foil tape along the stagnation line of the

cylinder and connecting it to one pole of a power supply. The other pole of the power supply is connected to a conducting metal plate located in the flow at some arbitrary distance downstream from the model. When a voltage difference is applied between the lead foil (anode) and the conducting plate (cathode), a dense white cloud of lead particles precipitate into the flow. These particles can be observed and recorded as they convect through a laser light sheet.

An advantage to using this technique over a smoke or hydrogen bubble technique is that the origin of the seed particles can be located on the surface of the model, where the vorticity is generated. This is ideal for visualization of the shear layer because the particles precipitate directly into the boundary layer. Also, since the lead foil is thin it can be molded to most any desired shape thereby providing a non-intrusive method of seeding the flow.

7.3 Experimental Apparatus

Two water channels were used for the lead precipitation flow visualization technique. One was located in the hydraulics laboratory of the Department of Aeronautics of Imperial College in London, England, with a working section of 24 inches wide, 27 inches deep and 70 inches long and capable of producing flow speeds up to 1.0 ft/s. The other water channel was an Eidetics International Model 1520, located in the Hessert Center for Aerospace Research at the University of Notre Dame. The working section in this channel is 15 inches wide, 20 inches deep and 60 inches long. The flow is generated by a 900 gpm Cascade Model 8P axial-flow pump driven by a Baldor variable speed (up to 1175 rpm) 2 HP electric motor. Factory specifications quote a turbulence intensity level of less than 1.0% RMS, flow uniformity to within ±2%, and mean flow angularity within ±1.0 degrees in both pitch and yaw. The flow rate is variable up to 1.0 ft/s. A schematic of the Notre Dame water channel is shown in Figure 7.1 and a photograph of the tunnel is shown in Figure 7.2.

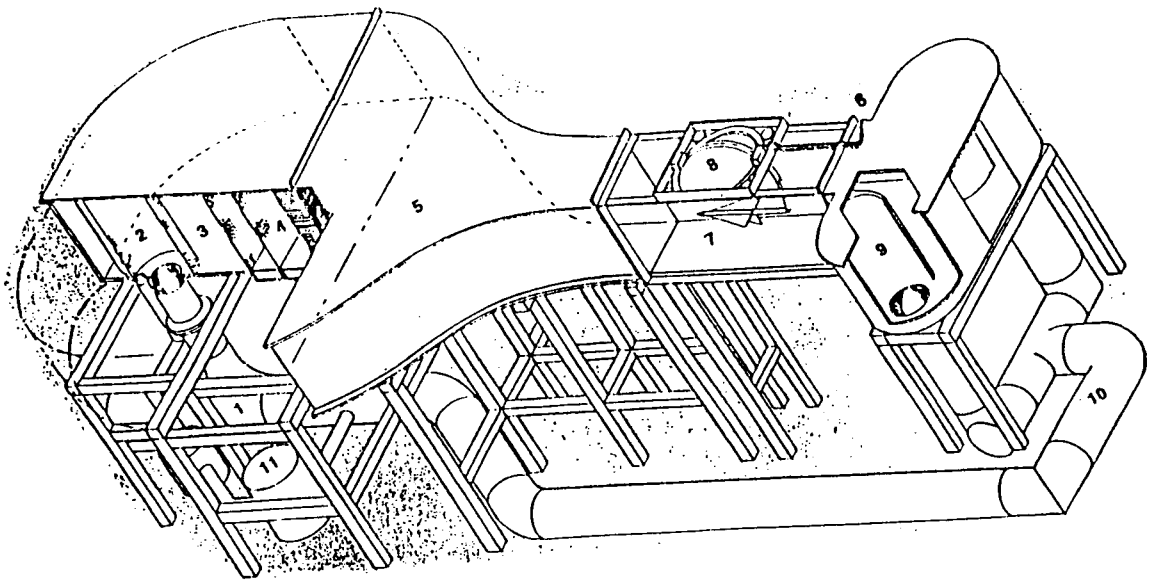

Key: 1. pump 2. perforated inlet 3. delivery plenum
4. flow conditioning elements 5. contraction section
6. dye lines 7. test section 8. model support
9. discharge plenum 10. return piping 11. filter system

Figure 7.1. Schematic of Eidetics International Model 1520 flow visualization water tunnel.

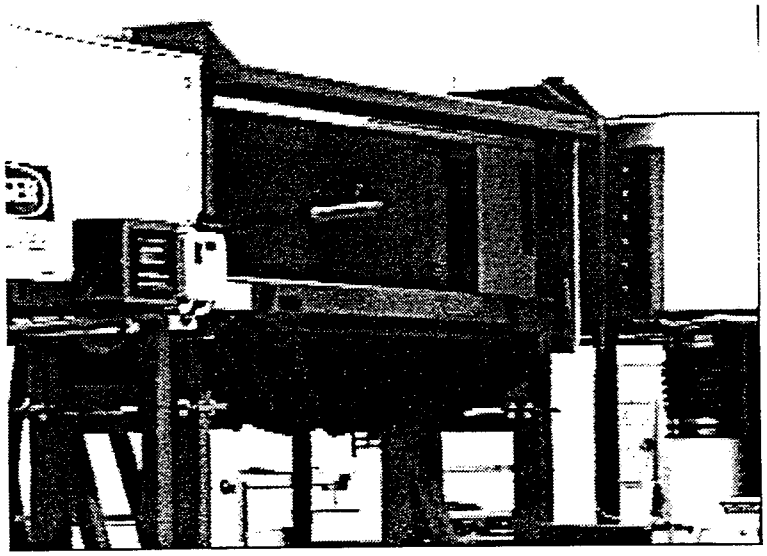

Figure 7.2. Water channel located in the Hessert Center for Aerospace Research at the University of Notre Dame.

A linear shear flow was generated in the water channel by inserting a variable resistance screen upstream of the test section into the channel. The screen was constructed by attaching strips of wire fabric to a frame arranged in a step fashion so that there were many more layers at the bottom than at the top. The wire fabric was a medium mesh screen with 20 x 20 wires per inch of 0.016 dia. stainless steel wire. This screen created a variable resistance to the flow that increased from top to bottom and thus produced a mean shear flow in the channel. A schematic of the shear screen is shown in Figure 7.3. Figure 7.4 presents a time sequence of hydrogen bubble flow visualization images of the mean shear profile produced by this device.

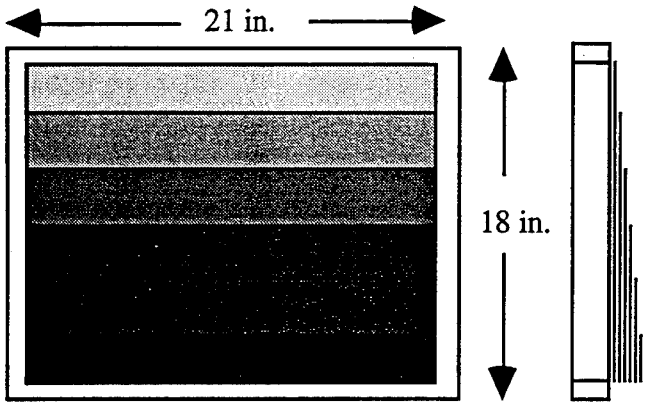

Figure 7.3. Schematic of shear generating screen for water channel.

The models used for the lead precipitation flow visualization were constructed from 1.25 or 1.375 inch diameter plastic pipe or rod or 2.0 inch diameter wood rod (Imperial College). The materials were selected based on their electrical insulator properties and for ease of fabrication. End plates were constructed of 0.125 x 5 x 7 inch rectangular Plexiglas and positioned to provide an aspect ratio of 8. The leading edge of the end plate was positioned approximately one diameter from the leading edge of the cylinder. A 0.0625 inch wide and 0.125 inch deep slot was cut along the trailing edge of the models so that a

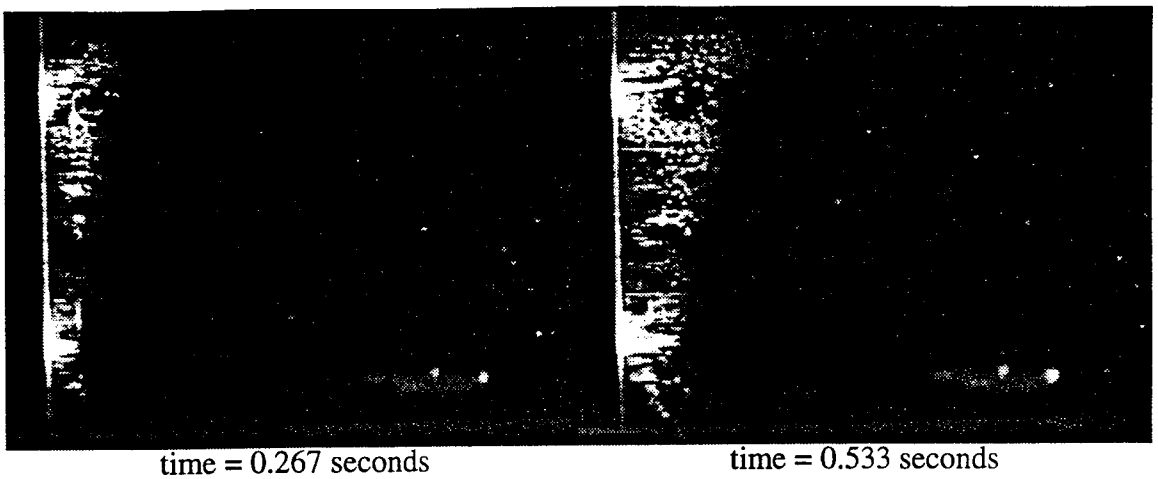

time = 0.267 seconds time = 0.533 seconds

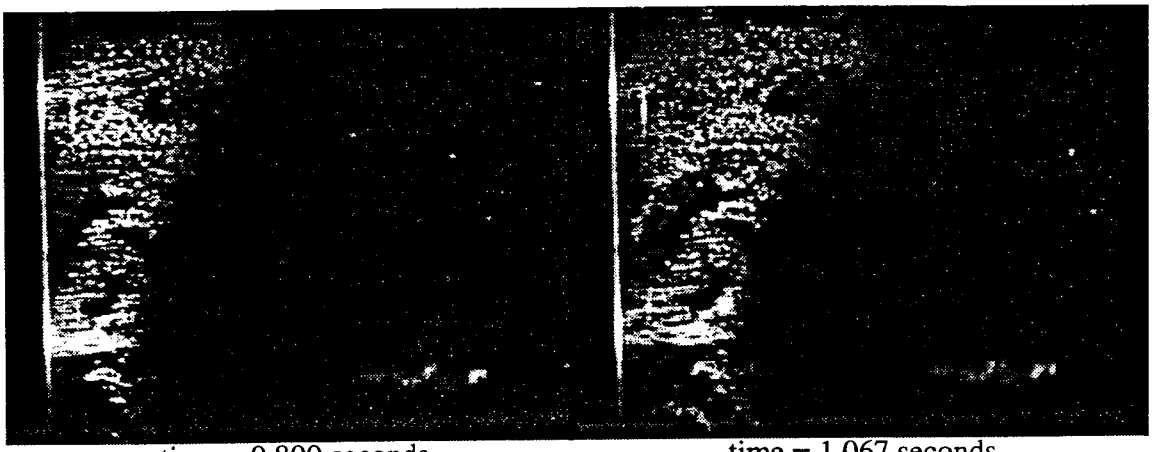

time = 0.800 seconds time = 1.067 seconds

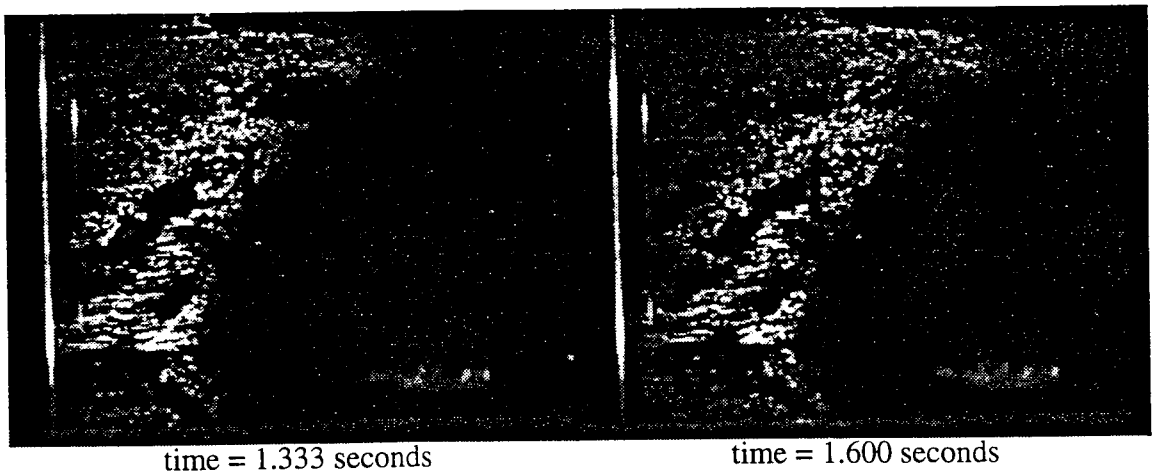

time = 1.333 seconds time = 1.600 seconds

Figure 7.4. Sequence of video images showing hydrogen bubble flow visualization of mean shear velocity profile in water channel.

splitter plate could be attached. A lead foil strip with dimensions of 0.005 x 0.5 x 10.0 inches was secured by a self-adhesive backing to the cylinder along its stagnation line.

The models were either suspended vertically from the top of the tunnel or secured horizontally across the tunnel with a spring compression mechanism. Figure 7.5 shows one of the plastic cylinder models with end plates.

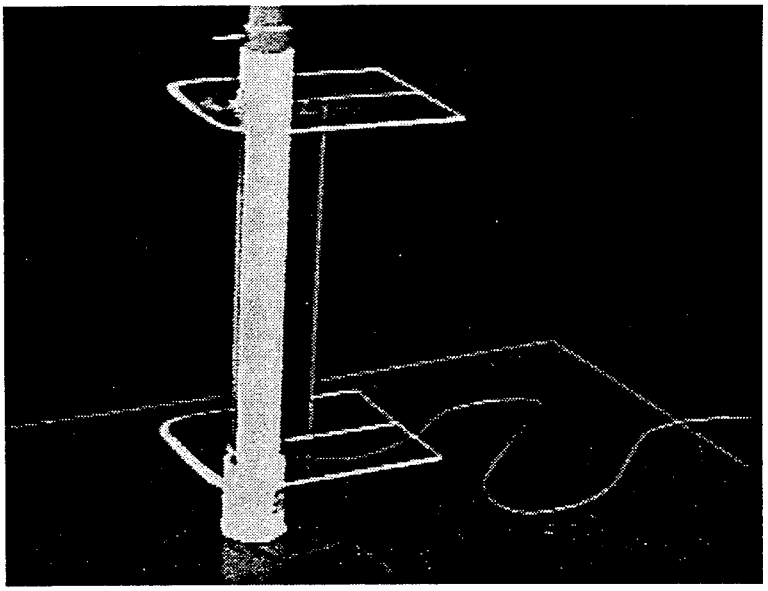

Figure 7.5. Plastic circular cylinder with end plates and splitter plate attached.

The splitter plates used in the flow visualization experiments were constructed from 0.0625 inch thick aluminum plates of various length ranging from $\ell/D = 0.25 - 1.50$.

The tapered model had a maximum diameter of 1.375 inches that linearly decreased to a minimum diameter of 0.75 inches over a 10.0 inch span that resulted in a taper ratio, $dD/dL = 0.0625$. A slot was cut along the cylinder trailing edge to allow for the attachment of a splitter plate.

A voltage difference ranging between 15-40 volts was required to produce satisfactory precipitation. The proper voltage for a given flow speed was determined by increasing the voltage level while observing the precipitate in the laser light sheet until it became dense enough to produce high quality images. If the voltage became too high, bubbles would begin to precipitate along with the lead reducing the quality and accuracy of the images. With the proper voltage applied, a thick white cloud would precipitate from the strip and convect with the flow. It was found that the location of the conducting plate within the test section was arbitrary and had no noticeable affect on the amount of lead precipitated into the flow. Table 7.1 shows the approximate voltages required for various flow rates used in the flow visualization experiments.

U (ft/s)	Reynolds #	voltage
0.28	2700	15
0.39	3700	20
0.47	4500	25
0.60	5700	30
0.69	6650	35
0.78	7550	40

Table 7.1. Approximate voltage settings for satisfactory lead precipitation at various flow rates in water channel. Based on lead foil strip, 12 x 0.5 x 0.005 inches.

The precipitate was illuminated with a planar light sheet generated by directing the beam from either a 2 Watt (Imperial College) or 1 Watt (Notre Dame) Argon laser through a cylindrical lens. For the Imperial College experiments the light sheet was directed up through the glass bottom of the water channel with a flat mirror oriented at a 45 degree angle to the beam path. The Notre Dame water channel had a glass window located at the end of the channel that allowed the flow to be viewed from a streamwise orientation. The

light sheet was directed through that window eliminating the need for a mirror to redirect the light sheet. A benefit gained by directing the beam in the upstream direction was that for the end view visualizations the top and bottom shear layers were both entirely illuminated. The end view images produced at the Imperial College facility suffered from having the splitter plate block the upward directed light sheet from portions of the top shear layer. Schematics of the Notre Dame and Imperial College water channel experiment arrangements are shown in Figure 7.6.

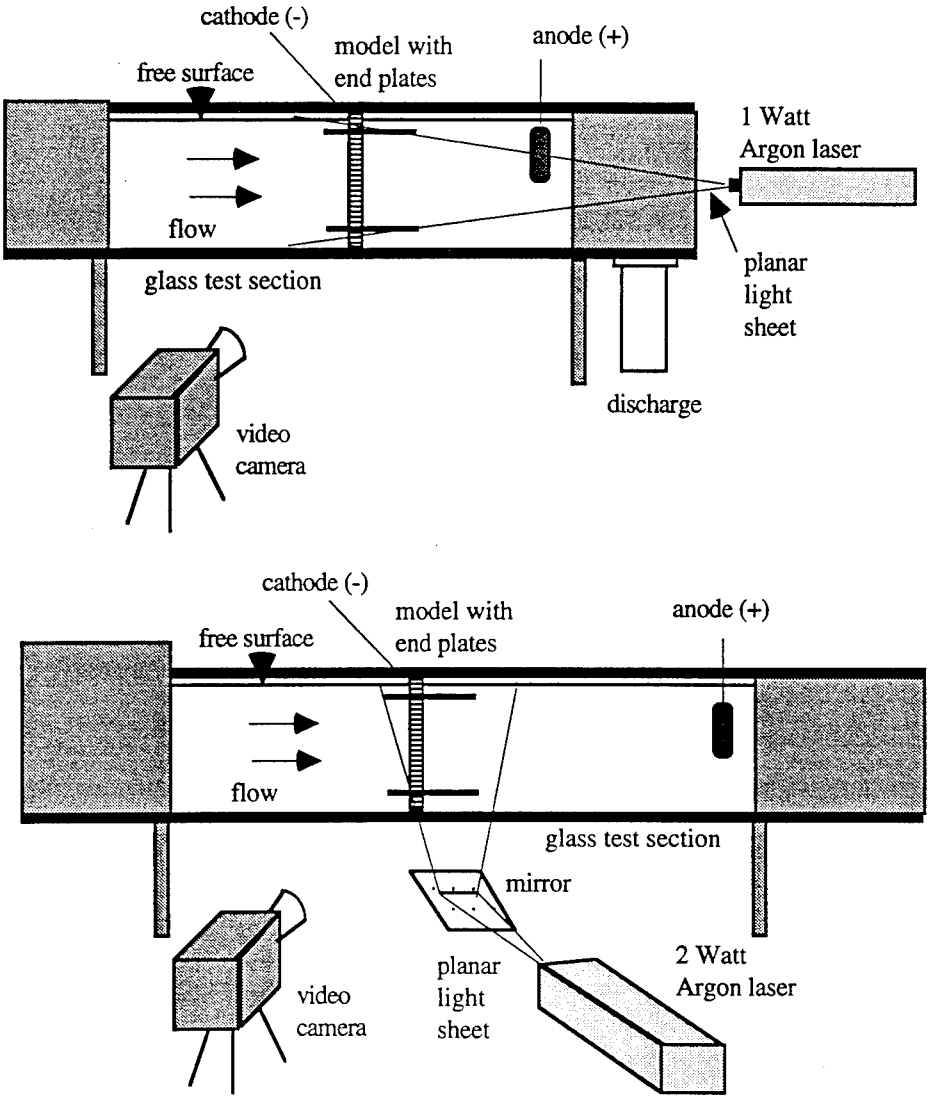

Figure 7.6. Schematics of Notre Dame (top) and Imperial College (bottom) water tunnel arrangement for lead preciptation flow visualization experiments.

The lead precipitation flow visualization images presented in this document were recorded on video tape using a Sony model SSC-S20 color video camera at a frame rate of 1/30 second and a shutter speed of 1/250 second.

7.4 Hydrogen Bubble Technique

The hydrogen bubble technique of flow visualization was used in the Notre Dame water tunnel for the purpose of viewing the larger flow structures that are difficult to see with the lead precipitation technique. This method was also used to quantify the shear velocity profile for the shear flow experiments.

Hydrogen bubble and lead precipitation techniques are similar in that both involve the use of an electric current to generate seed particles in water. The main difference between them being that a thin wire spanning the channel was used to generate the particle seed in the hydrogen bubble technique instead of lead foil tape. The positive lead from the power supply was connected to the brass plate (anode) immersed in the test section and the negative lead is connected to the thin wire (cathode). Note that for best results, the power supply polarity was reversed from the configuration used to produce the lead precipitation. A voltage difference of approximately 35 volts between the electrode and the wire gave adequate bubble generation. Again, a planar light sheet produced from a 1 Watt Argon laser was used to illuminate the bubbles. The hydrogen bubble images were recorded on video tape using the same method described in the lead precipitation section.

7.5 Smoke Rake Technique

Flow visualization with smoke was accomplished through the use of a kerosene smoke generator and smoke rake located at the inlet of the subsonic indraft wind tunnel. This technique produced visualization of the larger flow structures.

The smoke generator consisted of four 750 Watt heating elements enclosed in a sealed manifold. Kerosene was dripped onto the heating elements from reservoirs located above the elements. The drip rate could be controlled and determined the amount of kerosene vaporized by the heating elements. The vaporized kerosene produced a dense white smoke that was directed through the manifold to the smoke rake by means of a blower. Within the rake assembly, the smoke was directed by blower pressure to a series of parallel 0.5 inch diameter outlet tubes spaced 2.5 inches apart. These tubes were positioned flush against the anti-turbulence screens at the front of the inlet. This system produced dense smoke filaments within the test section that could be viewed on a video system when illuminated by a high intensity light source. The smoke rake apparatus is shown in Figure 7.7.

A series of four high intensity strobe lights were used to illuminate the smoke through glass windows on the top and bottom of the test section. The models were mounted horizontally in the test section and the video camera was oriented with a spanwise viewing direction. The strobe lights were synchronized to the shedding frequency of the Kármán vortices to phase lock the flow field for the video recording.

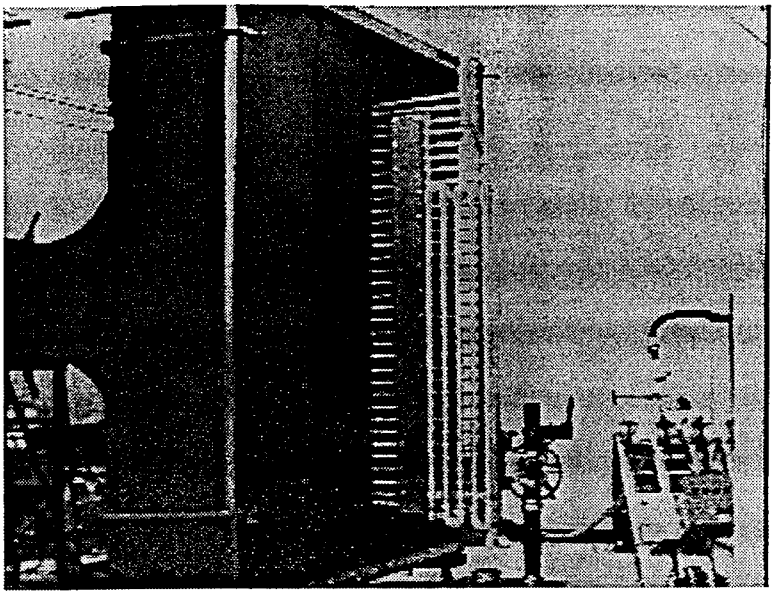

Figure 7.7. Kerosene smoke rake assembly positioned at the wind tunnel inlet.

The wind tunnel and models used in the smoke flow visualization experiments were described in Chapter 2.

7.6 Results and Discussion

Flow visualization results are presented for the various techniques that were incorporated in this research. The lead precipitation technique in the water channel was used primarily for the analysis of the shear layer instabilities. The smoke rake and hydrogen bubble techniques were used to visualize the large scale wake topology in the wind tunnel and water channel respectively.

Although the majority of the hot wire results in this study were produced within the Reynolds number range of 20,000 - 40,000, the water channel flow visualization results were limited to a Reynolds number range of 2700 - 7750. The upper limit of this range identifies the highest flow rate at which quality images could still be produced by the lead precipitation technique. Although both Reynolds number ranges were within the sub-

critical regime, the difference in Reynolds number must be considered when making comparisons between the flow visualization results and hot wire measurements.

Figure 7.8 shows hydrogen bubble flow visualization of various circular cylinder/splitter plate configurations in uniform flow at a Reynolds number of 4500. The images show the lengthening of the formation region with increasing splitter plate length (ℓ/D). By defining the streamwise location that the bubbles cross the centerline (y/D = 0) of the cylinder as the formation length and referencing the length measurements to the image of the cylinder cross section, formation length measurements were made. The results are presented in Table 7.2.

ℓ/D	ℓ_f/D
0.00	1.0
0.25	1.6
0.50	2.0
1.00	2.6
1.50	3.3

Table 7.2 Vortex formation length versus splitter plate length from hydrogen bubble flow visualization at Reynolds number = 4500.

Smoke flow visualization for a circular cylinder in uniform flow at Re = 30,000 with various length splitter plate configurations are shown in Figure 7.9. Formation length measurements were not scaled from these images due to the difficulty in synchronizing the strobe lights to a phase in the shedding cycle where the smoke first crossed the cylinder centerline. Although, evidence of the elongation of the formation region with increasing splitter plate length was clearly observed.

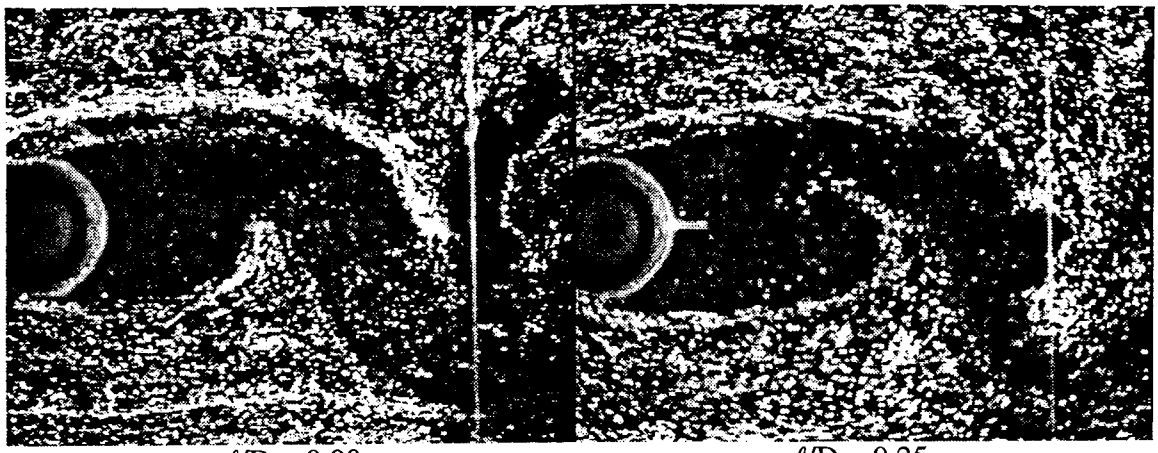

ℓ/D = 0.00 ℓ/D = 0.25

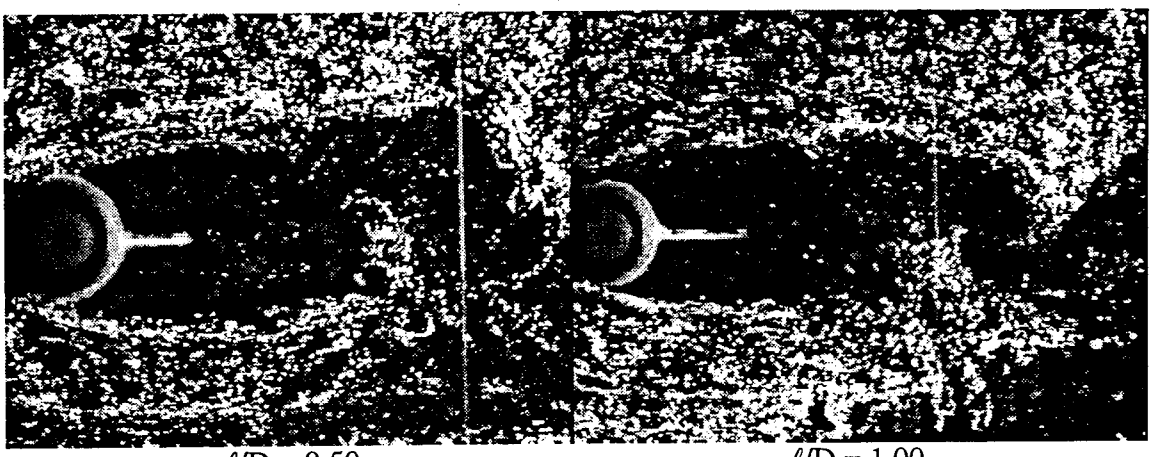

ℓ/D = 0.50 ℓ/D = 1.00

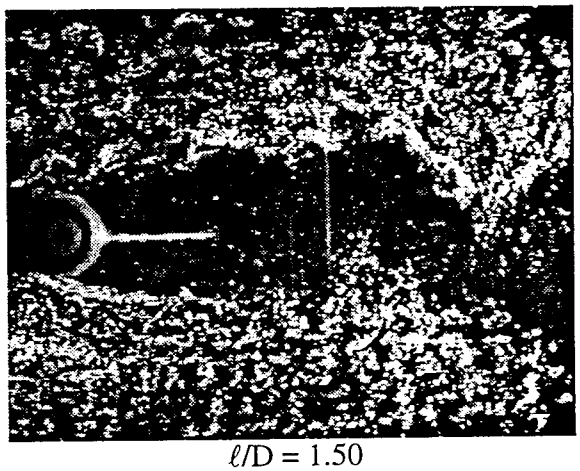

ℓ/D = 1.50

Figure 7.8. Video images showing hydrogen bubble flow visualization of flow past a circular cylinder for various length (ℓ/D) splitter plates. Re = 4500.

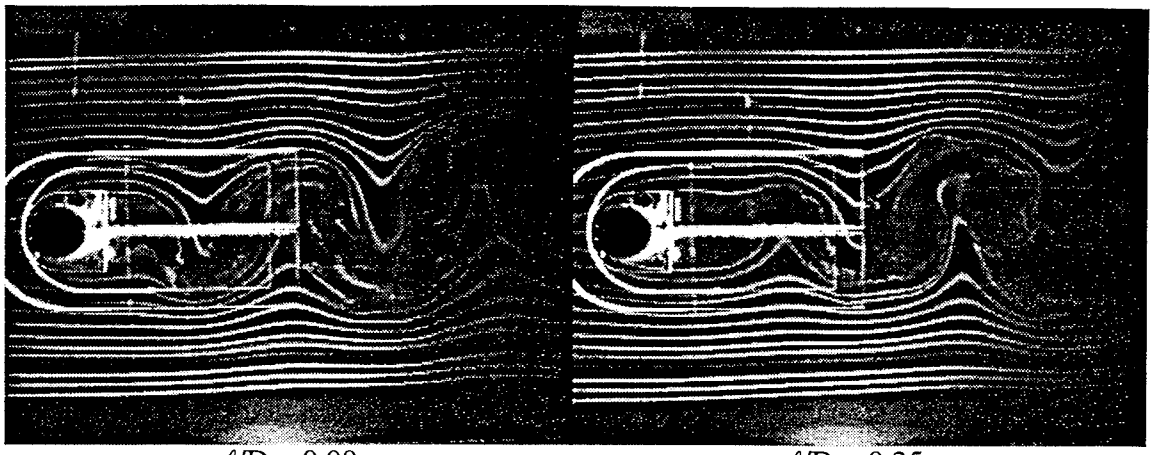

ℓ/D = 0.00 ℓ/D = 0.25

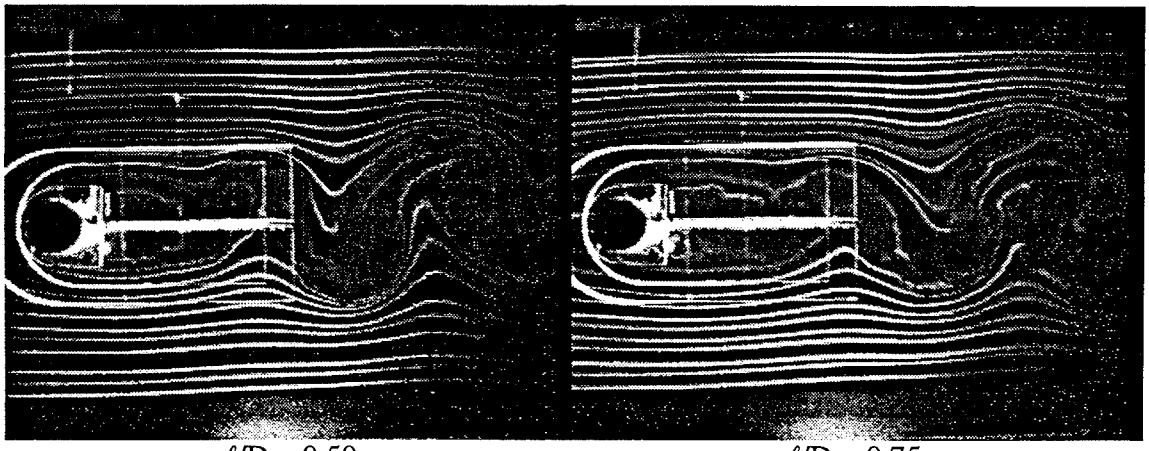

ℓ/D = 0.50 ℓ/D = 0.75

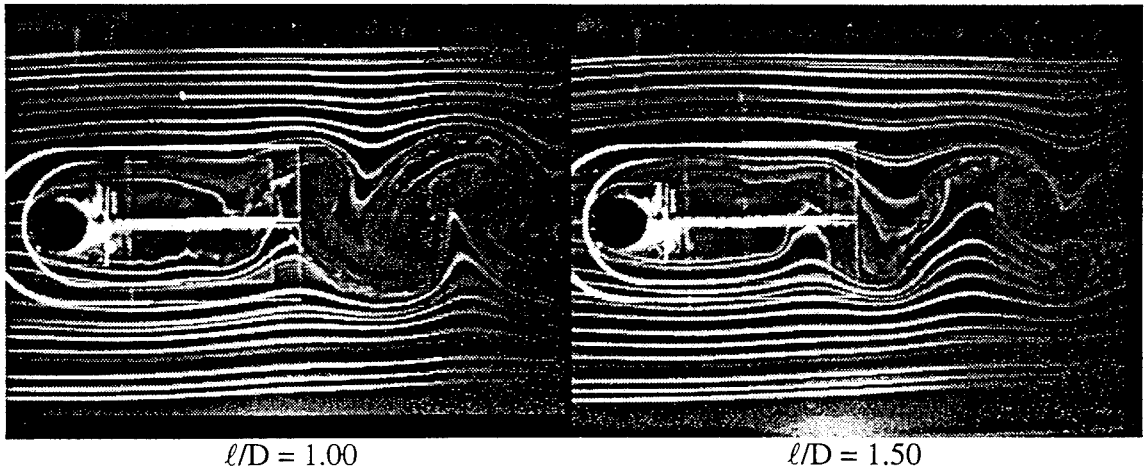

ℓ/D = 1.00 ℓ/D = 1.50

Figure 7.9. Video images of smoke rake flow visualization showing flow past a circular cylinder for various length (ℓ/D) straight trailing edge splitter plate configurations. Re = 30,000.

Figures 7.10 - 7.14 present video images of shear layer instabilities at various Reynolds numbers and for different splitter plate lengths. The images show that the size and spacing of the transition vortices are not constant for a given Reynolds number and splitter plate length but vary about some average values and those average values decrease with increasing Reynolds number. This result confirms that the frequency of the transition vortices are not directly proportional to the flow velocity for a fixed cylinder diameter and fluid. If that direct proportionality did exist, the spacing between the vortices would remain constant for all flow speeds. Also, the fact that there is some randomness associated with the transition vortex size and spacing suggest a possible reason why it is difficult to identify a characteristic vortex passage frequency from fixed probe measurements. The flapping of the shear layer and variable amplitude of the instability waves will introduce intermittancy to measurements taken from any fixed probe location.

Although the shear layer images confirm the increase in formation region length with increasing splitter plate length, they do not indicate any other significant changes in the shear layer caused by the splitter plate. The average spacing between the transition vortices appear to decrease with increasing Reynolds number by approximately the same proportion regardless of splitter plate length. The splitter plate does act to elongate the shear layer which allows more instability waves to roll up before being entrained by the primary vortices, a result that greatly benefits flow visualization of the vortices.

It can be inferred from the lack of seed particles in the formation region, as illustrated in Figures 7.10 - 7.14, that very little of the outer flow is directly transferred to the formation region of the wake. This is supported by observation of the lead precipitation video tapes that show relatively slow moving lead particles in the formation region. The slow particle motion suggests a low rate of fluid replenishment in the base region and

therefore a low rate of entrainment of formation region fluid into the primary vortices. Without a splitter plate attached the particles slowly 'slosh' back and forth across the cylinder base in phase with the primary shedding cycle. The attachment of a splitter plate to the cylinder blocks the fluid from moving across its base and results in relatively stagnant fluid and very slow particle motion. Observation of the lead precipitation particles in the video sequences also indicate that the fluid in the formation region that is entrained and carried away by the shear layer is replenished by fluid moving upstream from the end of the formation region at each half shedding cycle. This agrees with Gerrard's [1966] diagram of the entrainment process in the vortex formation region described in Chapter 1.2.

Figure 7.15 shows a time sequence taken from a video tape of uniform flow past a circular cylinder with a splitter plate of $\ell/D = 0.90$ at a Reynolds number of 5700. The sequence of images show a time period where the upper and lower shear layers were symmetric and in-phase with each other. This so called 'phase locking' of the shear layers indicate communication between the shear layers that must initiate from either an upstream disturbance or upstream feedback of a downstream disturbance. There should not be any communication in the transverse direction between the shear layers within the base region because of the solid boundary provided by the splitter plate. The phenomenon occurred with some regularity, often enough to suggest that it was more than a consequence of the two shear layers, with identical stability characteristics and transition wave frequency, being matched in phase occasionally due to random perturbations of the flow. If random phase shifts had been the cause, it would be expected that a similar number of image sequences would be found where the transition vortices were out of phase by say, a half cycle. Those images are found to occur only rarely whereas the 'phase locking' is a relatively common occurrence, a result that suggests a preference for this mode. These results are also supported by Gerrard's [1978] observation of a phase coupling between the two sets of shear layer transition vortices.

Time sequence spanwise views of the shear layer from a straight circular cylinder in uniform flow at a Reynolds number of 4500 are shown in Figures 7.16 and 7.17. The Figures illustrate the large amount of 3-dimensionality in the shear layer and show clear evidence of discontinuities or 'holes' similar to the 'spot' structures described by Williamson [1991] that occur in Kármán vortices at much lower Reynolds numbers. These structures typically have an associated spanwise length scale of 0.5 to 1.5 diameters and a streamwise scale the same as the instability wave spacing. Figure 7.16 presents a time sequence of six images with a time step of 0.1 seconds between each successive image. The 0.5 second elapsed time between the first and last image is sufficient for about 5 instability waves to form. The images show that once a discontinuity forms in the shear layer it tends to remain at a stationary position over a number of cycles. The discontinuity initially grows with time to a maximum size and then remains relatively stable and stationary throughout anywhere from two to several primary shedding cycles. Figure 7.17 presents a time sequence taken from the same configuration but the time step between the images is 0.033 seconds. The smaller time step corresponds to the each successive frame from a video tape with a frame rate of 1/30 second. The elapsed time between the first and last image of 0.166 seconds shows the topological evolution of various discontinuities during the formation of approximately one instability wave. These images show more clearly the development of the discontinuities with time. The streaklines indicate that the shear layer fluid tends to bend around either side and bottom of the discontinuity in a 'bowl' shape, concave down when viewed from above the upper shear layer.

Figure 7.18 presents a time sequence of images showing the development of shear layer instability waves for a circular cylinder with an attached straight trailing edge splitter plate of $\ell/D = 0.90$. The images show discontinuities similar to those shown previously for the cylinder without a splitter plate although their occurrence is much less frequent. The

discontinuities that do form display the previously described bowl shape but tend to develop further downstream than in the case of no splitter plate. Observation of several minutes of video showing the two configurations suggest that the use of a splitter plate decreases the number of discontinuities formed and increases the spanwise coherence of the shear layer compared to the no splitter plate configuration.

Figure 7.19 shows a sequence of images produced by a tapered circular cylinder in uniform flow. The light sheet was angled to run parallel to the cylinder surface for all tapered cylinder flow visualization presented unless otherwise specified. This orientation was chosen to give a consistent view of the separated shear layer along the span. The images show the evolution of shear layer instability waves and indicate strong spanwise correlation despite the 3-dimensionality imposed by the cylinder taper. Although direct measurement of primary vortex shedding frequency was not attempted in the water channel, it can be assumed based on previous studies, Gaster [1971], Papangelou [1992], Piccirillo and Van Atta [1992], that the primary vortex shedding from the tapered model exhibited a spanwise structure of constant shedding frequency cells. The flow visualization results though, do not indicate such a spanwise structure in the shear layer instability waves which suggests that the two phenomena are not coupled.

Figure 7.20 shows the tapered cylinder in uniform flow again, but in this sequence the light sheet had been repositioned nearer the centerline of the cylinder. That orientation allowed better observation of the lead precipitate as it convected with the primary, Kármán vortices. Each successive image represents approximately one half shedding cycle of the primary vortices. The Δtime noted below the images represent the time period between each successive image, or half cycle. The images describe a 'chevron' type pattern slightly tilted so that the oblique shedding angle near the small diameter end is less than the oblique angle near the large diameter end. The vertex of the chevron is positioned near the mid-

span point of the cylinder. The pattern shown in the images would produce the spanwise structure of constant shedding frequency cells described for a tapered cylinder flow. The difference in the oblique shedding angles would result in shedding frequency measurements that are lower in the region of the large diameter end than those at the small diameter end, which is consistent with the published tapered cylinder studies.

Figure 7.21 shows spanwise views of the circular cylinder in uniform flow, Re = 4500, in three splitter plate configurations; no splitter plate, straight or 2-D splitter plate with $\ell/D = 1.0$, and periodic or 3-D splitter plate with $\ell/D = 1.0$ and $\lambda/D = 2.0$. It should be noted for comparison purposes that the camera zoom is different between the three configurations and that the images shown represent the most typical flow structures observed in the video sequences. The images indicate an increase in spanwise coherence of the instability waves by the introduction of the splitter plate. The coherence appears to increase further as a consequence of the 3-dimensionality imposed by the periodic trailing edge splitter plate.

Figure 7.22 shows spanwise views of the circular cylinder with a periodic trailing edge splitter plate attached in uniform flow at various Reynolds numbers. As with the previous Figure, these images show strong spanwise coherence in the instability waves. The level of spanwise coherence appears unchanged over the various Reynolds numbers examined and was consistently stronger than for the no splitter plate and 2-D splitter plate cases. The spacing between the waves decrease with increasing Reynolds number indicating a non-linear relationship between the transition frequency and Reynolds number.

Figure 7.23 below presents a close up view of the flow past a cylinder with the periodic splitter plate attached at Re = 3700. This image clearly shows symmetric discontinuities bounding the peak of the sinuous trailing edge with a spanwise length scale

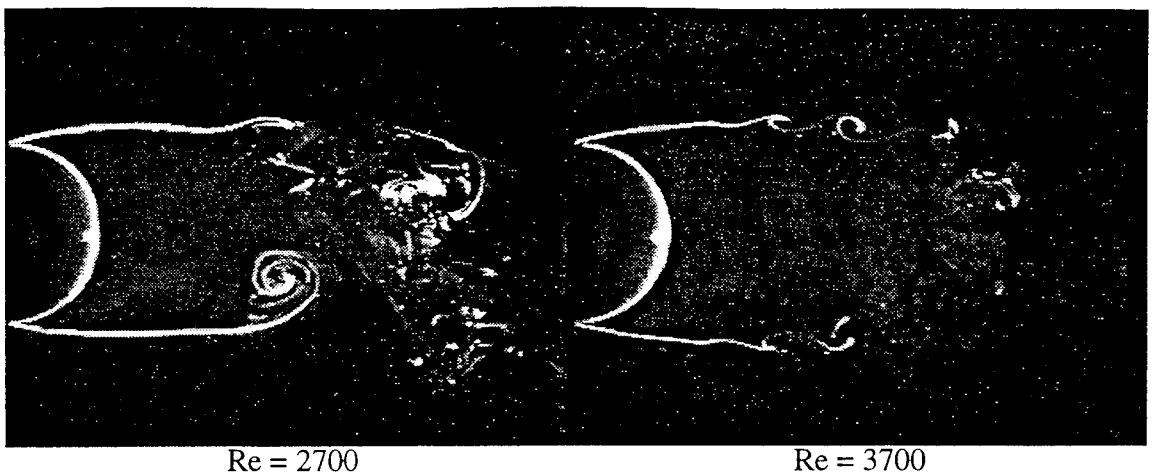

Re = 2700 Re = 3700

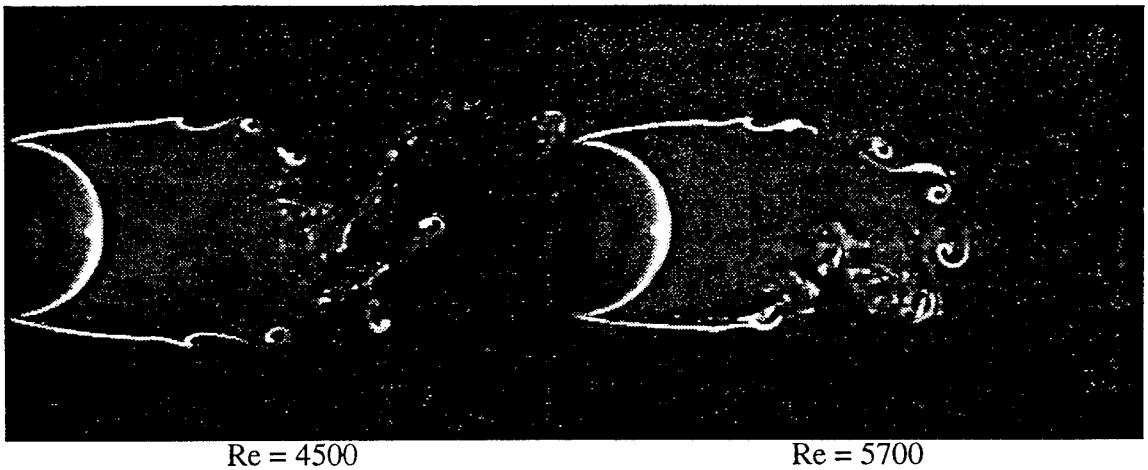

Re = 4500 Re = 5700

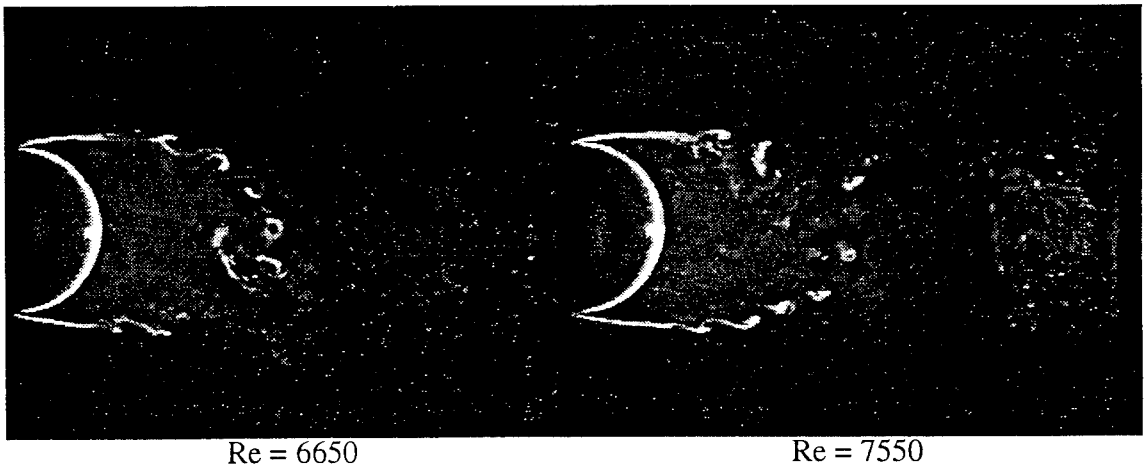

Re = 6650 Re = 7550

Figure 7.10. Video images showing shear layer instabilities at different Reynolds numbers for a circular cylinder without splitter plate, $\ell/D = 0.0$.

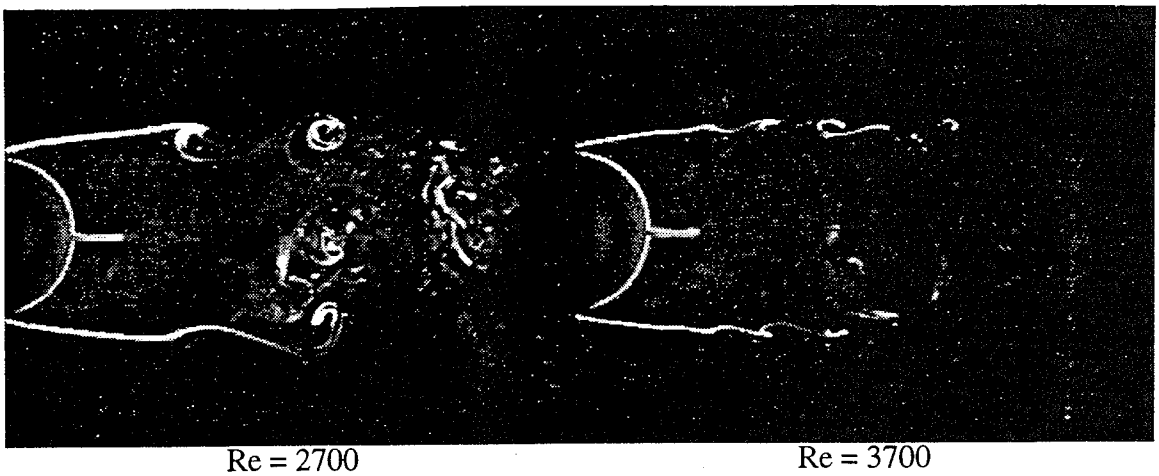

Re = 2700 Re = 3700

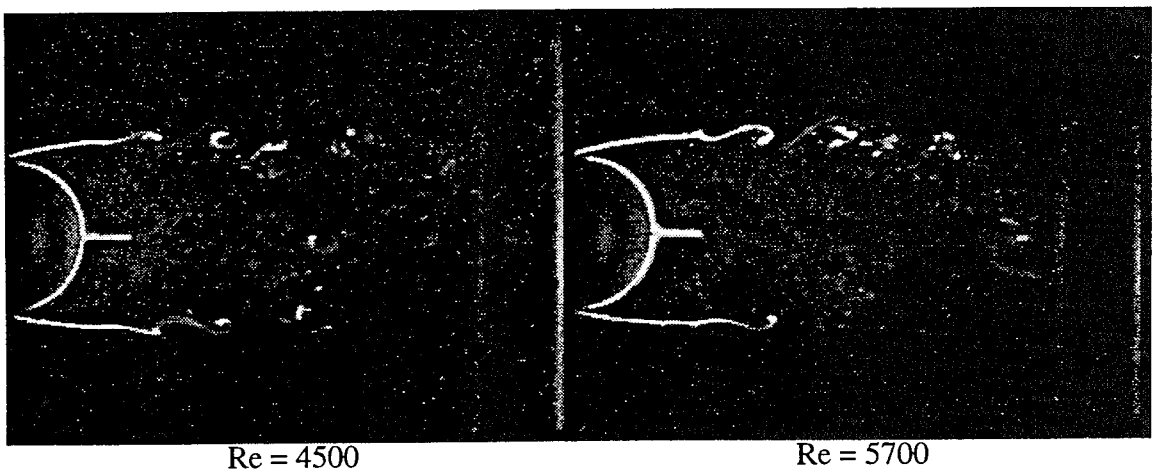

Re = 4500 Re = 5700

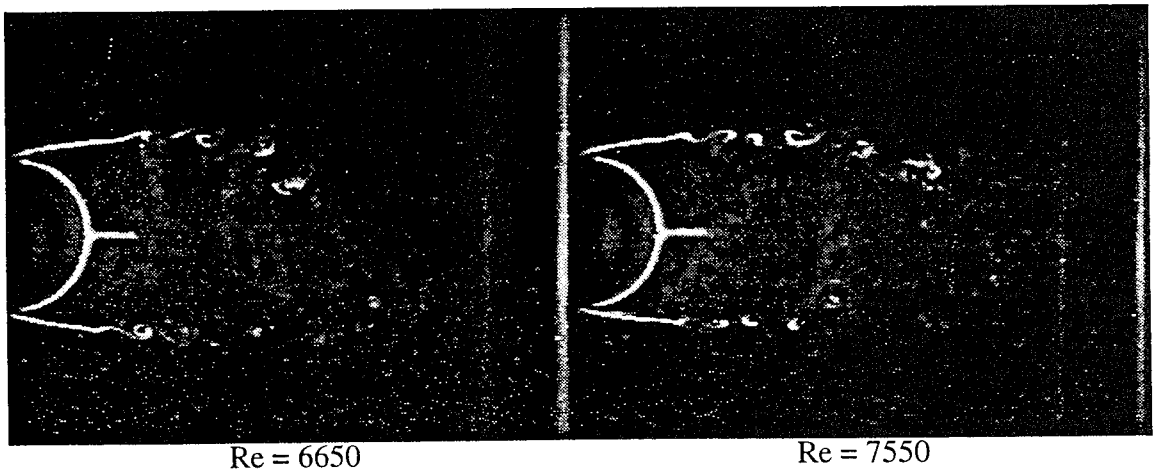

Re = 6650 Re = 7550

Figure 7.11. Video images showing shear layer instabilities at different Reynolds numbers for a circular cylinder with splitter plate, $\ell/D = 0.25$.

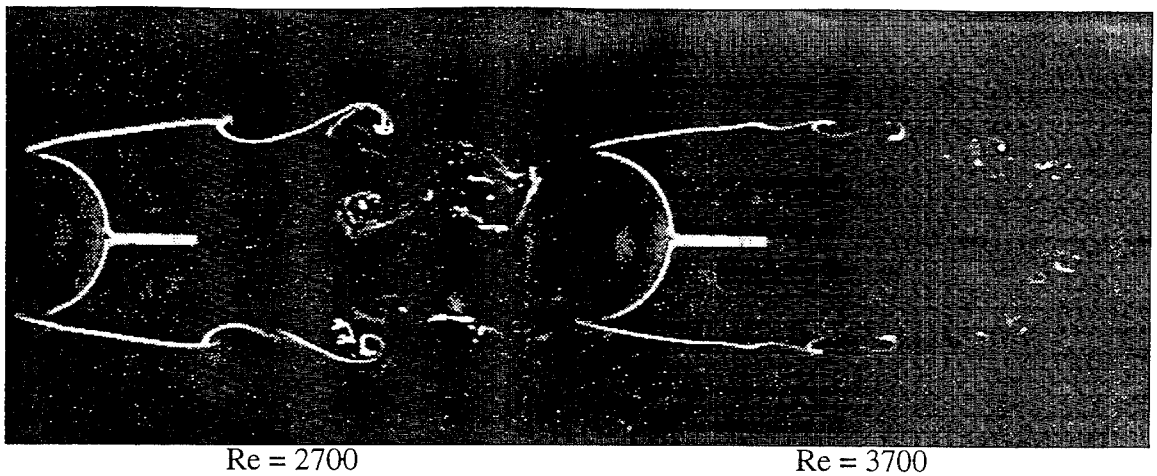

Re = 2700 Re = 3700

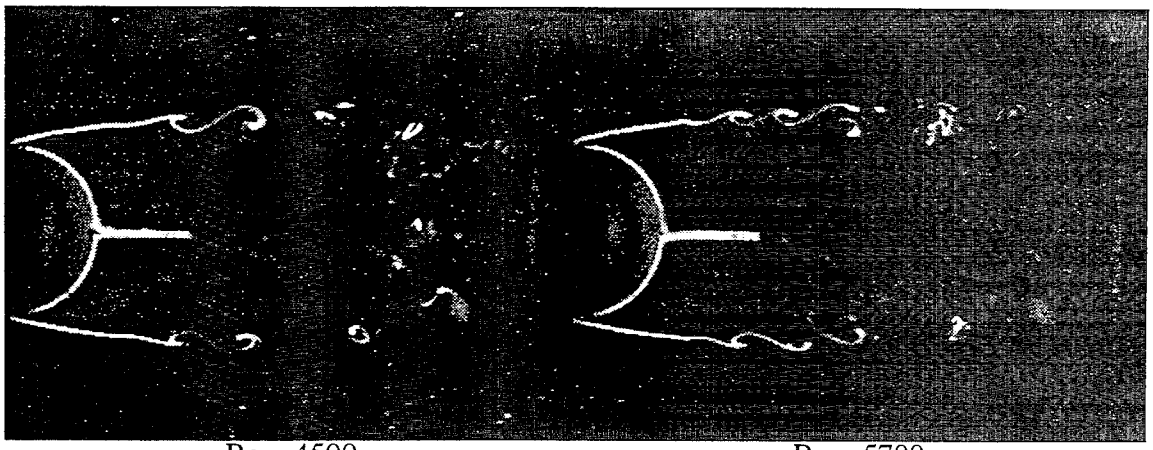

Re = 4500 Re = 5700

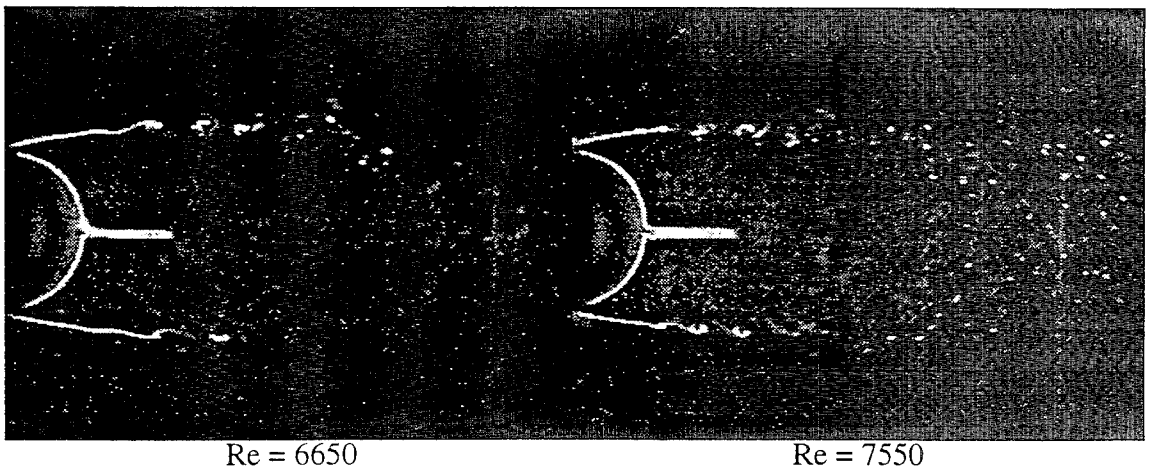

Re = 6650 Re = 7550

Figure 7.12. Video images showing shear layer instabilities at different Reynolds numbers for a circular cylinder with splitter plate, $\ell/D = 0.50$.

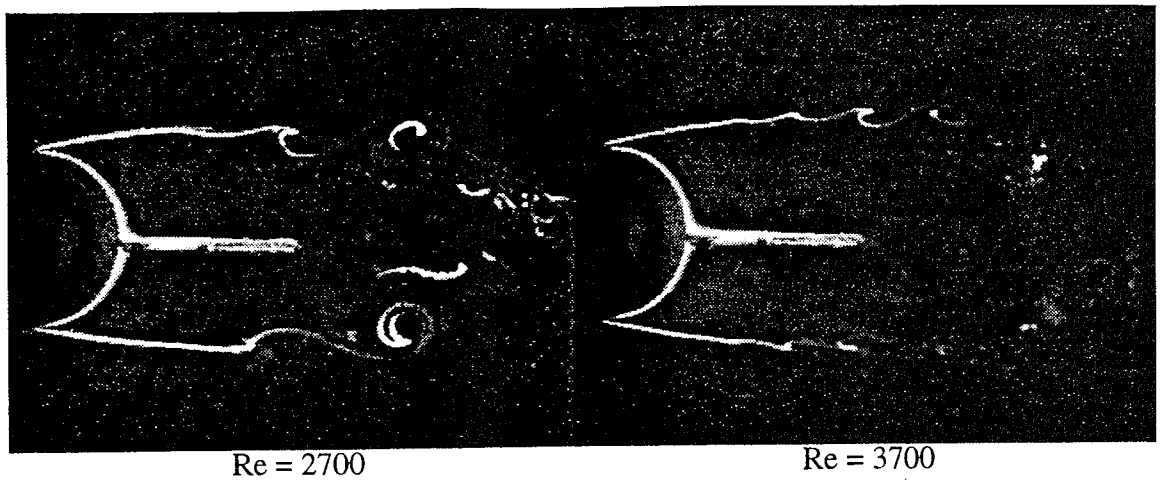

Re = 2700 Re = 3700

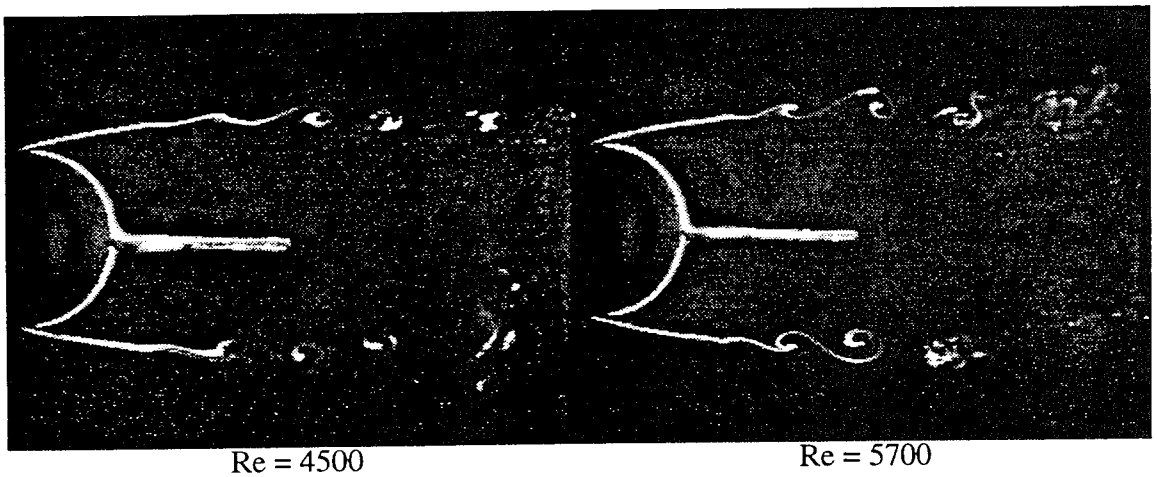

Re = 4500 Re = 5700

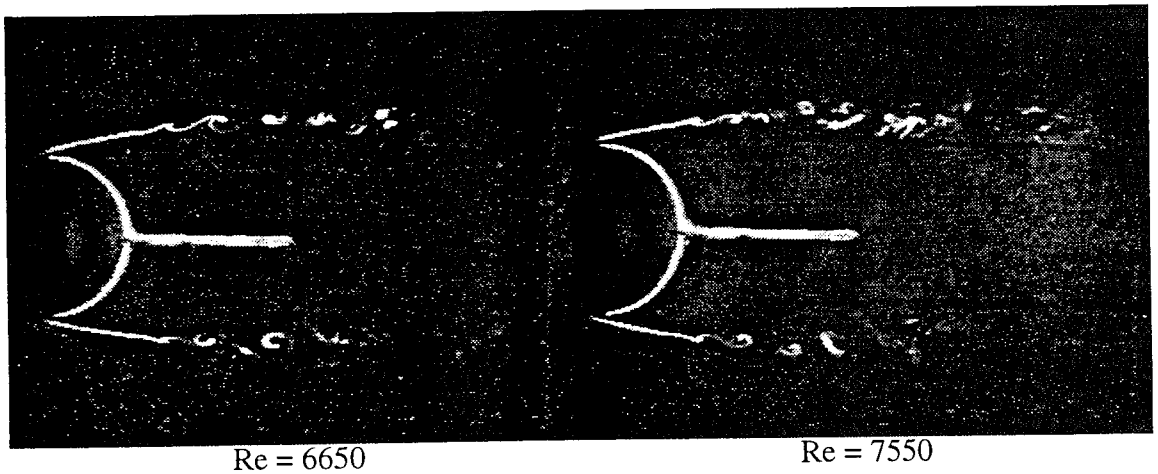

Re = 6650 Re = 7550

Figure 7.13. Video images showing shear layer instabilities at different Reynolds numbers for a circular cylinder with splitter plate, $\ell/D = 1.0$.

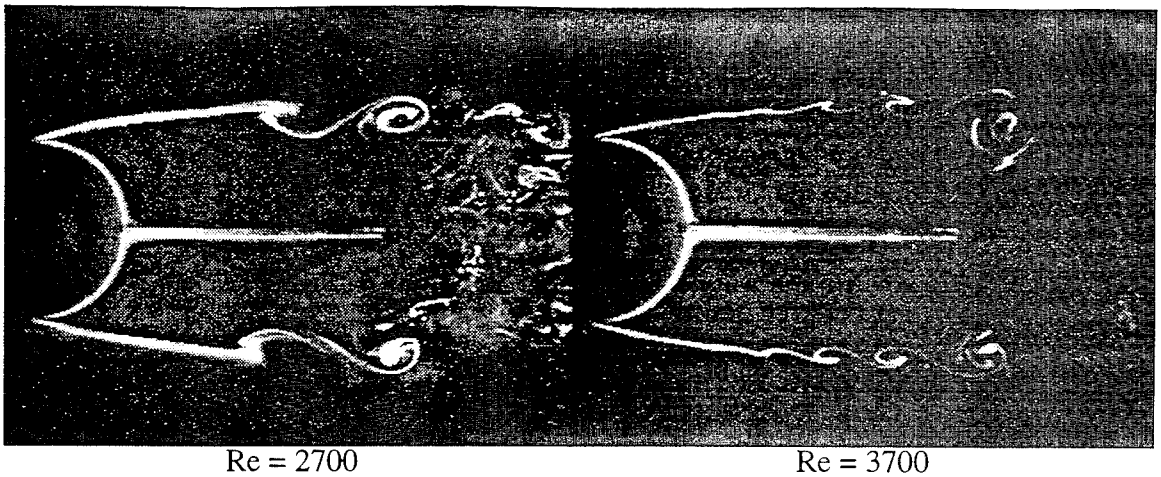

Re = 2700 Re = 3700

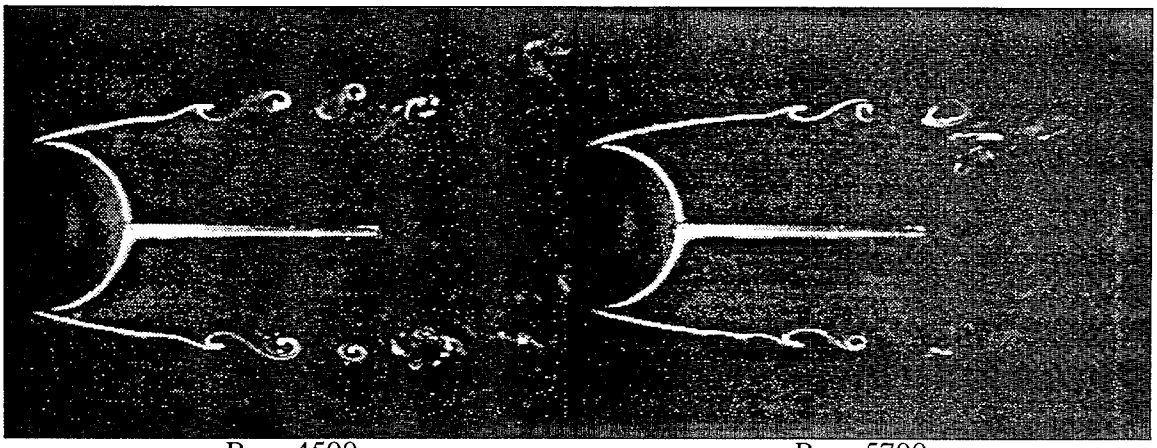

Re = 4500 Re = 5700

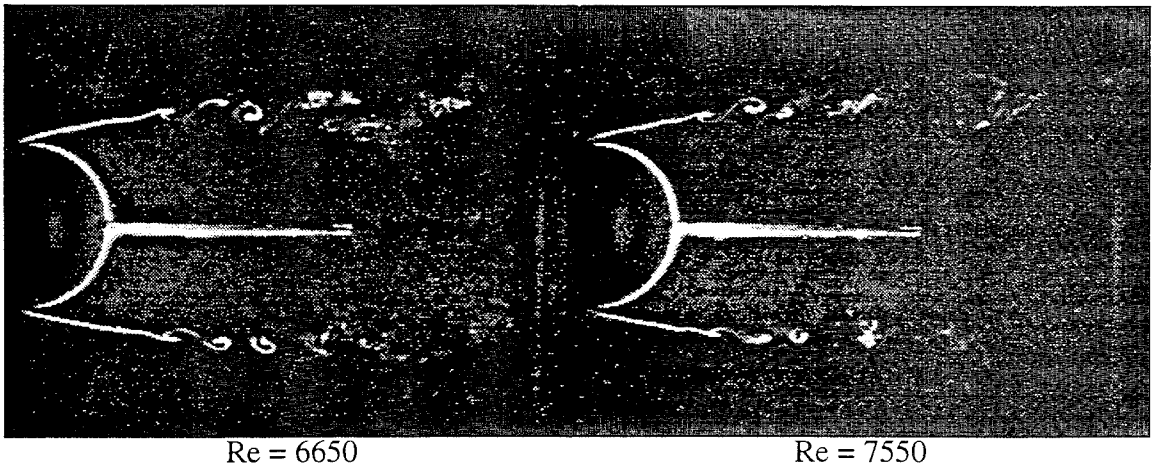

Re = 6650 Re = 7550

Figure 7.14. Video images showing shear layer instabilities at different Reynolds numbers for a circular cylinder with splitter plate, ℓ/D = 1.50.

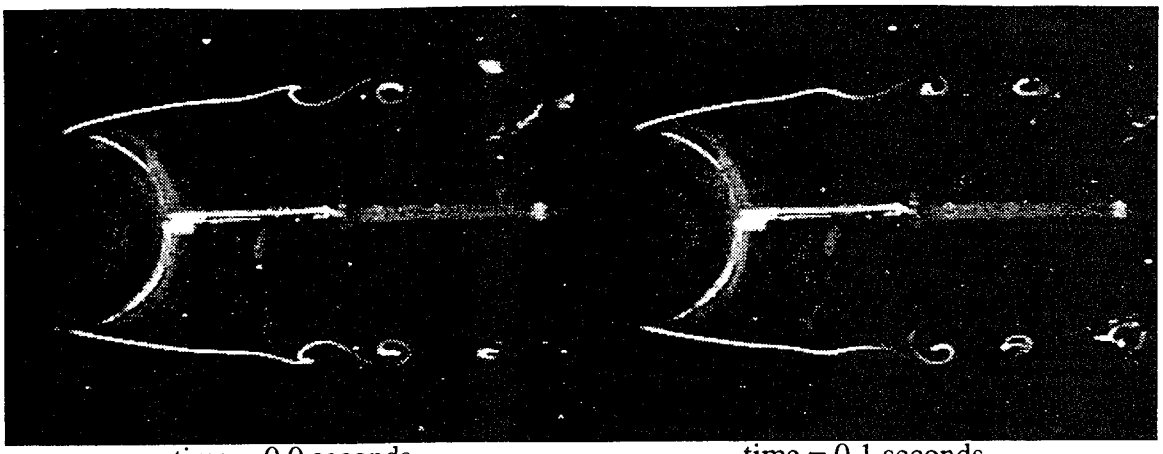

time = 0.0 seconds time = 0.1 seconds

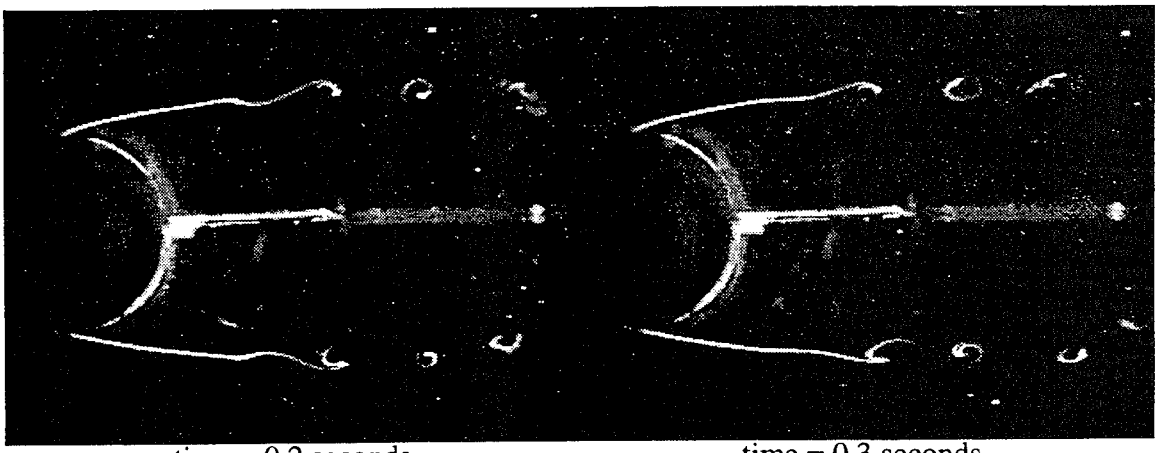

time = 0.2 seconds time = 0.3 seconds

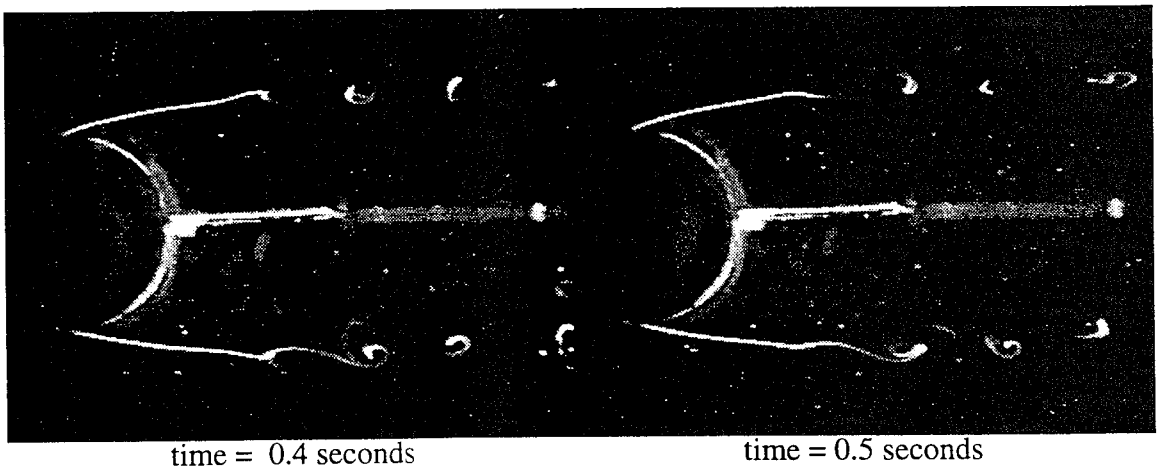

time = 0.4 seconds time = 0.5 seconds

Figure 7.15. Time sequence of video images showing the evolution of shear layer instabilities. Images indicate 'phase locking' and symmetry between the two shear layers. 1.25 inch diameter circular cylinder with splitter plate, $\ell/D = 0.90$, Re = 5700.

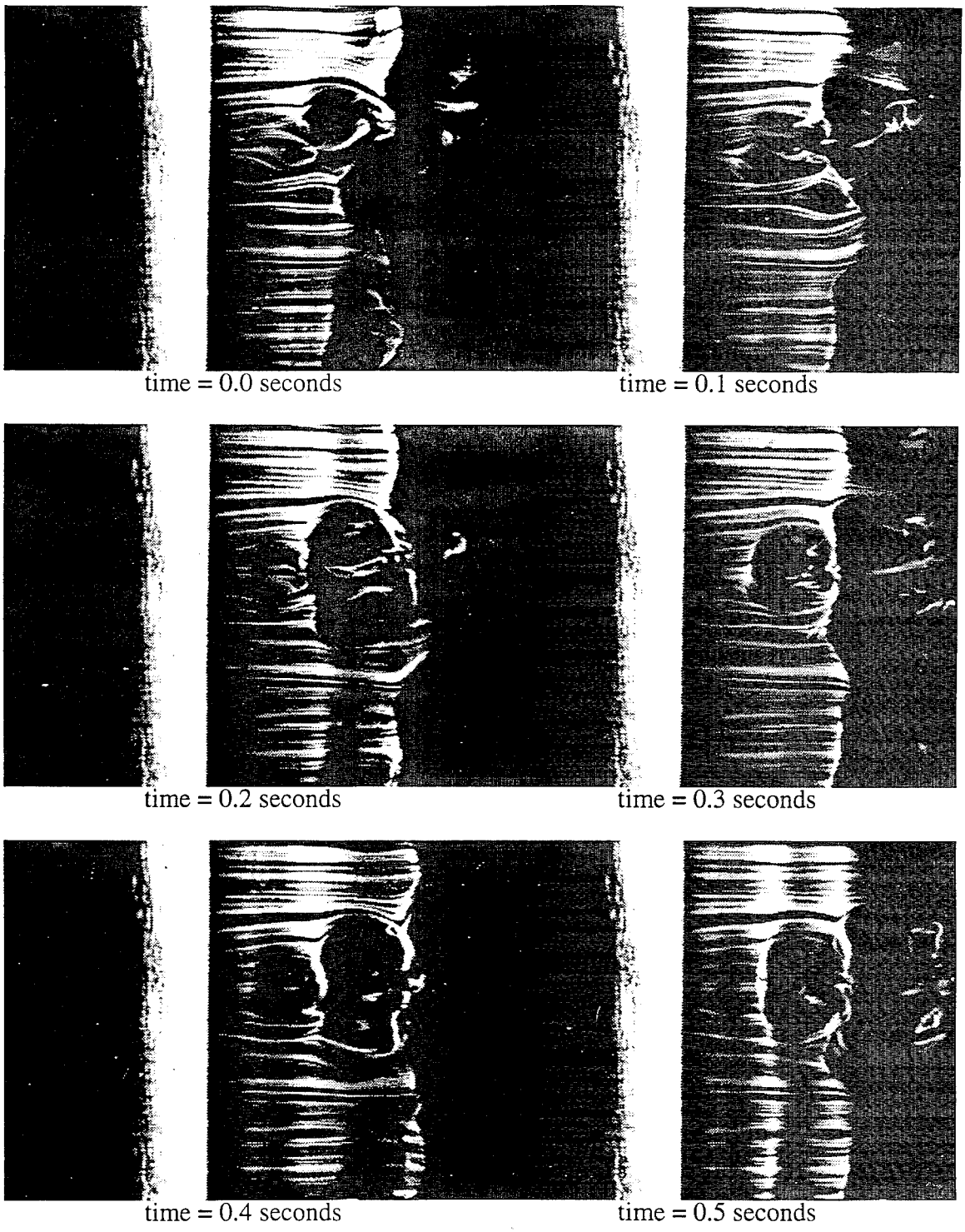

Figure 7.16. Time sequence of flow visualization images showing 3-dimensionality in shear layer for circular cylinder in uniform flow at Re = 4500.

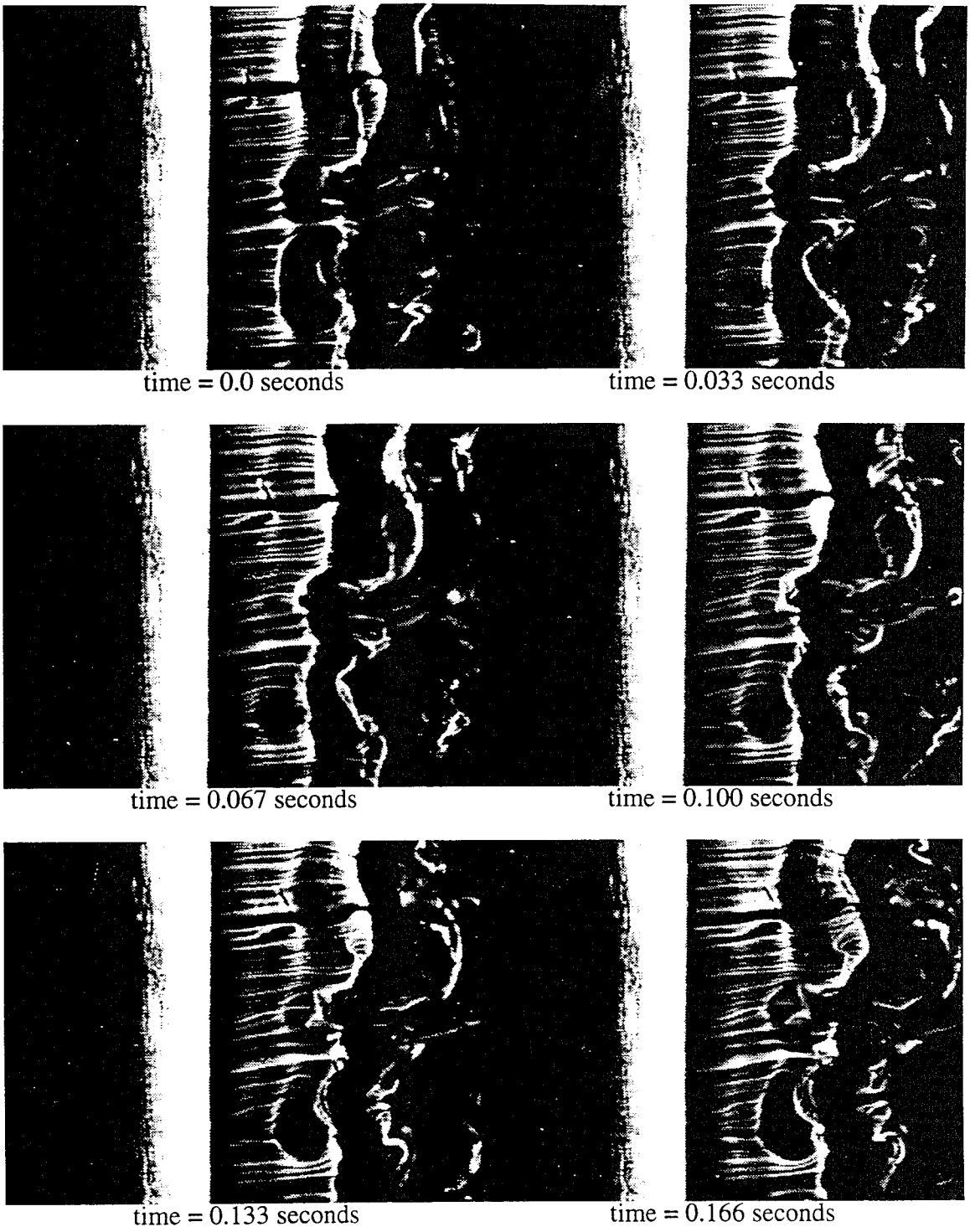

Figure 7.17. Time sequence of flow visualization showing 3-dimensionality in shear layer for circular cylinder in uniform flow at Re = 4500.

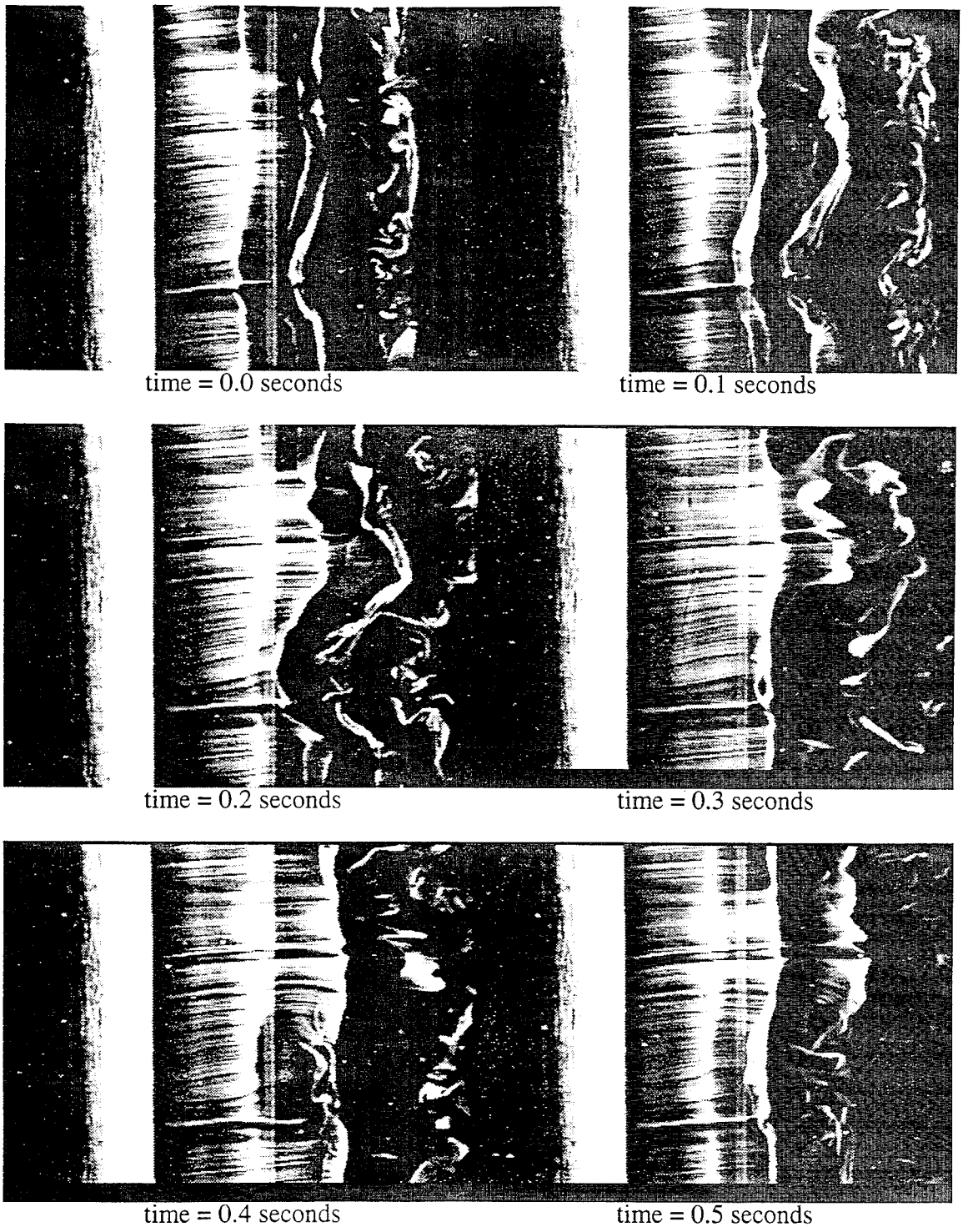

Figure 7.18. Time sequence of video images showing the spanwise evolution of shear layer instabilities. 1.25 inch diameter cylinder with splitter plate, $\ell/D = 0.90$, Re = 4500.

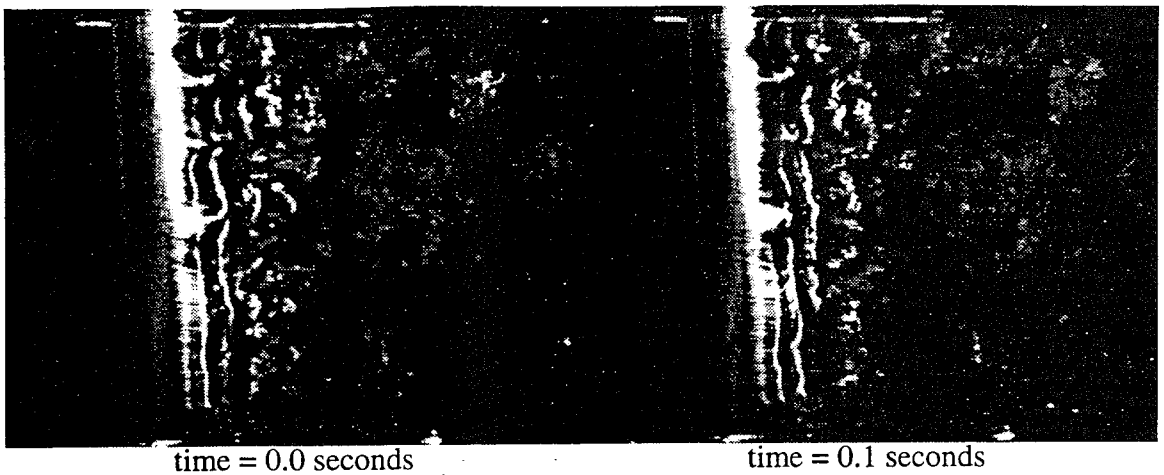

time = 0.0 seconds time = 0.1 seconds

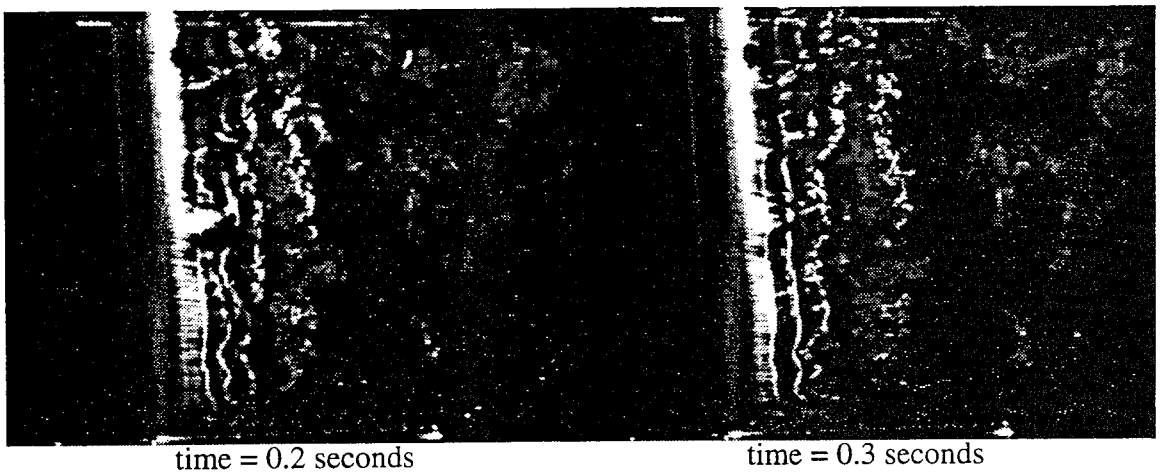

time = 0.2 seconds time = 0.3 seconds

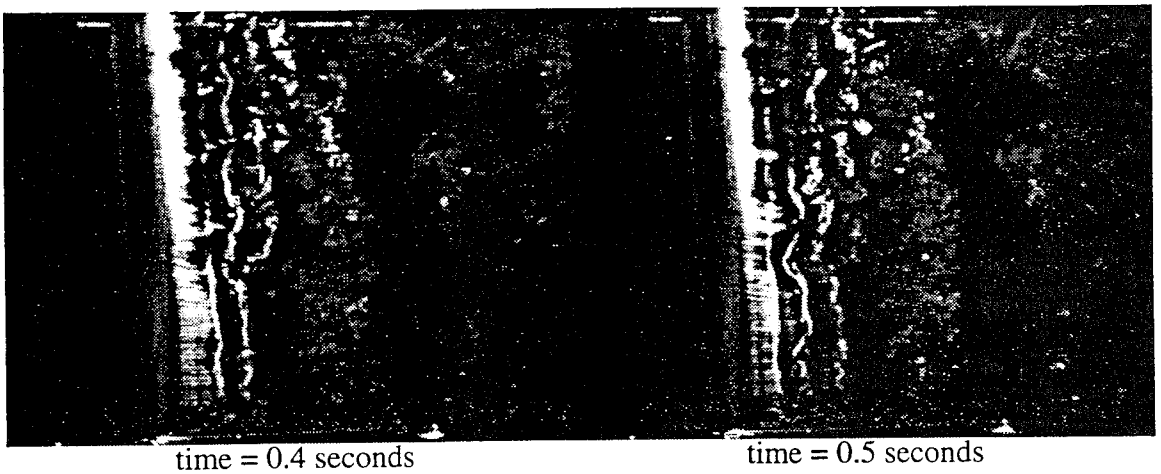

time = 0.4 seconds time = 0.5 seconds

Figure 7.19. Sequence of video images for a tapered cylinder in uniform flow showing spanwise coherence of shear layer instability waves. Flow velocity = 0.465 ft/s., max dia. = 1.375 in., min dia. = 0.75 in., span = 10.0 in.

time = 0.00 seconds Δtime = 0.40 seconds

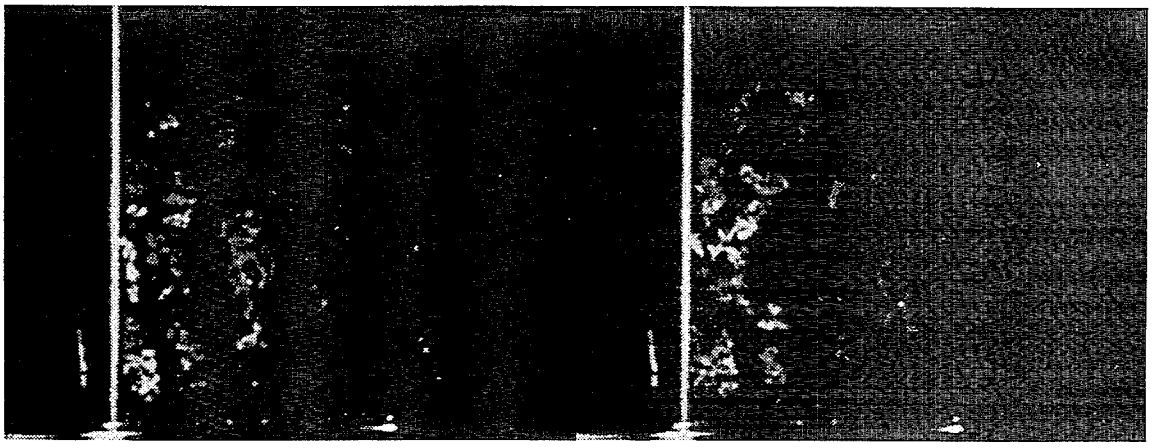

Δtime = 0.47 seconds Δtime = 0.43 seconds

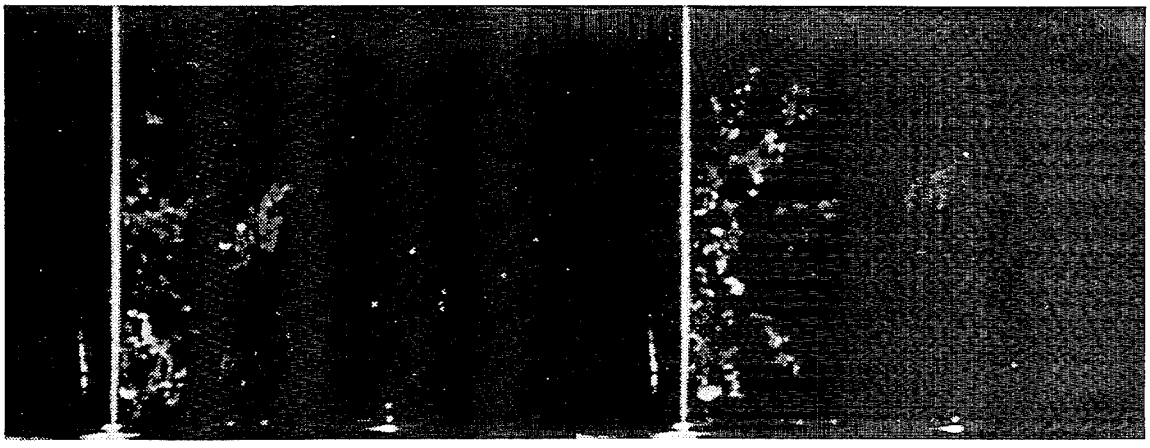

Δtime = 0.50 seconds Δtime = 0.43 seconds

Figure 7.20. Sequence of video images for a tapered cylinder in uniform flow. Light sheet positioned on cylinder centerline (y/D=0) showing primary vortices. Δtime = time between successive images. Flow velocity = 0.465 ft/s, max dia. = 1.375 in., min dia. = 0.75 in. span = 10.0 in.

ℓ/D = 0.0, time = 0.0 seconds ℓ/D = 0.0, time = 0.1 seconds

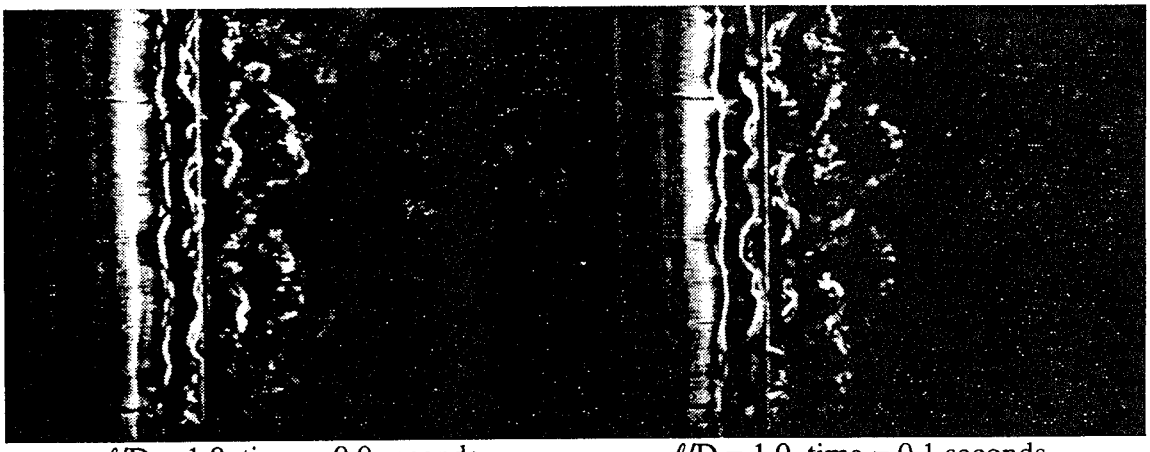

ℓ/D = 1.0, time = 0.0 seconds ℓ/D = 1.0, time = 0.1 seconds

ℓ/D = 1.0, λ/D = 2.0, time = 0.0 seconds ℓ/D = 1.0, λ/D = 2.0, time = 0.1 seconds

Figure 7.21. Video sequences showing spanwise development of shear layer instabilities for different cylinder/splitter plate configurations. Re = 4500.

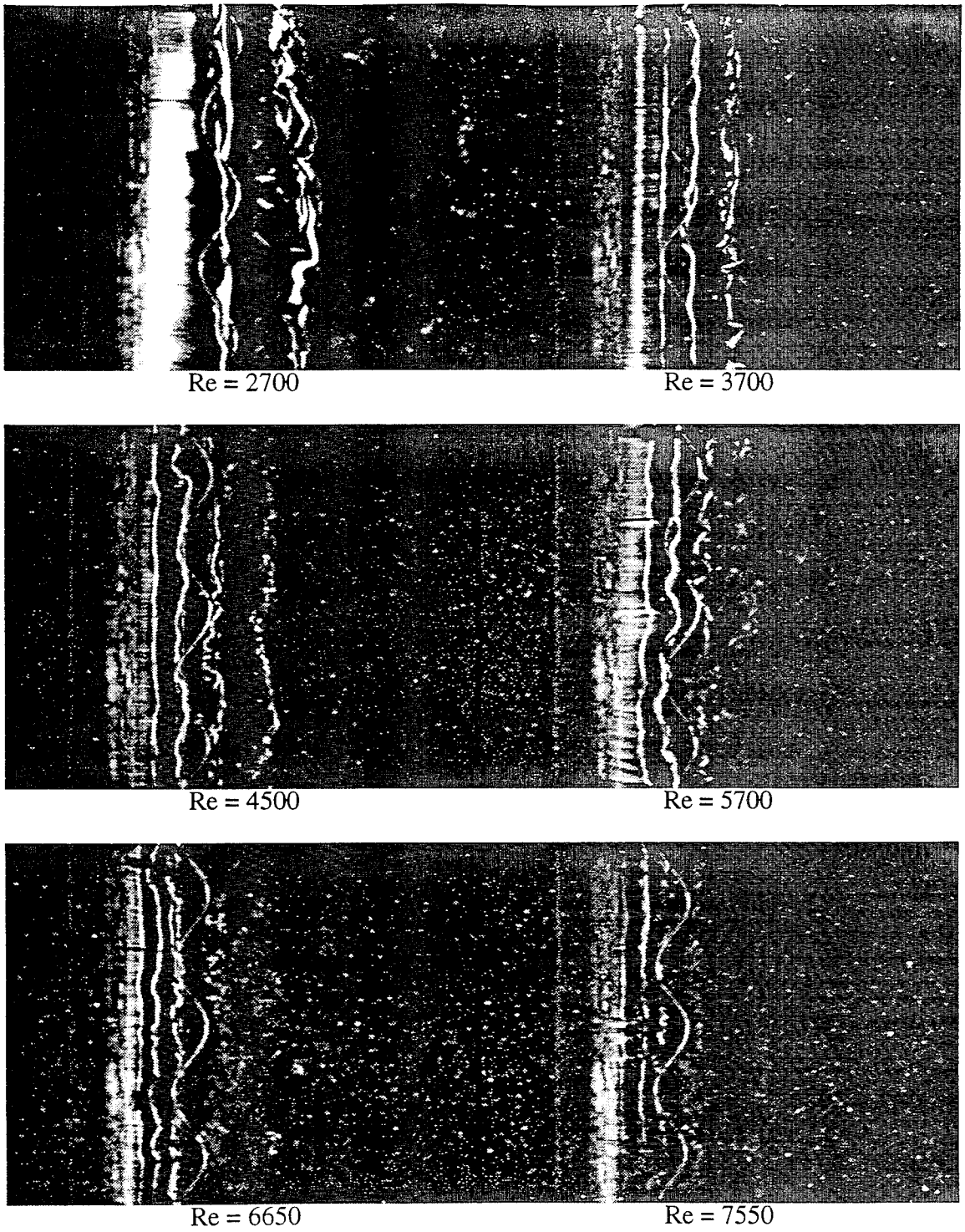

Figure 7.22. Video images showing spanwise development of shear layer instabilities at different Reynolds numbers for circular cylinder with periodic trailing edge splitter plate, $\ell/D = 1.0$, $\lambda/D = 2$.

of one half the splitter plate wavelength, or $\lambda/2$. Although results indicate that the periodic trailing edge splitter plate generally increases the spanwise coherence in the shear layer, this image suggests that the 3-dimensionality of the plate may influence the size and location of the discontinuities. The result is consistent with an increase in the organization of the shear layer caused by the introduction of a periodic trailing edge splitter plate. In addition, the image shows remarkable resemblance to images produced by Breidenthal [1980] for the wake from a splitter plate with a 3-dimensional, square wave, trailing edge. In Breidenthal's investigation, spanwise discontinuities, or vortex loops, formed at locations corresponding to the edges of the square wave. The resulting 3-dimensional wake maintained its basic geometry well downstream of the trailing edge. Breidenthal's step function trailing edge could be considered a limiting case of the sinuous trailing edge used in the present study. The flow visualization results for the two cases seem consistent in that the discontinuities form at spanwise locations corresponding to the maximum trailing edge gradient namely, the edges of the square wave in Breidenthal's investigation, and midway between peak and valley locations in the present study.

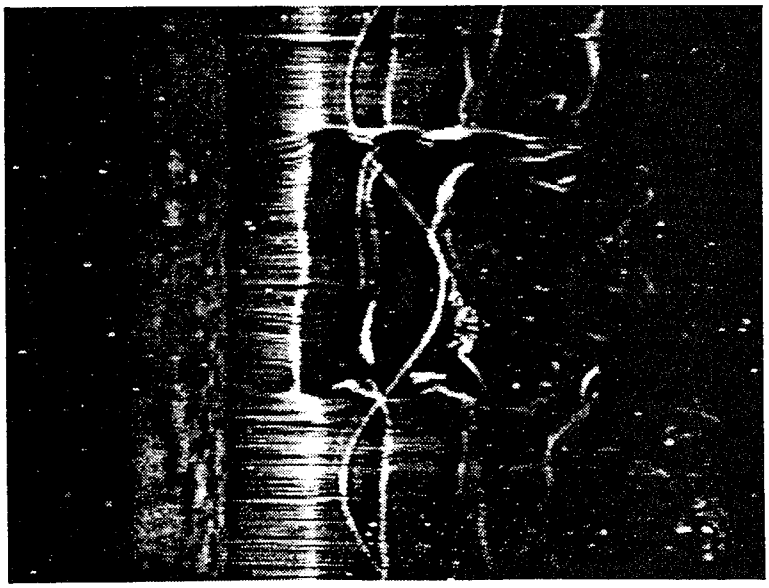

Figure 7.23. Circular cylinder with sinuous trailing edge splitter plate, $\ell/D = 1$, $\lambda/D = 2$, AR = 8, Re = 3700.

Figure 7.24 compares configurations that involve imposed 3-dimensionality by the use of cylinder taper and mean shear flow. The configurations consist of a tapered cylinder in shear flow, tapered cylinder in uniform flow, and a straight cylinder in shear flow. The generation of mean shear caused an increase in the freestream turbulence level and introduced substantial transverse vorticity to the flow. The spanwise correlation of the instability waves became very low for the shear flow cases possibly indicating that the shear layer is more sensitive to 3-dimensionality in the mean flow than in the model. The images of the tapered cylinder in shear flow indicate an oblique shedding orientation of the primary vortices with the vertex of the angle near the small diameter, low velocity end of the cylinder. The dimensions of the cylinder taper were determined to match the shear velocity profile in such a way that the expected shedding frequency would be constant across the span. This was accomplished by first determining the shear velocity profile and then designing a linear taper so that the ratio U/D = constant. The oblique angle shedding pattern observed in the images would produce such a constant shedding frequency consistent with a constant local Strouhal number concept.

Figure 7.25 shows various end views of a straight circular cylinder in shear flow with a mid-span Reynolds number of approximately 4500. The velocity increases with increasing spanwise station, z/D. The images clearly indicate a decrease in formation length for the mean shear flow compared to the uniform flow case. The amount of entrainment of shear layer fluid also increases as indicated by the large amount to precipitate found in the formation region (for comparison see Figure 7.10). The video sequences show that the formation of instability waves were irregular and accompanied by vortex pairing indicating significant 3-dimensionality. The evidence was inconclusive regarding any spanwise trends in formation region length with exception of the last image, z/D = 2.0, which clearly demonstrates a longer formation length.

Shear and taper, time = 0.0 seconds Shear and taper, time = 0.1 seconds

Uniform and taper, time = 0.0 seconds Uniform and taper, time = 0.1 seconds

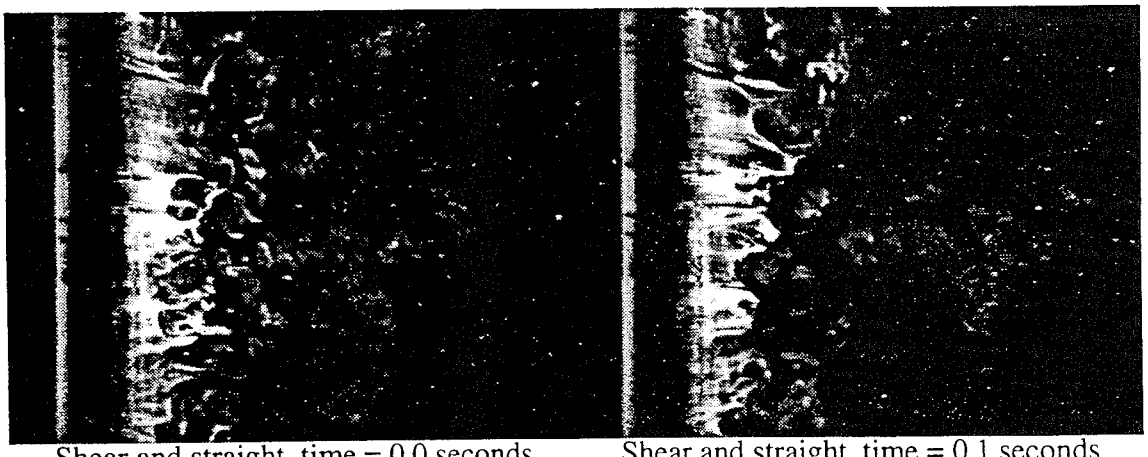

Shear and straight, time = 0.0 seconds Shear and straight, time = 0.1 seconds

Figure 7.24. Time sequence of video images comparing shear layer instabilities of straight and tapered cylinders in shear flow (velocity increases to top of picture) and uniform flow. Taper; max dia. = 1.375 in., min dia. = 0.75 in. span = 10.0 in. Straight cyl. dia. = 1.25 in. mean shear gradient, dU/dL = 0.375 sec^{-1}, uniform flow velocity = 0.465 ft/s, Re = 4500.

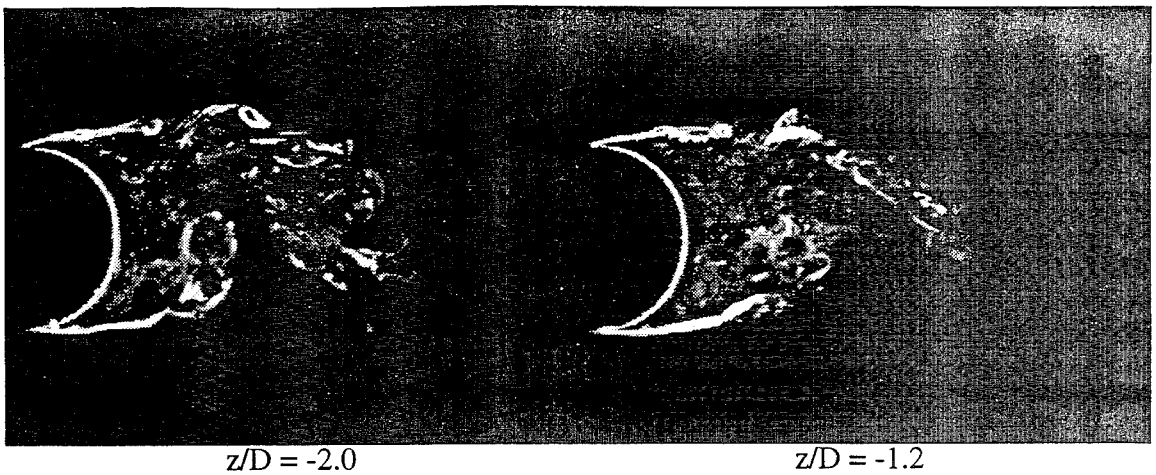

z/D = -2.0 z/D = -1.2

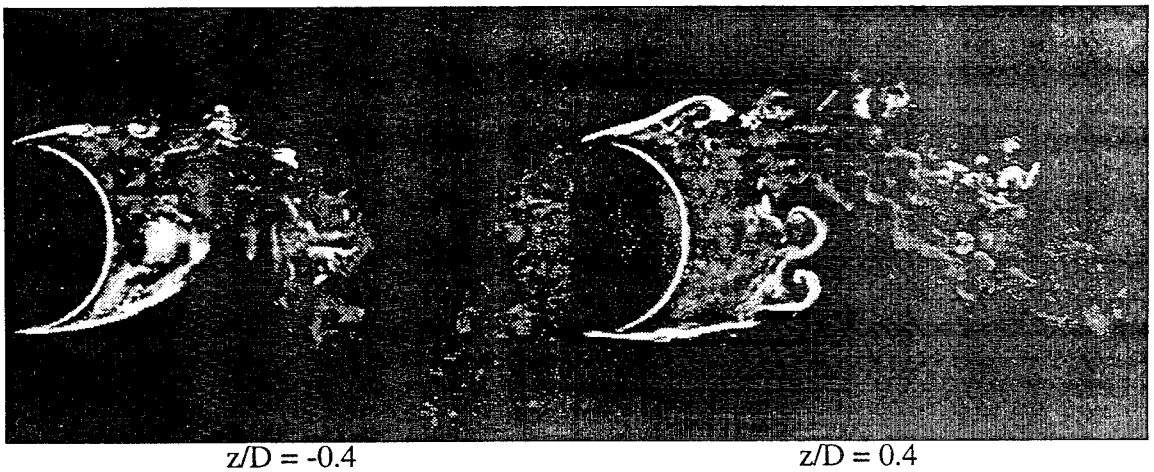

z/D = -0.4 z/D = 0.4

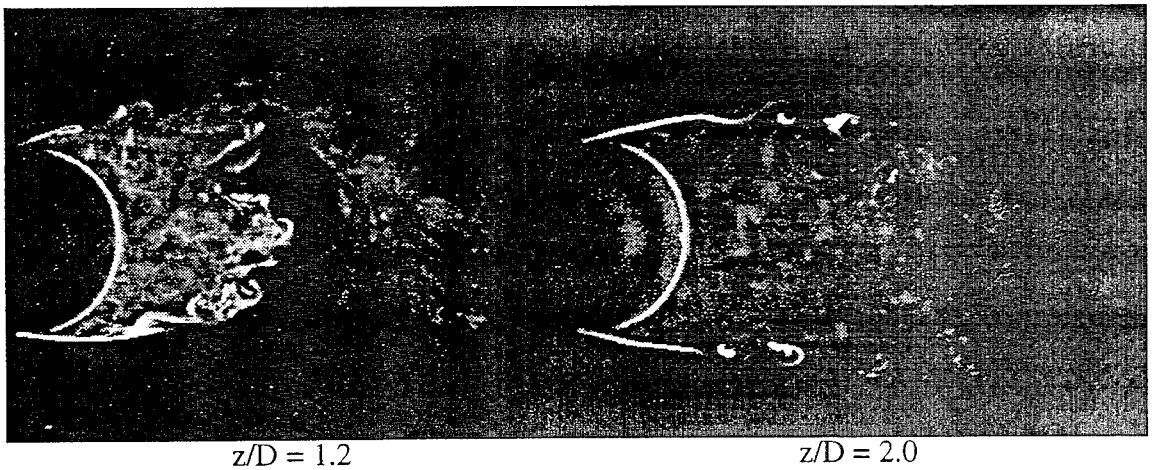

z/D = 1.2 z/D = 2.0

Figure 7.25. Video images showing shear layer instabilities at different spanwise locations for a circular cylinder (ℓ/D = 0) in mean shear flow. Reference Reynolds number = 4500. Mean shear velocity increases with increasing z/D.

CHAPTER 8. SHEAR LAYER STABILITY ANALYSIS

8.1 Introduction

In this section, the inviscid stability characteristics of the shear layer behind a circular cylinder are studied. The purpose of this study was twofold. First, to investigate the coupling between the shear layer instability mode and the primary Kármán shedding mode. Second, to compare the instability modes observed experimentally with the modes predicted by inviscid stability theory. Similarities between the structure of the shear layer behind a circular cylinder and that of mixing layers and jets, suggests the possibility of modeling the shear layer stability characteristics. Many of the same assumptions and analysis techniques in studying the linearized stability problem for an inviscid fluid can be utilized. For a thorough review of the stability characteristics of those flows, the interested reader is referred to Thomas [1991].

In the subcritical regime, where the transition occurs in the shear layer which develops from the separation point in the laminar boundary layer, the structure of the shear layer instability waves and vortices can be detected by flow visualization techniques. Figure 8.1 presents a typical video image of the instabilities in the shear layer behind a circular cylinder with a splitter plate attached. The image was produced using a laser light sheet, lead-precipitation technique (described in Chapter 7) in a water channel at Reynolds number of 5,700.

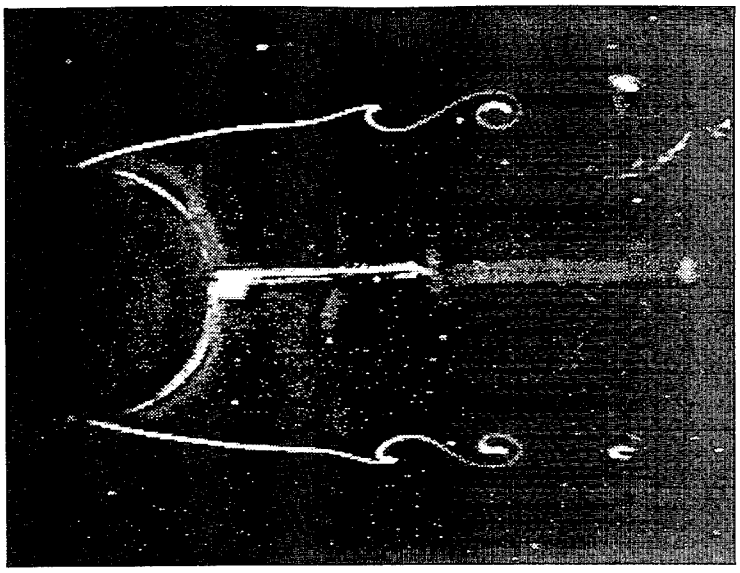

Figure 8.1. Image of the shear layer instabilities behind a circular cylinder with splitter plate, ℓ/D=0.90. Reynolds number = 5,700.

There is experimental evidence in the literature, Bloor [1964], Unal and Rockwell [1988], and Kourta et al. [1987], that at lower Reynolds numbers (Re < 15,000), coupling exists between the shear layer vortices and the primary Kármán vortices. Bloor argued that the frequency of the shear layer vortices should be proportional to a characteristic velocity divided by a characteristic length of the shear layer. Consider a developing laminar boundary layer that separates from circular cylinder. The characteristic scales are the boundary layer thickness δ, and the freestream velocity U. The boundary layer thickness, grows as

$$\delta \propto \left(\frac{\nu X}{U}\right)^{1/2} \tag{8.1}$$

where, X is the distance from the stagnation point and therefore proportional to the cylinder diameter D. Assuming that this trend continues to be valid in the initial region of the shear layer, it follows that the characteristic, or transition frequency, f_t is

$$f_t \propto \frac{U}{\delta} = \frac{U^{3/2}}{(\nu D)^{1/2}} \tag{8.2}$$

In the subcritical Reynolds number regime (300 < Re < 100,000) the Strouhal number,

$$S_t = \frac{f_s D}{U}$$

is nearly constant so the Kármán or primary shedding frequency,

$$f_s \propto \frac{U}{D}$$

The ratio of transition frequency to primary shedding frequency should then be proportional to the square root of the Reynolds number.

$$\frac{f_t}{f_s} \propto \frac{U^{3/2}}{(\nu D)^{1/2}} \frac{D}{U} = R_e^{1/2} \tag{8.3}$$

Experimental results produced by Bloor [1964] and presented in Figure 8.2 support this trend for Reynolds numbers in the range 5,000 - 30,000.

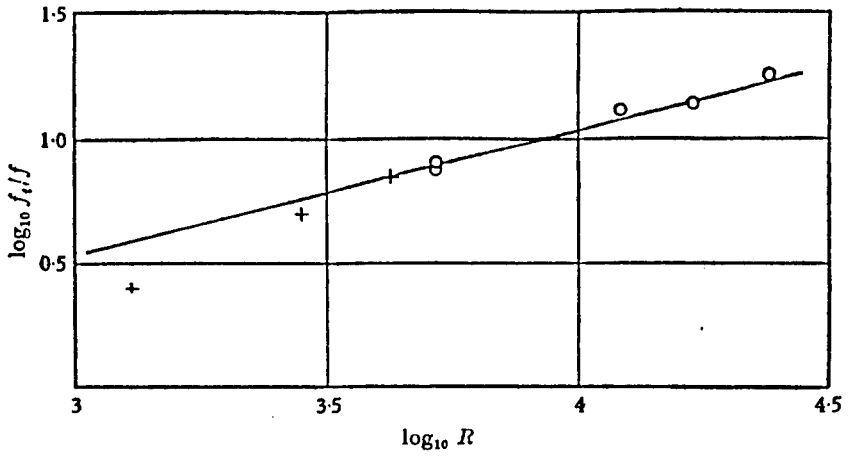

Figure 8.2. The ratio of transition wave frequency to fundamental frequency as a function of Reynolds number. o, D=1 in.; +, D=0.25 in. From Bloor [1964].

It is important to note that the frequency ratio measurements of Bloor were taken directly from an oscilloscope by counting the number of higher frequency transition waves superimposed on the primary Kármán waves. It was found in the present study that by employing this method an average frequency for the transition waves was identified whereas it was not detected through traditional FFT analysis.

Unal and Rockwell [1988] were able to detect the shear layer transition frequency from FFT analysis, although only for relatively low Reynolds numbers. Results indicate a transition frequency which is on the order of 10 times the primary shedding frequency at Reynolds numbers of 3645 and 5040. No results for the higher Reynolds number range, Re > 15,000, where the transition frequency appears to become irregular were presented.

Kourta et al. [1987] observed a strong coupling between the Kármán frequency and the transition frequency at low Reynolds numbers, 2,400 - 15,000 which agrees with Unal and Rockwell. At the high Reynolds numbers though, 16,000 - 60,000 the two modes

become disconnected and spectral peaks at the transition frequency were not detected. The authors suggest that this is a result of the length scale differences, small length scale in the transition instability compared to that of the Kármán vortices.

Wei and Smith [1986] detected the shear layer instabilities behind a circular cylinder using both hydrogen bubble flow visualization and hot wire techniques in the Reynolds number range $1{,}200 < \mathrm{Re} < 11{,}000$. Their results indicate a power law relationship

$$\frac{f_t}{f_s} = \left(\frac{\mathrm{Re}}{470}\right)^{0.87} \tag{8.4}$$

This result is contrary to the square root proportionality proposed by Bloor (Eq. 8.3). Addressing the discrepancy between their results and those of Bloor Wei and Smith report two serious limitations to Bloor's analysis. The first limitation being her assumption that f_t should scale with the boundary layer thickness. It appears more reasonable to assume that the transition vortices are generated as a result of a free-shear layer instability. Therefore, the appropriate length scale should be the shear layer momentum thickness. Second, Bloor supports her analysis on only three data points, two of which were taken at the same Reynolds number.

Wei and Smith also address the difficulties with using hot wire anemometry to detect the transition wave frequency in the shear layer. The problem comes from attempting to detect a developing Lagrangian phenomenon with a stationary Eulerian probe. Due to the flapping of the shear layer the probe only senses the instabilities intermittently. The intermittency of the signal can give rise to spurious peaks in the power spectrum when transferred into the frequency domain.

Gerrard [1978] observed the shear layer transition waves from a circular cylinder using dye injection flow visualization in a water tunnel. He noticed that the transition waves were in-phase on the two sides of the wake. This coupling occurred even when the periodic shedding of primary vortices was suppressed through the use of a splitter plate which suggest that the coupling was not caused by forcing from the Kármán shedding.

8.2 Linear Stability Analysis

The following linearized inviscid stability analysis incorporates many of the simplifying assumptions used in the analysis of plane mixing layers and jets. Although the shear layer produced by a cylinder is similar in many ways to these flows, there are important differences which should be noted about a shear layer produced from separation on a cylinder and its resulting profile. First, the shear layer behind a cylinder exists in an unsteady environment. The shedding and roll up of the primary Kármán vortices causes the shear layer to flap in-phase with the shedding frequency. When measured using time-averaged techniques this flapping action can produce a 'smearing' of the velocity profile . Secondly, the shear layer instability waves will be exposed to low frequency fluctuations which are generated by the Kármán vortex shedding process and those oscillations could have a modulating effect on the higher frequency shear layer modes. Finally, the parallel flow assumption which is accurate from the potential region through most of the shear layer may breakdown inside the wake where reverse flow and three dimensionality exists.

The numerical method used in the present analysis to compute the eigenvalues of the Rayleigh equation was previously used successfully by Thomas and Chu [1989] in their study of the 2-D jet. This method accurately predicted the initial frequency dependent growth rates, phase velocities and cross stream eigenmode profiles for the spatial amplification of infinitesimal wave-like disturbances.

The analysis begins with the linearization of the 2-D inviscid vorticity equation

$$\frac{\partial \Omega}{\partial t} + u\frac{\partial \Omega}{\partial x} + v\frac{\partial \Omega}{\partial y} = 0 \tag{8.5}$$

where, $$\Omega = \frac{\partial v}{\partial x} - \frac{\partial u}{\partial y}$$

and, $$\overline{U} = (u, v, 0) \ \textit{and} \ \nabla \mathrm{x} \overline{U} = (0, 0, \Omega)$$

Consider a small perturbation superimposed on a steady base flow,

$$u = U + \varepsilon u_1, \quad v = \varepsilon v_1, \quad \Omega = \Omega_o + \varepsilon \Omega_1 \tag{8.6}$$

where, $$\Omega_o = -\frac{\partial U}{\partial y}$$

and, $$\varepsilon << 1$$

Substitution into 8.5 and simplification gives

$$\frac{\partial \Omega_1}{\partial t} + (U + \varepsilon u_1)\frac{\partial \Omega_1}{\partial x} - \nu_1 \left(U'' - \varepsilon \frac{\partial \Omega_1}{\partial y} \right) = 0 \tag{8.7}$$

Primes denote differentiation with respect to y. Equation 8.7 is linearized by assuming that

$$U >> |\varepsilon u_1|, \quad |U''| >> \left| \varepsilon \frac{\partial \Omega_1}{\partial y} \right| \tag{8.8}$$

which is equivalent to neglecting the interactions between instability waves. The resulting linearized disturbance equation is independent of ε.

$$\frac{\partial \Omega_1}{\partial t} + U\frac{\partial \Omega_1}{\partial x} - v_1 U'' = 0 \qquad (8.9)$$

Consider a disturbance stream function given by

$$\Psi_1 = \text{Real}\left[\phi(y)\exp\left(i(\alpha x - \beta t)\right)\right] \qquad (8.10)$$

where, $$u_1 = \frac{\partial \Psi_1}{\partial y}, \quad v_1 = -\frac{\partial \Psi_1}{\partial x}, \quad and \quad \Omega_1 = \frac{\partial v_1}{\partial x} - \frac{\partial u_1}{\partial y} \qquad (8.11)$$

and $\phi(y)$ is the complex amplitude of the disturbance, α is the wave number, and β is the frequency.

Incorporation of relationships (8.11) into the linearized disturbance equation, (8.9) results in the Rayleigh equation

$$\left(U - \frac{\beta}{\alpha}\right)\left(\phi'' - \alpha^2\phi\right) - U''\phi = 0 \qquad (8.12)$$

B.C.'s
$$\phi(+\infty) = \phi(-\infty) = 0$$
$$\phi'(+\infty) = -\alpha\phi$$
$$\phi'(-\infty) = \alpha\phi$$

All variables have been non-dimensionalized by appropriate length and velocity scales to be presented later.

The numerical solution technique is simplified by further transformation of the governing equation.

$$\text{let,} \qquad \begin{aligned} \phi &= \exp\left(\int \Phi dy\right) \\ \phi' &= \Phi \exp\left(\int \Phi dy\right) \\ \phi'' &= \Phi' \exp\left(\int \Phi dy\right) + \Phi^2 \exp\left(\int \Phi dy\right) \end{aligned} \tag{8.13}$$

Substitution into the Rayleigh equation (8.11) results in a Ricatti, first order ordinary differential equation,

$$\Phi' = \alpha^2 - \Phi^2 + \frac{U''}{U - \beta/\alpha} \tag{8.14}$$

B.C.'s $\qquad \Phi(+\infty) = -\alpha, \quad and \quad \Phi(-\infty) = \alpha$

Equation 8.14 was solved numerically using a Runge-Kutta integration scheme. The eigenvalues α and β are complex and can be expressed as,

$$\alpha = \alpha_r + i\alpha_i, \quad \beta = \beta_r + i\beta_i \tag{8.15}$$

Substitution of these values into the disturbance stream function gives,

$$\Psi = \phi(y)\exp i\left((\alpha_r + i\alpha_i)x - (\beta_r + i\beta_i)t\right) \tag{8.16}$$

If β_i=0 then,

$$\Psi = \phi(y)\exp\left(i\alpha_r x - \alpha_i x - i\beta_r t\right) = \phi(y)\underbrace{\exp i\left(\alpha_r x - \beta_r t\right)}_{oscillatory\ term} \cdot \underbrace{\exp\left(-\alpha_i x\right)}_{S.\ amp.\ term}$$

where α_i gives the spatial (S) amplification rate of a infinitesimal wave-like disturbance.

If α_i=0 then,

$$\Psi = \phi(y)\exp\left(i\alpha_r x - i\beta_r t + \beta_i t\right) = \phi(y)\underbrace{\exp i\left(\alpha_r x - \beta_r t\right)}_{\textit{oscillatory term}} \cdot \underbrace{\exp\left(\beta_i x\right)}_{\textit{T. amp. term}}$$

where β_i gives the temporal (T) amplification rate of a infinitesimal wave-like disturbance.

It has been clearly shown, see Thomas [1991], that the spatial amplification formulation is correct in describing the initial growth stage of the shear layer instability. Thus, the results of the stability analysis presented herein are based on that spatial formulation, namely β_i=0.

8.3 Velocity Profile and Parameter Scaling

The shear layer velocity profile used in the stability analysis was determined from a curve fit of the measured data to a modified hyperbolic tangent function given by

$$U^*(y^*) = 0.5\left\{1 - \tanh y^*\left[1 + \operatorname{sech}^2 y^*\left(C1\tanh y^* + C2\right)\right]\right\} \quad (8.17)$$

where,

$$y^* = \frac{y_{\dim} C3}{2\theta}$$

$$U^* = \frac{U(y)_{\dim} - U_{\min}}{U_{\max} - U_{\min}}$$

and, θ = momentum thickness of the shear layer defined by,

$$\theta = \int_{-\infty}^{\infty} \frac{U(y)}{U_c}\left(1-\frac{U(y)}{U_c}\right)dy, \quad U_c = U_{\max} - U_{\min} \qquad \text{(x.18)}$$

Coefficients, C1, C2, and C3 were used to produce an accurate match and representation of the measured data. The velocity U(y) and the curvature of velocity U"(y), used in the evaluation of the Rayleigh equation can be determined from the best determined modified hyperbolic tangent function. For a more thorough description of the curve fit see Chu [1993].

The eigenvalues that were obtained from the numerical solution of the Rayleigh equation are in the following non-dimensional form

$$\alpha^* = \alpha\frac{2\theta}{C3}, \quad \beta^* = \frac{2\pi f_t}{U_{\max}}\frac{2\theta}{C3} = \frac{\omega_t}{U_{\max}}\frac{2\theta}{C3} \qquad (8.19)$$

where, f_t and ω_t are the instability wave frequencies in cycles/second and radians/second respectively. The dimensional eigenvalues were obtained from the numerical results through the following relationships

wave number, $$k = \frac{\alpha_r^* C3}{2\theta}, \quad \left[\frac{1}{\mathrm{L}}\right] \qquad (8.20)$$

spatial amplification rate, $$-\alpha_i = -\frac{\alpha_i^* C3}{2\theta}, \quad \left[\frac{1}{\mathrm{L}}\right] \qquad (8.21)$$

frequency, $$f_t = \frac{\beta^* U_{\max} C3}{4\pi\theta}, \quad [\mathrm{Hz}] \qquad (8.22)$$

and phase velocity, $$c_p = \frac{\omega}{k} = \frac{\beta^*}{\alpha_r^*}U_{\max}, \quad \left[\frac{\mathrm{L}}{\mathrm{T}}\right] \qquad (8.23)$$

8.4 Conditional Sampling Technique

Results of Nebres [1992] and those produced in the present study indicate that although the shear layer flaps, the shape of the velocity profile remains essentially constant. Therefore, conditional sampling was used to 'freeze' the shear layer and produce a more accurate, phase averaged velocity profile for the stability computations. This technique was accomplished by using two single-wire hot wire probes. One probe could be traversed through the shear layer to obtain the mean velocity profile. The other probe, located at x/D=3 and y/D=-1.5 was used as the trigger source for the conditional sampling.

The Kármán shedding frequency was approximately 50 Hz. in all experiments so the analog signal from the trigger source was low pass filtered at 100 Hz. to eliminate any high frequency components. The trigger source was AC coupled with a high pass filter setting of 3 Hz. This produced in a near sinusoidal trigger signal with zero mean. Analysis of the oscilloscope images found that the frequency of the transition waves could be estimated at around 600 Hz. A low pass filter setting of 2000 Hz was chosen for the shear layer signal, which was sufficient to assure that the instability waves would not be filtered out for the FFT experiments. For the mean velocity traverses the shear layer signal was DC coupled and calibrated against a reference pitot-static tube. A typical representation of the trigger and shear layer probe voltage time trace is presented in Figure 8.3.

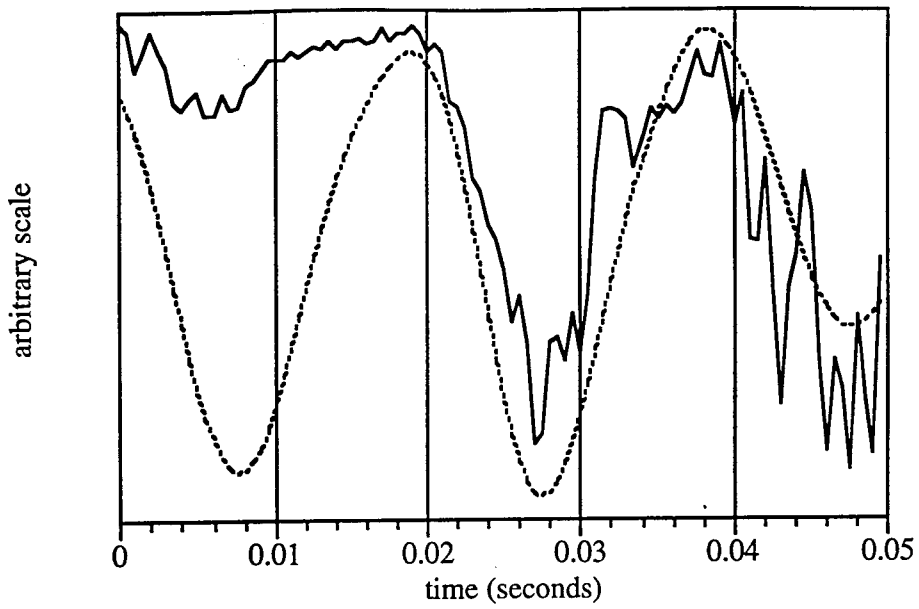

Figure 8.3. Typical voltage time traces from the trigger source (dashed) and shear layer (solid) hot wire probes.

The conditional sampling of the shear layer was accomplished by setting a trigger that would initiate data acquisition only if a preset voltage level was attained on either a positive or negative slope from the trigger probe signal. Two data samples were acquired per trigger cycle at a sample rate of 2000 Hz. The trigger level and slope was varied so that the shear layer could be captured at different phases during the shedding cycle. A total of 100 triggered shear layer samples (200 points) were averaged together at each probe location and then converted to streamwise velocity through the hot wire calibration.

Example phase-averaged velocity profiles obtained at a streamwise position of x/D=0.25 are presented in Figure 8.4. Figure 8.5 shows the same profiles shifted so that they all pass through the point y=0 at U*=0.5. These figures illustrate that although the shear layer flaps in-phase with the primary shedding frequency, the shape of the mean profile remains essentially constant throughout the cycle.

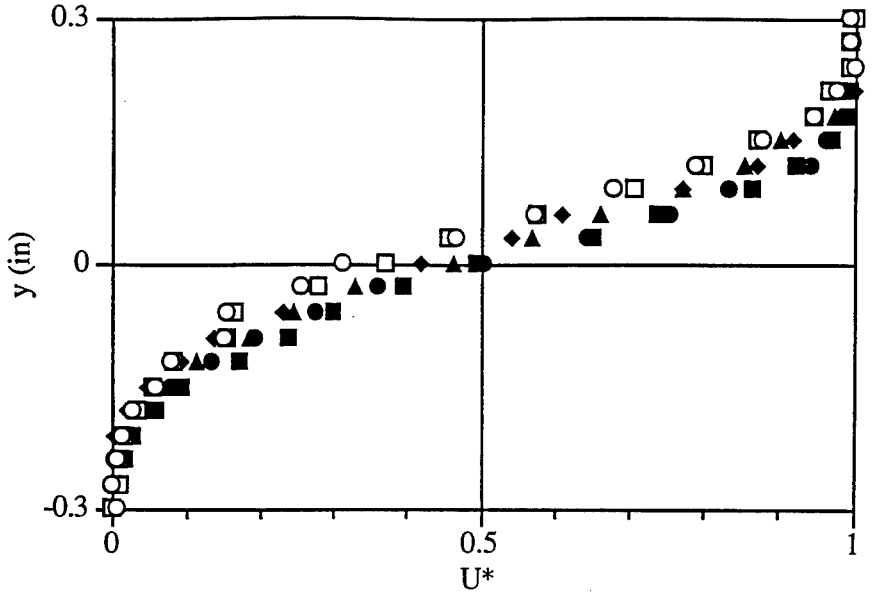

Figure 8.4. Phase averaged shear layer profiles obtained at x/D=0.25. Each symbol represents the profile at a different phase during the primary shedding cycle.

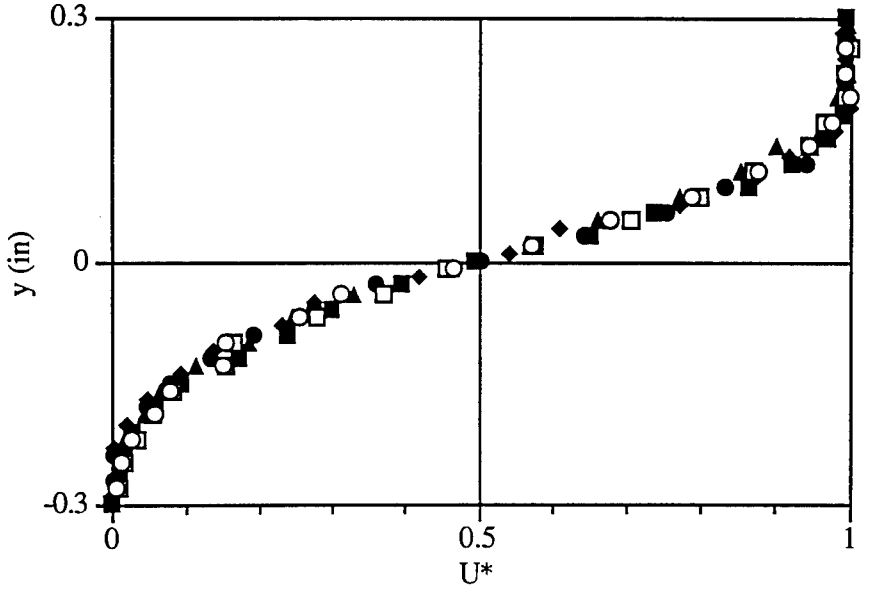

Figure 8.5. Phase averaged shear layer profiles obtained at x/D=0.25. Profile shifted in y so that data passes through y=0 at U*=0.5. Each symbol represents the profile at a different phase during the primary shedding cycle.

8.5 Results

The following results were obtained from the numerical solution of the Rayleigh equation and are based on experimentally determined, mean velocity profiles suitably fitted to a modified hyperbolic tangent function. The experiments were conducted on a straight circular cylinder in uniform flow at a Reynolds number of approximately 30,000. End plates were placed to provide an aspect ratio of 8. The configurations considered were the plain cylinder case, and two cases with a straight trailing edge splitter plate with length to diameter ratios of ℓ/D=0.5 and 1.0 respectively.

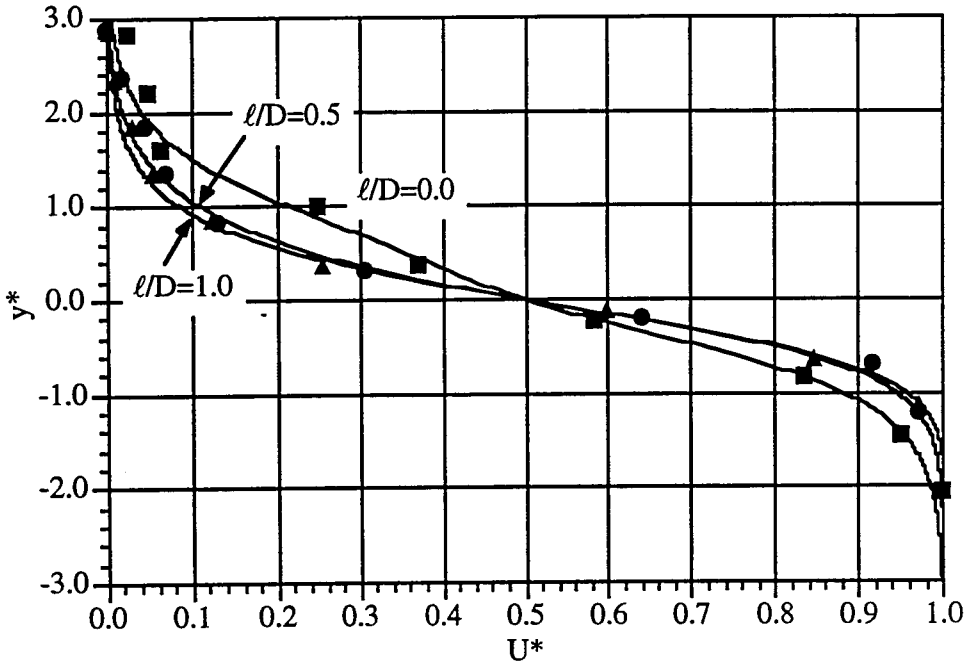

Figure 8.6. Measured shear layer profiles and corresponding curve fits for phase averaged velocity profiles. x/D=-0.125, Re=30,000.

	ℓ/D=0.0	ℓ/D=0.5	ℓ/D=1.0
θ (mm)	0.7366	0.4041	0.4030
C1	-0.40	-0.28	-0.13
C2	-0.30	0.26	0.30
C3	1.1789	0.8132	0.7870

Table 8.1. Momentum thickness and curve fit coefficients for profiles shown in Figure 8.6.

The streamwise location of the profile measurement affects the results of the stability analysis. The most unstable frequencies predicted by the stability analysis scale with $1/\theta$ where θ is the momentum thickness of the velocity profile. The momentum thickness increases with streamwise distance so care was taken to measure the mean profile at a location near the transition point. Since it was difficult to determine the precise streamwise location where transition occurred in the shear layer, an estimate was made by viewing the hot wire signal on an oscilloscope at various locations. The profiles presented in Figure 8.6 were measured at a streamwise position of x/D=-0.125. That location was close to the origin of the shear layer so that the spreading was minimized while still producing the distinct signal trace of the instability waves on the oscilloscope.

Spatial resolution of the traverse suffered due to the thin shear layer but appeared adequate to reconstruct the general shape of the velocity profile. The two cases with splitter plates attached to the cylinder had similar profiles with higher maximum velocity gradients than the case without a splitter plate. The spatial amplification rates for the three configurations are presented in Figure 8.7.

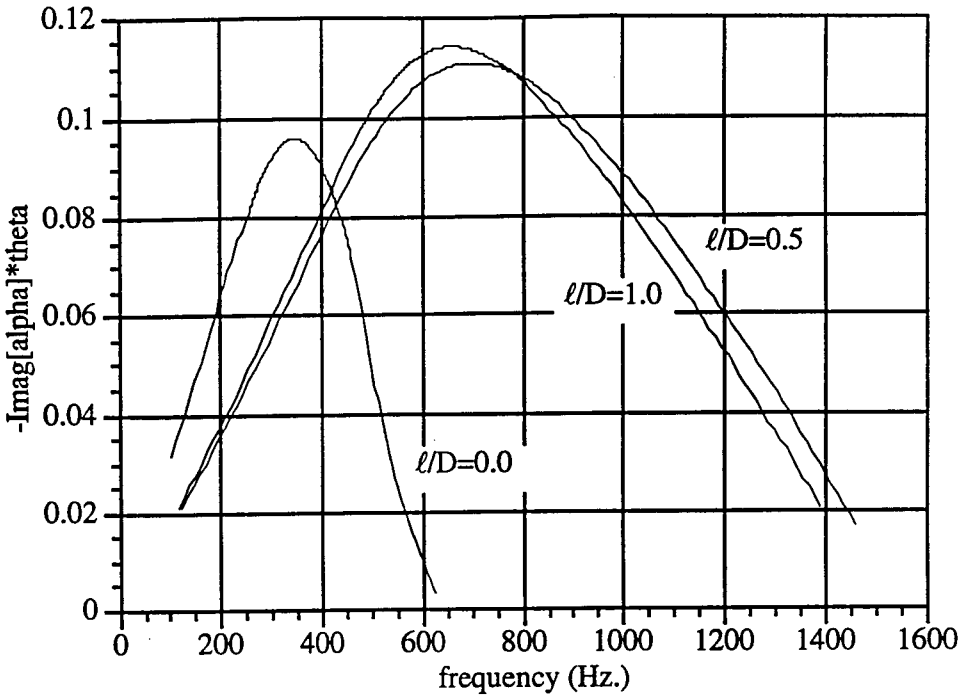

Figure 8.7. Spatial amplification rates versus instability wave frequency for the shear layer behind a circular cylinder at Re = 30,000 and x/D=-0.125.

Figure 8.7 shows that the most unstable frequency predicted for the case with no splitter plate is significantly lower than for the cases with splitter plates attached. Also, the amplification rates for the cases with splitter plates are higher than for the no splitter plate case. Although it was not possible to obtain transition frequency data by processing the experimental data through FFT methods, the average transition frequencies observed with the oscilloscope are in good agreement with the numerical predictions. The primary shedding frequency was approximately 50 Hz. so the range of ratios of transition frequency to shedding frequency is 7-14.

Figure 8.8 show typical time series records of the trigger and shear layer probes for each configuration.

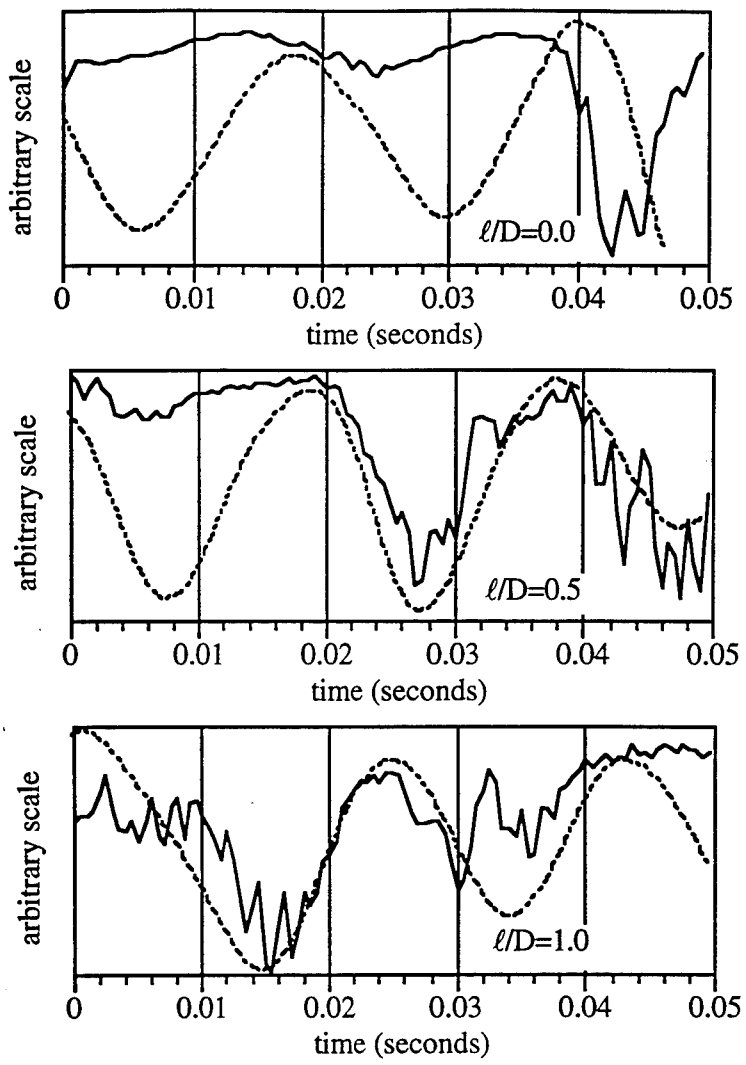

Figure 8.8. Typical time series from the shear layer (solid) and trigger (dash) hot wire probes for the various configurations. Sample rate = 2000 Hz., low pass filtered at 2000 Hz.

Although the shear layer disturbances do not appear to possess a single frequency mode, they do indicate an average frequency that is in the range of the predicted results. The disturbance waves for the cylinder-splitter plate configurations appear to be more regular and have a higher frequency than for the cylinder without the plate.

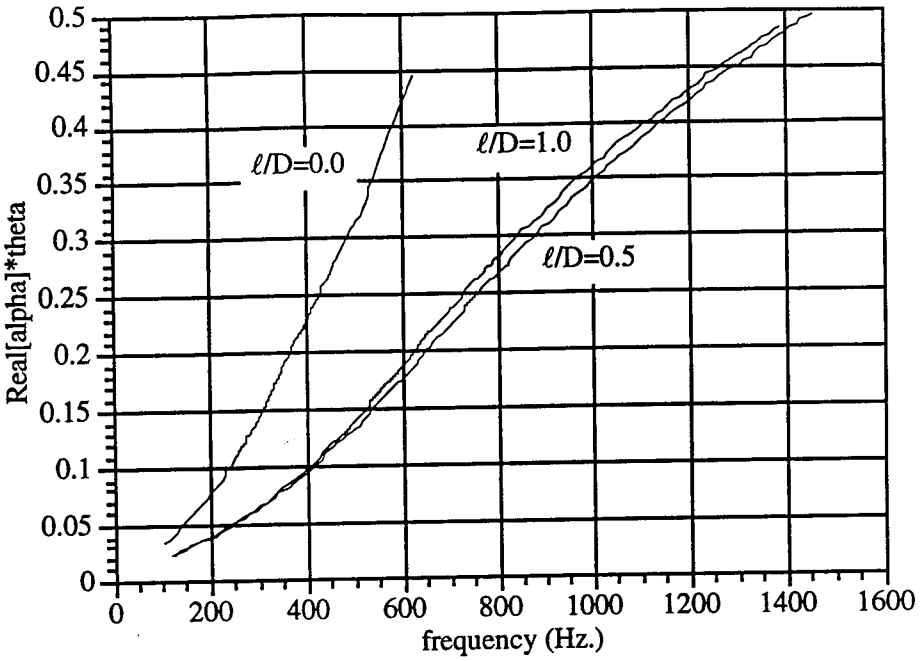

Figure 8.9. Non-dimensional wavenumber versus instability wave frequency for the shear layer behind a circular cylinder at Re = 30,000 and x/D=-0.125.

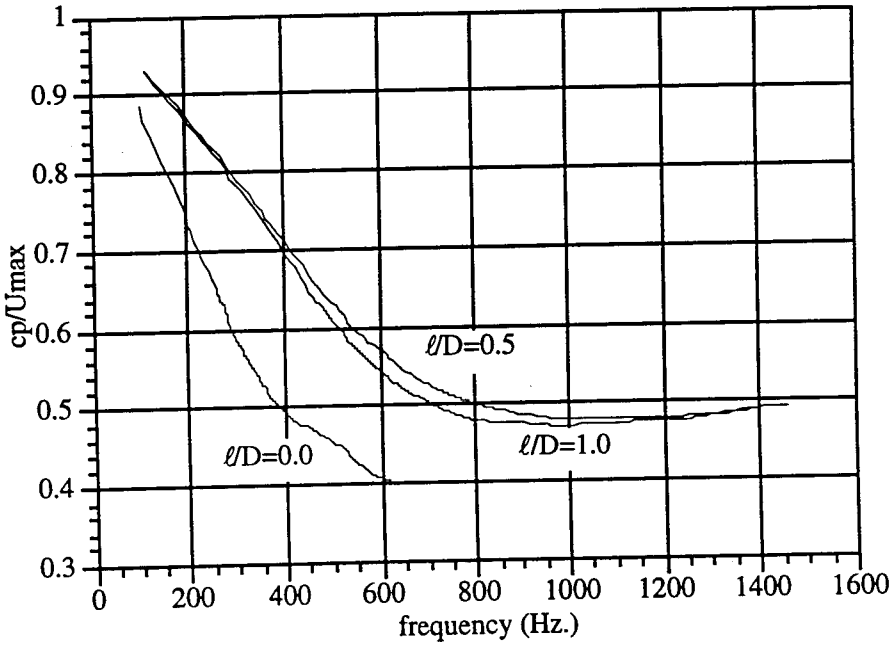

Figure 8.10. Non-dimensional phase velocity versus instability wave frequency for the shear layer behind a circular cylinder at Re = 30,000 and x/D=-0.125.

Figures 8.9 and 8.10 present the non-dimensional wavenumber and phase velocity versus disturbance frequency respectively. These results again indicate that the shear layer stability characteristics of the splitter plate configurations are similar to each other and different from that of a cylinder without the splitter plate. The phase velocity at the most unstable frequency is similar in all cases at a value of about 50% the maximum value of the mean profile. Table 8.2 summarizes the results of the linear stability analysis.

	ℓ/D=0.0	ℓ/D=0.5	ℓ/D=1.0
most unstable freq., f_m (Hz)	350	700	650
f_m/f_s (f_s=50 Hz.)	7	14	13
spatial amp. rate, $-\alpha_i\theta$	0.096	0.110	0.114
wavenumber, $\alpha_r\theta$	0.191	0.208	0.212
phase velocity, c_p/U_{max}	0.525	0.537	0.521

Table 8.2. Stability characteristics of the shear layer at the most unstable frequency.

Wei and Smith's suggested length scale, namely the shear layer momentum thickness, is related directly to the separating boundary layer thickness used in Bloor's analysis. At a fixed streamwise position the free shear layer momentum thickness, θ_{fs} is,

$$\theta_{fs} \propto \left(\frac{1}{U}\right)^{1/2} \qquad 8.24$$

Whereas the initial momentum thickness is determined by the thickness of the boundary layer at separation. Both the boundary layer thickness and boundary layer momentum thickness are,

$$\delta_o \propto \theta_o \propto \left(\frac{\nu D}{U}\right)^{1/2} \qquad 8.25$$

Before roll-up the momentum thickness grows linearly with respect to the streamwise coordinate, Chu [1993]. Thus at a fixed streamwise position prior to roll-up the momentum thickness of the shear layer is proportional to the initial momentum thickness at separation or,

$$\theta_{fs} \propto \theta_o \qquad 8.26$$

Therefore, Wei and Smith's suggestion to use the more appropriate length scale namely, the momentum thickness of the shear layer instead of the boundary layer thickness at separation produces the same result proposed by Bloor.

Using the appropriate length and velocity scales and assuming that the velocity scale for both the transition wave and primary shedding frequency are, if not the same, only differ by a constant, the following conclusion can be drawn

$$\frac{f_t}{f_s} \propto \frac{D}{\theta} \qquad (8.27)$$

Rearranging the terms produces

$$\frac{f_t \theta}{U} \propto \frac{f_s D}{U} = S_t \qquad (8.28)$$

Which, since the Strouhal number is essentially constant in the subcritical regime implies that,

$$\frac{f_t \theta}{U} = \text{constant} \qquad (8.29)$$

This parameter was calculated using data from the present study with the results presented in Table 8.3. Unfortunately the sample size of three points available in this study is too small to confirm or discount Eq. 8.29.

	Umax (m/s)	θ (mm)	f_t (Hz.)	$f_t\theta/U$
ℓ/D=0.0	16.417	0.7366	350	0.0157
ℓ/D=0.5	15.090	0.4041	700	0.0187
ℓ/D=1.0	14.723	0.4030	650	0.0178

Table 8.3. Results for non-dimensional shear layer transition frequency

8.7 Discussion of Results

Phase average sampling techniques were employed in an attempt to measure the frequency of the shear layer instability waves. Results of the experiments run at Reynolds number = 30,000 indicate that the disturbance waves are not coupled to the primary Kármán frequency. FFT methods can identify the transition wave frequencies in free mixing layers and jets that are not subjected to the large scale oscillations of the Kármán vortices. Therefore, it is concluded that the Kármán vortex shedding acts to inhibit the regular formation of shear layer instability waves.

When viewed on the oscilloscope, it is possible to determine an average disturbance frequency that is in good agreement with the most unstable frequency predicted through the linear stability analysis. The inability of the FFT method to detect the transition frequency is probably due to the very small wavelength of the disturbance compared to the Kármán

wavelength as suggested by Kourta et al. [1987]. Band pass filter techniques employed in an attempt to isolate the disturbance frequency proved unsuccessful.

Conditional sampling produced a phase averaged velocity profile of the shear layer during a selected portion of the primary shedding cycle. Therefore, the disturbance frequency was essentially isolated from the primary frequency. This method was also unsuccessful in detecting a disturbance frequency primarily due to the lack of frequency resolution capability. The frequency resolution suffered because of the small sample times required in sampling only a portion of the primary shedding cycle period. To illustrate this problem we consider the example where the shear layer is to be sampled for only one half of the primary shedding cycle. The primary shedding frequency is 50 Hz. so the sample period is 1/100 seconds. The frequency resolution of an FFT depends only upon the sample period (for a fixed sample period) and is equal to its reciprocal. Therefore, the frequency resolution in this example is equal to 100 Hz. This poor frequency resolution prevents the conditional sampling technique from achieving success.

The measured momentum thickness used in the stability analysis to determine the transition wave frequency depends on the initial thickness of the separating boundary layer. That result leads directly to the 0.5 power law Reynolds number relationship proposed by Bloor. From dimensional analysis arguments we can also conclude that the ratio of transition wave frequency to primary shedding frequency is proportional to the ratio of cylinder diameter to momentum thickness of the shear layer. If we assume that within the subcritical Reynolds number regime the Strouhal number remains essentially constant, then it follows that the nondimensional transition frequency, $f_t\theta/U$ should also be constant. More data is required to fully substantiate the conjecture.

Finally, disturbance frequency measurements have been obtained for the shear layer behind a circular cylinder, Bloor [1964] ($1{,}300 < Re < 24{,}000$), Unal and Rockwell [1987] ($140 < Re < 3{,}600$) and Kourta et al. [1988] ($2{,}400 < Re < 15{,}000$). Their results suggest a coupling between the disturbance frequency and the primary frequency however they are limited to relatively low Reynolds numbers. The evidence of this study suggests that at higher Reynolds numbers, $Re > 15{,}000$, the two phenomena are independent.

CHAPTER 9. DISCUSSION

9.1 Straight Trailing Edge Splitter Plate in Uniform Flow

The combined results from the current and previous investigations provide a more complete description of the flow phenomena that govern the selection of shedding frequency from bluff bodies. The vortex shedding frequency from a circular cylinder with a splitter plate is altered by different processes depending on the length of the splitter plate. Four regions have been defined covering splitter plate lengths $0.0 < \ell/D < 2.0$. Within each region a different phenomenon dominates the vortex shedding frequency selection. The variation in Strouhal number and typical power spectra versus ℓ/D for each region is presented in Figures 9.1 and 9.2 respectively. Figure 9.3 summarizes the effect of splitter plate length on the shear layer and shedding frequency for each region.

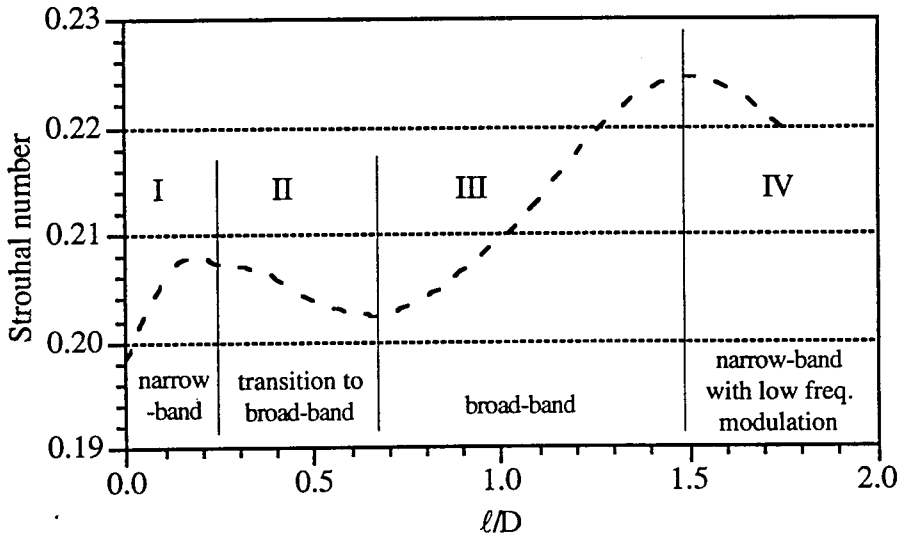

Figure 9.1. Splitter plate length regions and their effect on Strouhal number.

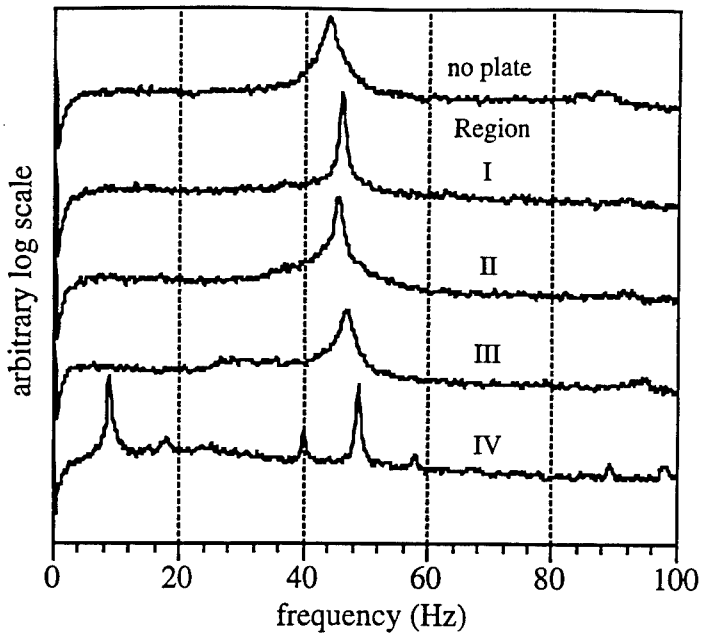

Figure 9.2. Typical power spectra for splitter plate regions.

The different regions are classified as,

I. stabilizing region

II. shear layer elongation region

III. reduced entrainment region

IV. splitter plate-vortex interaction region

In region (I), $0 < \ell/D < 0.25$, there is a progressive stabilization of the separation points and suppression of shear layer oscillation, accompanied by an increase in the shedding frequency with splitter plate length. The RMS fluctuation intensity maps, see Figure 3.17, indicate a significant narrowing of the region of relatively high fluctuation intensity in the wake by the splitter plate. Flow visualization for the plain cylinder case indicates that fluid in the base region was able to move freely along the cylinder surface in-phase with the shedding frequency. This fluid motion is necessary to sustain the shear layer oscillation. Even a very short splitter plate, $\ell/D = 0.125$, was sufficient to impede this transverse fluid motion and eliminate most of the shear layer flapping. Conditionally

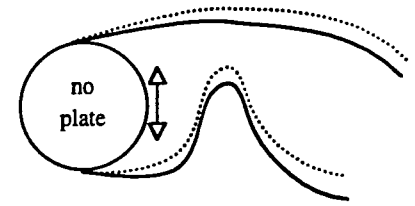

Transverse shear layer oscillation, 'flapping'
Relatively thick, diffused shear layer
Formation length of approximately x/D = 0.70
High 3-dimensionality observed in flow visualization

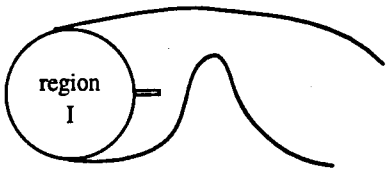

Stabilizing region
Progressive stabilization of shear layer flapping
Thin shear layer with concentrated circulation
Formation length increases with increaseing ℓ/D
Relatively strong spanwise coherence
Strouhal number increases with increasing ℓ/D
Drag decreases with increasing ℓ/D

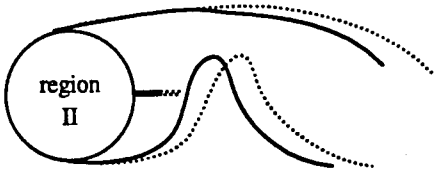

Shear layer elongation region
Increased shear layer entrainment due to increased length
Formation region increases with increasingℓ/D
Strouhal number decreases with increasing ℓ/D
Drag decreases with increasing ℓ/D

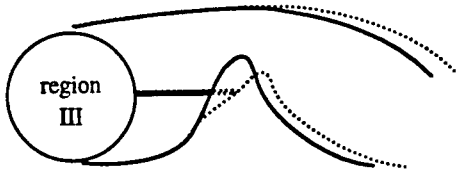

Reduced entrainment region
Plate progressively blocks entrainment of vortical fluid from across the wake
Formation length increases with increasing ℓ/D
Strouhal number increases with increasing ℓ/D

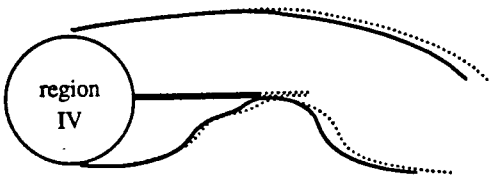

Splitter plate-vortex interaction region
Plate progressively interferes with normal vortex formation
Formation region remains near constant at x/D = 2.5
Strouhal number decreases with increasing ℓ/D
Drag increase with increasing ℓ/D however it remains well below the no splitter plate configuration

Figure 9.3. Effect of splitter plate length on shear layer.

sampled shear layer profiles, see Chapter 8, indicate that the splitter plate reduced the phase-averaged momentum thickness of the shear layer by approximately 45%. The circulation is more concentrated in the narrower shear layer which facilitates the interaction between the two shear layers thereby increasing the shedding frequency. The shedding frequency is lower for the plain cylinder because the thicker, more diffused shear layer requires a larger concentration of circulation to initiate shedding. It is expected that the vorticity shed from the boundary layer does not change significantly between the two configurations because the separation point remains fixed. The increase in shedding frequency in region (I) was accompanied by a substantial reduction in base suction and drag coefficient with a more narrow-band peak in the power spectrum.

Region (II) is defined as the shear layer elongation region and extends from ℓ/D = 0.25, where the Strouhal number had a local maximum, to ℓ/D = 0.7 - 0.8 and a local minimum in the Strouhal number. Relationships presented by Gerrard [1966] and Apelt et al. [1973] however, suggest that the local minimum in the Strouhal number corresponds to ℓ/D = 1.0. This discrepancy can perhaps be explained by the improved data resolution in the Strouhal number - ℓ/D relationship in the current investigation. Between ℓ/D = 0.4 and 1.0, Gerrard has one data point at ℓ/D = 0.65. Judging from the scatter in the three data points he obtained at ℓ/D = 1.0, the uncertainty in the measurement could easily allow the ℓ/D = 0.65 point to occur at the same Strouhal number as the ℓ/D = 1.0 point. In that case a smooth fit though the data would result in a minimum Strouhal number between ℓ/D = 0.65 - 1.0 which agrees with the results of the current investigation. A similar argument could be posed regarding the results of Apelt et al. since in that investigation there are no data points between ℓ/D = 0.5 and 1.0. In the current investigation the data resolution was improved substantially over the previous investigations by obtaining measurements for every 0.071 ℓ/D between ℓ/D = 0.0 to 1.57.

By the end of region (I), the shear layer oscillation was effectively suppressed and therefore, no longer a major factor in the determination of shedding frequency. In region (II) the action of the splitter plate was to progressively increase the length of the formation region with increasing splitter plate length. In Figure 3.24 it is shown that the formation length increased linearly with increasing ℓ/D up to approximately $\ell/D = 0.8$. This increased formation length was accompanied by an elongation of the shear layers. According to Gerrard [1966], a longer shear layer will entrain more opposite-sign vorticity from across the wake thereby producing a weaker vortex and reducing the shedding frequency. Within region (II) there was a marked reduction in shedding frequency with increasing ℓ/D up to $\ell/D = 0.7$.

In Gerrard [1966], Apelt et al. [1973], and the current investigation, the base pressure parameter and drag coefficient continued to decrease throughout region (II). As ℓ/D increased the formation length extended further downstream and its ability to affect the base region through Biot-Savart induction was reduced. Flow visualization support the progressive decrease in the base region fluid motion due to the increased formation length. The power spectra in this region show a transition from the narrow-band peak at $\ell/D = 0.25$ to a relatively broad-band peak at $\ell/D = 0.75$ reminiscent of the plain cylinder spectrum peak.

Region (III) is defined as the reduced entrainment region and covers $\ell/D = 0.7$ - 1.5. In region (II), variations in the splitter plate length altered the shedding frequency through elongation of the shear layers. However, beyond $\ell/D = 0.8$ the formation region remained at a relatively constant length of $\ell_f/D = 2.5$. The splitter plate length for which the minimum Strouhal number occurred, $\ell/D = 0.7$, corresponds to the plain cylinder formation region length, ℓ_{fo}/D. For a splitter plate length less than ℓ_{fo}/D the formation of the vortex occurs far enough downstream from the plate so that an adequate supply of

opposite-sign vorticity is entrained from the opposing shear layer to reduce the strength of the forming vortex. Further increases in the plate length narrows the gap between the trailing edge of the splitter plate and the forming vortex which impedes the entrainment of opposite-sign circulation by the forming vortex. The reduced entrainment results in a net circulation increase in the shear layer which facilitates the shear layer interactions (beyond the plate trailing edge) thereby increasing the shedding frequency. In region (III) there was a progressive increase in Strouhal number with splitter plate length. The drag coefficient and base pressure parameter experience little change although a minimum for both parameters occurred near $\ell/D = 1.0$. Data from Borg [1992] indicates that a minimum in the base pressure fluctuation intensity also occurs near $\ell/D = 1.0$. The power spectra show relatively broad-band peaks throughout region (III).

Region (IV) may be characterized as the splitter plate - vortex interaction region. The beginning of region (IV) is defined by the maximum in Strouhal number which occurred at $\ell/D = 1.5$. Beyond $\ell/D = 1.5$ the shedding frequency decreased with progressive splitter plate length increases up to $\ell/D = 2.0$, which was the maximum ℓ/D in the current study. Gerrard [1966] and Apelt et al. [1973] show the Strouhal number continuing to increase beyond $\ell/D = 2.0$. However, in a later investigation Apelt and West [1975] indicate that the maximum Strouhal number is located at $\ell/D = 1.75$ and show it to be decreasing at $\ell/D = 2.0$. The shedding frequency continued to decrease linearly with increasing plate length to $\ell/D = 5$ beyond which the regular formation of vortices was suppressed. A slight increase in drag and base pressure fluctuation magnitude was indicated beyond $\ell/D = 1.5$.

It was proposed that in region (III) the shedding frequency increased with increasing ℓ/D because the entrainment of opposite-sign circulation from the opposing shear layer was impeded by the splitter plate. It is further proposed that in region (IV) the

entrainment of opposite-sign circulation into the shear layer is effectively eliminated by the splitter plate and the decrease in shedding frequency is due to a progressive decrease in vortex strength with increasing plate length caused by cancellation of vorticity at the plate surface.

The power spectra in region (IV) indicate relatively narrow-band peaks with low frequency modulation. The modulation peak became more prominent and decreased in frequency with increasing ℓ/D, see Figure 3.21. The modulation appeared to be a near wake phenomenon since there was a reduction in the magnitude of the modulation and side-band peaks the further downstream the measurements were obtained.

The previous arguments represent an explanation for the variation in shedding frequency and drag coefficient with splitter plate length. Previous investigations, Roshko [1954], Gerrard [1966], Apelt et al. [1973], and Apelt and West [1975] confirm the general trends in the variation although there exist differences in the location of the various regions and in the magnitude of the shedding frequency. The current investigation indicates a much higher maximum Strouhal number (at $\ell/D = 1.5$) than was recorded in the previous investigations. A combination of effects might be the cause of this. Figure 3.27 indicates that an increase in aspect ratio translated the St - ℓ/D curve to higher ℓ/D's and lower Strouhal numbers. The aspect ratio of 8 used for most of the results in the current investigation compares to an aspect ratio of 12.2 in Apelt and West [1975]. Comparison of Strouhal number versus ℓ/D results shown in Figure 3.28 from two different wind tunnels with solid blockage of 5.9 and 8.3% and freestream turbulence levels of 0.5 and 0.05% respectively showed similar results although the higher turbulence level resulted in a lower maximum Strouhal number. The variation in Reynolds number had little noticeable affect on the Strouhal number.

Flow visualization indicated the presence of vortex dislocations in the shear layer similar to the Λ-structures observed by Williamson [1992], see Figures 7.16 and 7.17. The dislocations occurred for both the plain cylinder and splitter plate configurations however they occurred more frequently for the plain cylinder indicating a higher degree of 3-dimensionality. Their formation was not regular and did not indicate a spanwise preference for location. At the low Reynolds number (Re > 180) of Williamson's investigation, the shear layer was stable and the dislocations occurred in the primary vortices triggering a transition to 3-dimensionality. In the current investigation small scale vortices formed in the unstable shear layer where the vortex dislocations first occurred. The formation of the dislocations in the shear layer vortices and not the primary vortices indicate an earlier transition to 3-dimensionality consistent with the higher Reynolds number. These results give further evidence to support Bearman's [1993] claim that the dislocations are a fundamental feature of the wakes of 2-dimensional bluff bodies and are in agreement with the findings of Williamson [1992] that suggests the dislocations are a generic feature in the transition to 3-dimensionality in all shear flows.

9.2 Sinuous Trailing Edge Splitter Plate in Uniform Flow

The effect of a sinuous trailing edge splitter plate on the near wake characteristics of a circular cylinder was also investigated. Flow visualization indicated that the spanwise coherence of the vortex shedding remained strong and possibly increased for the sinuous splitter plate in comparison to the straight trailing edge splitter plate, see Figure 7.21. However there was indication of a relatively weak feedback effect from the sinuous plate that results in an occasional spanwise variation in the shear layer transition vortices. The power spectra are for all practical purposes identical at peak and valley measurement locations, even at the relatively near-wake streamwise position of x/D = 2.0, see Figures 3.23 and 3.24 . Results by Borg [1992] indicate that the sinuous trailing edge splitter plate did not produce a spanwise variation in the separation point. In most respects the time-

averaged near wake measurements gave no indication of the presence of the sinuous splitter plate. Downstream, 1 - 2 diameters from the end of the formation region however, a spanwise variation in RMS fluctuation intensity was observed. Figure 3.20 shows lower intensity at the spanwise regions corresponding to the splitter plate peak than at the valley locations.

The variation in Strouhal number with sinuous trailing edge splitter plate length was similar in almost every respect to the variation described for the straight trailing edge plates when the average length of the sinuous plate was used. The peaks in the power spectra had essentially the same shape and the formation length, wake width, Strouhal number, base pressure coefficient, and shear layer velocity clearly matched the average straight splitter plate results. It is suggested that a similar behavior between the two configurations will occur as long as the spanwise coherence length scale of the shedding is of the same length or larger than the sinuous splitter plate wavelength. If that condition is attained, the stabilization of the separation points, elongation of the shear layer, and entrainment characteristics of the near wake must be considered as an average over the spanwise coherence length scale. As described by Brown and Roshko [1974] and confirmed by Breidenthal [1980], the asymptotic state for a shear layer containing vorticity of essentially one sign is 2-dimensional. A preference for 2-dimensionality in the shear layer would naturally result in a high spanwise coherence in the shedding of vortices. However, a 3-dimensional asymptotic state is expected in wake interactions because they involve vorticity of two signs. This preference for 3-dimensionality in the wake is consistent with the spanwise variation in RMS fluctuation intensity indicated beyond the formation length for the sinuous splitter plate, see Figure 3.20.

In a similar investigation, Tombazis [1993] observed spanwise variations in the near wake characteristics for a D-shaped bluff body with a sinuous trailing edge.

However, separation occurs at the trailing edge for D-shaped bluff bodies and therefore the sinuous trailing edge used in Tombazis investigation produced a spanwise variation in the separation point. In the present investigation the continuous surface of a circular cylinder allowed the separation point to adjust to the flow characteristics and maintain a relatively fixed location along the span. Therefore, the transition frequency and location, and initial thickness of the shear layer from a circular cylinder with a sinuous splitter plate should be relatively constant across the span compared to those same characteristics for the sinuous trailing edge D-shaped model.

Vortex dislocations similar to those discussed in the previous section were observed in the shear layer of the sinuous splitter plate configuration however, unlike the previous cases they appeared to have a preference for the spanwise location at which they occurred. Flow visualization results indicate that the periodic trailing edge eliminates some of the randomness associated with the spanwise placement of the vortex dislocations. The dislocations formed symmetrically above the peaks in the sinuous trailing edge splitter plate with spanwise boundaries that corresponded to the maximum gradient points on the splitter plate's sinuous trailing edge, see Figure 7.23. Hence, the sinuous trailing edge imposes a preference on the formation location of the dislocations and therefore has an organizing effect on the near wake. Similar dislocations were observed by Breidenthal [1980] for a flow past a flat plate with a square wave type trailing edge. The square wave could be considered a limiting case of a spanwise periodic trailing edge.

9.3 Straight Trailing Edge Splitter Plate in Shear Flow

In this section the effect of a mean shear approach flow on the circular cylinder is investigated. Experiments were conducted on a circular cylinder oriented such that the mean velocity increased across the span from z/D = 3.0 to -3.0. Consideration must be given to the increased 3-dimensionality in the vorticity distribution of the flow field as well

as the 3-dimensionality introduced by the local variation in mean velocity across the span. The freestream shear generates vorticity that initially has a transverse orientation although it is turned into the streamwise direction as the fluid convects around the cylinder. This streamwise vorticity interacts with the primary vortices being shed from the body and significantly increases the 3-dimensionality of the wake region.

The vorticity that is shed from the boundary layer to produce the Kármán vortices varies in strength across the span due to the local variation in mean velocity. In order to conserve circulation along the primary vortex filaments spanwise cells of constant circulation strength are formed. This spanwise cell structure is well documented in investigations by Maull and Young [1973], Rooney and Peltzer [1981]. Rooney and Peltzer [1982], and Woo et al. [1989]. In the current investigation two spanwise cells were observed for a cylinder with aspect ratio of 8. The cell located on the high velocity side had a dominating effect over the low velocity side due to its greater momentum and vorticity. This is supported by power spectra results showing that the shedding characteristics for the low velocity cell are more 3-dimensional, because they are susceptible to modulation effects and changes in aspect ratio than those for the high velocity cell, see Figure 4.12. Various other results indicate that the wake characteristics are more 3-dimensional at the low velocity side. The time-average RMS intensity shear layer profile is thicker indicating a more diffused shear layer. Flow visualization shows an increase in 3-dimensional characteristics, e.g., vortex pairing and irregular formation of transition vortices. And finally, the power spectrum shows a more broad-band peak indicating a higher degree of 3-dimensionality.

These differences in the level of organization between the low and high velocity sides have an effect on the local shedding characteristics. For the shear flow configuration the non-dimensional shear layer velocity, U_S/U, decreased with increasing velocity across

the span. One would expect a constant value of U_s/U along the span if the shear layer velocity scaled in proportion to the local velocity. The decrease in the shear layer velocity at the high velocity side though is consistent with the uniform flow results and can be attributed to the relative increase in 2-dimensionality in that region compared to the low velocity side. The uniform flow results indicated a more 2-dimensional shedding process for the splitter plate configuration compared to the plain cylinder case. This increase in 2-dimensionality resulted in a decrease in the base pressure parameter and shear layer velocity, see Section 9.1. Therefore it follows for the shear flow configuration that the shear layer velocity decreases at the high velocity side of the span where the flow is more 2-dimensional. The formation length and wake width increased with increasing mean velocity across the span.

In Figure 9.1 the Strouhal number variation with ℓ/D for the uniform flow configuration was divided into four regions in which different phenomena dominate the shedding frequency selection process. Analysis of those results and the formation length results for both uniform and shear flow configurations shown in Figures 3.25 and 4.14 indicate two important characteristics. First, for the low velocity portions of the span in the shear flow configuration the formation length for a given ℓ/D is less than the uniform flow formation length at the same ℓ/D. Therefore it can be argued that due to the closer proximity of the vortex to the plate trailing edge the shedding characteristics should be evaluated at a higher ℓ/D region in Figure 9.1. Second, at the high velocity portion of the span the formation length is greater than it is for the uniform flow case at the same ℓ/D. However, the shedding frequency varies in a similar manner to that predicted by Figure 9.1 without translation of the data to account for the change in formation length. The reason that the Strouhal number - ℓ/D relationship does not need to be translated for the high velocity cell is due primarily to its greater spanwise coherence. This stronger spanwise coherence allows the high velocity cell to be evaluated as a single coherent structure. The

influence that the variation in formation length has on the shedding characteristics must therefore be considered in terms of an average effect over the entire cell. The reduced coherence in the low velocity region allows the shedding characteristics to be influenced more by the local length and velocity scales and therefore the local reduction in formation length is experienced as an effective increase in ℓ/D across the span.

The dominant frequency mode at the low velocity side of the ℓ/D = 0.50 configuration was very broad-band and indicated a higher frequency than that at the high velocity side. A secondary, lower frequency mode was also observed in the spectra at the low velocity side. This secondary mode decreased in frequency with decreasing freestream velocity across the span. The same phenomenon is more clearly shown in the spectra for the ℓ/D = 0.75 case, see Figure 4.3. The primary mode at the high velocity side remains relatively well defined. However, beyond mid-span the shedding becomes more broad-band and the secondary mode appears. The presence of the double peaks in the spectra at the low velocity side may be caused by amplitude modulation effects in that region. For example, a primary shedding mode at frequency, f_s, that is modulated in amplitude by a low frequency mode, f_m, can be expressed as,

$$f(t) = A\sin(2\pi f_m t)\cos(2\pi f_s t) \tag{9.1}$$

where A is a constant that determines the magnitude of the modes. The power spectrum for this function is shown in Figure 9.4.

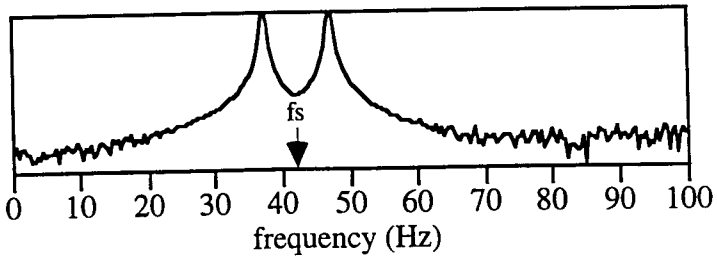

Figure 9.4. Power spectrum of amplitude modulated signal represented in Eq. 9.1.

The power spectrum shows two peaks located at $f_s \pm f_m$, however there is no peak indicated at f_s. The significance of this example is illustrated by comparison of the spanwise variation in dominant shedding modes for the $\ell/D = 0.75$ and $\ell/D = 0.0$ configurations shown in Figure 9.5. The square symbols represent the frequency of the dominant peaks in the power spectra in both configurations and the round symbols represent the average of the two dominant peaks found at the low velocity side of the $\ell/D = 0.75$ configuration. The dominant shedding mode on the low velocity side is actually lower than the mode at the high velocity side. It does not show up in the power spectrum because it is modulated in amplitude by a low frequency mode. Also, the modulation frequency appears to be a function of distance from the cell boundary. Near the cell boundary the modulation frequency is equal to the difference in frequency between the two cells. Measurements further away from the boundary show an increase in the modulation frequency. The reason that the modulation effects are not present at the high velocity side relates back to the previously discussed differences between the relatively weak and 3-dimensional low velocity side and the stronger and more 2-dimensional high velocity side. The dual peaks in the spectrum at the low velocity side were also observed for the $\ell/D = 1.0$ configuration although they were not as well defined as for the $\ell/D = 0.75$ configuration.

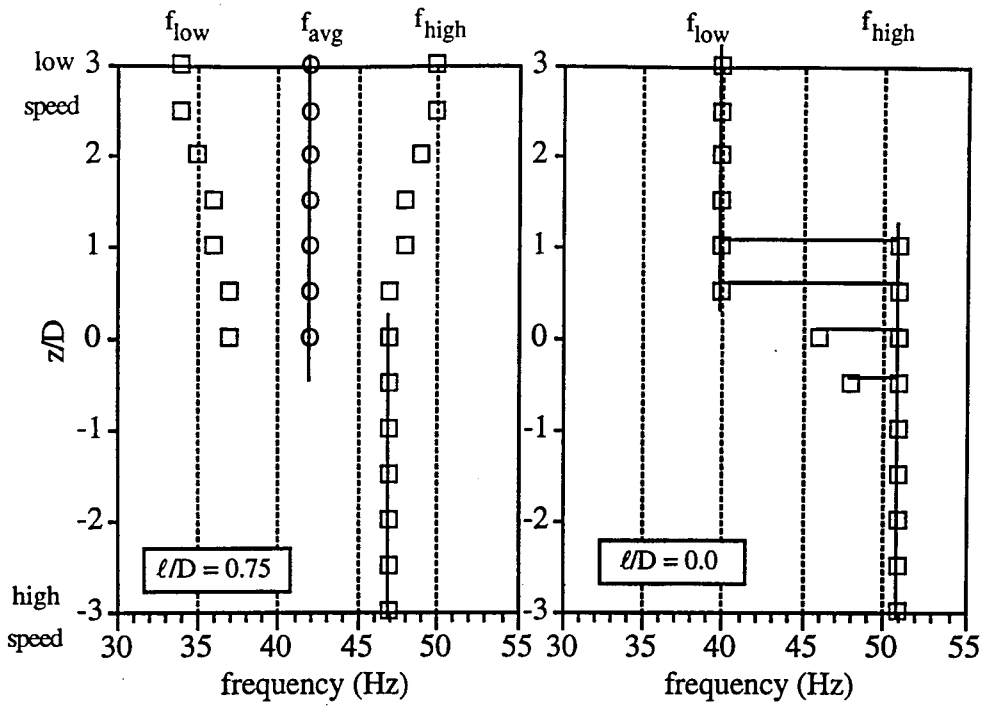

Figure 9.5. Comparison of dominant shedding modes between $\ell/D = 0.75$ and $\ell/D = 0.0$ configurations in shear flow.

The modulation observed in the power spectra for the $\ell/D = 0.5$, 0.75, and 1.0 configurations could be caused by an oscillation in the low velocity region between a spanwise correlated, cell type mode and a more 3-dimensional, local type mode. The average shedding frequency indicated at the low velocity region in Figure 9.4 is an example of a spanwise correlated mode. The entire cell behaves as a single structure and maintains a constant shedding frequency. The dual peaks in the power spectrum are produced by a modulation between the frequency of this cellular shedding mode and the local shedding mode. The spanwise variation in the local velocity affects the local mode and causes the modulation frequency to vary across the span.

The higher shedding frequency observed at the low velocity side of the $\ell/D = 1.0$ configuration is consistent with the significant increase in Strouhal number expected in region (III). The results for $\ell/D = 1.25$ are similar to the $\ell/D = 1.0$ case and show the low

velocity cell to have a shedding frequency slightly higher than the high velocity cell. For $\ell/D = 1.5$, the spanwise shedding characteristics should be evaluated between regions (III) and (IV). Based on the previous arguments, one would expect the high velocity cell to be at its highest frequency and the low velocity cell frequency to be decreasing in region (IV). Figure 4.6 shows that the shedding frequency of the high velocity cell is in fact the highest of any of the investigated splitter plate configurations and that the frequency of the low velocity cell is less than that for the high velocity cell for the first time since $\ell/D = 0.5$. The formation length at a given spanwise position remained relatively constant for plate lengths greater than $\ell/D = 1.0$ which is a similar characteristic to that observed for the uniform flow case, see Figure 3.24. The constancy of the formation length suggest that different processes dominate the shedding characteristics of the longer plates than those for the lower plate lengths and therefore could explain the lack of modulation in the spectra for the longer plate configurations.

Strouhal number versus ℓ/D for both ends of the span and for different Reynolds numbers were compared in Figure 4.10. The results are consistent with the previous arguments. The variation in Strouhal number with respect to ℓ/D for the high velocity cell is similar to the trend observed in Figure 9.1 for the uniform flow configuration with the same minimum located near $\ell/D = 0.7$. For the low velocity cells the variation in Strouhal number is similar to the uniform flow results in Figure 9.1 except that the curve is translated by approximately -0.6 ℓ/D. This translation is in agreement with the reduction in formation length at the low velocity side. Variation in Reynolds number between 26,500 - 49,100 had little effect on the Strouhal number of the different cells and indicated flow similarity over that Reynolds number range as shown in Figure 4.10.

Investigation of the spanwise variation in RMS fluctuation intensity along the wake centerline of a plain cylinder revealed an increase in formation length along the span

although the maximum fluctuation intensities remained relatively constant. The ℓ/D = 0.5 and 1.0 configurations showed a similar variation in formation length however the maximum fluctuation intensity progressively decreased towards the low velocity side. The reduction in intensity at the low velocity side is in agreement with the broad-band spectra in that region and indicates reduced vortex strength in that region due to an increase in the vorticity decay rate. With increasing ℓ/D the fluctuation intensity curves become flatter with less defined maximum points at the high velocity side. On the other hand at the low velocity side well defined maximum locations were disclosed, although a reduction in intensity was observed.

The vortex convection velocity results indicated an increase in the convection velocity with increasing mean velocity across the span for the plain cylinder case as shown in Figure 4.20. However, the results for the ℓ/D = 0.5 and 1.0 configurations showed a higher convection velocity at the low velocity regions of the span than that observed at the high velocity region. These results are again in agreement with the power spectra that indicated relatively high frequency modes at the low velocity side due to modulation effects. The correlation curves shown in Figures 4.17 - 4.19 demonstrate that the shedding process has strong periodicity across the span for the plain cylinder case and at the high velocity side of the ℓ/D = 0.5 and 1.0 configurations. The periodicity however deteriorates at the low velocity side for both splitter plate configurations and may be attributed to the high 3-dimensionality and modulation in that region.

9.4 Sinuous Trailing Edge Splitter Plate in Shear Flow

The effect of a sinuous trailing edge splitter plate on the near wake characteristics of a circular cylinder in shear flow was examined. The results were similar to those obtained for the uniform flow configurations that suggested the use of an average plate length in comparisons between straight and sinuous splitter plates. The side by side comparisons of

the spanwise variation in power spectra between a straight trailing edge plate and a sinuous trailing edge plate of identical average length are shown in Figures 4.2 - 4.5. The shape and frequency of the primary shedding peak in the spectrum were nearly identical in all comparisons with the exception of the straight $\ell/D = 0.25$ and sinuous $\ell/D = 0.5$ comparison. The dominant frequency across the span matched well between the two configurations however the high velocity side indicated a secondary mode of slightly lower frequency for the sinuous plate configuration. The lower frequency mode is of the same frequency as the dominant shedding mode at the low velocity side. For the remainder of the comparisons however, the shedding characteristics, including the modulation effects described previously, correlate well between the straight and sinuous plates of similar average length.

The other wake parameters, formation length, wake width, base pressure, and shear layer velocity also correlate well between the two configurations when the average splitter plate length was used. It is concluded that the sinuous trailing edge of the splitter plate has only a mild effect on the time-averaged characteristics of the near wake. The RMS fluctuation intensity map for the sinuous plate in a uniform flow shows that the sinuous trailing edge splitter plate affects the flow beyond the formation region, see Figure 3.9. The results disclose that there is a decrease in the RMS fluctuation intensity in regions corresponding to the peaks in the sinuous trailing edge of the splitter plate. This indicates a reduction in the vorticity in peak regions and could be due to an increase in the entrainment at the valley locations since at those locations the opposing shear layers 'see' each other for a longer period of time. This increased entrainment at the valleys draws fluid away from the peak and hence, reduces the energy in that region.

9.5 Tapered Cylinder in Uniform and Shear Flow

In this section the near wake characteristics of a tapered cylinder in both uniform and shear flow are examined. For the tapered cylinder the vorticity shed from the boundary layer decreases across the span with decreasing local diameter and results in a spanwise variation in the strength of the primary vortices. As with the straight cylinder in a shear flow the primary vortex filaments arrange themselves into coherent spanwise cells of constant circulation strength. The shedding characteristics of a cell should therefore be evaluated with respect to the average length and velocity scales over the spanwise extent of the cell. The number of spanwise cells increases with aspect ratio and the size of each cell decreases with taper ratio.

A local variation in mean velocity across the span imposed a 3-dimensionality on the entire flow field for the shear flow configuration. However, the 3-dimensionality imposed by the spanwise variation in diameter of the tapered cylinder has a more local effect and as a result the flow outside the wake remains relatively 2-dimensional. Flow visualization of the tapered cylinder in uniform flow indicated that the shear layer was relatively unaffected by the taper and the spanwise coherence of the transition vortices remained relatively strong, see Figure 7.19. In the uniform flow case the shear layer contains vorticity of essentially one sign (despite the taper) and therefore the stable configuration for the shear layer is 2-dimensional. The mean shear flow introduces an additional component of vorticity to the flow field and therefore decreases the ability of the shear layer to maintain a 2-dimensional structure. The formation of transition vortices in the shear layer became more irregular and their spanwise coherence decreased significantly in the shear flow configuration as seen in Figures 7.24 and 7.25. The effect of the taper on the flow field was more noticeable beyond the formation length where the spanwise variation in the strength of the Kármán vortices is more important.

Comparison of the spanwise variation in power spectra between a tapered cylinder in uniform flow and a straight cylinder in shear flow was shown in Figure 5.1. The spectra indicated that a spanwise cellular shedding structure is present for both flow configurations. The high frequency cells were located at the high velocity and smaller diameter end of the span for the shear and tapered configurations respectively. The similarities between the tapered cylinder in uniform flow and the straight cylinder in shear flow provided the motivation to examine the combined effect of a tapered cylinder in shear flow. In the experiments the small diameter end of the tapered cylinder was oriented at the high velocity side of the shear flow. The cylinder was designed so that the taper ratio matched the shear flow velocity profile in a way that based on the local conditions a constant shedding frequency could be expected across the span. The results confirmed that this arrangement does produce a spanwise constant shedding frequency, see Figure 5.2. A cylinder with a slightly higher taper ratio was also investigated and revealed a spanwise cell structure with the high frequency cell located near the small diameter end of the cylinder.

In the uniform flow-tapered cylinder configuration the influence of the constant velocity flow outside the wake is to maintain a relatively constant vortex convection velocity across the span. This will tend to straighten out the primary vortex filaments and produce a uniform formation length across the span. Experimental results for the uniform flow-tapered configuration indicated that the formation length normalized by the local diameter increased for the smaller diameter span positions, see Figure 5.3, whereas for the shear flow configuration higher vortex convection velocities were observed in the high velocity region of the span. This feature of the flow will tend to orient the vortex filament at an oblique angle to the cylinder axis and thereby increase the formation length at the high velocity end and decrease it at the low velocity end. This is in agreement with Figure 4.14 which shows a decrease in non-dimensional formation length with increasing velocity across the span.

9.6 Comments Regarding Strip Theory

The ability to apply a strip theory to a nominally 2-dimensional body and accurately predict the resulting aerodynamic forces is a useful tool and has been applied to wing design for quite some time. However, for 3-dimensional bluff body flows such as those investigated herein, the presence of spanwise cells of constant shedding frequency have impeded the strip theory approach. The results of the current investigation however, indicate that the strip theory approach can be useful in the analysis of bluff body wake characteristics provided some knowledge is available of the spanwise coherence length scales or, cell size. Cell size determines the region over which the local flow conditions (mean velocity, diameter, etc.) must be averaged to predict the cell's shedding frequency. Therefore, in a strict mathematical sense involving integration of infinitesimal strips across the span of a 3-dimensional bluff body strip theory is not valid. However, a strip theory is applicable to the bluff body flow if the strips are finite and equivalent in length to the experimentally observed cell size. Unfortunately, currently no accurate methods exist for the prediction of the size of the spanwise cells. Results from the current investigation revealed that the cells decrease in size with increasing taper and shear gradient or, in other words with increasing 3-dimensionality.

In some cases there are significant differences in the level of 3-dimensionality across the span. The shear flow configurations for $\ell/D = 0.5$, 0.75, and 1.0 were examples of this. For those configurations a relatively organized cell was observed on the high velocity side that covered approximately half the span. However, on the low velocity side the shedding was very broad-band and accompanied by modulation effects with weak spanwise coherence. In this situation a strip theory approach would have to accommodate the spanwise variation in 3-dimensionality as well as the local change in characteristic scales. Hence, the degree of 3-dimensionality is significant in determining the

effectiveness of a strip theory. Certainly, very high levels of 3-dimensionality will tend to invalidate any strip theory approach however, the current results suggest that for mild 3-dimensional bluff body flows some type of modified strip theory may be used.

9.7 Shear Layer Transition Vortices

The transition or, Bloor-Gerrard vortices in the shear layer from a bluff body were investigated through flow visualization, phase-averaged velocity measurements, and linear stability analysis. The results indicate that the Bloor-Gerrard and Kármán vortices are different phenomena and in terms of stability characteristics the there is no direct coupling between the two. However, feedback of the Kármán shedding could provide a mechanism that under certain conditions allows phase-locking of the transition vortices between the two shear layers.

Flow visualization results show that a 2-dimensional shear layer exists in all of the straight and tapered cylinder uniform flow configurations. By the introduction of a splitter plate and through its ability to suppress the transverse oscillations of the shear layer a more parallel shedding i.e., 2-dimensionality is assured. The organization was increased further by the sinuous trailing edge splitter plate as indicated by a reduction in the number of pairing events and vortex dislocations. The sinuous plate also influenced the spanwise location at which the dislocations were formed. It is proposed that the increase in 2-dimensionality observed in the shear layer is due to a reduction in the degrees of freedom available to the flow. Within the formation region the pressure gradients in the spanwise and transverse direction are relatively small. Therefore, there are many possible paths that the fluid elements can follow that depend only on the instantaneous non-uniformity in the local flow. The introduction of the straight trailing edge splitter plate eliminates most of the transverse options available to the fluid elements and effectively reduces its degrees of freedom. The sinuous trailing edge imposes a mild 3-dimensional structure to the near

wake flow field which also by imposing structure reduces the spanwise flow options available to the fluid elements. Hence, the degrees of freedom in the flow are further decreased and a more organized wake results.

A frequent phase-locking phenomena was observed between the shear layers for most of the uniform flow configurations. The time sequence of images presented in Figure 7.15 illustrates the strong symmetry of the two phase-locked shear layers. A significant characteristic is that the phenomena occurs even in the splitter plate configurations and therefore, the phase-locking cannot be a result of direct communication between the shear layers. This suggests that it must be caused by feedback from the primary shedding process. It is assumed that the shear layers from both sides of the cylinder have identical stability characteristics and therefore the relatively low frequency modulation from the primary shedding should affect both shear layers in an identical manner. The 2-D jet is similar in many respects to the wake shear layer with the exception of the modulation effects from the primary vortex shedding. Chu [1993] found that an acoustic excitation of the 2-D jet effected the shear layer instability modes. If the modulation of the wake shear layer by the primary vortex shedding affects the phase of the shear layer transition waves then a phase-locking between the two shear layers should be expected.

For the tapered cylinder configuration a 3-dimensional chevron pattern was revealed in the Kármán vortices, see Figure 7.20. On the large diameter side of the span the oblique angle was greater than the angle on the small diameter side which is consistent with a lower shedding frequency in that region. However, the shear layer transition vortices remained relatively 2-dimensional and demonstrated strong spanwise coherence, see Figure 7.24. These results provide further evidence that the Bloor-Gerrard and the Kármán vortices are independent phenomena.

As previously discussed in sections 9.1 and 9.2 vortex dislocations were observed in the shear layer that had a strong similarity in appearance to the Λ-structures described by Williamson [1992], see Figures 7.16 and 7.17. The occurrence of the dislocations was rather random in both frequency and location although they were observed less often in the splitter plate configurations. This is consistent with a more organized or 2-dimensional shear layer and also supports Williamson's conclusion that the dislocations trigger a transition to 3-dimensionality and are a fundamental feature of the wakes of 2-dimensional bluff bodies.

The shear flow configuration significantly increased the 3-dimensionality of the shear layer as indicated by the irregular formation of the transition vortices and the significant increase in the number of vortex pairing events as seen in Figure 7.25. The shear layer was more diffused and indicated a spanwise oscillation in-phase with the local shedding frequency. There was also an increase in the amount of seed particles observed in the base region compared to the uniform flow configurations. This suggests that in the in the more 3-dimensional shear flow configuration the entrainment of the shear layer fluid occurs closer to the cylinder. The vortex dislocations observed in the uniform flow configurations were not observed in the shear flow configurations due to the already high 3-dimensionality of the near wake flow field.

9.8 Near Wake Characteristics and the Universal Parameter

Results from the current investigation allow the evaluation of a universal parameter from a 3-dimensional point of view. Many of the previous investigations, e.g., Roshko [1955] and Bearman [1967] assume nominal 2-dimensionality in the near wake. These methods become ineffective for flows that contain significant 3-dimensionality such as with the flow configurations investigated here, namely freestream shear and taper configurations and near wake modification by a splitter plate.

The typical universal parameter consists of the traditional Strouhal number modified by a characteristic wake width and velocity scale. The reason that it becomes ineffective in the case of the splitter plate configurations is due to its non-monotonic variation in shedding frequency for different length of splitter plate. The results presented in Figure 3.18 and discussed in section 9.1 describe that the Strouhal number - ℓ/D relationship varies in different ways and is dependent on how the shear layer interactions are effected by the splitter plate. The shedding frequency not only depends on the distance between the shear layers but also on the shear layer's level of turbulence, circulation strength, and entrainment capabilities. These characteristics are very difficult to predict for a bluff body flow. However, the variations in wake width and base pressure with respect to ℓ/D are relatively smooth and free of inflection points. Therefore, a universal parameter based on the combination of the Strouhal number, wake width and base pressure parameter will not be invariant for the splitter plate configurations.

The shedding frequency can also be influenced by 3-dimensional effects such as those produced by the freestream shear and tapered cylinder used in the current investigation. These effects were shown to produce spanwise cells with relatively constant shedding characteristics. The cell size depends on the level of 3-dimensionality in the flow (e.g., shear gradient, taper ratio, freestream turbulence, etc.) and therefore also very difficult to predict. A universal parameter that relies only on the local conditions cannot account for this cellular behavior. It will be less accurate in regions where the local characteristic length and velocity scales are different than the average characteristics of the cell which determine the cell's shedding frequency.

However, these questions of applicability in certain bluff body flow configurations do not invalidate the universal parameter approach. The current investigation indicated that

the Strouhal number of the cell is typically around 0.20 when based on the local conditions mid-way across the cell. This implies that the error introduced by using local conditions instead of the average conditions over the span of the cell cannot become very large. Once the local velocity and length scales differ from the average scales in the cell region by some limiting condition that depends on the flow, a new cell is formed which again has an average Strouhal number of 0.20. This characteristic also indicates that a strip theory may be used to evaluate the average shedding characteristics over the span of a 3-dimensional bluff body flow.

Although for all of the configurations investigated the shedding frequency did not correlate well with the other near wake parameters, see Figures 6.24 and 6.25, the relationship between the other parameters indicated fairly strong correlations. The results indicate that an increase in base pressure, which corresponds to a reduction in drag, is accompanied by an increase in the size of the formation region, see Figures 6.21 - 6.23. The pressure imposed on the near wake by the outer flow is assumed to remain relatively constant for all the uniform flow configurations and locally constant for all the shear flow configurations. Also the average pressure within the formation region varies little from the base pressure value. Therefore, the increase in pressure of the base region forces the outer flow away from the wake and increases the size of the formation region. Typically, a decrease in the bluff body drag is assumed to correspond to a decrease in the wake width. However, in the current investigation the decrease in wake width was caused by the splitter plate's ability to suppress the shear layer oscillations. These oscillations effectively widen the wake when time-averaged measurements are used. The transverse distance between the primary vortices was determined by the distance between the maximum RMS fluctuation intensities across the wake. The results showed an increase in this distance with the splitter plate (reduced drag) configurations. However the RMS fluctuation intensity dropped off significantly beyond the maximum intensity points for the splitter plate configurations

compared to the more gradual decrease observed for the higher drag, plain cylinder configuration, see Figure 3.3. Therefore, the region of relatively high fluctuation energy is narrower in the low drag configurations although the transverse distance between the maximum RMS intensity points is greater.

A strong correlation between the base pressure parameter and the shear layer velocity was indicated as seen in Figure 6.21. A higher base pressure parameter (lower base pressure) corresponded to a reduction in shear layer velocity. This is consistent with Roshko's [1955] formulation of the base pressure parameter which relates the base pressure to the velocity of the shear layer just beyond the separation point. However, the shear layer velocity presented in the current investigation is based on the velocity corresponding to the maximum RMS intensity point in the shear layer. It uncovered a much lower shear layer velocity than predicted by Roshko. This is primarily due to the measurement location in the current investigation being further downstream and beyond the transition point in the shear layer. The fluctuations produced by the convection of the transition vortices past the hot wire will reduce the measured time-average mean voltage and as a consequence reduce the mean velocity.

In the current investigation 180 sets of wake parameters were obtained that define the near wake for all the configurations investigated. Data was acquired at 15 equally spaced locations across the span for each configuration to account for 3-dimensional effects. The wake parameters considered were the formation length, wake width, base pressure parameter, shear layer velocity, and Strouhal number. All parameters were based on the local flow conditions. The parameters were combined in various ways to investigate the concept of an invariant universal parameter. The results revealed that the traditional parameters were not accurate for the 3-dimensional configurations. The reason for this inaccuracy can be traced to the ratio of non-dimensional wake width to base pressure

parameter, (d'/D) / K, which is commonly used in the universal formulations. The results from Figure 6.23 indicate that an increase in base pressure parameter is accompanied by a reduction in wake width and therefore the ratio of the two parameters will produce a large variation. However, the product of the two parameters will result in a more constant value.

Three different Strouhal number formulations were presented in Figure 6.24. The traditional Strouhal number,

$$St = \frac{f_s D}{U} \tag{9.1}$$

indicated a relatively constant value around St = 0.20. When the universal parameter is based on the common 2-dimensional formulation the current data indicate and average of St' = 0.16 where,

$$St' = \frac{St}{K}\left(\frac{d'}{D}\right) \tag{9.2}$$

However, there was a large scatter in the results that was caused primarily by the 3-dimensional configurations. When the universal parameter was modified by using the product of the non-dimensional wake width and base pressure parameter instead on the ratio the results indicate a relatively constant parameter value of approximately St* = 0.14 where,

$$St^* = \frac{St}{\left(\frac{d'}{D}\right)K} \tag{9.3}$$

The largest deviations from this value occur at the low velocity span positions in the 3-dimensional configurations. These are primarily where the modulation effects discussed in

section 9.3 occurred which produced relatively high frequency peaks in the power spectra. At the mid-span location and at the high velocity side where the wake characteristics are more 2-dimensional, the scatter is much smaller than at the low velocity side. This indicates that the effectiveness of a universal parameter depends on the degree of 3-dimensionality in the flow. For flows where the 3-dimensional effects are mild the universal parameter proposed in Eq. 9.3 should produce relatively accurate predictions.

CHAPTER 10. CONCLUSIONS AND RECOMMENDATIONS

10.1 Conclusions

The near wake characteristics of a circular cylinder bluff body in nominal 2 and 3-dimensional configurations and at subcritical Reynolds numbers were investigated. The 2-dimensional configurations consisted of a straight circular cylinder in uniform flow with a base mounted splitter plate. Cylinder taper and mean shear flow were incorporated to investigate the effects of 3-dimensionality in the wake. The results of this investigation allow various conclusions to be drawn regarding the behavior of bluff body wakes.

The vortex shedding frequency from a circular cylinder with a splitter plate was altered in different ways depending on the length of the splitter plate. It was shown that shear layer characteristics such as circulation strength, ability to entrain fluid, and stability have a significant effect on the Kármán shedding frequency. The variation in Strouhal number over the range of splitter plate lengths from $\ell/D = 0.0 - 2.0$ was divided into four different regions; (I) stabilizing, (II) shear layer elongation, (III) reduced entrainment, and (IV) splitter plate - vortex interaction. The name given each region identifies the flow phenomenon that dominates the selection process of the shedding frequency within that region. These results illustrate the importance of the shear layer conditions in determining the bluff body shedding characteristics.

The shape of the Stouhal number - ℓ/D curve was in agreement with the results of Apelt and West [1975] and relatively independent of Reynolds number (Re = 30,000 - 40,000) and solid blockage (5.9% and 8.3%). However, an increase in aspect ratio from 8

to 16 translated the St - ℓ/D curve to higher ℓ/D's and lower Strouhal numbers. A minimum drag coefficient approximately 30% lower than the plain cylinder coefficient was indicated at ℓ/D = 1.0. This result was also in agreement with previous investigations.

A splitter plate reduced the level of 3-dimensionality in the formation region by stabilizing the transverse 'flapping' of the shear layers. The presence of a splitter plate prevented transverse fluid motion across the cylinder base and thereby produced a more 2-dimensional shear layer. Flow visualization substantiated this conclusion and a more narrow-band primary peak in the power spectrum was observed.

A sinuous trailing edge splitter plate in the near wake was also investigated and it was shown that when the straight and sinuous trailing edge plates were compared using the average ℓ/D of the sinuous plate the formation length, wake width, shear layer velocity, base pressure parameter, and the shape and frequency of the primary power spectrum peak were strongly correlated. However, beyond the formation region differences between the two configurations were revealed. It was concluded that the sinuous splitter plate imposed order on the shear layer by introducing spanwise constraints on the flow in the formation region. Flow visualization indicated that this further increased the 2-dimensionality of the shear layer over the straight splitter plate configuration. Beyond the formation region the RMS fluctuation intensity revealed a spanwise periodic variation and lower intensities corresponding to the peaks in the sinuous trailing edge were observed. It was suggested that the varying length of the sinuous splitter plate causes a spanwise variation in the entrainment capability of the shear layer which in turn results in a spanwise variation in primary vortex strength. This effect would be more evident beyond the formation region.

Vortex dislocations similar to the Λ-structures described by Williamson [1992] were observed in the shear layers for all of the uniform flow configurations. However, the

dislocations occurred most frequently in the plain cylinder configuration. The introduction of a splitter plate reduced the number of dislocations and is related to an increase in the organization or, 2-dimensionality of the shear layer. The use of a sinuous trailing edge on the splitter plate further reduced the number of observed dislocations and produced a spanwise preference in the location of their formation. The dislocations appeared to form primarily over the peaks in the sinuous trailing edge which indicates an increase in the spanwise organization of the shear layer.

Shear flow past a straight circular cylinder produced spanwise cells of constant shedding frequency in the wake. For a given shear gradient the cell size was essentially constant however the number of cells was found to be dependent on the aspect ratio of the cylinder. At an aspect ratio of 8 and steepness parameter of $\beta = 0.03$, two constant frequency cells were produced. The cell at the low velocity end of the cylinder produced a more broad-band power spectrum peak which indicated a higher degree of 3-dimensionality in that region.

The effect of a splitter plate on the shedding characteristics in the shear flow configuration was shown to be similar to that indicated in the uniform flow configuration when based on the average flow conditions across the cell. Both the high and low velocity cells revealed a variation in shedding frequency with respect to ℓ/D similar to the uniform flow trends however the St - ℓ/D curve for the low velocity cell was translated to higher ℓ/D's. This translation was a result of the reduced formation length at the low velocity end which can be considered equivalent to an effective increase in ℓ/D. Between $\ell/D = 0.5$ - 1.0 amplitude modulation effects were evident in the low velocity cell. It was shown that these effects can be caused by an oscillation in the low velocity cell between a correlated cell-type shedding mode and an uncorrelated local-type shedding mode. The increase in 3-dimensionality in the low velocity cell reduced its spanwise correlation and made the cell

more susceptible to the local flow conditions. The interaction of both modes produce an amplitude modulation indicated in the power spectra. The high velocity cell revealed a much more 2-dimensional behavior and only the cell-type shedding characteristics were observed.

The tapered cylinder ($dD/dz = 0.031$) in the uniform flow configuration produced three constant frequency spanwise cells. The cell structure was similar to the cells produced by the straight cylinder in shear flow however the shear layer in the taper-uniform flow configuration indicated a much more 2-dimensional behavior. The local non-dimensional formation length increased with decreasing cylinder diameter across the span. This was due to the strong spanwise coherence of the shear layer and the uniform external flow that kept the Kármán vortices relatively parallel to the cylinder axis.

An overall increase in the number of dislocations, vortex pairing events, and the irregular formation of transition vortices show that the shear flow significantly increases the 3-dimensionality of the shear layer compared to the uniform flow configurations. In all of the uniform flow configurations, including the tapered cylinder, the shear layer was relatively 2-dimensional.

Finally, the combined effect of shear flow and cylinder taper was investigated. The cylinder was oriented in the flow so that, assuming a constant Strouhal number based on local conditions, the shedding frequency would be constant across the span. This assumption was found to be valid and the constant shedding frequency was produced. Due to the high 3-dimensionality introduced by the shear flow the flow visualization results were inconclusive regarding the spanwise coherence of the Kármán vortices in this configuration. A cylinder with slightly larger taper ratio, $dD/dz = 0.042$, was also investigated. This configuration produced a spanwise constant frequency cell structure. It

was concluded from these results that if a constant local Strouhal number is maintained along the span of a bluff body with mild 3-dimensionality, a constant shedding frequency can be produced.

The applicability of a strip theory for bluff bodies with mild 3-dimensionality was also considered. The strip theory appears to be a valid and useful approach to predicting the shedding characteristics of the bluff body provided information regarding the spanwise coherence length scale (cell size) is available. However, prediction of the cell size is difficult and appears to be dependent on the level of 3-dimensionality in the flow, i.e. shear gradient, cylinder taper, turbulence level, etc. The usefulness of the strip theory depends on the accuracy required in the result. In the current investigation the Strouhal number based on the average flow conditions across the cell was approximately 0.20. Therefore the use of a strip theory can never produce local errors greater than the difference between the average conditions of the cell and the local conditions at the cell boundary.

The stability characteristics of the shear layer transition (Bloor-Gerrard) vortices were investigated by linear stability analysis. The inviscid stability characteristics were studied by evaluation of the Rayleigh equation for phase-averaged shear layer velocity profile measurements and flow visualization. Various hot wire time-average and phase-average sampling techniques were incorporated with FFT analysis to measure the frequency of the transition waves for comparison with the stability analysis results. However, these techniques were unsuccessful in identifying a transition wave frequency. It was concluded that 3-dimensionality and feedback from the Kármán vortex shedding act to inhibit the regular formation of shear layer instability waves and therefore traditional FFT measurement techniques were ineffective. However, when viewed on an oscilloscope an average transition frequency could be identified that was in agreement with the results of the linear stability analysis. Therefore, the stability characteristics of a bluff body shear

layer can be modeled with relatively high accuracy using a 2-dimensional inviscid linearized stability analysis approach based on a phase averaged velocity profile.

Flow visualization indicated a frequent phase-locking of the transition vortices between the shear layers in the uniform flow - splitter plate configurations. Since direct communication between the shear layers was obstructed by the splitter plate it was suggested that the phase-locking is a result of a feedback effect from the Kármán vortex shedding.

A strong correlation between the various near wake parameters was shown by the results of this investigation. A decrease in the base pressure parameter was typically accompanied by a decrease in the shear layer velocity and increases in formation length and wake width. However, the Strouhal number did not correlate well with these other parameters and therefore reduced the potential for obtaining a universal Strouhal number that would be invariant for bluff bodies with mild 3-dimensionality. The traditional universal Strouhal formulation,

$$St' = \frac{St}{K}\frac{d'}{D} \qquad (10.1)$$

resulted in a large variation when based in the results of the current investigation. However, by using the reciprocal of the wake width in the above formulation a much more constant parameter is obtained,

$$St^* = \frac{St}{K}\frac{D}{d'} \qquad (10.2)$$

10.2 Recommendations for Future Investigations

The results of the current investigation illustrate the significance of the spanwise coherence length scales or, cell size in determining the shedding characteristics of a bluff body. A systematic investigation should be conducted to determine the mechanisms that govern these length scales. Spanwise coherence measurements could be made in bluff body flows where the level of 3-dimensionality is controlled through variations in shear gradient, cylinder taper, and freestream turbulence. These results would be useful in the prediction of the size of the spanwise cells and facilitate the application of a strip theory approach to the analysis of 3-dimensional bluff body flows.

The effect of the sinuous trailing edge splitter plate was small in the formation region. However, further downstream there was a noticeable spanwise periodic variation in the RMS fluctuation intensity in the wake. A spanwise variation in primary vortex strength may be caused by the sinuous splitter plate which would only be detected beyond the formation region. These effects should be investigated to determine how far downstream the presence of the sinuous trailing edge can be detected.

The results of the current investigation are based on relatively low aspect ratios (AR = 8 - 16) and over a relatively small range of subcritical Reynolds numbers (Re = 20,000 - 40,000) Whether these results are applicable at higher aspect ratios and Reynolds numbers should be investigated.

An investigation could be undertaken to evaluate the universal parameter defined in Eq. 10.2 for other bluff body shapes with mild 3-dimensionality. The results would determine if the improvement over the traditional formulations indicated by the current study is consistent for other bluff bodies.

Analysis of the stability characteristics of the shear layer suggested that a transition Strouhal number produced by the combination of transition wave frequency, shear layer momentum thickness, and shear layer velocity ($f_t\theta/U$) may be invariant. Measurement of the phase averaged shear layer profiles from circular bluff bodies of varying diameter and freestream velocity is required to determine the validity of this conjecture.

APPENDIX A. RESULTS USED FOR DETERMINATION OF THE WAKE PARAMETERS

A.1 Determination of the Wake Parameters

The results used to determine the wake width, formation length, and shear layer velocity presented in Chapters 3 - 6 are presented in this section. Uniform and shear flow and straight and tapered cylinder configurations were investigated. Straight splitter plates of $\ell/D = 0.0$, 0.25, 0.5, and 1.0 and a sinuous splitter plate of $\ell/D = 1.0$, $a/D = 0.5$, and $\lambda/D = 3$ were evaluated for the straight cylinder configurations. The tapered cylinder configurations are based on a taper ratio, $dD/dL = 0.031$ and the shear flow configurations were based on a steepness parameter, $\beta = 0.03$. A distance of 16 inches between end plates was used in all configurations which produced an aspect ratio of 8 for the 2.0 inch diameter straight cylinder configuration. The wake parameters were evaluated at 15 equally spaced spanwise locations for each configuration.

The wake width is defined as the transverse distance between the maximum RMS fluctuation intensity points that occur in the shear layers at a streamwise location of $x/D = 0.65$. A sample frequency of 1000 Hz was used instead of the 200 Hz sample rate used in most of the power spectrum results because of the relatively high frequency transition waves in the shear layers. However, the 200 Hz rate was sufficient further downstream where the flow oscillations are dominated by the lower frequency (approximately 50 Hz) primary vortex shedding. Each data point is based on 20 ensemble averages of 1024 samples at a rate of 1000 Hz for a total period of 20.48 seconds. The distance between successive transverse locations was $\Delta y/D = 0.025$. The data used to determine the wake widths for the investigated configurations are presented in Figures A.1 - A.6.

The streamwise location of the maximum RMS fluctuation intensity along the centerline of the wake defines the length of the formation region. Data was acquired at successive streamwise locations separated by $\Delta x/D = 0.05$. The resulting variation in RMS fluctuation intensity along the wake centerline for each configuration is presented in Figures A.7 - A.12. A total time period of 51.2 seconds was required for each data point based on 10 ensembles of 1024 samples at a rate of 200 samples/second.

The shear layer velocity was determined from the wake width traverses and are therefore based on the same sampling parameters. The variations in RMS fluctuation intensity with respect to mean velocity for all the investigated configurations are presented in Figures A.13 - A.18. The shear layer velocity was defined as the velocity corresponding to the maximum RMS fluctuation intensity in the wake. The maximum RMS intensity points are generally considered to correspond to the location of the shear layer.

Table A.1 presents the relevant sampling parameters used to produce the results presented in Figures A.1 - A.18.

	wake width (d'/D)	formation length (ℓ_f/D)	shear layer velocity (U_s/U)
Figures	A.1 - A.6	A.7 - A.12	A.13 - A.18
sample rate	1000 Hz.	200 Hz.	1000 Hz.
total sample time	20.48 seconds	51.2 seconds	20.48 seconds
traverse resolution	$\Delta y/D = 0.025$	$\Delta x/D = 0.05$	$\Delta y/D = 0.025$

Table A.1. Sample parameters used to produce the wake width, formation length, and shear layer velocity results.

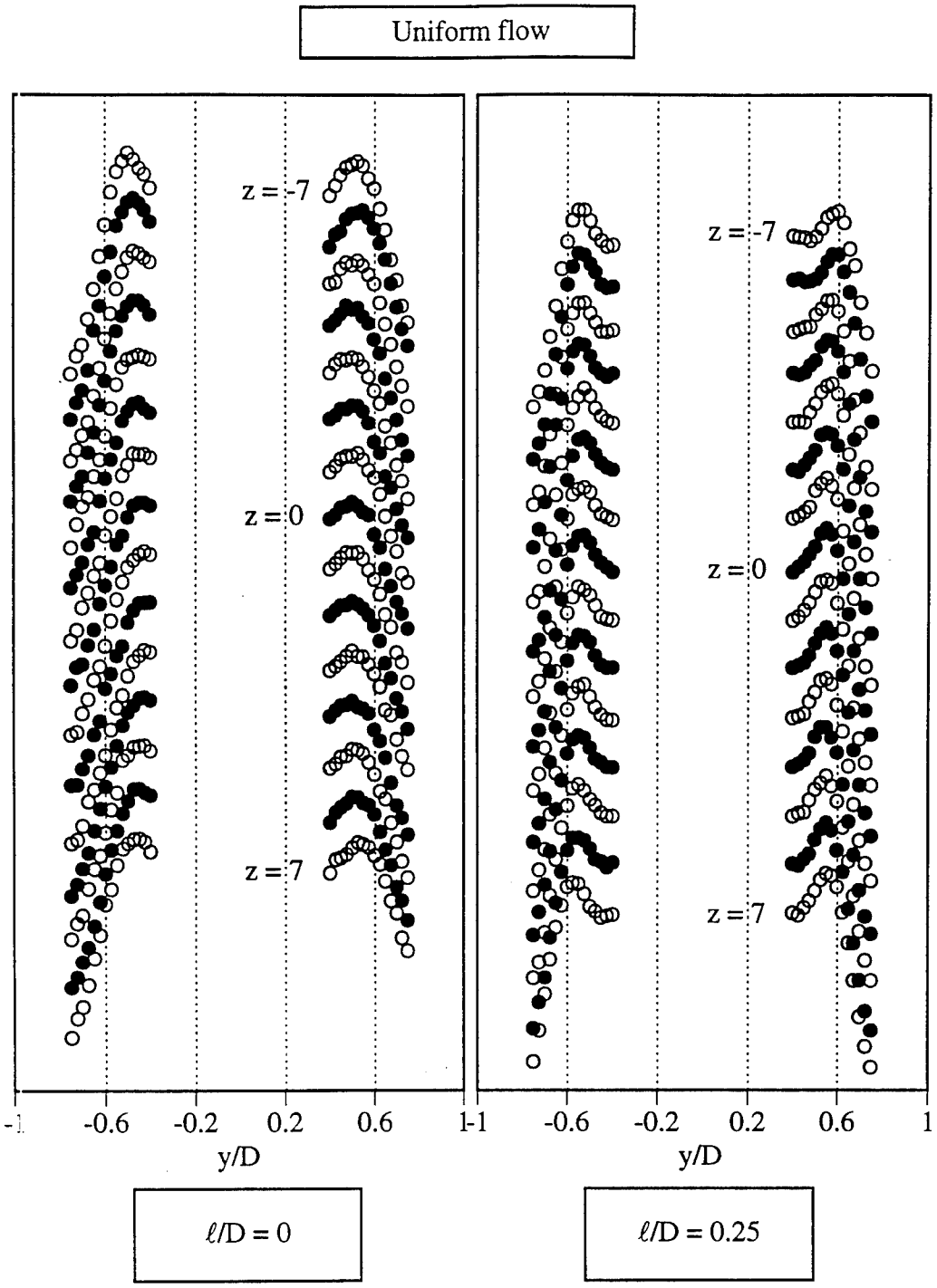

Figure A.1. Transverse variation in RMS of fluctuations across span. Straight cylinder in uniform flow. x/D = 0.65, 20 ensembles of 1024 samples at 1000 Hz.

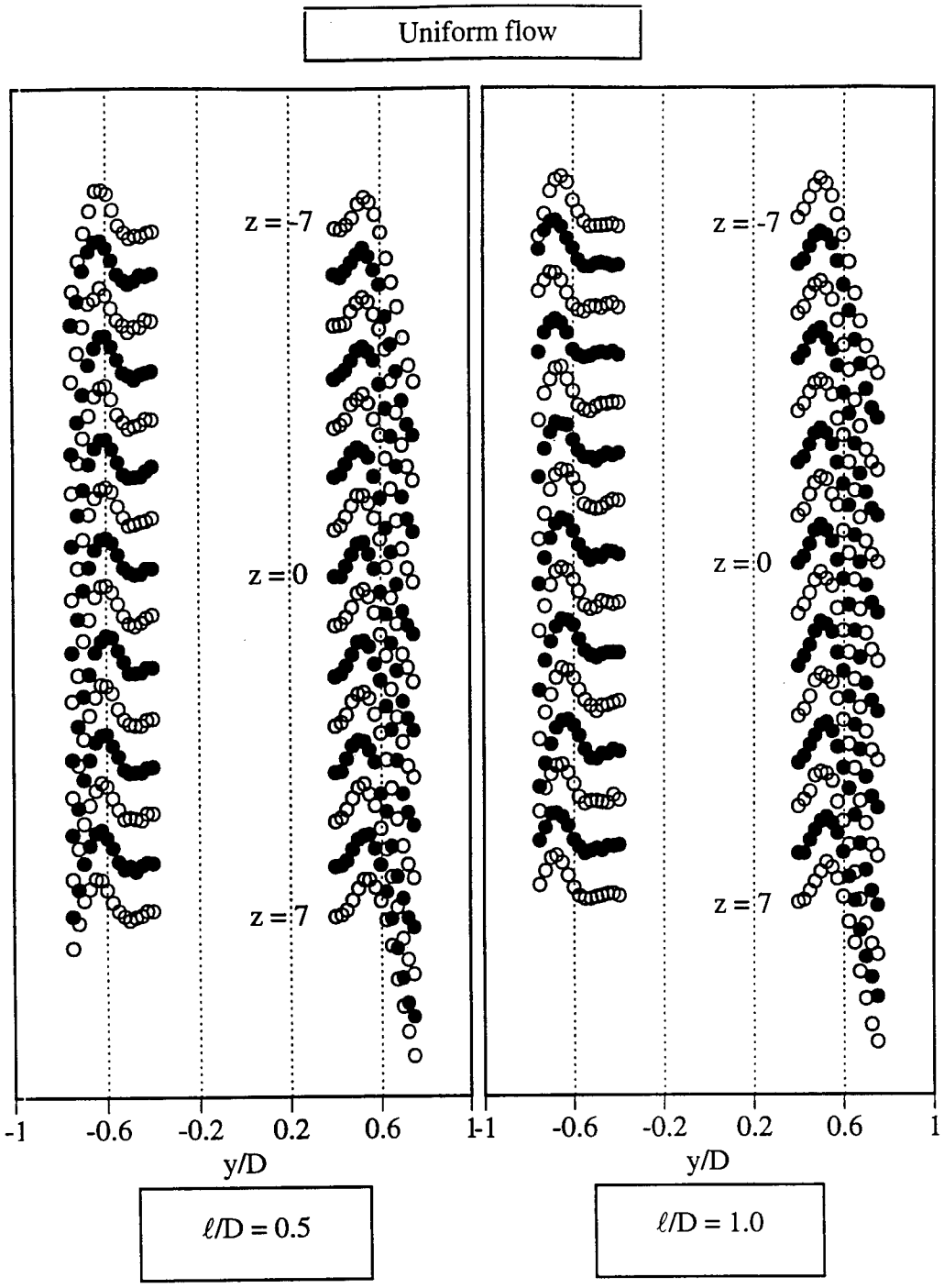

Figure A.2. Transverse variation in RMS of fluctuations across span. Straight cylinder in uniform flow. x/D = 0.65, 20 ensembles of 1024 samples at 1000 Hz.

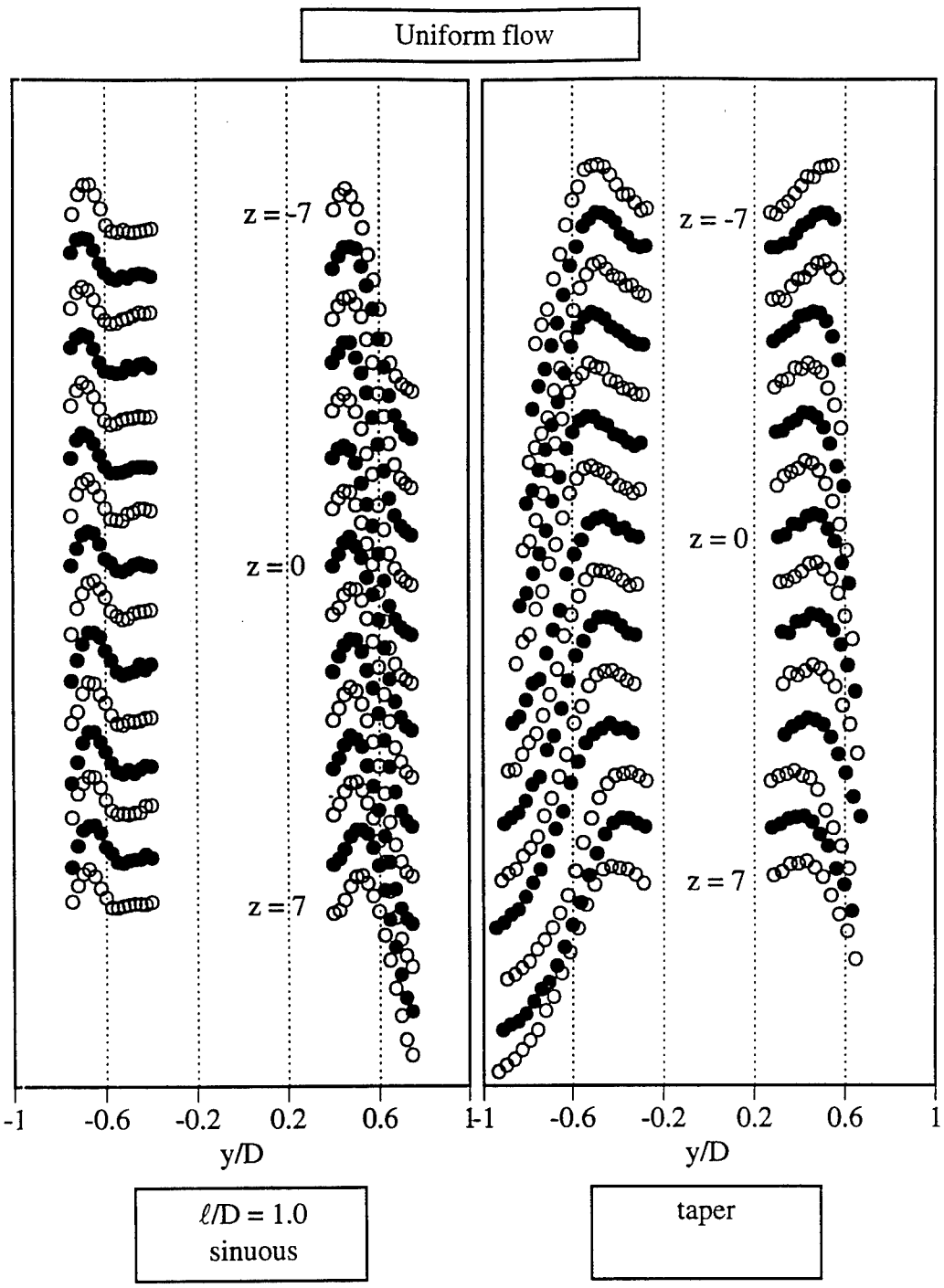

Figure A.3. Transverse variation in RMS of fluctuations across span. Straight and tapered cylinder in uniform flow. x/D = 0.65, 20 ensembles of 1024 samples at 1000 Hz.

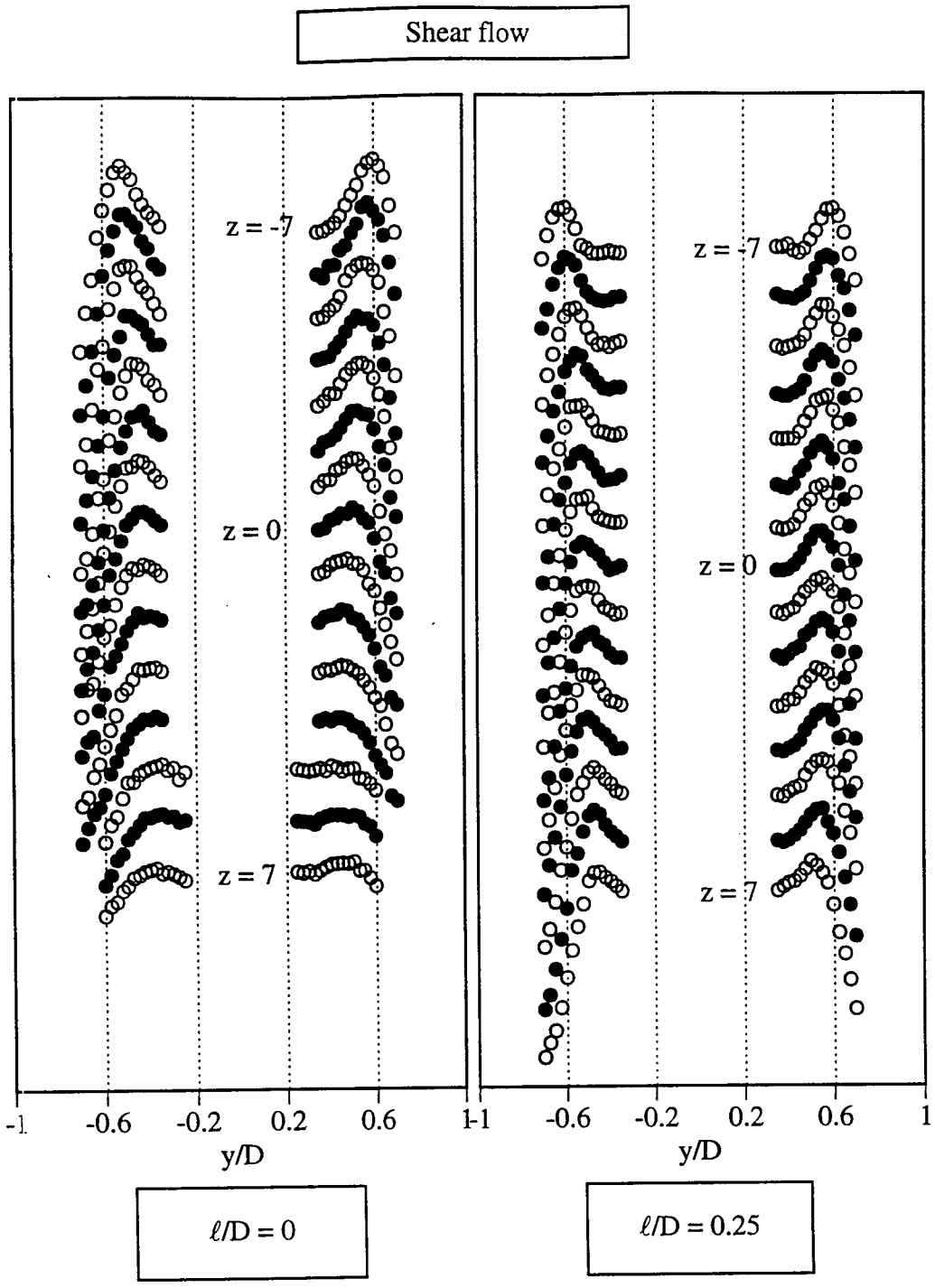

Figure A.4. Transverse variation in RMS of fluctuations across span. Straight cylinder in shear flow. x/D = 0.65, 20 ensembles of 1024 samples at 1000 Hz.

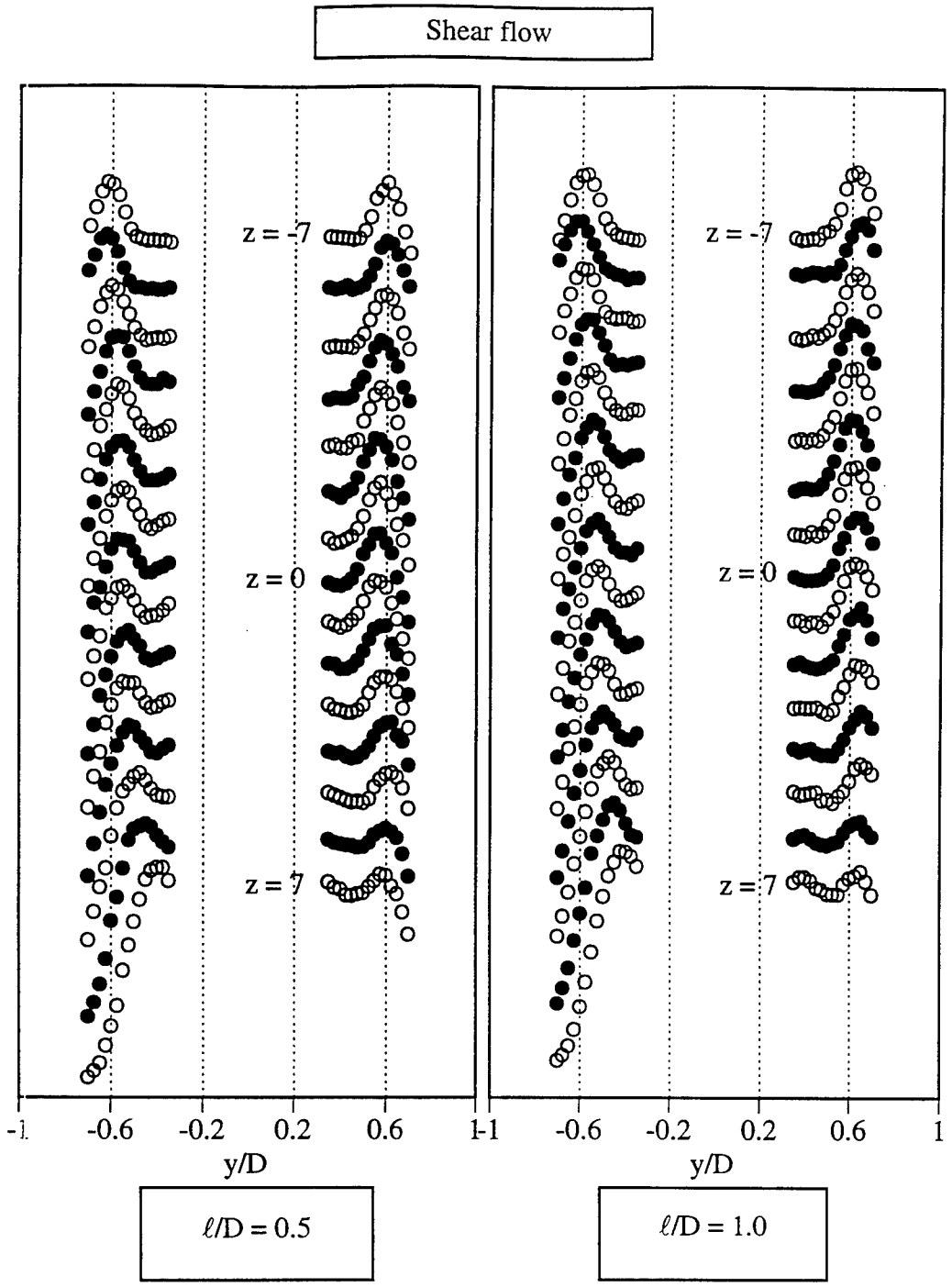

Figure A.5. Transverse variation in RMS of fluctuations across span. Straight cylinder in shear flow. x/D = 0.65, 20 ensembles of 1024 samples at 1000 Hz.

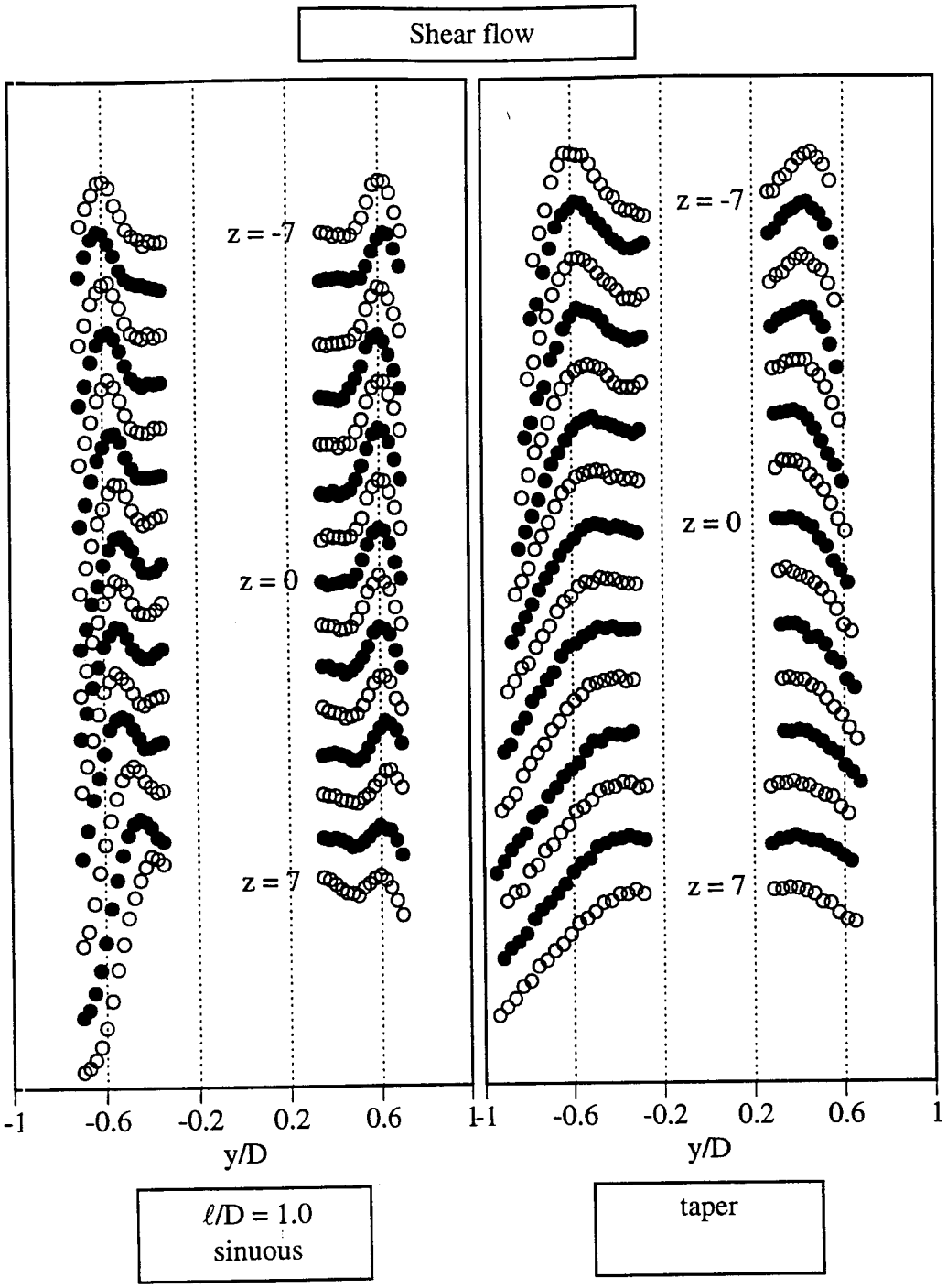

Figure A.6. Transverse variation in RMS of fluctuations across span. Straight and tapered cylinder in shear flow. x/D = 0.65, 20 ensembles of 1024 samples at 1000 Hz.

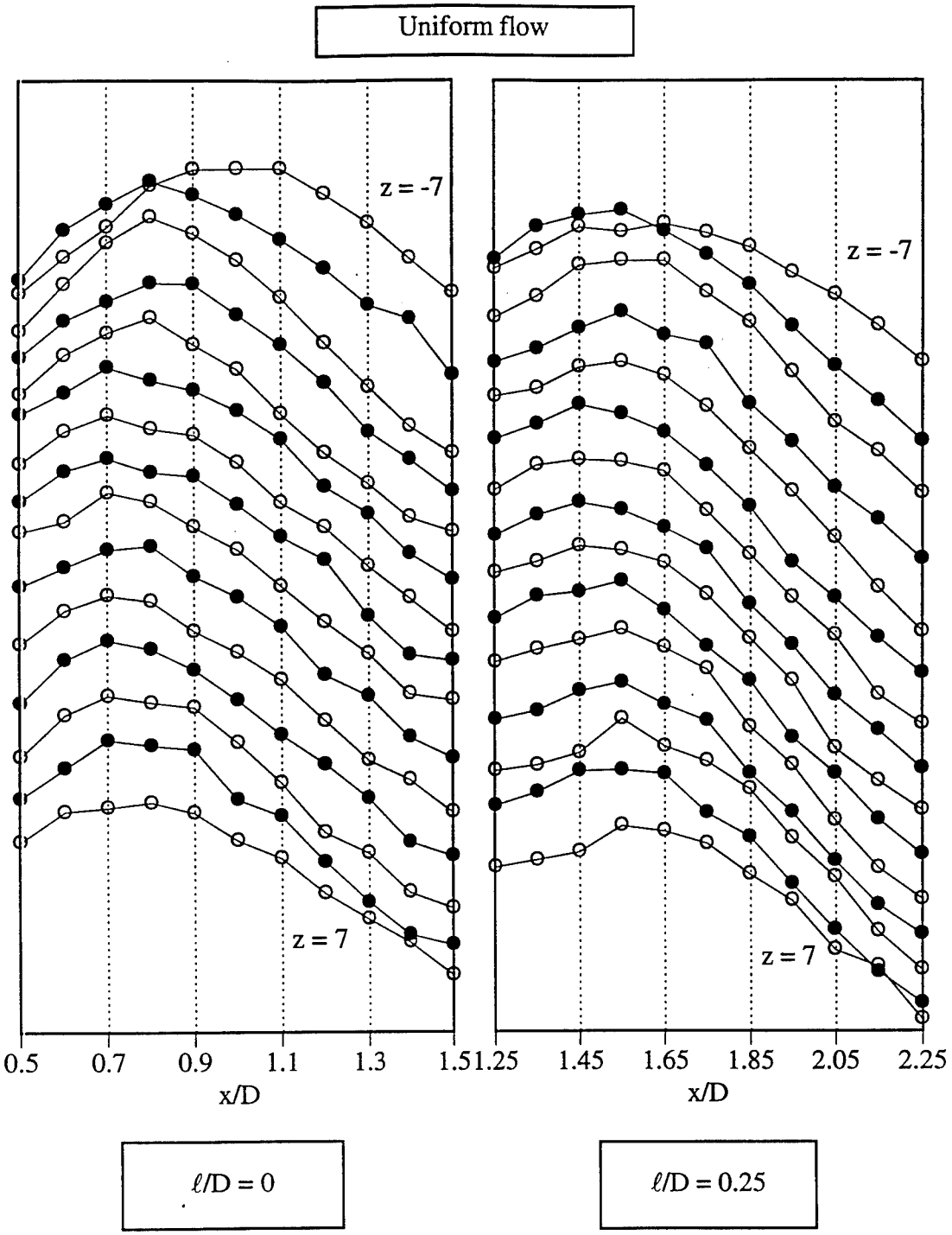

Figure A.7. Streamwise variation in RMS of fluctuations across span. Straight cylinder in uniform flow. y/D = 0, 10 ensembles of 1024 samples at 200 Hz.

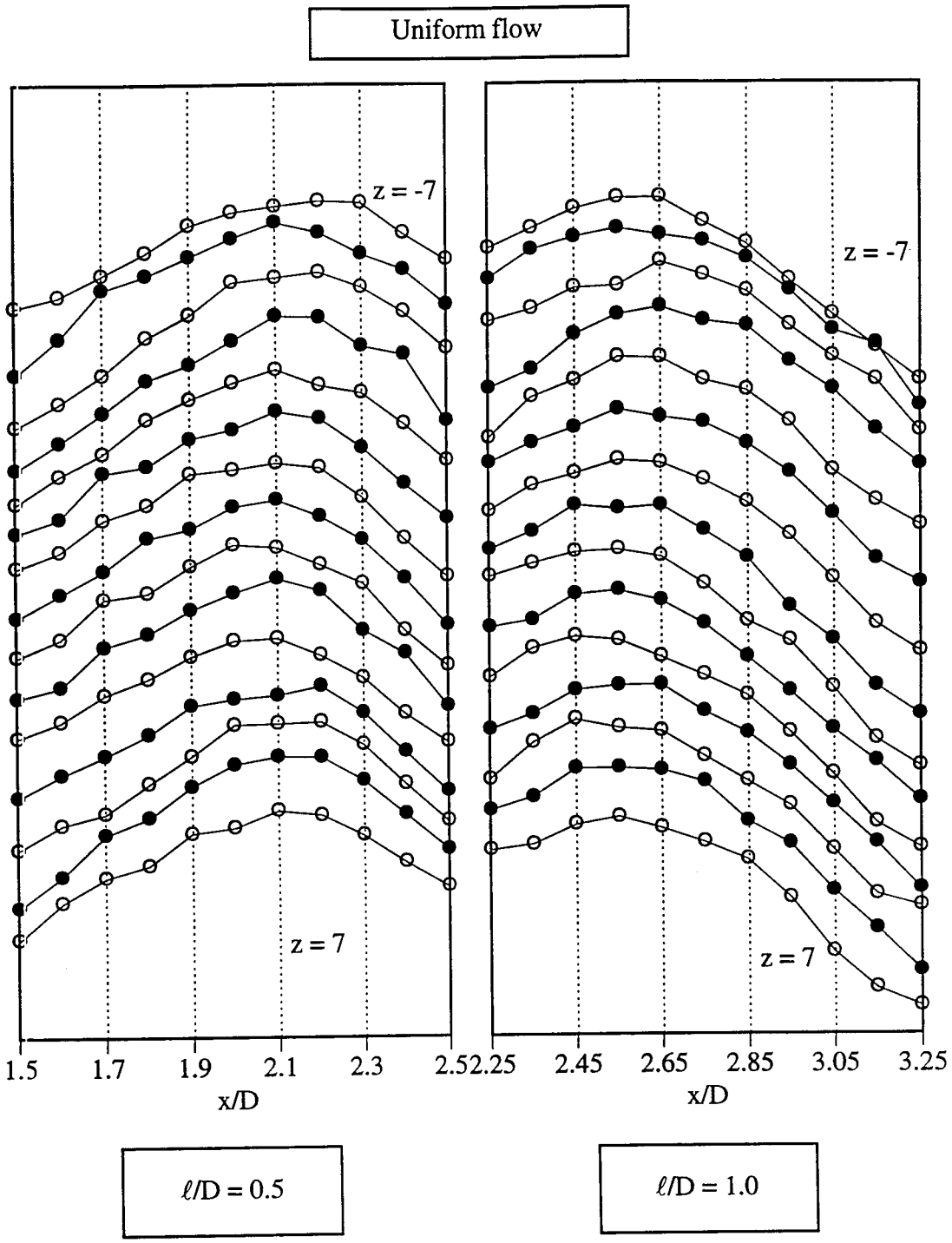

Figure A.8. Streamwise variation in RMS of fluctuations across span. Straight cylinder in uniform flow. y/D = 0, 10 ensembles of 1024 samples at 200 Hz.

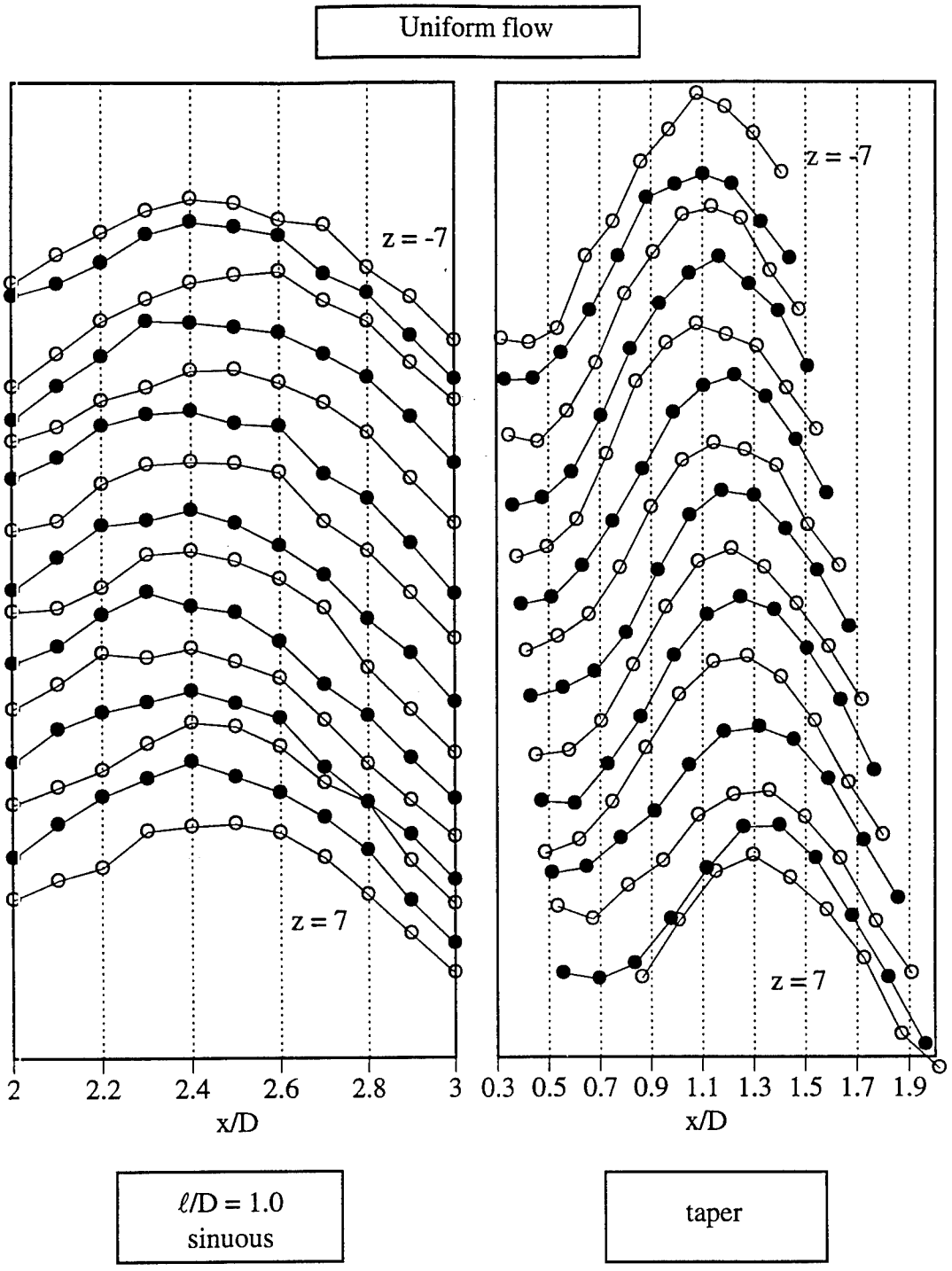

Figure A.9. Streamwise variation in RMS of fluctuations across span. Straight and tapered cylinder in uniform flow. y/D = 0, 10 ensembles of 1024 samples at 200 Hz.

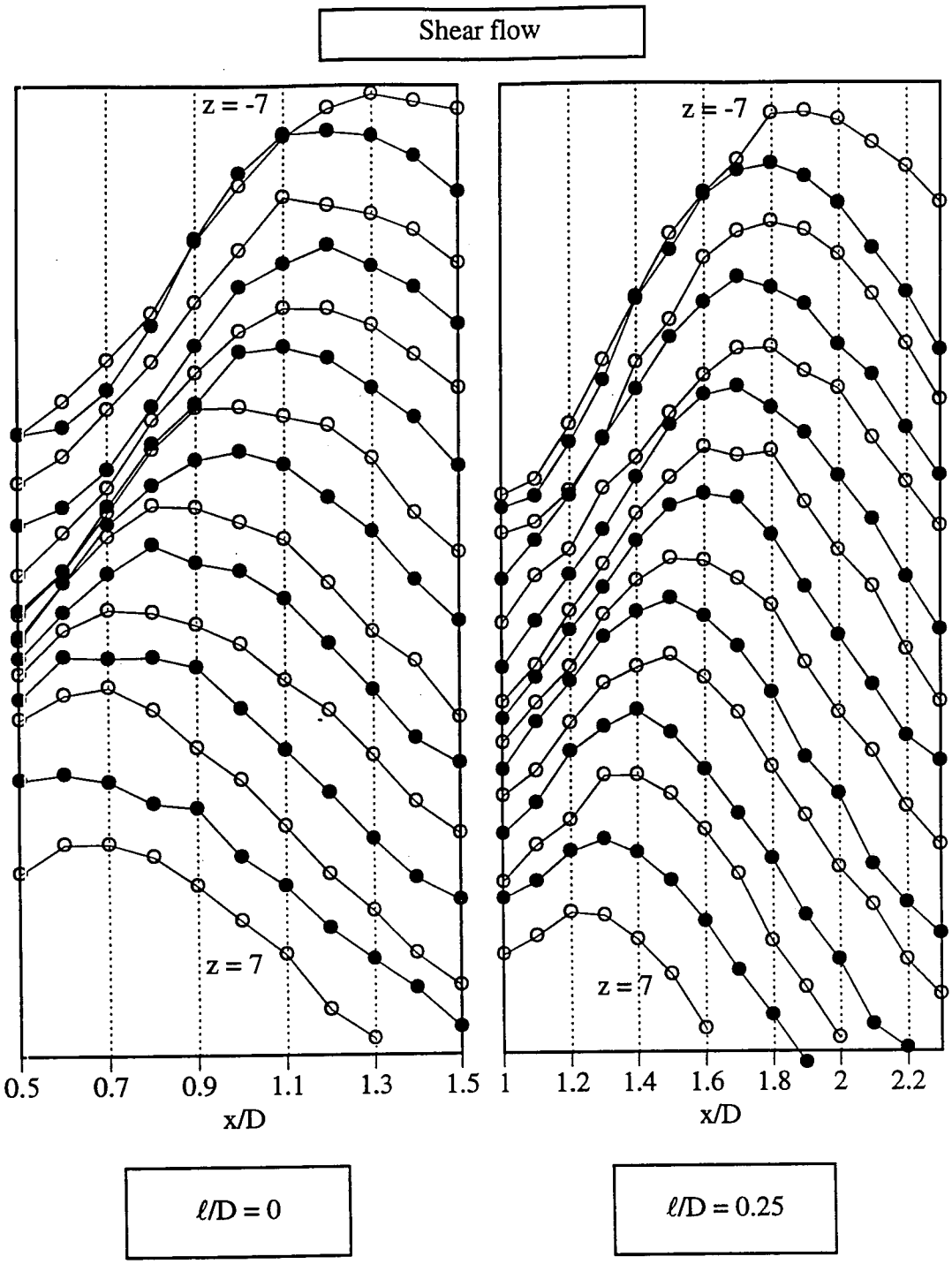

Figure A.10. Streamwise variation in RMS of fluctuations across span. Straight cylinder in uniform flow. y/D = 0, 10 ensembles of 1024 samples at 200 Hz.

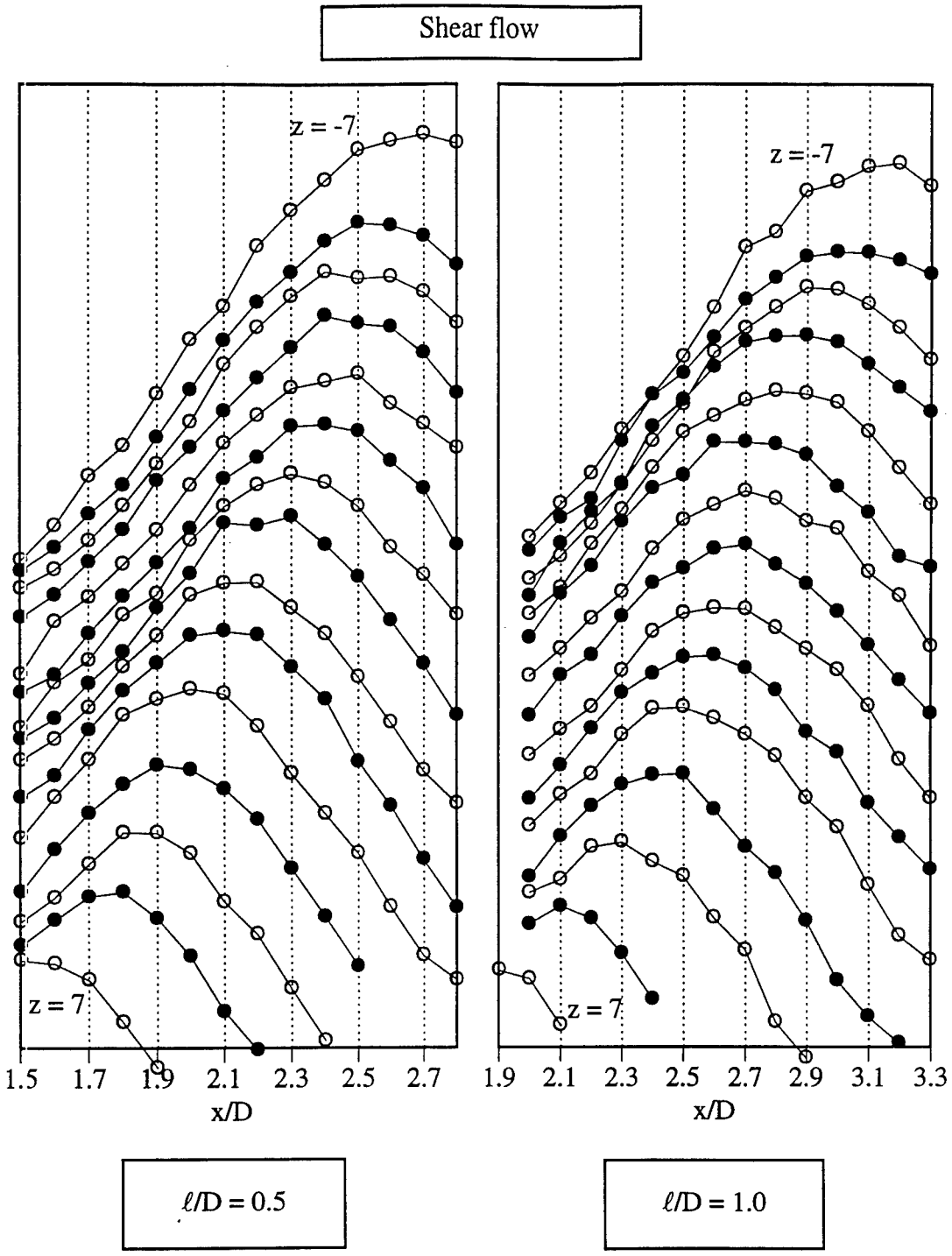

Figure A.11. Streamwise variation in RMS of fluctuations across span. Straight cylinder in uniform flow. y/D = 0, 10 ensembles of 1024 samples at 200 Hz.

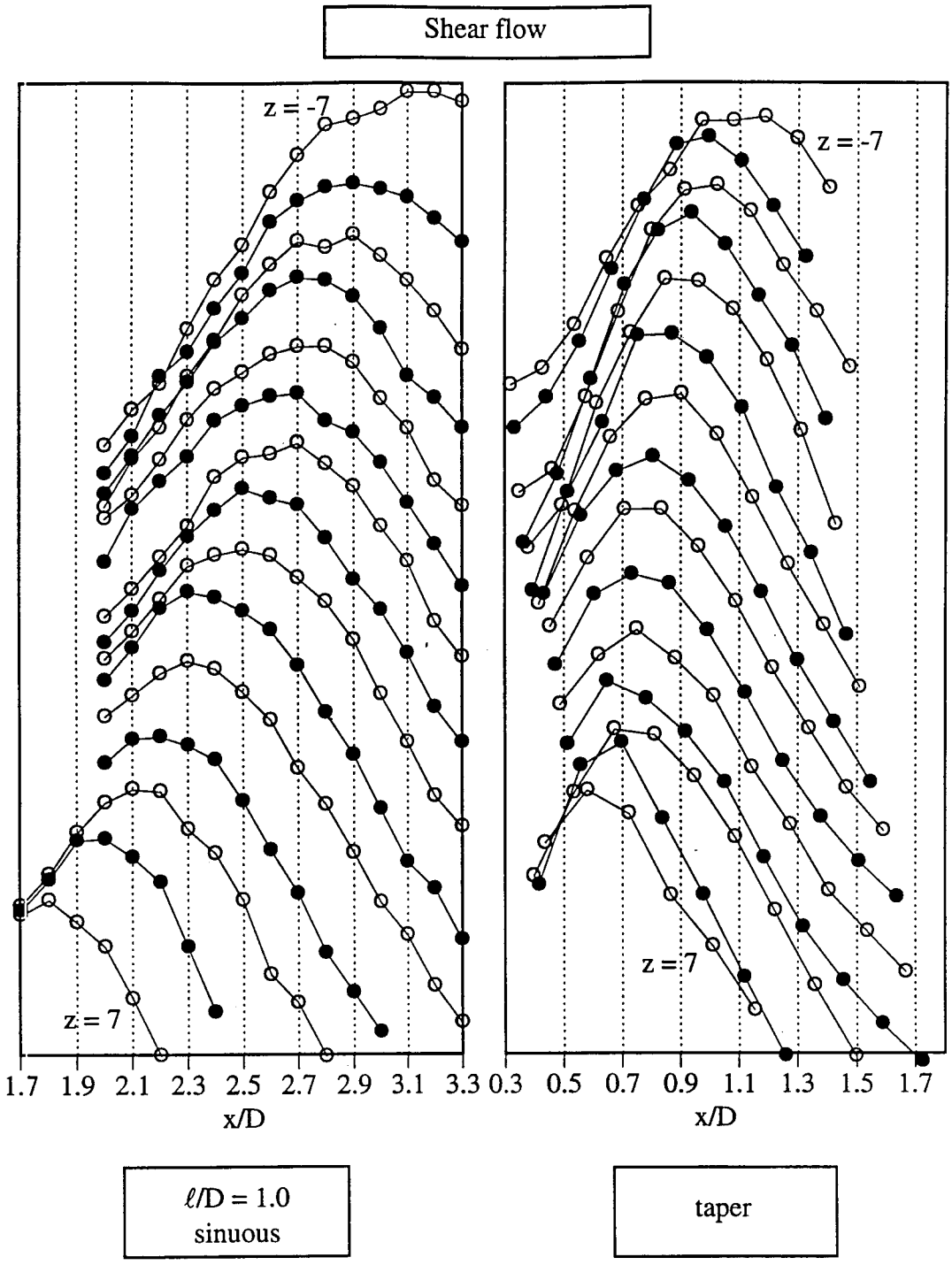

Figure A.12. Streamwise variation in RMS of fluctuations across span. Straight and tapered cylinder in shear flow. y/D = 0, 10 ensembles of 1024 samples at 200 Hz.

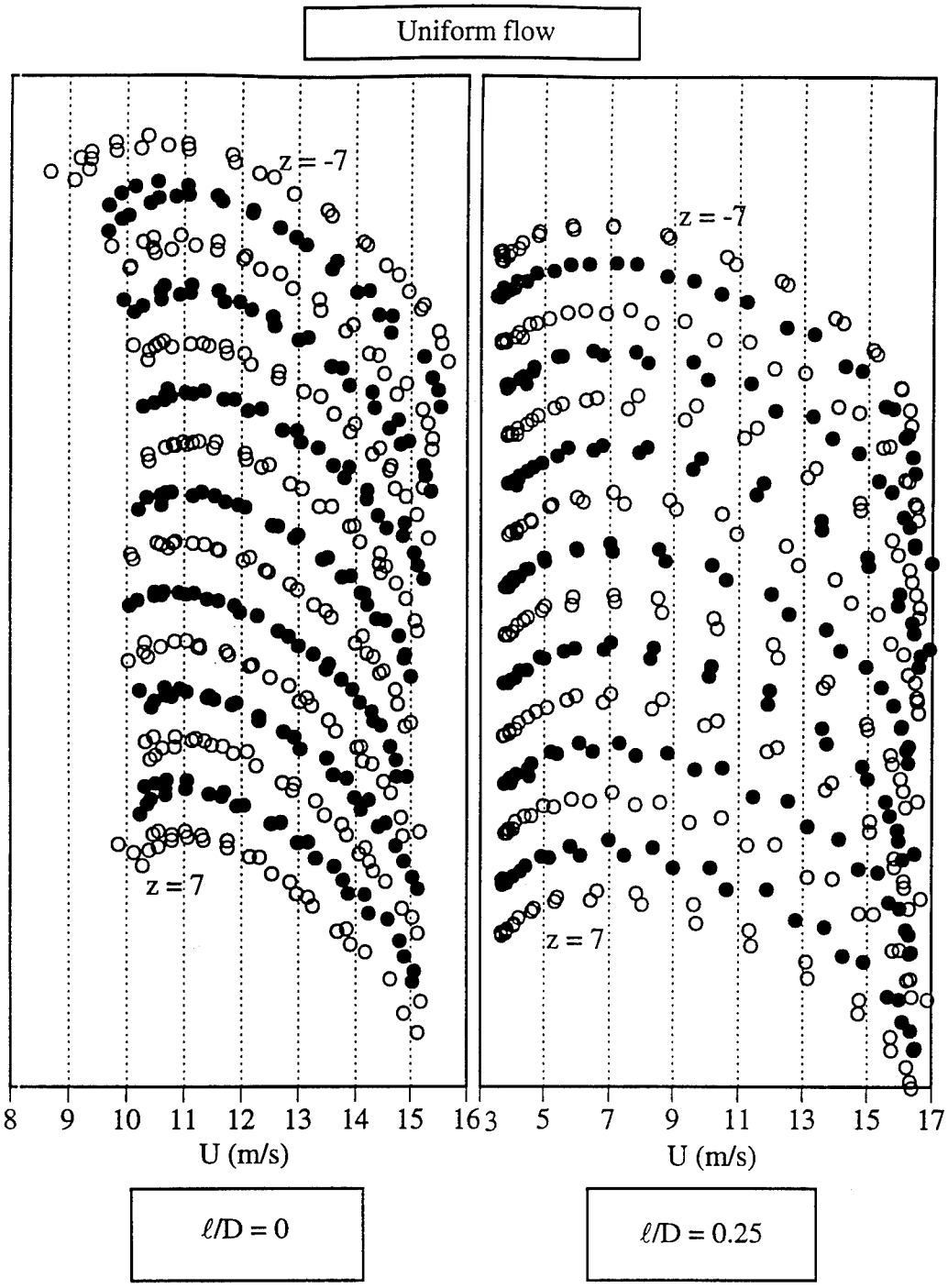

Figure A.13. RMS of fluctuations versus mean velocity. Straight cylinder in uniform flow. x/D = 0.65, 20 ensembles of 1024 samples at 1000 Hz.

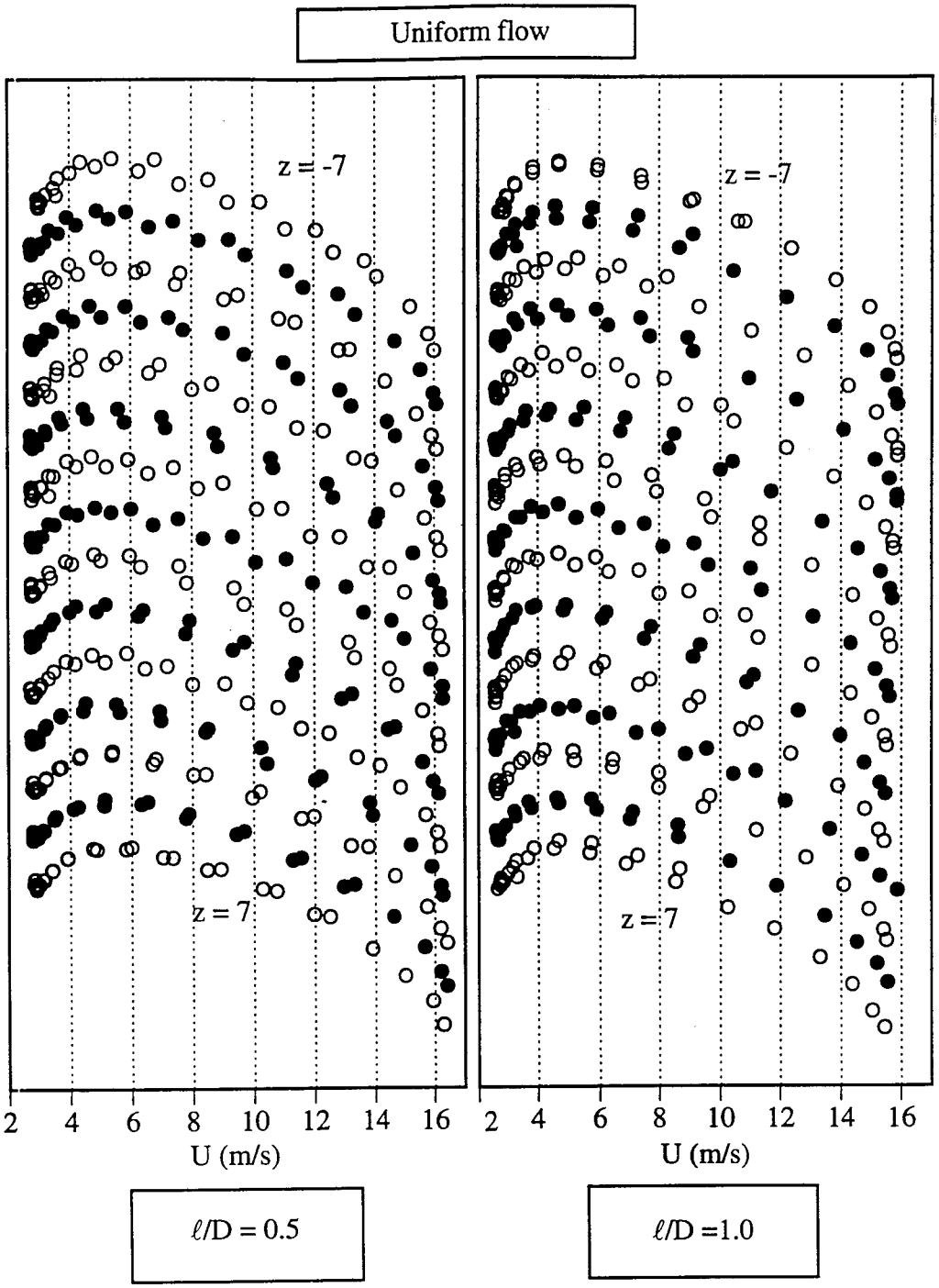

Figure A.14. RMS of fluctuations versus mean velocity. Straight cylinder in uniform flow. x/D = 0.65, 20 ensembles of 1024 samples at 1000 Hz.

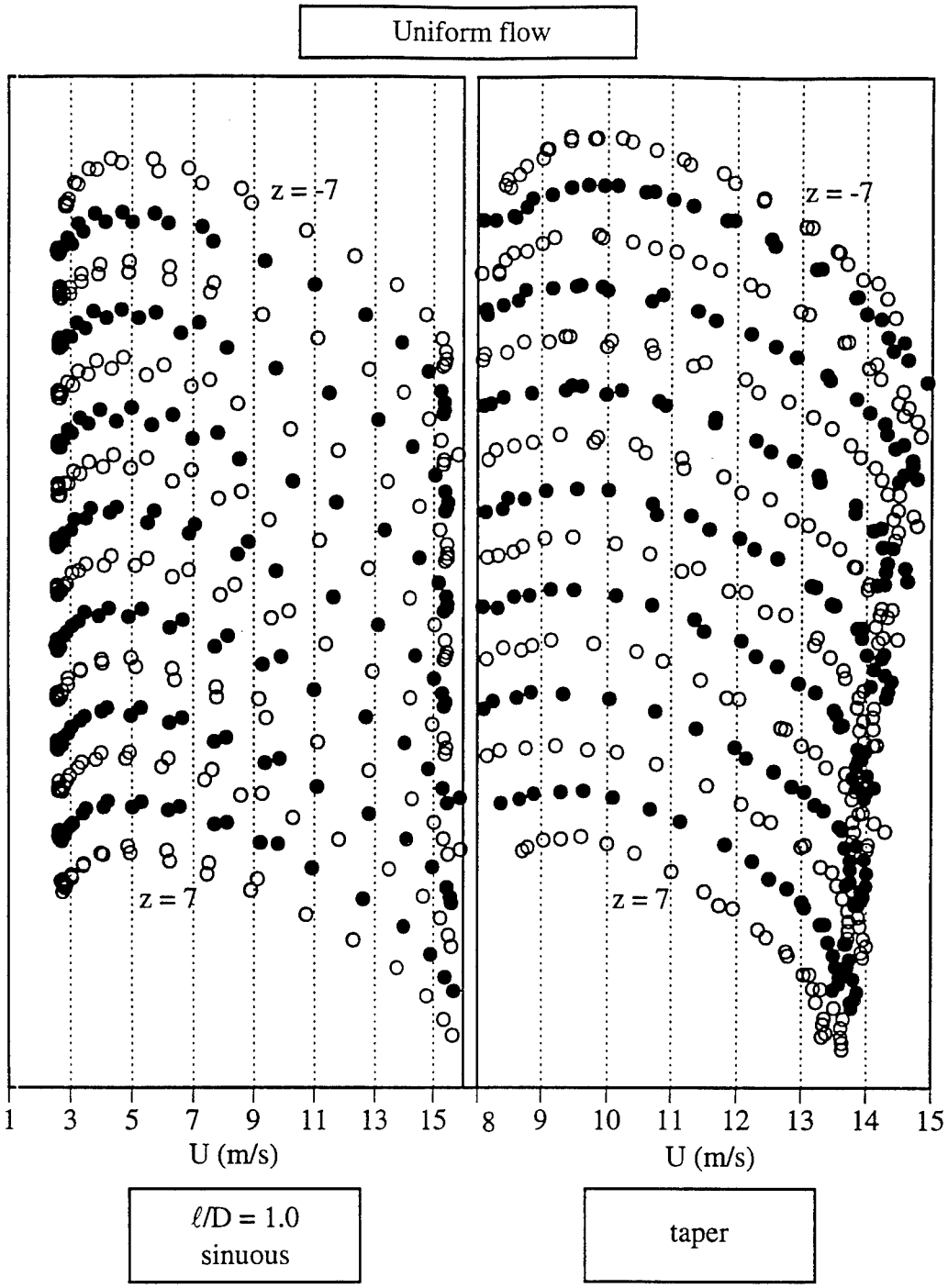

Figure A.15. RMS of fluctuations versus mean velocity. Straight and tapered cylinder in uniform flow. x/D = 0.65, 20 ensembles of 1024 samples at 1000 Hz.

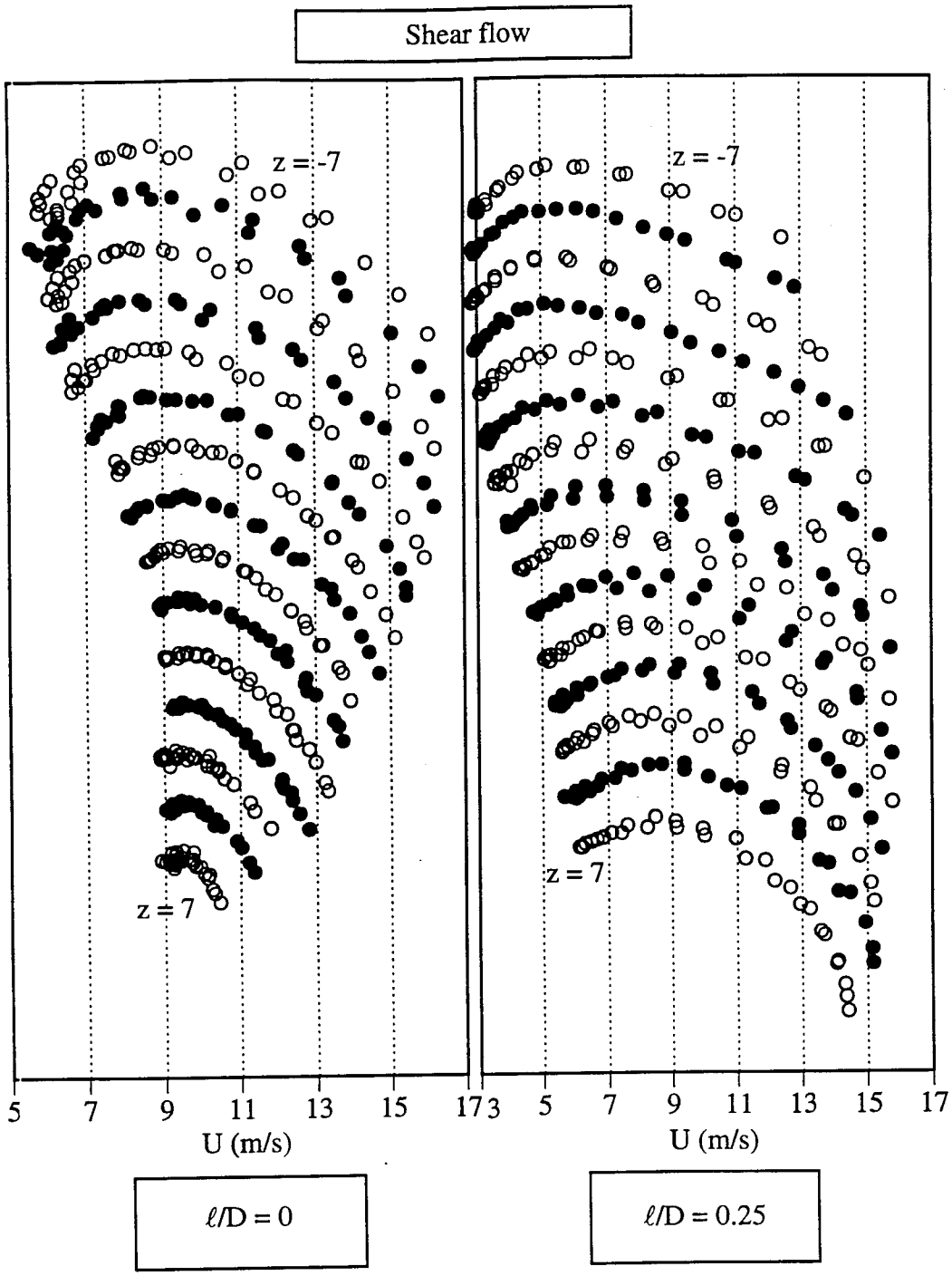

Figure A.16. RMS of fluctuations versus mean velocity. Straight cylinder in shear flow. x/D = 0.65, 20 ensembles of 1024 samples at 1000 Hz.

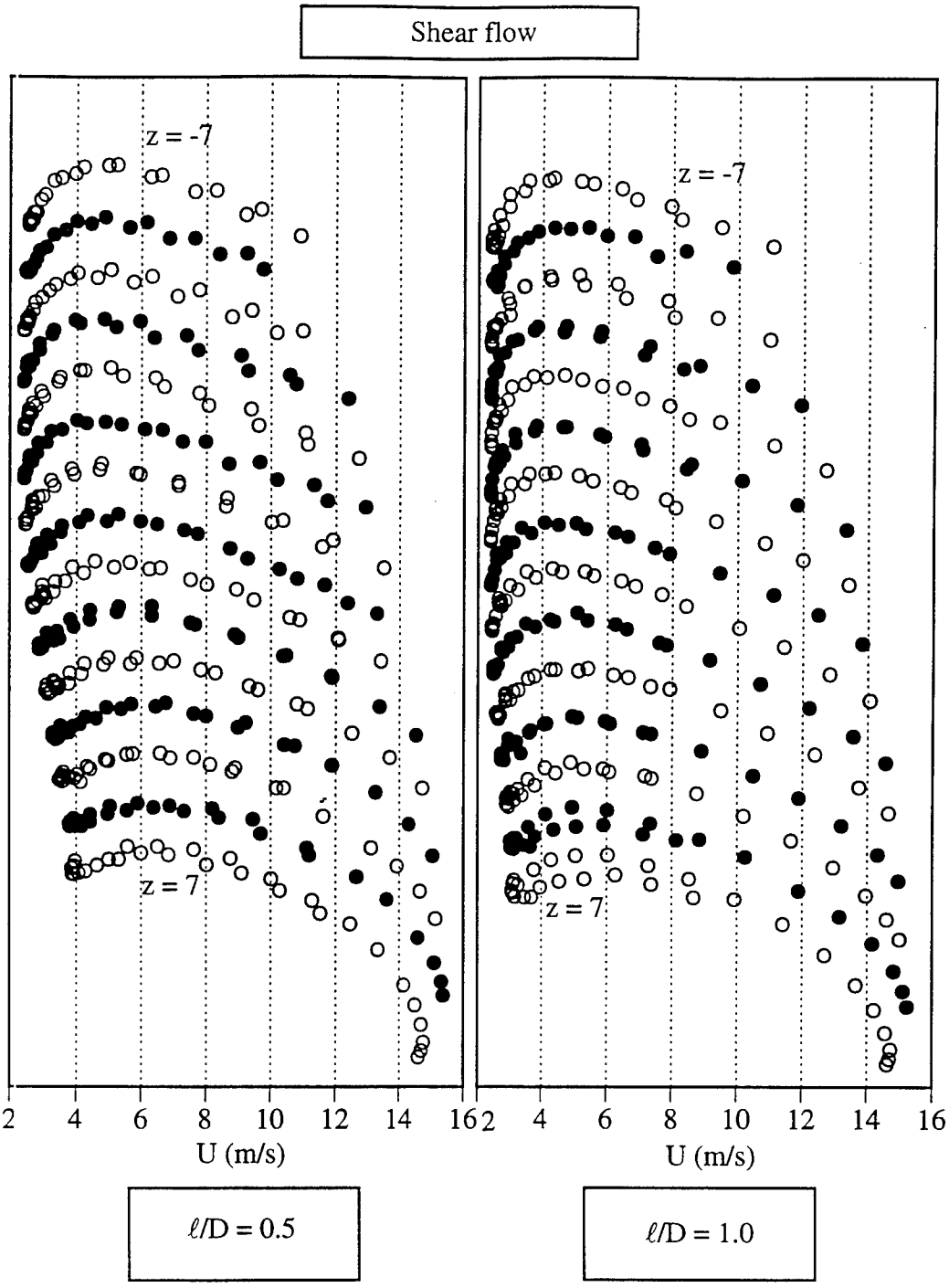

Figure A.17. RMS of fluctuations versus mean velocity. Straight cylinder in shear flow. x/D = 0.65, 20 ensembles of 1024 samples at 1000 Hz.

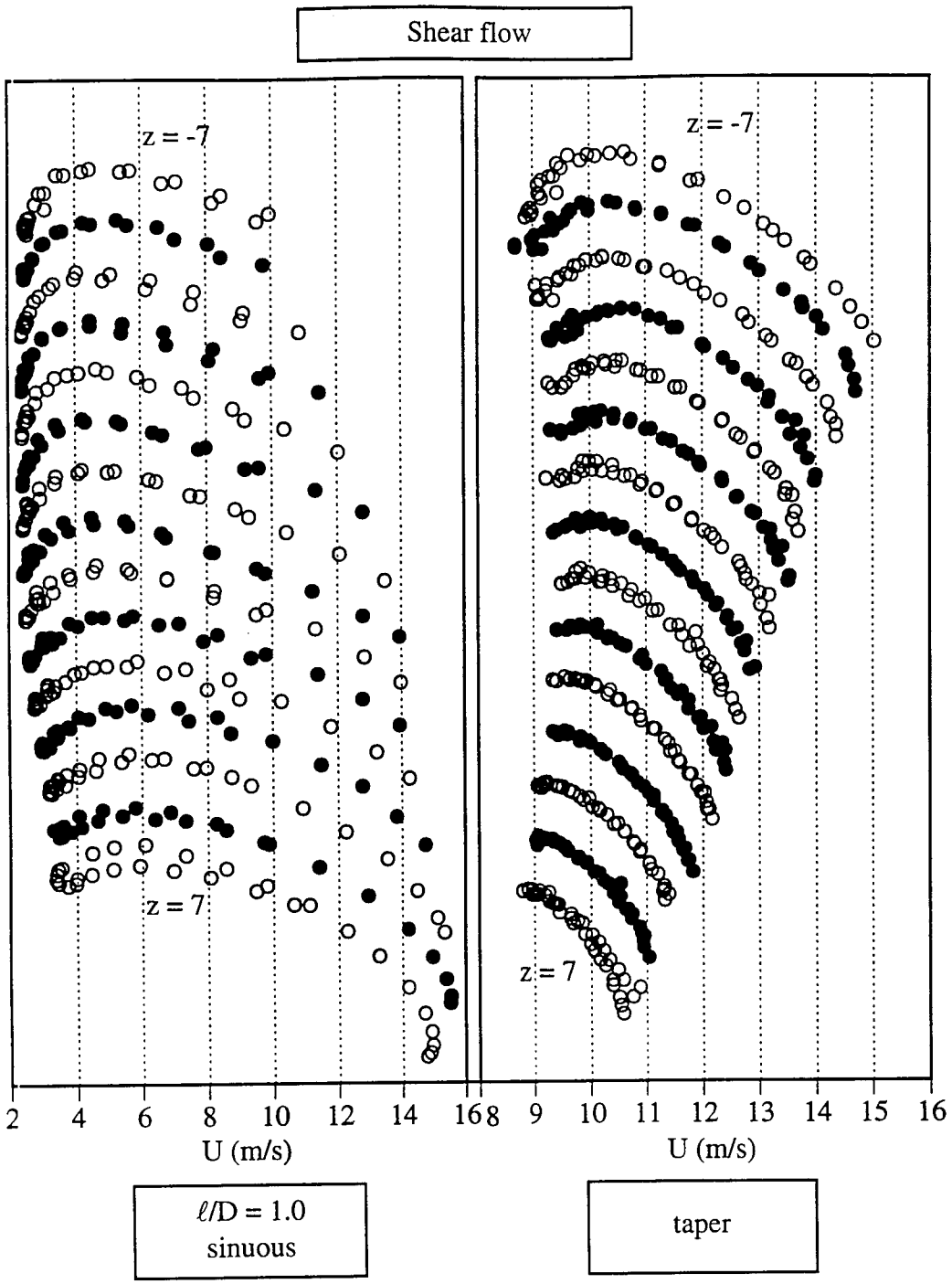

Figure A.18. RMS of fluctuations versus mean velocity. Straight and tapered cylinder in shear flow. x/D = 0.65, 20 ensembles of 1024 samples at 1000 Hz.

APPENDIX B. WIND TUNNEL BLOCKAGE AND UNCERTAINTY ANALYSIS

B.1 Wind Tunnel Blockage Effects

Wind tunnels are commonly used to simulate unbounded flow past a finite body. However, wind tunnel walls impose boundaries on the flow and the interaction of these boundaries with the flow past a body introduces blockage effects. Ideally, the body to be studied should be small enough so that any flow disturbance produced by it will not be significantly influenced by the presence of the wind tunnel walls. In practical applications though this is not always possible and corrections are used to remove the wall interference effects. Various theoretical methods are available to address the effects of wind tunnel blockage on experimental measurements. Maskell [1963] and Rae and Pope [1984] provide techniques that are used to correct wind tunnel data for wall interference effects and thereby allow valid comparisons to be made between data obtained in different wind tunnels. Blockage produced from a bluff body can be divided into four basic types,

1. longitudinal buoyancy
2. wake blockage
3. streamline curvature
4. solid blockage

Longitudinal buoyancy is produced by the increase in the boundary layer thickness on the tunnel walls with downstream distance. The boundary layer is a region of relatively slow moving fluid and therefore in order to satisfy continuity the fluid away from the walls must increase in velocity (assuming parallel tunnel walls). This increase in flow velocity

will produce a streamwise pressure gradient that will impose a force on the body that acts in the same direction as the drag force. Wake blockage has a similar effect and is caused by the relatively slow moving fluid in the wake of the bluff body. As the fluid outside the wake increases in velocity to satisfy continuity a decrease in the downstream pressure is produced. The wind tunnel walls also interfere with the normal bending of the streamlines around the body. This type of blockage can effect the aerodynamic forces and moments acting on the bluff body. Solid blockage is the simplest of all the blockage effects to estimate. The freestream flow must accelerate as it approaches the model due to the reduction in the flow area at the model location. The average increase in velocity can be calculated from incompressible flow conservation laws.

However in the current investigation, the introduction of a splitter plate was shown to effect the shape of the mean velocity profile near the model as seen in Figures 3.10 and 3.11. The longer splitter plates pushed the region of relatively high velocity further downstream and thereby modified the pressure imposed on the wake by the outer flow. Also the shear flow configurations introduced a significant spanwise variation to the blockage effects. Currently there is no accurate theory to account for blockage effects on these flow configurations. Therefore, the corrections used in this investigation are based strictly on experimental measurements.

The mean tunnel velocity was monitored from a reference pitot-static tube located at a mid-span position approximately 36 inches upstream of the model and 4 inches from the top tunnel wall. This location was considered to be essentially free from blockage effects. Data sampling of the reference probe occurred at the same time as the hot wire or pressure measurements so that all measurements could be referenced to the actual tunnel velocity experienced during the sample period. The Strouhal number and pressure coefficient data

recorded in the output file were based on this reference velocity, U_{ref} and dynamic pressure, q_{ref}, respectively.

Vertical mean velocity traverses were performed to account for the variation in velocity between the reference location and the local spanwise positions at the model location. An example of the results for a shear flow configuration is presented in Figure B.1. The example indicates an increase in velocity of over 30% between the flow away from the body at y/D = 3.0 and the flow at y/D = 0.75. Beyond y/D = 3.0 the profile maintained a relatively constant velocity. This transverse position was selected for the measurement of a representative local velocity to be used in the blockage corrections, $U_m(z)$.

The relationship between U_{ref} and $U_m(z)$ was recorded for each configuration and for each span position. The Strouhal number and base pressure measurements were then corrected to reflect the local flow conditions. The Strouhal number presented herein was corrected using the formula,

$$St(z) = St_{ref}\left(\frac{U_{ref}}{U_m(z)}\right) \tag{B.1}$$

The base pressure coefficient was similarly corrected to reflect the local dynamic pressure,

$$C_{pb}(z) = C_{pb_{ref}}\left(\frac{U_{ref}}{U_m(z)}\right)^2 \tag{B.2}$$

B.2 Uncertainty Analysis

Many of the results presented in the current investigation are calculated by formulas that involve other measured quantities. An example would be the Strouhal number which

is produced by the combination of diameter, velocity, and shedding frequency measurements. The individual uncertainties in each measurement contributes to the overall uncertainty in the Strouhal number. The root-sum-square (RSS) method is commonly used to estimate the overall uncertainty in a experimental quantity that depends on other measured quantities. For a given quantity, Q, which is a function of n independent variables, q_1, q_2,...,q_n,with individual uncertainties δq_1, δq_2,...,δq_n, the overall uncertainty in Q can be given by,

$$\delta Q = \sqrt{\left(\frac{\partial Q}{\partial q_1}\delta q_1\right)^2 + \left(\frac{\partial Q}{\partial q_2}\delta q_2\right)^2 + ,\ldots, + \left(\frac{\partial Q}{\partial q_n}\delta q_n\right)^2} \qquad \text{(B.3)}$$

This procedure requires that the functional form of Q can be determined and the partial derivative can be evaluated. The following is an example of the application of this method to estimate the uncertainty in the air density measurement. Using the ideal gas law the air density is evaluated as a function of temperature and pressure,

$$\rho = \frac{P_\infty}{RT_\infty} \qquad \text{(B.4)}$$

where P_∞ is the ambient lab pressure, T_∞ is the ambient lab temperature, and R is the universal gas constant which is assumed to have negligible uncertainty. Partial differentiation of Eq. B.4 produces the relationships required to evaluate Eq. B.3,

$$\frac{\partial \rho}{\partial P_\infty} = \frac{1}{RT_\infty}, \text{ and } \frac{\partial \rho}{\partial T_\infty} = \frac{P_\infty}{RT_\infty^2} \qquad \text{(B.5)}$$

The uncertainty in the density measurement can be expressed as,

$$\delta\rho = \sqrt{\left(\frac{\delta P_\infty}{RT_\infty}\right)^2 + \left(\frac{P_\infty}{RT_\infty^2}\delta T_\infty\right)^2} \qquad \text{(B.6)}$$

where, δP_∞ and δT_∞ are the measurement uncertainty in the lab pressure and temperature respectively. Based on typical ambient conditions the uncertainty in the air density was estimated to be 0.17%. Table B.1 presents the mean values and uncertainty estimates for the measurements obtained in the current investigation.

A bias error can be encountered if the device used to make the measurement is out of calibration. For example, in the current investigation a bias error could be introduced from a time drift in the electronic manometer's zero reference. This bias error was minimized by resetting the zero reference before each experiment. In many cases the effect of bias errors were neglected since the results were based on one measured value relative to some other value. The change in Strouhal number with respect to ℓ/D is one example of this type of result. For these situations it is assumed that the bias errors were the same for all of the compared values and therefore they are neglected in the uncertainty estimates.

Ensemble averaging was used to eliminate time dependence from the mean parameter values. The number of ensemble averages used to determine the power spectra was typically 20 although in some cases 100 ensembles were used (Figures 3.12 - 3.17). Each ensemble consisted of 1024 points acquired at a sample frequency of 200 Hz. The effect of ensemble averaging on the power spectrum is shown in Figure B.2. A relatively broad-band signal was used in the comparison to better illustrate the importance in an adequate number of averages in determining accurate frequency measurements. It is clearly shown that the identification of a dominant peak in the spectrum that accurately reflects the dominant frequency mode in the flow requires more than 5 ensembles. The uncertainty estimates presented in this section assume that the number of ensembles was sufficient to

produce frequency measurements that were accurate to the frequency resolution of the spectrum. The typical sample period used for these measurements was 5.12 seconds which produces a frequency resolution of 0.195 Hz.

variable	dependence	value used in calculation	uncertainty	% of value
laboratory temperature		T_∞=295.23 K	δT_∞=0.56 K	0.20
laboratory pressure		P_∞=98,544 Pa	δP_∞=34 Pa	0.03
diameter		D=0.0508 m	δD=1.27E-4 m	0.25
manometer voltage		E_m=2.5 v	δE_m=0.006 v	0.24
hot wire voltage		E_{HW}=2.5 v	δE_{HW}=0.006 v	0.46
pressure transducer const.		C_t=24.9 Pa/v	δC_t=0.249 Pa/v	1.00
air density	T_∞, P_∞	ρ=1.157kg/m3	$\delta\rho$=0.002kg/m3	0.17
kinematic viscosity	T_∞	ν=1.82E-5m2/s	$\delta\nu$=2.7E-8m2/s	0.15
streamwise distance		x/D	δx/D=0.02	
transverse distance		y/D	δy/D=0.004	
wake width	y/D	d'/D=1.2	δd'/D=0.025	2.10
formation length	x/D	ℓ_f/D=1.0	$\delta\ell_f$/D=0.05	5.00
shedding frequency	T (1)	f_s=43 Hz	δf_s=0.195 Hz	0.45
dynamic pressure	Ct, E_m	q=70 Pa	δq=0.15 Pa	0.21
mean velocity (manometer)	q, ρ	U_m=11.0 m/s	δU_m=0.25 m/s	2.27
mean velocity (hot wire)	q, ρ, E_{HW} (2)	U=11.0 m/s	δU=0.39 m/s	3.55
Reynolds number	D, U, ν	Re=30,000	δRe=700	2.34
Strouhal number	f_s, D, U	St=0.20	δSt=0.007	3.50
base pressure differential	C_t, E_m	ΔP_b=-70 Pa	$\delta\Delta P_b$=0.15	0.21
base pressure coefficient	q, ΔP_b	C_{pb}=1.0	δC_{pb}=0.003	0.30
drag coefficient	q, ΔP	C_d=1.4	δC_d=0.037	2.64

Table B.1 Uncertainty estimates for experimental measurements. (1); T = sample period = 5.12 seconds, (2); hot wire calibration based on 4th order polynomial curve fit.

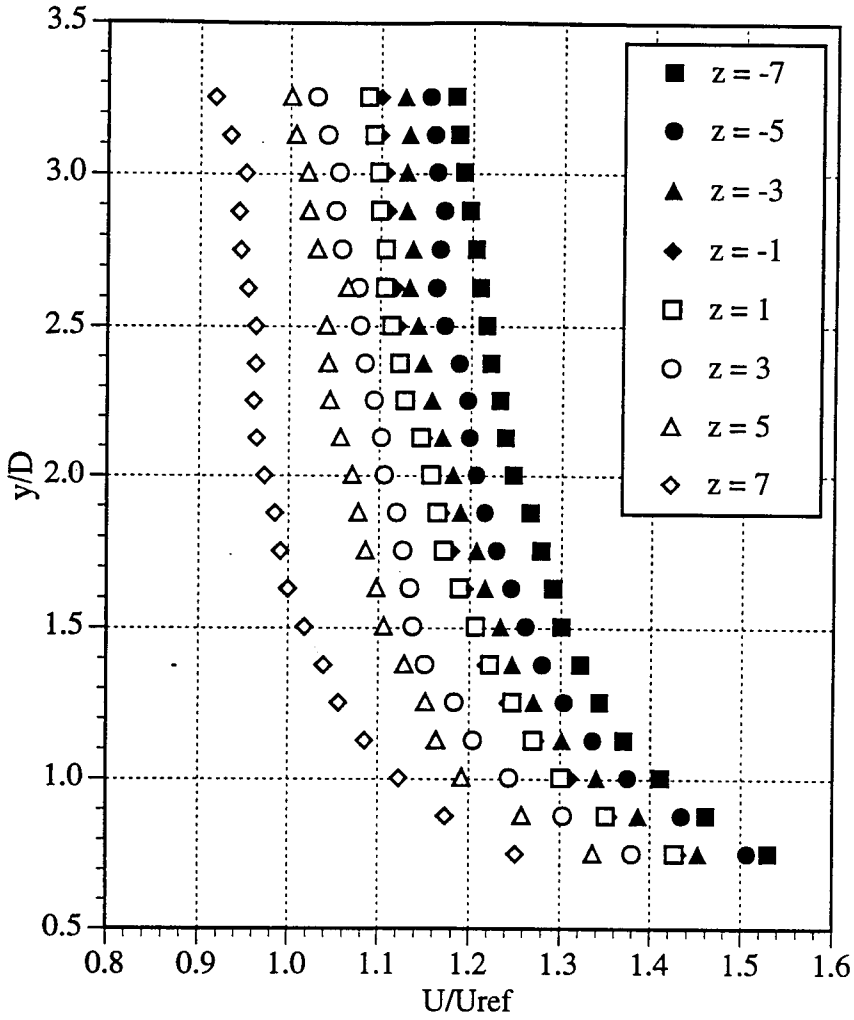

Figure B.1. Vertical velocity profiles for straight cylinder in shear flow. Uref=11.0 m/s, 20 ensembles of 1024 samples at 1000 Hz., x/D=-0.5.

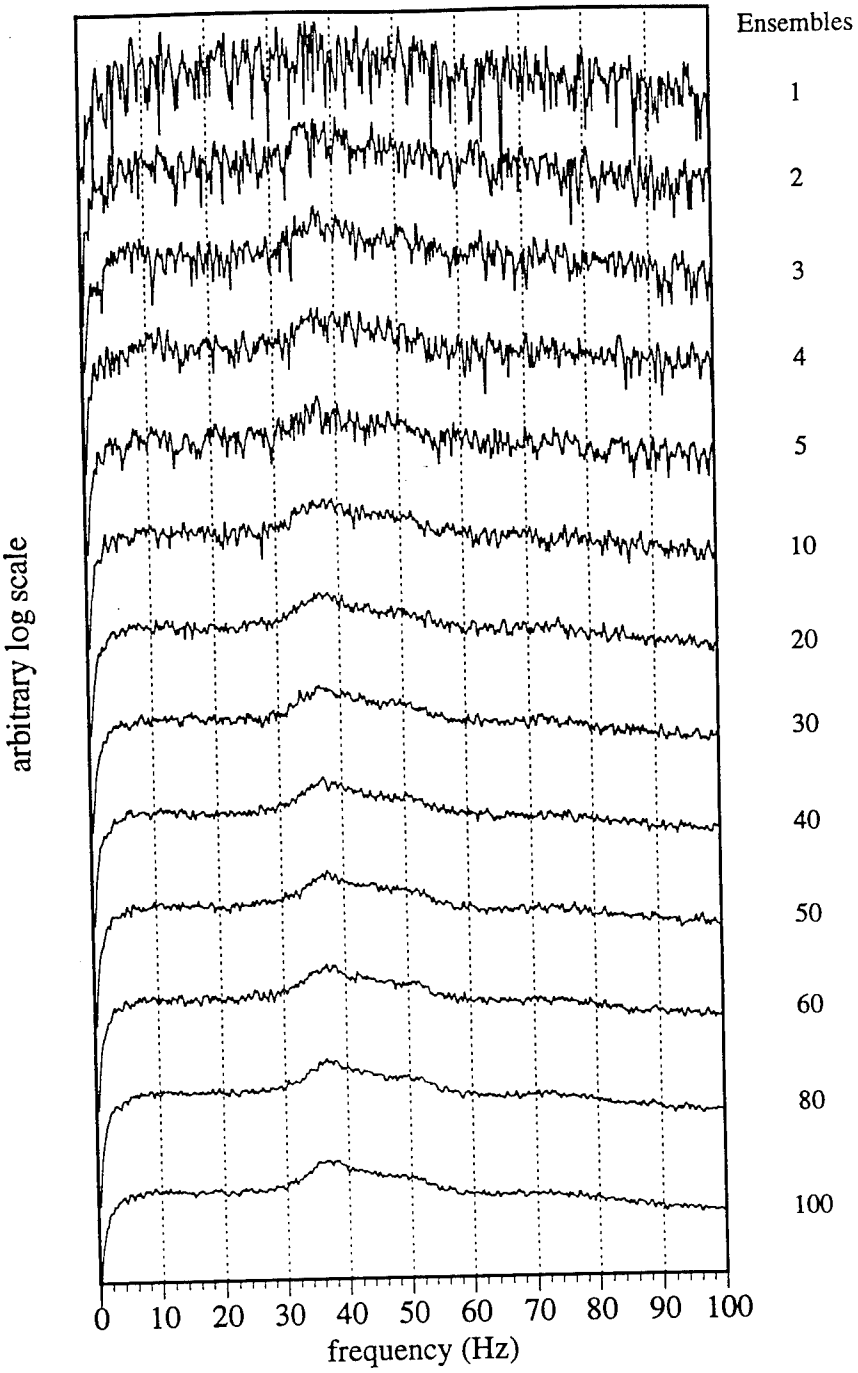

Figure B.2. Power spectrum versus number of ensemble averages. Re = 30,000, 1024 samples, 200 Hz sample rate.

REFERENCES

Apelt, C. J. and West, G. S., 1975 "The effects of wake splitter plates on bluff-body flow in the range 10^4<R<5x10^4." *Journal of Fluid Mechanics*, **71 (part 1)**: pp. 145-160.

Apelt, C. J., West, G. S. and Szewczyk, A. A., 1973 "The effects of wake splitter plates on the flow past a circular cylinder in the range 10^4<Re<5x10^5." *Journal of Fluid Mechanics*, **61, part 1**: pp. 187-198.

Bearman, P. W., 1966 "On vortex street wakes." *Journal of Fluid Mechanics*, **28**(part 4): pp. 625 - 641.

Bearman, P. W.,1993 "The effects three-dimensional imposed disurbances on bluff body near wake flows.", *U. S. Office of Naval Research, Ocean Technology Program Report* No. ONR32194-10.

Bendat, J. S. and Piersol, A. G., *Random Data Analysis and Measurement Procedures* (John Wiley & Sons, 1986).

Bers, A., *Basic Plasma Physics I.* M. N. Rosenbluth, R. Z. Sagdeev, Eds., Handbook of Plasma Physics (North Holland Publishing Co., Amsterdam, Holland, 1983), vol. I Chapter 3.2.

Bloor, M. S., 1964 "The transition to turbulence in the wake of a circular cylinder." *Journal of Fluid Mechanics*, **19**: pp. 290-304.

Bloor, M. S. and Gerrard, J. H., 1966 "Measurements on turbulent vortices in a cylinder wake." *Proceedings of the Royal Society of London, Series A*, **294**.

Borg, J., 1992 "Unsteady base pressure measurements on a bluff body with imposed three-dimensionality" , M.S., Univ. of Notre Dame, Notre Dame, IN.

Borg, J. and Szewczyk, A. A., 1992 "Unsteady base pressure measurements in the near wake of a cylinder with imposed three-dimensional disturbances." in *Proc. IUTAM Symp. on Bluff-Body Wakes, Dynamics, and Instabilities*.

Breidenthal, R., 1980 "Response of plane shear layers and wakes to strong three-dimensional disturbances." *Physics of Fluids*, **23**(10): pp. 1929-1933.

Brown, G. L. and Roshko, A., 1974 "On density effects and large structure in turbulent mixing layers" *Journal of Fluid Mechanics*, **64**: pp. 775.

Cantwell, B. and Coles, D., 1983 "An experimental study of entrainment and transport in the turbulent near wake of a circular cylinder." *Journal of Fluid Mechanics*, **136**: pp. 321-374.

Chomaz, J. M., Huerre, P. and Redekopp, L. G., 1988 "Absolute and convestive instabilities in non-linear systems." *Phys. Rev.Lett.*, **60**: pp. 25.

Chu, H. C., 1993 "An experimental study of the non-linear wave coupling and energy transfer characterizing the transition of a planar jet shear layer." , PhD., Notre Dame, Notre Dame, IN.

Coutanceau, M. and Defaye, J., 1991 "Circular cylinder wake configurations: A flow visualization study." *Applied Mechanics Reviews*, **44**(No. 6): pp. 255 - 305.

Davies, M. E., 1976 "A comparison of the wake structure of a stationary and oscillating bluff body, using a conditional averaging technique." *Journal of Fluid Mechanics*, **75, part 2**: pp. 209-231.

Eisenlohr, H. and Eckelmann, H., 1989 "Vortex splitting and its consequences in the vortex street wake of cylinders a low Reynolds number." *Physics of Fluids*, **A 1 (2)**(February): pp. 189-192.

Elder, J. W., 1959 "Steady flow through non-uniform gauzes." *Journal of Fluid Mechanics*, **5**: pp. 355.

Elsner, S. J., 1982 "A critical investigation of the universal Strouhal number for a bluff body in a linear shear flow.", MS Thesis, University of Notre Dame, Notre Dame, IN.

Fage, A. and Johansen, F., 1927 "The structure of vortex streets." *A. R. C. Reports and Memoranda*, **No. 1143**.

Fiscina, C., 1977 "An Investigation into the Effects of Shear on the Flow past Bluff Bodies." , M.S., University of Notre Dame, Notre Dame, IN.

Gaster, M., 1969 "Vortex shedding from slender cones at low Reynolds numbers." *Journal of Fluid Mechanics*, **38**: pp. 565-576.

Gaster, M., 1971a "Vortex shedding from circular cylinders at low Reynolds numbers." *Journal of Fluid Mechanics*, **46, part 4**: pp. 749-756.

Gaster, M., 1971b "Vortex shedding from slender cones." *Proceedings of a Symposium Volume; Recent Research on Unsteady Boundary Layers,* , Vol 2, Quebec, Canada, pp. 1499-1533.

Gerrard, J. H., 1965 "A disturbance sensitive Reynolds number range of the flow past a circular cylinder." *Journal of Fluid Mechanics*, **22**: pp. 187.

Gerrard, J. H., 1966 "The mechanics of the formation region of vortices behind bluff bodies." *Journal of Fluid Mechanics*, **25, part 2**: pp. 401-413.

Gerrard, J. H., 1978 "The wakes of cylindrical bluff bodies at low Reynolds number." *Phil. Trans. Royal Soc. Lon. A*, **288**: pp. 351-382.

Griffin, O. M., 1981 "Universal similarity in the wake of stationary and vibrating bluff structures." *ASME Journal of Fluids Engineering*, **103**(March): pp. 52-58.

Griffin, O. M., 1985 "Vortex shedding from bluff bodies in a shear flow: a review." *ASME*, **107**: pp. 298-306.

Hammache, M. and Gharib, M., 1989 "A novel method to promote parallel vortex shedding in the wake of circular cylinders." *Physics of Fluids A*, **1**(10).

Konig, M., Eisenlohr, H. and Eckelmann, H., 1990 "The fine structure in the Strouhal-Reynolds number relationship of the laminar wake of a circular cylinder." *Physics of Fluids A*, **2**: pp. 1607.

Konig, M., Eisenlohr, H. and Eckelmann, H., 1992 "Visualization of the spanwise cellular structure of the laminar wake of wall-bounded circular cylinders." *Physics of Fluids A*, **4**: pp. 869-872.

Kourta, A., Boisson, H. C., Braza, M., Chassaing, P. and Mihn, H. H., 1987 "Wake-shear layer interaction and the onset of turbulence behind a circular cylinder." *Turbulent Shear Flows 5, Springer-Verlag*, : pp. 82-97.

Kronauer, R. E., 1964 "Predicting eddy frequency in separated wakes." in *IUTAM symposium on concentrated vortex motions in fluids*. Univ. of Michigan, Ann Arbor, Michigan, 6-11 July.

Maskell, E. C., 1963 "A theory of the blockage effects on bluff bodies and stalled wings in a closed wind tunnel." *British ARC R&M no. 3400*, .

Maull, D. J. and Young, R. A., 1973 "Vortex shedding from bluff bodies in a shear flow." *Journal of Fluid Mechanics*, **60, part 2**: pp. 401-409.

National Instruments, *LabVIEW 2 Analysis VI Library Reference Manual* (National Instruments Corp., 1991).

Meiburg, E. and Lasheras, J. C., 1988 "Experimental and numerical investigation of the three-dimensional transition in plane wakes." *Journal of Fluid Mechanics*, **190**: pp. 1-37.

Milne-Thomson, L. M., *Theoretical Hydromechanics* (Macmillan, London, 1938).

Monkewitz, P. A. and Nguyen, L. N., 1987 *Journal of Fluids Structures*, **1**: pp. 165.

Morkovin, M. V., 1964 "Flow around circular cylinder- a kaleidoscope of challenging fluid phenomena." in *ASME Symposium on Fully Separated Flows*. Philadelphia, Pa.

Nebres, J. V., 1992 "Wake similarity and vortex formation for two-dimensional bluff bodies." , PhD., Univ. of Notre Dame, Notre Dame, IN.

Oertel, H., 1990 "Wakes behind bluff bodies." *Annual Review of Fluid Mechanics*, **22**: pp. 539-564.

Papangelou, A., 1992 "Vortex shedding from slender cones at low Reynolds numbers." in *IUTAM Symposium on bluff body wakes, dynamics and instabilities*. Göttingen, Germany.

Payne, F. M., 1987 "The structure of leading edge vortex flows including vortex breakdown." , PhD., Univ. of Notre Dame.

Pearson, L. F. and Szewczyk, A. A., 1992 "The near-wake of a circular cylinder with a spanwise periodic trailing edge splitter plate." in *Proc. Symp. Flow-Induced Vib. ASME-WAM*.

Petrusma, M. S. and Gai, S. L., 199x "Flow topology and Reynolds shear stress in the wake of a segmented blunt trailing edge aerofoil." 11th Australasian Fluid Mechanics Conference.

Piccirillo, P. S. and Atta, C. W. V., 1992 "Experiments on vortex shedding behind linearly tapered cylinders." in *IUTAM Symposium on bluff body wakes, dynamics and instabilities*. Göttingen, Germany:

Provansal, M., Mathis, C. and Boyer, L., 1987 "Bérard-von Kármán instability: transient and forced regimes." *Journal of Fluid Mechanics*, **182**.

Rae, W. H. and Pope, A., *Low-speed wind tunnel testing* (John Wiley and Sons, New York, 1984).

Rodriguez, O., 1991 "Base drag reduction by control of the three-dimensional unsteady vortical structures." *Experiments in Fluids*, **11**: pp. 218-226.

Rooney, D. M. and Peltzer, R. D., 1981 "Pressure and vortex shedding patterns around a low aspect ratio cylinder in a sheared flow at transitional Reynolds numbers." *Transactions of the ASME, Journal of Fluids Engineering*, **103**(March): pp. 88-96.

Rooney, D. M. and Peltzer, R. D., 1982 "The effects of roughness and shear on vortex shedding cell lengths behind a circular cylinder." *Transactions of the ASME, Journal of Fluids Engineering*, **104**(March): pp. 72-80.

Roshko, A., 1953 "On the development of turbulent wakes from vortex streets." *NACA TN 2913* .

Roshko, A., 1954 "A new hodograph for free-streamline theory." *NACA Technical Note #3168*, : pp. 1 - 39.

Roshko, A., 1955 "On the wake and drag of bluff bodies." *Journal of the Aeronautical Sciences*, (February): pp. 124-132.

Sarpkaya, T., 1979 "Vortex-induced oscillations, a selective review." *Journal of Applies Mechanics*, **46**(June): pp. 241-258.

Schlichting, H., *Boundary Layer Theory* (McGraw-Hill, 1979).

Simmons, J. E. L., 1977 "Similarities between two-dimensional and axisymmetric vortex wakes." *Aeronautical Quarterly*, **28**(part 1): pp. 15-20.

Stansby, P. K., 1974 "The effects of end plates on the base pressure coefficient of a circular cylinder." *Aeronautical Journal*, (January).

Szepessy, S. and Bearman, P. W., 1992 "Aspect ratio and end plate effects on vortex shedding from a circular cylinder." *Journal of Fluid Mechanics*, **234**: pp. 191-217.

Thomas, F. O., 1991 "Structure of mixing layers and jets." *Appl. Mech. Rev.*, **44**(3): pp. 119-153.

Thomas, F. O. and Chu, H. C., 1989 "An experimental investigation of the transition of a planar jet: subharmonic suppression and upstream feedback." *Phys Fluids A*, **3**(6): pp. 1544-1559.

Tombazis, N., 1993 "Effects of three-dimensional disturbances on bluff body near wakes." , PhD., Imperial College, London.

Triantafyllou, G., Triantafyllou, M. and Chryssostomidis, C., 1987 "Stability analysis to predict vortex street characteristics and forces on circular cylinders." *Transactions of the ASME, Journal of Offshore Mechanics and Arctic Engineering*, **109**: pp. 148-154.

Triantafyllou, G. S., Triantafyllou, M. S. and Chryssostomidis, C., 1986 "On the formation of vortex streets behind stationary cylinders." *Journal of Fluid Mechanics*, **170**: pp. 461 - 477.

Unal, M. F. and Rockwell, D., 1988 "On vortex formation from a cylinder. Part 1. The initial instability." *Journal of Fluid Mechanics*, **190**: pp. 491-512.

Wei, T. and Smith, C. R., 1986 "Secondary vortices in the wake of circular cylinders." *Journal of Fluid Mechanics*, **169**: pp. 513-533.

White, F. M., *Fluid Mechanics* (McGraw-Hill, 1986).

Williamson, C. H. K., 1989 "Oblique and parallel modes of vortex shedding in the wake of a circular cylinder at low Reynolds numbers." *Journal of Fluid Mechanics*, **206**: pp. 579-627.

Williamson, C. H. K., 1991 "The natural and forced formation of spot-like lambda-structures caused by vortex dislocations in a wake." in *Eighth symposium on turbulent shear flows*. Technical University of Munich.

Williamson, C. H. K., 1992 "The natural and forced formation of spot-like 'vortex dislocations' in the transition of a wake." *Journal of Fluid Mechanics*, **243**: pp. 393-441.

Woo, H. G. C., Cermak, J. E. and Peterka, J. A., 1989 "Secondary flows and vortex formation around a circular cylinder in constant-shear flow." *Journal of Fluid Mechanics*, **264**: pp. 523-542.